Imperial College London

Department of Materials

Developing small scale fracture tests for polycrystalline diamond

Giorgio Sernicola

January 2018

Submitted for the degree of

Doctor of Philosophy (PhD)

Declaration of originality

I hereby declare that this thesis reports my original work. Any contributions to the work, other than my own, has been properly acknowledged.

Giorgio Sernicola

Abstract

Opening ceramics up to a wider range of applications, where their high hardness and high strength are required, necessitates our understanding and improving of their fracture properties. In the last three decades, such improvements have been sought through developing our understanding of toughening mechanisms, typically involving microstructure control that focuses on crack deflection and grain bridging at grain boundaries and interfaces. However, these are often difficult to engineer, as changing microstructural processing (e.g. through heat treatment, chemistry or powder processing) does not result in a one-to-one correlation with performance, since the influence of microstructure on crack path is varied and complex.

Recent developments on characterisation at the micro-scale therefore present an opportunity to broaden our understanding of the role of individual factors on the bulk performance.

To investigate the fracture properties of individual features (i.e. individual crystallographic planes, grain boundaries or interfaces), a testing method was developed. This approach is based on the double cantilever wedging to measure the fracture energy change during stable crack growth and was successfully applied at the micron scale inside a scanning electron microscope. Direct view of the crack growth in the sample and measurement of the energy absorbed during fracture, without use of load-displacement data, is afforded through the combination of a stable test geometry with an image based analysis strategy.

In addition to these precise tests, characterisation of the role of microstructure on crack paths in polycrystalline metal-ceramic composites was carried out. The focus has been on using high angular resolution electron backscatter diffraction combined with microindentation, to correlate intragranular residual stress gradients, due to thermal expansion mismatches, to crack deflection.

Fracture energy of individual crystallographic planes and interfaces was measured in both brittle and brittle/ductile systems. In addition, local residual stresses and microstructure in diamond were related to fracture path.

Acknowledgements

I would like to express sincere thanks to my supervisors Dr Ben Britton and Dr Finn Giuliani for their constant personal and professional support and guidance. Their motivation, passion and enthusiasm has been genuinely contagious.

I am grateful to Element Six for providing financial support for the research presented in this thesis and for allowing me to use their facilities. In particular I want to extend my sincere thanks to the many people at the Global Innovation Centre that helped me with sample production and preparation and that contributed to steer the research towards interesting routes, with a special mention for Dr Valentine Kanyanta, Dr Roger Nilen, Dr Serdar Özbayraktar Dr Xiaoxue Zhang and Dr Jonee Zunega.

My sincere thanks go to Dr Daniel Balint, Tommaso Giovannini, Dr Rui Hao, Dr Tea-Sung Jun, Dr James Kermode, Punit Patel and Garry Stakalls for their help and collaboration on key aspects of this project.

I would like to thank Prof Eduardo Saiz and Dr Luc Vandeperre for the stimulating discussions on my work and for being always available to share their expertise.

My gratitude goes also to all the people that have orbited the CASC office and the Department of Materials for all the great moments spent together over the past four years. I am truly lucky to have found many friends here.

It would be an understatement to say that my family deserves my deepest gratitude. We have had to endure some hard times, but your unconditional love and encouragement has given me the strength to carry this work on to its final stage.

Most importantly, I cannot begin to express my gratitude to Valentina for brightening most of otherwise dull moments, for listening to and having to tolerate me during the writing of this dissertation. Thank you for bringing me back every time I was on the brink.

Table of contents

List of figures

List of tables

List of abbreviations

AFM   Atomic Force Microscope

AMDCB   Applied Moment Double Cantilever Beam

CCD   Charge-Coupled Device

CNB   Chevron-Notch Beam

CTE   Coefficient of Thermal Expansion

CVD   Chemical Vapour Deposition

DCB   Double Cantilever Beam

DT   Double Torsion

EBSD   Electron Backscatter Diffraction

EBSP   Electron Backscatter Pattern

FIB   Focused Ion Beam

FSD   Forescatter Detector

G30   Grade 30 (powder)

G4   Grade 4 (powder)

HPHT   High Pressure-High Temperature

IPF   Inverse Pole Figure

LPS   Liquid Phase Sintering

LV   Liquid-Vapour

OPS   Oxide Polishing Suspension

PCD   Polycrystalline Diamond

PQ   Pattern Quality

RGB   Red, Green and Blue (colour model)

SCF   Surface Crack in Flexure

SEM	Scanning Electron Microscope
SENB	Single-Edge Notch Beam
SEPB	Single-Edge Pre-cracked Beam
SEVNB	Single Edge V Notched Beam
SL	Solid-Liquid
STD	Standard substrate
SV	Solid-Vapour
TC	Tape Casted
TRS	Transverse Rupture Strength
WOF	Work Of Fracture

List of publications and conferences

Part of the work of this thesis has been presented in the following publications and conferences.

Publications

- Bhowmik A, Lee J, Britton T Ben, Liu W, Jun T-S, Sernicola G, Karimpour M, Balint DS, Giuliani F (2018) Deformation behaviour of [001] oriented MgO using combined in-situ nano-indentation and micro-Laue diffraction. Acta Mater 145:516–531. doi:https://doi.org/10.1016/j.actamat.2017.12.002.

- Sernicola G, Giovannini T, Patel P, Kermode JR, Balint DS, Britton T Ben, Giuliani F (2017) In situ stable crack growth at the micron scale. Nat Commun 8:108. doi:10.1038/s41467-017-00139-w.

- Jun T-S, Sernicola G, Dunne FPE, Britton TB (2016) Local deformation mechanisms of two-phase Ti alloy. Mater Sci Eng A. doi: 10.1016/j.msea.2015.09.016

- Jun T-S, Zhang Z, Sernicola G, Dunne FPE, Britton TB (2016) Local strain rate sensitivity of single α phase within a dual-phase Ti alloy. Acta Mater. doi: 10.1016/j.actamat.2016.01.057

- Bhowmik A, Dolbnya IP, Britton TB, Jones NG, Sernicola G, Walter C, Gille P, Dye D, Clegg WJ, Giuliani F (2016) Using coupled micropillar compression and micro-Laue diffraction to investigate deformation mechanisms in a complex metallic alloy Al13Co4. Appl Phys Lett. doi: 10.1063/1.4944486

- Ferraro C, Garcia-Tuñon E, Rocha VG, Barg S, Fariñas MD, Alvarez-Arenas TEG, Sernicola G, Giuliani F, Saiz E (2016) Light and Strong SiC Networks. Adv Funct Mater 26:1636–1645. doi:10.1002/adfm.201504051.

Conferences

- In situ stable crack growth at the micron scale; poster presentation at GRC, Lewiston, USA, 2016.

- In situ fracture tests of silicon carbide bi-crystals; talk at MRS Fall, Boston, USA, 2015;

- In situ fracture tests of brittle materials at the microscale; talk at ECI, Albufeira, Portugal, 2015;

- HR-EBSD on Polycrystalline Diamond, poster presentation at the De Beers Diamond Conference, Warwick, UK, 2015;

- In situ fracture tests of brittle materials at the microscale, talk at ICM 12, Karlshruhe, Germany, 2015;

- Stress gradients measurements on polycrystalline diamonds, talk at 1-DRAC, London, UK, 2015;

- HR-EBSD on Polycrystalline Diamond, poster presentation at the RMS EBSD conference, Glasgow, UK, 2015;

Introduction

Polycrystalline diamond composites (PCD) were first sintered in the 1970s following research efforts focused on producing new, more durable materials to use as cutting tools [1,2]. These composites are a perfect example of a complex microstructure composed of two phases with very different properties. The first, diamond, constituting between 80 and 95 vol% of the material, is extremely hard, stiff, with low thermal expansion coefficient and characterised by brittle fracture preferentially along weak cleavage planes. The other is a metal binder, often cobalt, and is softer, ductile and with a thermal expansion coefficient up to 10 times larger than diamond. The product is typically sintered at 5-10 GPa and 1400-1800 °C to form a dense material in which diamond grains are held together through a network by the metal phase or bonded directly to other diamond grains.

These materials are required to have a very high hardness for wear resistance but also a good fracture toughness to avoid catastrophic failure. However, optimising both of these properties is challenging and still a major issue for the industry. It is not always possible to link one or more mechanical properties, such as hardness, strength, wear resistance and fracture toughness to changes in grain size, metal content, sintering conditions etc., when investigating the bulk material. This is due to the impossibility of changing only one parameter at a time and to isolate individual effects. For instance, it was found that a change in the starting powder size also yields a change in cobalt content in the final material [3,4]. In turn, a change in cobalt content was found to alter the residual stress state in the material [5,6]. While our current knowledge of the fracture of brittle materials comprehensively explains the link between grain size and fracture toughness, findings in these studies cannot conclusively define the role of cobalt and residual stresses on the performance.

Fracture in single crystal diamond tends to follow the easy cleavage {111} planes, but in PCDs transgranular fracture is most often observed with intergranular occurring in some particular conditions (e.g. high loading rate, high temperature or after exposure to high temperatures) [7–9]. However, even under macroscopic transgranular fracture, local crack deflections within the grains or along the boundaries have been observed, but their origin was not extensively justified [7]. The presence of residual stresses varying across the whole cutter but also at the lengthscale of the microstructure, attributed to the thermal expansion coefficient mismatch between the different components, was shown in several studies [5,6,10–19]. Therefore a hypothesis for this work was that stress variations within individual grains might be present in PCDs and have a role on the fracture path.

The aim of this work was, therefore, to relate the fracture behaviour observed at the macroscale in the literature to the intrinsic properties of diamond and that of microstructural features of PCD. The focus was on developing a novel technique that enables the measurement of fracture energy evolution with (stable) crack growth along crystal planes/boundaries/interfaces. Specifically, double cantilever beams of micrometre size were fabricated using focused ion beam and tested *in situ* a SEM using a displacement-controlled nanoindenter.

In addition, measurement of in-plane stress gradients within crystallographic grains was carried out in PCDs through analysis of electron backscatter diffraction patterns. After mapping the residual stress gradients in selected areas of a PCD sample, microindentation was used to generate cracking in a mapped area to investigate the effect of residual stress gradients and microtexture on fracture path.

Structure of the thesis

The problems of interest for this work are not exclusive of PCDs but common to many real advanced polycrystalline ceramics for which the knowledge of the role of grain boundaries,

interfaces and residual stresses on the fracture mechanics built upon the theory has been often difficult to test experimentally employing conventional methods. Therefore, a summary of the fundamental theory of fracture mechanics in brittle materials is presented in chapter 1 together with a discussion on the scope and limitations of conventional and novel testing techniques currently used to investigate it. In particular, here some of the limitations of these test approaches that inspired part of this thesis work to address them and develop an innovative solution are discussed. Following, a literature review of the properties of PCDs highlighting the issues most relevant to this work is provided in chapter 2. Details of the materials and methods used in this work can be found in chapter 3, including the production and preparation of the PCD samples investigated, the setup used for the *in situ* mechanical testing and background on the high angular resolution EBSD, i.e. the technique used to map the local stress variations within diamond grains. Chapter 4 provides the details on the fabrication and testing of double cantilever beams at the microscale, along with the results obtained on the single and bi-crystals tested, whilst chapter 5 discusses the effect of processing parameters on the final microstructure in PCD components and how this affects the fracture behaviour. Finally overall key aspects of this work are provided in the conclusions and some ideas for further work discussed.

Fracture in polycrystalline ceramics

Mechanical tests conducted on different ceramics readily highlight one of their most common feature and major limitation: they are intrinsically brittle. As such their toughness is a major concern when designing the production process of structural components. However, the failure behaviour and so the toughness can greatly differ between single crystals and polycrystalline ceramics, suggesting that fracture toughness can be manipulated with microstructure. Therefore, our ability to improve ceramics performance relies on our understanding of the effect of microstructure on the fracture properties and our ability to measure it.

An overview of the classic concepts of fracture mechanics of brittle materials is provided together with a discussion of the role of microstructure on the failure of polycrystalline ceramic materials. Most of the fundamental concepts presented in the paragraph 1.1 can be found in classic academic books as those from Lawn [20] and Anderson [21].

1.1 Fracture of brittle solids

Mechanical behaviour of ceramics is generally characterised by elastic deformation and brittle failure in tension. Many ceramics exhibit a degree of nonlinearity in their stress-strain curve, however this is usually rather small at room temperature and overcome by cracking in macroscopic samples. Under these conditions the fracture of ceramics is described with linear elastic fracture mechanics.

Three different basic modes are usually used to describe the crack displacement in fracture mechanics, but of these the opening of the crack under tensile stress applied on the crack walls, also known as mode I, is the most severe for the study of failure in brittle materials.

The theory developed by Griffith [22] describes the effect of the presence of a crack in a plate under tensile stress on the load at fracture. Griffith theory builds upon the earlier considerations

drawn by Inglis on the effect of an elliptical hole on the stress distribution in a plate under uniform stress. Inglis [23] showed that the local stress in the proximity of the ellipses corner was several times higher than the remotely applied stress.
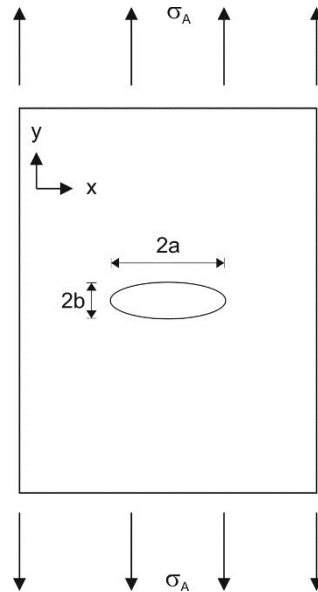
Figure 1.1 — Plate under tensile stress σ$_A$ containing an elliptical hole of semi-axes a,b.

The presence of a hole *2a* long and *2b* wide, as drawn in Figure 1.1, in a plate with both height and width much bigger than the hole, loaded in tension perpendicularly to the major axis of the hole with a stress σ_A, according to Inglis modifies the stress at the tip of the major axis to:

$$\sigma_{tip} = \sigma_A \left(1 + \frac{2a}{b} \right) \tag{1.1}$$

This alone suggests that the presence and geometry of a crack, which can be seen as a very narrow ellipse (a≫b), acts as a stress concentrator and could dramatically impact on the fracture properties of a component. However, Inglis' analysis shows no dependency on the crack size when in practice longer cracks appeared to propagate more easily than smaller ones. Later, Griffith conducted experiments to investigate the relationship between flaw size and stress applied in tensile tests on glass specimens, finding that the product of the stress at fracture and the square root of the flaw length resulted to be nearly constant. To describe such observations, Griffith analysed the problem

from a thermodynamic perspective by seeking the configuration that minimised the total free energy of the system.

As described by Lawn [20], the total energy U in a system where a crack growth takes place can be separated into two terms:

$$U = U_M + U_S \tag{1.2}$$

where U_M is the mechanical energy supplied by the internal strain energy and external forces, and U_S is the free energy required to create two new surfaces, under the assumption that for a linear elastic material the energy is not dissipated through plastic deformation or otherwise, therefore is a thermodynamic reversible process.

The mechanical energy term can be itself divided in two terms, i.e. $U_M = U_E + U_A$ where U_E is the strain potential energy elastically stored in the material and U_A is the potential energy supplied by external loading. A conflict between this two terms arises as the crack extends since the first tends to decrease with crack extension $(dU_M/da < 0)$, while the latter increases $(dU_S/da > 0)$. This is often named the Griffith energy-balance concept, which at equilibrium reduces to [20]:

$$dU/da = 0 \tag{1.3}$$

Griffith calculated the mechanical energy terms of Equation (1.2) for a plate containing a crack of length $2a$ subjected to a constant uniform tensile stress σ. Under such conditions, in a material obeying Hooke's law (i.e. linear elastic), during crack formation or extension:

$$U_A = -2U_E \tag{1.4}$$

Using the Inglis analysis Griffith calculated the strain energy density for unit width of crack front as:

$$U_E = \frac{\pi a^2 \sigma^2}{E'} \tag{1.5}$$

where E' equals the Young's modulus E if loading conditions are of plane stress or $E/(1 - v^2)$ for plane strain (with v being the Poisson's ratio). Griffith then considered that the extension of the crack is associated with the creation of two surfaces, so that for unit width of crack front:

$$U_S = 4a\gamma \tag{1.6}$$

where γ is the free surface energy per unit area.

Applying the equilibrium condition of Eq. (1.3) to Eqs. (1.5) and (1.6) we obtain conditions for the fracture stress:

$$\sigma_F = \left(\frac{2\gamma E'}{\pi a}\right)^{1/2} \tag{1.7}$$

Irwin [24] defined the term $G = -dU_M/da$, namely the energy available to an increment of crack extension, as *mechanical-energy-release rate*, where the term rate here refers to the rate of change of the energy with crack area and not time.

From the definition of G and the Eqs. (1.3), (1.5) and (1.6) it is readily evident that crack extensions occurs when G reaches the critical°value:

$$G_c = dU_S/da = 4\gamma \tag{1.8}$$

Therefore, G_c represents the initial fracture energy of the material. For the system described so far, a uniform wide plate under tensile stress containing a crack of length $2a$, we obtain:

$$G = \frac{2\pi\sigma^2 a}{E'} \tag{1.9}$$

Eq. (1.8) is only valid for an initially homogeneous solid that the crack separates in two like half-bodies. Irwin and Orowan independently conceived an extension of the Griffith concept to take into consideration dissipative processes taking place at the crack tip. The assumption of this approach is that the crack tip remains sharp, however the stresses at the front may be affected within a very small area compared to the dimensions of the loaded piece. Within this generalisation of the Griffith concept a term $R = dU_S/da$ can be defined that identifies the crack resistance energy, so that:

$$dU = dU_M + dU_S = -Gda + Rda \tag{1.10}$$

At equilibrium, crack extension occurs when $G - R = 0$ and $G = G_c$, giving $G_c = R$ (the crack extends at $G_c > R$ and retracts at $G_c < R$). Therefore R can be used as an indication of material

toughness for a broader range of materials than in Griffith's analysis. For instance, with this formulation:

- $R = 2\gamma_B$ for the separation of two like half-bodies;

- $R = \gamma_A + \gamma_B - \gamma_{AB}$ for the separation of two unlike but coherent half-bodies (A-B);

- $R = 2\gamma_B - \gamma_{GB}$ for the separation along a grain boundary where γ_{GB} is the configurational energy of the boundary relative to the virgin B-B state.

- $R = \gamma_A + \gamma_B - \gamma_{IB}$ for the separation along an interphase boundary, where γ_{IB} is the formation energy of the interphase boundary

Although the energy required for crack extension is not dependent on whether the body is loaded in displacement control or load control, the crack growth can be of stable or unstable nature depending on how G and R evolve with the crack extension.

While the variation of R with crack length is related to the material behaviour, variation of G with crack length stems from the loading configuration. It can be easily shown [20,25] that a stress applied in load control to a cracked specimen is generally associated to a net increase in strain energy with crack extension ($dG/da > 0$), whereas displacement-controlled loading is generally associated to a net decrease in strain energy ($dG/da < 0$). Therefore, for a material with a flat R-curve (i.e. R is constant with crack extension) or rising R-curve the following condition holds true at constant displacement (i.e. fixed ends):

$$\frac{dG}{da} \leq \frac{dR}{da} \tag{1.11}$$

After an increment of crack extension da, the system releases a component of the energy stored. Under the conditions in Eq. (1.11), the energy stored decreases until this is no more sufficient to extend the crack of a further da; thus resulting in a stable crack growth.

Analytical solutions for the stress and displacement fields near the crack tip in an isotropic material with linear elastic behaviour were proposed by several authors, as reported by Anderson [25], and can be reduced in simple forms to:

$$\sigma_{ij} = \left(K/\sqrt{2\pi r}\right) f_{ij}(\theta) \tag{1.12}$$

in which σ_{ij} is the stress tensor, r and θ are defined as in Figure 1.2, f_{ij} is a dimensionless function of θ, and K is defined as the stress intensity factor;

$$u_i = (K/2E)\sqrt{r/2\pi}\, f_i(\theta) \tag{1.13}$$

in which u_i is the displacement tensor, E the Young's modulus.
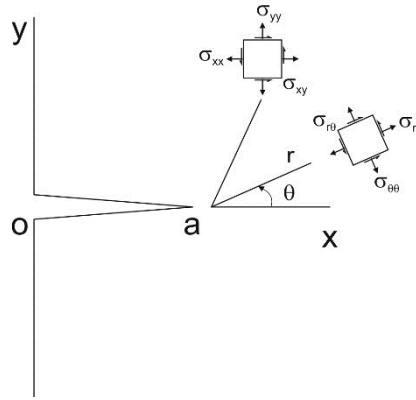
Figure 1.2 — Stress field at Irwin slit-crack tip *a* showing rectangular and polar-coordinate components. Adapted from [20].

The stress intensity factor for the same system considered in (1.9) is:

$$K_I = \sigma\sqrt{\pi a} \tag{1.14}$$

A unique relationship exists between G, which describes the global behaviour, and K, which is a local parameter, and can be shown that in mode I this reduces to:

$$G = \frac{K_I^2}{E'} \tag{1.15}$$

The stress intensity factor has been typically preferred to the energy release rate in certain engineering fields, that is where the design of structures is based on safe values of stress they can withstand, with the rationale that K_{Ic} provides the critical stress not to be overcome at the crack tip. Therefore, once the critical stress intensity factor K_{Ic} is known along with the operating stress,

it is possible to calculate the maximum crack length permissible in the structure to avoid rapid crack growth.

It is clear that the stress intensity factor and the energy release rate become of great importance when we can determine their value for a specific crack system knowing the external loading. This would allow an artificial crack to be introduced in a specimen of well-defined geometry subject to known loading conditions in order to determine the fracture properties of that specific material system.

1.2 Conventional tests for ceramics

A wide range of test geometries exist to investigate the fracture toughness or fracture energy of ceramics. These include a number of variations of flexural, double torsion, double cantilever beam tests and indentation methods (see Figure 1.3).

Each of these tests has advantages and disadvantages and a choice is made depending on the size and shape available for the material to be tested, fracture properties of interests (e.g. fracture toughness of large or small cracks, R-curve behaviour, etc.) and its other properties that can influence the good result of the test (e.g. hardness, elastic moduli, etc.).

Although fracture toughness is a material property, values measured using different test methods often differ greatly. Some of these methods are described by international standards in an attempt to enable a relatively easy testing routine to be performed that results in comparable values among different materials.
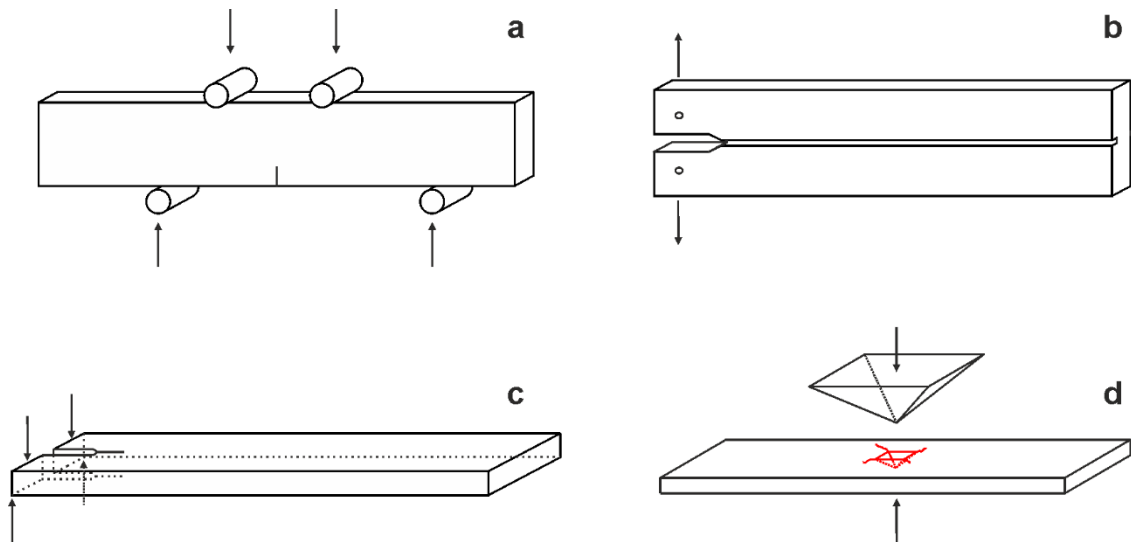
Figure 1.3 — Common techniques used to investigate fracture properties at the macroscopic scale. **(a)** Flexural testing, here represented in four point fixture configuration. The three point equivalent substitutes the two fixtures at the top with a single fixture on the top centre. **(b)** Double cantilever beam geometry. **(c)** Double torsion. **(d)** Indentation cracking.

1.2.1 Flexural testing

The ASTM C1421 [26] describes methods to determine the fracture toughness K_{Ic} of advanced ceramics at ambient temperature using a beam test specimen with a sharp crack in bending. The presence of the sharp crack is necessary for a correct measurement of the fracture toughness and the standard describes three methods to obtain a crack:

- **Straight-through crack via bridge flexure for the single-edge pre-cracked beam (SEPB).** To initiate a sharp crack one or a series of Vickers indents, a Knoop indent or a machined notch are placed at the centre of the bottom side of a bar. Successively the bottom is loaded in compression at either side with flat punches until pop-in to initiate a crack. A large pre-crack is so obtained and needs to be measured prior testing of the specimen.

- **Semi-elliptical surface crack via Knoop indentation for the surface crack in flexure (SCF).** A pre-crack is introduced by means of a Knoop indent. The pre-crack size is much smaller than in SEPB and can be tailored to needs with the advantage of representing

better the size of actual surface flaws. However its measurement requires fractographic techniques.

Prior to testing the residual stresses caused by the indentation need to be removed completely by polishing the surface.

- **Formed at the apex of a chevron notch in the chevron-notch bend test (CNB).** The chevron notch approach eliminates the difficult pre-cracking operation required for SEPB and SCF specimens and the need to measure the pre-crack size, however requires stable crack extension to be valid.

The beam is then loaded in four or three (the latter is not applicable to SCF) point fixture configurations with the crack positioned on the side under tensile stress. The fracture toughness is calculated from the fracture force, the test specimen size and the measured pre-crack size or maximum force applied after stable crack extension in the case of the chevron notched sample.

Two other flexural tests exist to measure fracture energy or toughness of brittle materials for which there are no standards, namely the single-edge notch bend (SENB) and the work-of-fracture (WOF) tests. In the former a notch is simply machined on one side of the bar and the test is conducted under the assumption that a crack is present at the bottom of the notch as consequence of the machining. The possible absence of a crack results in an overestimation of the fracture toughness; therefore, unless the assumption is verified, this method is unreliable.

The WOF test consists of bending a notched bar until the crack extends through the entire specimen while the load-displacement curve is recorded. The area under the curve is then used to measure the energy absorbed per unit of surface created during fracture, i.e. the fracture energy. As a consequence the value obtained is representative of an average value of the fracture energy of the region of the sample crossed by the crack rather than a critical value.

1.2.2 Double cantilever beam

With double cantilever beam (DCB) and double torsion (DT) configurations a stable crack growth can be obtained. In addition, using specific loading approaches a crack-length independent fracture toughness can be measured, therefore making these methods particularly useful for obtaining crack growth data.

The use of DCB for the study of fracture properties can be seen as an evolution of the configuration used in 1930 by Obreimov [27] to measure the fracture-surface energy of mica, where a blade was slid through a thick slab of mica to cause a moment capable of bending a thin foil and grow a crack. Here, the thickness of the mica slab is much smaller than the rest of the material so the system can be seen as the bending of a single cantilever of variable length equal to the crack length and clamped at the crack tip. If the thickness at both sides of the crack is comparable the blade will bend both beams and in the limit the DCB is an ideal symmetric system. The energy stored in the specimen to bend the beams is balanced by the surface energy to form two new surfaces.

Three different geometries are typically employed to ensure a bending of the two arms of the DCB that are: a tensile loading applied directly on the top each beam, a moment applied through the bending of two arms perpendicular to the long axis of the DCB (often referred as applied moment DCB or AMDCB) and a wedge slid through the opening at the top [28]. In both AMDCB and tensile loading, provided that in the latter the DCB is tapered with the right angle to allow constant compliance with crack growth, one can measure a fracture toughness that is crack length independent. An inherently stable crack growth, instead, ensues from the wedge loading configurations under a constant displacement since this generates a decreasing strain energy release rate with crack extension.

1.2.3 Double torsion

The double torsion specimen consists of a rectangular plate with a crack or a notch on one side [see Figure 1.3-(c)]. The specimen is loaded in four-point bending around the notch so that torsional deformation is produced on the two halves. In this loading configuration the stress intensity change at the tip of a growing crack is slow, compared to flexural beam testing, therefore giving rise to a relatively stable crack growth compared to flexural beam testing [29]. Moreover, the stress intensity factor is, under certain geometrical conditions and approximations and a range of crack lengths, independent of crack length, thus this test configuration is ideal for cases in which measurement of crack length is difficult. The classical analytical solution for double torsion testing requires a specimen with a width much larger than its thickness. It has been demonstrated by three-dimensional finite element stress analyses that the sample geometry has a significant effect on the measured value of fracture energy [29]. Therefore one of the drawbacks of double torsion geometry is that it practically requires big samples, since sample width should be 12 times greater than thickness, and specimen length should be greater than twice the width [30]. Typical dimensions are $2 \times 25 \times 75$ mm^3 [31].

1.2.4 Indentation

Indentation tests are widely adopted as standard test to measure a material hardness. Brinell, Rockwell, Vickers and Knoop tests are all based on the application of a force to an indenter to measure the resistance to the penetration opposed by a material. When the force is applied the portion of specimen under contact with the indenter will yield once a critical pressure is reached. After the removal of the force some plastic recovery may take place, however residual stress can remain and, a permanent deformation. Therefore, the hardness is generally determined with a measurement of one or more characteristic indent sizes (i.e. depth, area, width, etc.) at a specific

load applied. Different methods vary the load applied, the measurement method, indenter geometry and indenter material.

At the same time, indentation probing of brittle materials often results in cracking. For this reason indentation has been largely employed also to determine the fracture toughness of such materials. The basic idea is to use the size of indentation-induced cracks together with the peak load applied to quantify the fracture toughness. This technique is attractive because of the simplicity in execution and a relatively easy specimen preparation compared to that of more traditional fracture toughness tests where a sharp pre-crack is needed, which is often difficult to obtain. In addition, execution is quicker and little specialised equipment is required [32].

Lawn and Wilshaw [33] reviewed principles and application of indentation fracture, focusing on the stress field, mechanics of fracture, measurement of parameters and practical application of indentation. As the authors pointed out, the knowledge of the stress field present in the loaded system is the basis to build a theory of indentation fracture. This depends on the contact zone which itself is dependent on the shape of the indenter.

The differences between a Hertzian indenter (typically a hard sphere) and sharp indenters have been investigated. The former gives rise to a complex yet well-defined stress field up to the fracture point. The latter, including Vickers, Knoop and Berkovich, are more commonly employed in indentation testing [34,35], to generate high gradients or even singularities in the stress field underneath the tips. The advantage of sharp indenters over the Hertzian indenters rests in their geometrical self-similarity, which means that the ratio between the length of the diagonal and the depth of impression remains constant during the loading. Thus, the contact pressure is independent of the applied load and is given by [33]:

$$p_m = \frac{P}{\pi A^2} \qquad (1.16)$$

where P is the load and πA^2 is the contact area.

Moreover, the cracks ensuing from Hertzian indentation lies entirely beneath the surface, thus making not possible their direct observation in non-transparent materials [34].

Boussinesq in 1885 sought the solution for the stress field under the indent, which gave in the form [33]:

$$\sigma_{ij} = \left(\frac{P}{\pi R^2}\right)[f_{ij}(\phi)]_v \tag{1.17}$$

where R is the distance from the contact point and f is a function of the angle and Poisson's ratio, as shown in Figure 1.4.
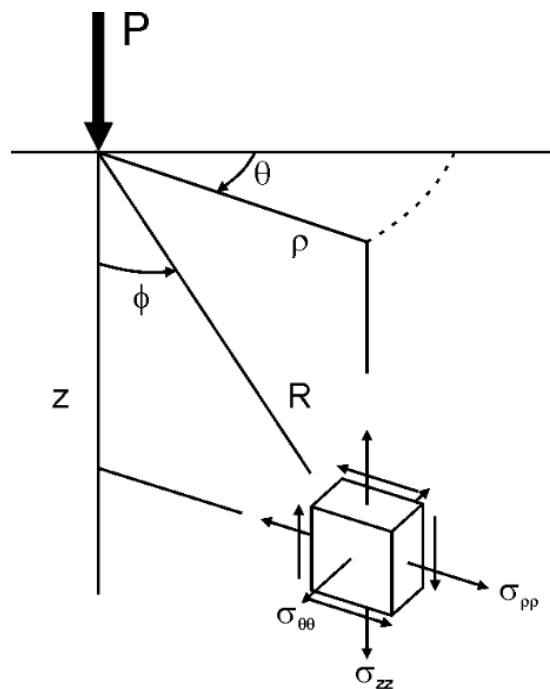
Figure 1.4 — Coordinate system for the stress field under the indenter contact point. Redrawn after [33]

It is evident that the equation leads to a singularity for $R = 0$, at the contact point. What happens in fact is that at the singular point there will be a non-linear, inelastic deformation to relieve the high stress concentration, which distributes the load over a non-zero contact area. This emphasises the complexity of the stress field under the tip. However, it has been shown that the field consists of two separable terms, nominally elastic and residual, thus facilitating the treatment based on the fracture mechanics theory.

The ensuing crack from a sharp indenter, albeit varies depending on the test system (shape of the indenter, load rate, etc.), has general features. Upon loading, at some threshold, a small crack, called median crack, forms on a symmetry plane where the contact axis lies; increasing the load results in a growth of the median vent. During unloading the median vent aim toward the closure, while lateral vents develop and extend toward the surface.
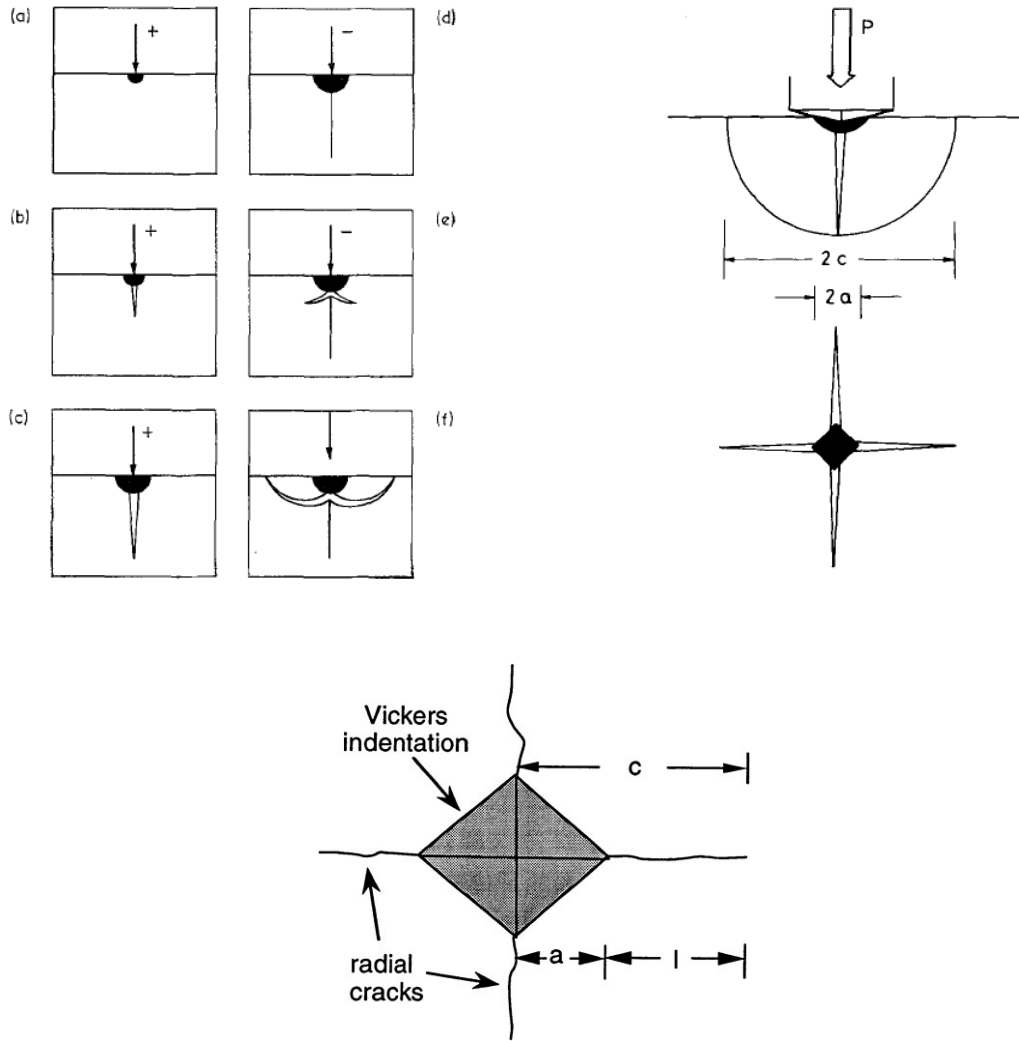
Figure 1.5 — Geometries of cracks ensuing from indentation. (top-left) a),b) and c) show the formation of the median crack upon loading whereas in d),e) and f) is shown the formation of the lateral vents during unloading. The other two schematics show the geometric variables used in the analysis of the cracks ensuing from indentation, in the case shown from a Vickers indenter. From [33,34,36]

It has been demonstrated through dimensional analyses that hardness H and toughness K_{Ic} are related to the peak load, P, and dimension of impression, A, and radial crack a, (shown in Figure 1.5) according to [34]:

$$H = \frac{P}{\alpha A^2} \tag{1.18}$$

$$K_{Ic} = \frac{P}{\beta a^{3/2}} \tag{1.19}$$

where α and β are essentially numerical constants which vary with the geometry of the indenter and the crack, respectively, and are determined by experimental calibration. Radial cracks are usually assumed to have the form of penny-like cracks and for symmetric stress fields (as those underlying symmetrical sharp indenters, say a Vickers for instance) these fractures satisfy the relation $P/a^{\frac{3}{2}} = constant$ [37]. Lawn and colleagues [35] have demonstrated that the relationship between fracture toughness and length of radial crack, for a well-behaved crack $(a \gg A)$ is given by:

$$K_{Ic} = \alpha \left(\frac{E}{H}\right)^{1/2} \left(\frac{P}{a^{3/2}}\right) \tag{1.20}$$

where P is the peak load, E the Young's modulus, H the hardness and α the empirical constant above-mentioned. The equation shows how easy is the implementation of indentation cracks to measure fracture toughness, provided that elastic modulus is known and a measure of the crack length is achievable, when hardness can be measured with the same test system.

Nonetheless, as shown by Anstis *et al.* [34], the use of this technique should be limited to comparative study of a material subjected to different processes, since the determination of absolute values is affected by great errors and uncertainty. Other authors [38] simply argue that Vickers indentation is not a suitable technique to measure fracture toughness due to the high uncertainty and scatter associated with the measurements. Such uncertainties arise from the complexity in crack formation, as already described, typical of indentation fracture. At the end of an indentation fracture not a single but multiple cracks have arrested in a post-test configuration and a complex residual stress field characterises the material; even major spalling often occurs especially in high-load tests. Multiple cracks do not remotely ascribe to definitions of fracture toughness that appear in many textbooks [38]. Thus, accurate results are possible only in presence of an empirical calibration for the force constants (α) to a similar material, otherwise the equation fails.

1.3 Fracture mechanics of interfaces

Experimental testing reveals that the measured values of fracture energy or toughness of polycrystalline ceramics can deviate greatly from those of the respective single crystals, due to the interaction of the crack with the microstructure. As already mentioned in section 1.1, the brittle nature of ceramics identifies with an absence or at least a reduced presence of intrinsic dissipative processes at the crack tip. However, microstructural defects can interact with the stress field ahead of or behind the crack tip and increase the energy expenditure required to propagate the fracture. This translates in an increased toughness of the material.

The mechanisms through which the net absorption of potential energy changes when microstructural defects interact with the crack depend mainly on the type of defect.

Lawn [20] distinguishes the interactions into two separate classes:

a) geometrical processes, involving deflections of the crack at specific boundaries;

b) shielding processes, involving interactions that can take place ahead or behind the tip.

The first is typical of the interaction between the crack and an interface that can cause a planar crack to deviate from its path, here the effect lasts only as much as the intersection. The second type of processes, instead, involve irreversible dissipation and are cumulative. These include phenomena such as microcracks clouds, phase transformation, ductile second phase at the crack wake or interfacial bridging behind the crack front.

When fracture occurs in polycrystalline materials the crack intersecting a grain or interphase boundary can follow two distinct possible paths: continue through the boundary and across the second grain, i.e. transgranular, or deviate along the boundary, i.e. intergranular.

The fundamental assumption is that the crack path followed is the one that maximises the decrease in total system free energy. It has been shown that when a straight plane crack in mode I loading changes plane by twisting or tilting the energy release rate decreases [20,25], essentially because the

crack is no longer perpendicular to the loading direction (i.e. maximum principal tensile stress) thus reducing the rate at which the compliance of the system increases for a given crack area increment. As a consequence, for the crack to deviate its path onto a boundary this needs to be 'weak' in order to compensate for the additional absorption of energy[1]. Specifically, the debonding energy of the interface needs to be one-fourth of the crack resistance of the second grain or secondary phase [20,39]. Since the crack goes around the grains rather than through them, the path is tortuous and the fracture surface area is bigger, resulting in an increase in net resistance, $G_c = R$.

The engineering of the strength of the boundaries is therefore a possible toughening mechanism in ceramics [40], however its transitory nature limits the maximum gain to 4 times the original fracture energy G_c, equivalent to twice the fracture toughness K_{Ic} [20].

Conversely, the cumulative effect of the shielding processes can result in a more significant influence on fracture toughness, thereby the great majority of toughening approaches focuses on these phenomena. Nonetheless, for shielding processes to be activated it is often necessary to promote geometrical processes, e.g. grain bridging does not occur when interfaces are too strong and fracture is transgranular. This is readily evident in simple geometries like ceramic plates bonded by weak interfaces [40]. Here, the crack, once it reaches the interface, tends to deviate along this preventing a catastrophic failure and raising the apparent fracture toughness to more than 4 times the value of the monolithic component.

However, toughening is not simply obtained by introducing weak interfaces; interfaces that are too weak could be detrimental. Grain boundaries and interface engineering is therefore an important but not trivial step towards the improvement of ceramic performance. There exist different ways to modify the strength of interfaces that include changes in the processing route,

---

[1] It is worth mentioning here that what should be referred to as fracture resistance of the interfaces or boundaries is often indicated as 'strength' in literature; therefore boundaries and interfaces are usually classified as 'weak' or 'strong' accordingly. Hereinafter, that same terminology is used.

that act mainly on the structure of the boundaries, and use of additives, that act mainly on the chemistry of the interface, and a combination of both.

An example of the first is provided by Al Nasiri *et al.* [41] who investigated the properties of silicon carbide samples obtained from liquid phase and solid state sintering. Although the microstructure of all the samples did not show any significant difference, the fracture toughness measured on liquid phase sintered samples resulted >75% higher than that of the solid state sintered ones. This was due to the difference in the mechanics of the fracture that changed from intergranular mode in the first to transgranular in the latter, likely brought by the changes in the properties of interfaces for the different sintering approaches.

In several other studies, the combined effect of additives and thermal treatment, beside a change in microstructure from equiaxed to elongated grains, is demonstrated again on silicon carbide [42–45]. Here fracture toughness was increased by more than a factor of three compared to that of commercial SiC. At room temperature the presence of an amorphous film along the grain boundaries is believed to promote intergranular fracture and, consequently, toughening through grain bridging. However, the same film becomes viscous at high temperatures, thereby a degradation of the properties was observed. This was resolved by selecting additives that crystallise at high temperature contrasting the viscous flow. The crystallised film not only improved the fracture resistance at high temperature (20% at ~1300 °C) but also that at room temperature; this was attributed to a higher frictional coefficient of the crystalline film that made the crack bridging more efficient by increasing the energy required to pull out against the sliding grain faces [46].

Although the mechanisms of crack growth at the boundaries are clear and have been exploited for some time, prediction of the crack path remains difficult, for it depends on several factors such as residual stresses, mismatches in elastic, plastic and thermal properties, and interfacial fracture resistance itself. In turn, interfacial fracture resistance depends on bonding, interface morphology, plasticity in the second phase and on the presence of interphases [47]. This is of particular relevance

for the crack growth at ceramic-metal interfaces [47–60], given the strong mismatches between the two materials. Ritchie *et al.* [55] conducted extensive work to test several ceramic/metal systems and understand the crack path selection (i.e. along, towards or away from the interface) in layered bi-crystals for crack initiated at or near interfaces. In their work a comparison is made between the predicted path using linear elastic interfacial and near-interfacial crack tip fields and the experimental results. In the presence of strong elastic mismatch between the two materials, the stress field ahead of the crack differs greatly from the far-field loading. Linear elastic interfacial and near-interfacial crack tip field theories predict the crack path selection in response to the ratio of normal to shear stresses ahead of a crack, as affected by the elastic mismatch. However, the authors could verify from experiments that the path followed depends also on the strength of interfaces, as in the presence of "weak" interfaces the crack would tend to follow them, regardless of the mode mixity at the crack tip. The authors could also observe extensive plastic deformation associated with crack tip blunting in the metal layer. However, in several cases, they observed that the extent of plasticity was constrained within the metal thickness by the ceramic; as a consequence the fracture toughness was well in excess of the ceramic toughness, yet small compared with the toughness of the bulk metal. Depending on the bonding technique, plasticity was also accompanied by relief of residual stresses introduced during the fabrication of the sandwich structures. These residual stresses further contributed to modify the stress at the crack tip.

This study highlights the need to know the local interfacial fracture energy for a correct prediction of crack path and therefore efficient design of composites as well as the need to investigate interfaces with thickness close to that present in real components. The difficulties encountered in restraining crack propagation along the interfaces poses a major issue for these investigations. Attempts to develop a testing technique suitable to measure the interfacial fracture resistance have been made using different loading geometries, the majority of which based on sandwich specimens [47,51,55,58,60–64]. Evans and Dalgleish [51] identify in residual stresses, crack trajectory and precracking the main issues that must be addressed to obtain an accurate measurement of the

interface fracture resistance. The first of these, residual stresses, mainly caused by misfit in the thermal coefficient between ceramic and metallic phase, can be reduced by reducing the thickness of the metal layer. Secondly, a deviation of the crack trajectory from the interface into the ceramic needs to be prevented using geometries that minimise a local shear loading at the crack front, for this sandwich geometries as depicted in [51] are best suitable. It is important to note that although these loading geometries promote crack propagation along the central axis, small deviations of the crack from its plane are difficult to avoid, thereby the fracture resistance measured from the far field loading is still affected by these dissipative processes.

Finally, a sharp crack must be introduced at the interface using mechanical procedures, as attempts using local contamination during bonding could not afford consistent results. In addition, the ratio of elastic constraint over plastic dissipation depends on the volume of metal enclosed between the two plates. Evans and Dalgleish show that a relation exists between layer thickness (varied in this work between 10 and 100 μm) and fracture energy measured. Therefore, if the layer thickness of material 2 is small compared to that of material 1 and all other dimensions of the specimen (including crack length) the fracture energy can be measured from the far field loading as for the homogeneous case, i.e. considering that the elastic strain energy is entirely absorbed in material 1 [65]. However, macroscopic tests in the studies mentioned were limited to a minimum thickness of ~10 μm.

Another significant aspect of these macroscopic tests is that fracture at this scale is affected by the presence of voids and defects at the interfaces; as a result the value obtained accounts for these in addition to the work of adhesion. Evans and Dalgleish suggest that an estimate of the work of adhesion can still be obtained by measuring the dihedral angle of the residual voids located on the fracture surface, provided that the fracture at the interface is of brittle nature [51]. The dihedral angle is indeed related to the solid grain boundaries surface energies through Eq. (2.3).

1.4 Residual stresses and fracture

Residual stresses are those stresses that are present in a component even after removal of their original source, whose effect is to create incompatible internal strains; as such they modify the stress field around the crack tip.

As already noted, the introduction of a second phase in a polycrystalline material does not only creates interfaces but causes elastic, plastic and thermal expansion mismatches. The latter are a common source of localised residual stresses when the material is cooled down from the processing to room temperature [66,67]. Single phase materials can be affected by analogous residual stresses too, in case of thermal expansion anisotropy with neighbouring grains [68,69].

In brittle materials the presence of localised residual stresses can lead to microfracture [68,69] or crack deflection [66,67], with important implications on the performance of the component, as discussed in chapter 2 relatively to PCDs. These mechanisms are commonly investigated in ceramic-matrix composites reinforced with a second phase in the form of fibres or particulates.

In this systems two opposite situations can take place:

  a) Thermal expansion of the reinforcing phase is greater than that of the matrix. By cooling down from processing temperature, the matrix contracts less than the fibre. Therefore, if contact between the fibre and the matrix is retained, circumferential compression and radial tension act on the matrix, whereas the fibre is in axial tension [Figure 1.6-(a)].

  b) Thermal expansion of the matrix is greater than that of the fibre. Here, again allowing contact between matrix and fibre to be retained, the matrix undergoes circumferential tensile and radial compressive stresses while the fibre is in axial compression [Figure 1.6-(b)].
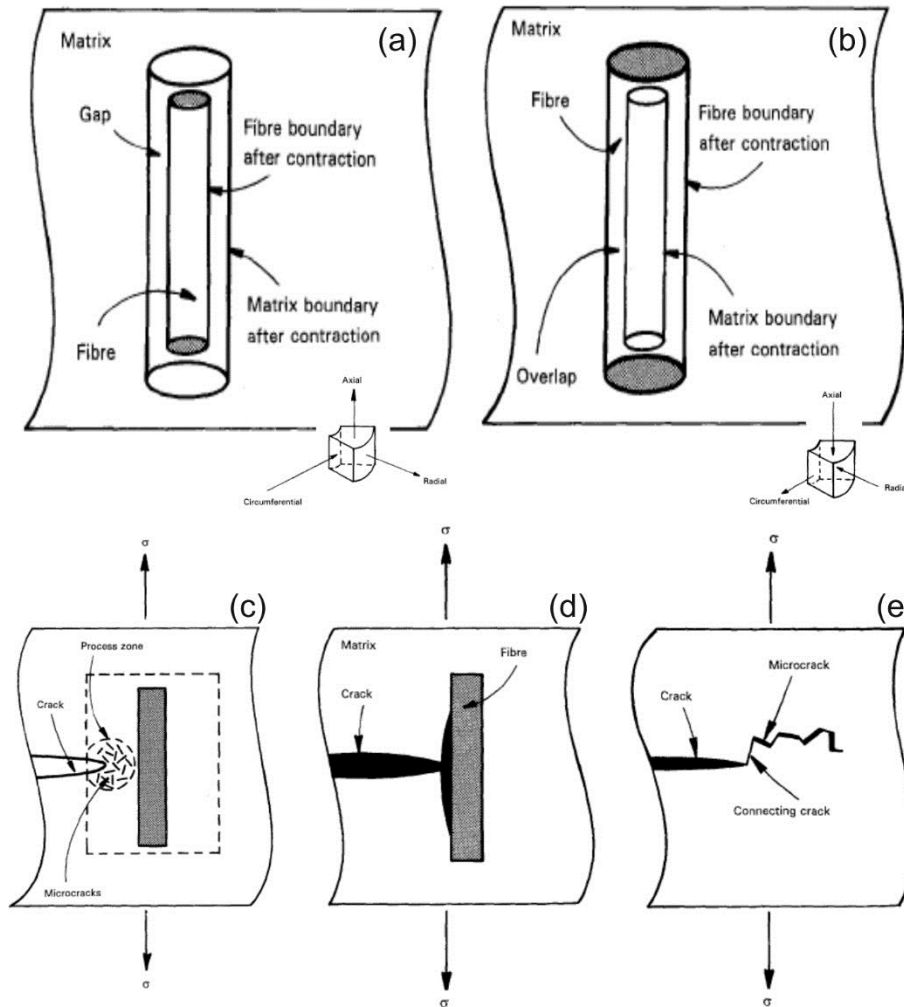
Figure 1.6 — Residual stresses induced by thermal expansion mismatches between fibre and matrix, and secondary toughening mechanisms activated. (a) Thermal expansion of the fibre is greater than that of the matrix; **(b)** thermal expansion of the matrix is greater than that of the fibre. **(c)** microcracks cloud; **(d)** crack deflection; **(e)** crack bridging. Adapted from [67].

As mentioned in 1.1 in brittle materials cracking occurs under mode I preferentially, thus a crack tends to propagate perpendicular to tensile stresses and parallel to compressive stresses. Consequently, in situation a) the crack tends to propagate around the reinforcement, conversely situation b) promotes radial propagation of the crack from the reinforcement [67].

The latter is likely to facilitate the networking of cracks ensuing radially from the different reinforcements, thus reducing the toughness. In contrast, since cracks around the particles/fibres tend to travel along or parallel to the interface can promote, besides crack deflection, the activation of secondary toughening mechanisms (e.g. fibre pull-out, crack bridging, etc.) as shown in Figure 1.6-(c–e).

The pressure that builds around the reinforcements is not only dependent on the thermal expansion mismatch, but also on elastic mismatches. In particular, the pressure to which a spherical particle is subject, for as sphere (subscript 2) in an isotropic material (subscript 1) is given by [66]:

$$P = \frac{\Delta\alpha\Delta T}{(1 + \nu_1)/2E_1 + (1 - 2\nu_2)/E_2} \tag{1.21}$$

where $\Delta\alpha$ is the difference in the two expansion coefficients, ΔT is the cooling range over which the matrix plasticity is negligible and $\nu_{1,2}$, $E_{1,2}$ the Poisson's ratio and Young's modulus of the matrix and particle respectively. Although equation (1.21) shows no dependence from size of the reinforcements, it appears from experimental results that spontaneous microcracking, i.e. in absence of an applied external loading, only occurs when the particle size is bigger than a certain critical value [66]. On one side, since spontaneous microcracking would reduce the strength through the introduction of flaws, the size of reinforcements must be kept below the critical value. On the other side, the formation of microcracks in the process zone of a propagating crack reduces the elastic modulus; as a consequence, the crack tip is shielded from the applied stress field. In addition, microcracks attract the propagating crack promoting deflection and branching. Therefore, if microcracking can be controlled during processing and activated only during the application of external load this could be exploited as a fracture toughening mechanism. In particular, a narrow distribution close to the critical size proves to enable the maximum toughness [67].

It is indeed worth noting that the cracking is not simply initiated when the internal stress reaches the macroscopic fracture stress, rather it depends on whether the flaw introduced is bigger than the inherent flaw size. For this reason, the spacing between reinforcements and their size play an important role.

1.5 Characterising fracture at the microscale

At present there are many standard tests which enable precise measurement of the fracture properties of brittle materials at a macroscopic lengthscale, yet only few available which enable direct measurement of individual grain boundaries. Macroscopic tests are very successfully used to understand bounds on component performance and to compare and contrast ceramic processing strategies, but as they test polycrystalline aggregates it is very difficult to understand the role of specific microstructural features. It is therefore crucial to gain new insight at the microstructural lengthscale, as failure of ceramics is controlled often by the weakest microstructural link. Moreover, tests at the microscale offer a solution to investigate materials whose dimensions are not suitable for conventional tests (e.g. thin films) or for which the use of conventional machining to shape specific specimen geometries result troublesome (e.g. for very brittle and hard materials). Nanoindentation has paved the way for small scale mechanical testing, however development of more complex, site specific testing of ceramics has advanced significantly in the last five years, using either photolithography or focused ion beam (FIB) machining, enabling preparation of a variety of microscopic tests specimen geometries in precisely specified locations and opening the door to high spatial resolution mechanical tests.

Typically, these test specimens are loaded using a nanoindentation platform as well with different tip geometries according to the test design (see Figure 1.7). These geometries include: single cantilever bending [70–76], double cantilever beam compression [77], clamped beam bending [78,79] and pillar splitting [80]. The philosophy of performing high spatial resolution testing, as employed with these geometries, enables assessment either of the local fracture properties of single grains or grain boundaries or of samples whose only small volumes are available, e.g. coatings.

The majority of these existing studies make use of a load controlled ramp to actuate the indenter and follow crack opening from changes in load-displacement data, both to identify the crack

nucleation and fracture load to be used in fracture toughness measurements. A discussion on these techniques follows and a panel with their geometries is presented in Figure 1.7.
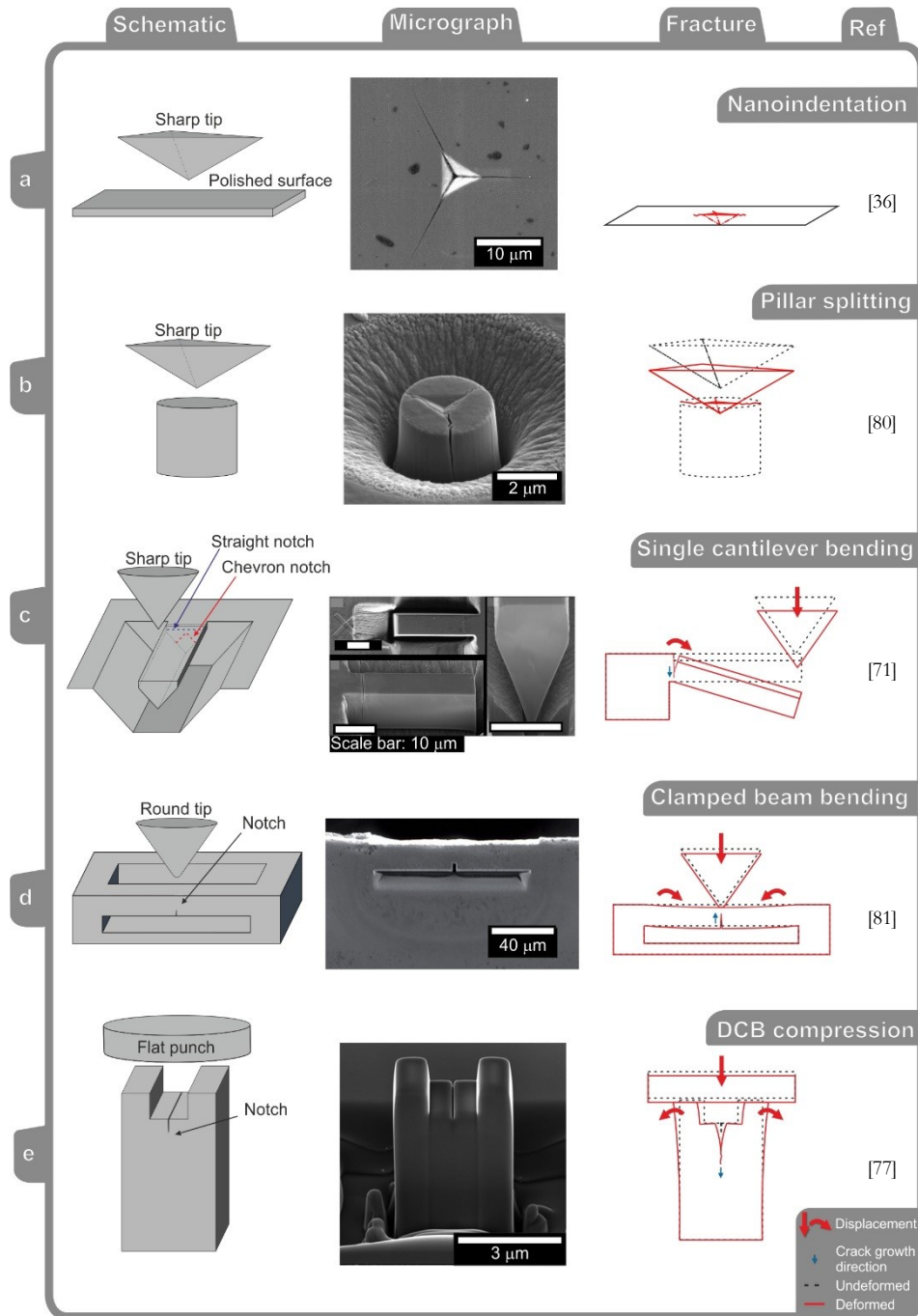
Figure 1.7 — Loading geometries employed for micro-mechanical fracture testing. (a) Flat surface loaded with a sharp indenter (commonly Berkovich, Vickers or cube-corner). At the cracking threshold, cracks originate in the volume surrounding the indenter; load and crack length are used to calculate the fracture energy. **(b)** Pillar splitting geometry loaded with a sharp indenter. FIB removal of material surrounding the pillar allows relaxation of residual stresses. The fracture toughness is calculated using cohesive zone finite element analysis. **(c)** Single cantilever bending geometry with pentagonal cross section and loaded with a sharp indenter. Rectangular cross section is only possible on a 90° edge [72,73] and a pentagonal cross section is towards the sample interior. Straight and chevron notch geometries sections are represented with blue and red dashed lines respectively. Straight notches provide inherently unstable fracture, whereas the chevron notices enable a stable crack growth for short cracks [73,76]. Dimensions measurements of notch and beam geometry are performed after the test [70–72]. **(d)** Schematic of a double clamped beam bending geometry loaded with a blunt tip. The beam is FIB milled on a 90° sharp edge and a notch at the bottom edge centre of it [81]. Stable crack growth is supported but freedom of positioning of the notch is limited [73]. **(e)** DCB geometry loaded with a flat punch. Stable crack growth is achieved. Friction between flat punch and sample, and compressive stress on struts need to be taken into account [77].

1.5.1 Nanoindentation

Nanoindentation was developed as an evolution of the macroscopic equivalent to test at smaller length scale and has been used in the last 30 years for measuring mechanical properties of thin films and small volumes of materials [see Figure 1.7-(a)]. Usually instrumented indentation gives an accurate control on either load or displacement with a continuous feedback on the data allowing the determination of the area function and some of the mechanical properties to directly analysing the data, rather than imaging the impression. It is possible, for instance, to map the properties of a specimen with a very small spatial resolution (about 1μm) [36], gathering information on hardness and elastic modulus of different areas of interest on a sample, so that all the parameters needed to measure the fracture toughness are readily available within the same test. It is also possible to test sample too thin to be tested with conventional techniques.

However, to initiate a crack by indentation in a material the load has to be higher than what is called the cracking threshold. This places severe limitations on the spatial resolution achievable with nanoindentation, as the size of the impression is proportional to the load applied, especially because the equation for the measurement requires the crack to be well-behaved ($c \gg a$ in Figure 1.5).

Moreover, the application of this technique on such a hard material as the PCD is limited by the fact that the hardness of the indenter and the sample is comparable while the toughness of the latter is usually higher. Practical problems arise from the attempt of indenting PCD, as shown in Figure 1.8.

These limitations add to the aforementioned (see 1.2.4) uncertainty on the values obtained by general indentation-induced fracture analysis.
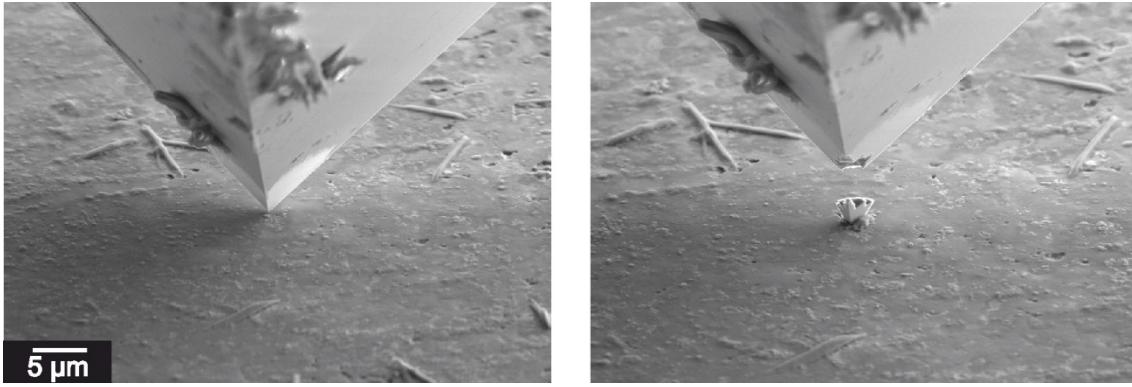
Figure 1.8 — Still images taken before (left) and after (right) an indentation test performed _in situ_ on a PCD sample. It is shown how the cube corner tip was damaged during the test.

1.5.2 Pillar splitting

Sebastiani _et al._ [80] proposed a variation of the nanoindentation fracture tests exploring the possibility to measure the fracture toughness by indenting a pillar fabricated via FIB until a crack is nucleated and propagated, see Figure 1.7-(b). With this technique the authors investigate the fracture toughness in thin films, where often the residual stresses present between the film and the substrate complicate the measurements. The advantage of this approach stems from the removal of material during the manufacturing of the pillar that promotes the relaxation of the residual stresses at the top of the pillar. Moreover, much of the simplicity of test execution typical of the indentation tests is retained. On the other hand, the fracture toughness measurement requires the use of cohesive zone finite element analysis and the authors point out that the effect of friction between the tip and the pillar on the fracture toughness value needs further investigation. The authors test, among other films, TiN coatings presenting a columnar structure with metallic micro-droplets and observe intergranular fracture, so that they interpret their value as grain boundary toughness. However, the application of the pillar splitting loading geometry to interrogate individual select boundaries appears cumbersome. The splitting, as occurs in the work by Sebastiani _et al._, is along the three indenter vertex directions, therefore it would be difficult to cause the cracking along a boundary alone.

Axial splitting can be also obtained during micropillar compression if the pillar is oriented so to form two intersecting slip bands. Here, the material from the top portion of the pillar essentially forms a wedge that opens and drives a crack as the load reaches a critical value. This phenomenon has been observed in Si [82,83], GaAs [84], InAs and $MgAl_2O_4$ [83]. The expression for the stress intensity factor on the axial crack of length l was proposed as [83,84]:

$$K_I = \beta S \sigma d / 2[\pi(l+z)]^{1/2} \tag{1.22}$$

where β is some geometrically dependent constant, S is the Schmid factor on the slip plane and in a direction from the top edge of the pillar to the line of intersection of the slip bands, σ is the uniaxial compressive stress applied, d is the pillar diameter, and z is the distance between the top of the pillar and the point where the slip planes intersect. The axial split is nucleated when the stress intensity factor in Eq. (1.22) for $l = 0$ equals the K_{Ic}. As a consequence, since the critical stress required to grow a crack is proportional to $K_{Ic}/\sqrt{d}$ [83] and this type of axial splitting is only possible if slip bands are formed, there exists a critical diameter below which the stress required to grow the crack is higher than the yield stress and splitting does not occur. Although a value of K_{Ic} can be obtained, it has typically been used to observe and explain ductile-to-brittle transition behaviour with pillar size.

1.5.3 Single cantilever beam

In the last 30 years, the demand for evaluation of mechanical properties of microelectromechanical systems and thin films moved many researchers to create adequate methods to test them. Attempts to study elasticity, plasticity, and in particular fracture have been made through deflection of cantilever microbeams.

The method was initially developed using silicon micromachining techniques [85,86], such as lithography and etching, and a nanoindenter to operate the deflection and register force and

displacement applied. Beams fabricated had typical dimensions of about 100 μm in length, 10 to 20 μm width, and a few μm in thickness [87].

The test is similar to the macroscopic counterpart of a cantilever beam fixed at one end. Thus, elastic beam bending theory can be applied to evaluate mechanical properties of the tested material. Johansson *et al.* [85] utilized this method *in situ*, in a SEM, to evaluate fracture properties of silicon cantilever beam. If I is the moment of inertia ($I = wt^3/12$ for a beam of rectangular cross section where w is the width and t the height), F the force applied and L the length of the beam, they extracted the maximum stress σ_m and the deflection δ from beam theory as:

$$\sigma_m = 6FL/wt^2 \tag{1.23}$$

$$\delta = FL^3/3EI \tag{1.24}$$

The fracture stress equation used by the authors is:

$$\sigma_f \approx K_{Ic}/(\pi a)^{1/2} \tag{1.25}$$

where K_{Ic} is the critical stress intensity factor and *a* the maximum flaw depth. However, this equation is the closed-form solution for the stress intensity factor in an infinitely wide plate with a through-thickness crack, which is not the case of the geometry investigated.

Therefore, the authors sought validation of the model by determining the Young's modulus E and comparing it to the corresponding E value obtained from experimental elastic stiffness constants. The measurements on <011> beam using the model gave $E = 177 \pm 18\,GPa$ whereas using experimental constants $E = 171\,GPa$, making the model reasonably valid.

Then, using known value of fracture toughness (K_{Ic}) from literature they could determine the maximum flaw size and list σ_f, ε_f and a for each experiment (where $\varepsilon_f = \sigma_f/E$).

It needs to be taken into account that the previous equations are valid for an isotropic and perfectly elastic material up to fracture and small deformations.

Di Maio and Roberts [70] used a similar testing technique to measure the toughness of brittle coatings. Their investigation was performed *ex situ*, using the tip in contact mode, similarly to an

AFM, to position it correctly on the beam. The main difference with the study of Johansson *et al.* [85], presented earlier, is brought by the preparation of the microbeams. Di Maio and Roberts employed FIB to mill the cantilever, which expands the possibility of fabricating microbeams on different materials, although limits the possibility of undercutting. For this reason, the beam in their work has a non-rectangular cross section, compare Figure 1.7-(c). The fabrication process consisted, firstly, of milling three trenches with the FIB column perpendicular to the sample surface, so as to create the shape of the beam of 10 μm length and 4 μm width. Subsequently, the sample was tilted to 45° with respect to the column on each side along the longest edge to cut the base of the beam, obtaining a symmetric pentagonal cross section. Finally, a narrow notch was milled close to the support of the beam (0.5 μm away).

The purpose of the notch was to emulate a sharp crack, so as to determine the fracture toughness (K_{Ic}), once known the fracture load, according to the following equation:

$$K_{Ic} = \sigma_c \sqrt{\pi a}\, F\left(\frac{a}{b}\right) \tag{1.26}$$

where σ_c is the fracture stress (related to the applied load P and distance from the crack L by $\sigma = My/I$, where $M=PL$ at the crack), a is the crack length and $F\,(a/b)$ is a dimensionless shape factor. The shape factor is a constant that depends on the geometry and the mode of loading [25]. Di Maio and Roberts found this constant to be $F = 1.58$ for their geometries. They performed tests on four Si samples with a (111) fracture plane to validate the technique, obtaining an average $K_{Ic} = 1.1 \pm 0.016\, MPa\, m^{0.5}$. The authors found the value to be slightly higher than the literature value of $0.83 - 0.95\, MPa\, m^{0.5}$ and attributed the difference to the extra-load required to nucleate a sharp crack at the bottom of the notch they deemed not to be narrow enough, albeit milled with a very low current (1pA). Nonetheless the results show the technique is sound and allows reproducible results to be obtained.

Armstrong *et al.* [71] employed similar fabrication method, geometries and testing technique with the intent of extending this type of investigation to the measurement of fracture properties of

single grain boundaries. The authors studied several bismuth embrittled grain boundaries at different misorientation angles identified through EBSD mapping.

The tests show that all the fractured samples had the fracture running along the grain boundary; however few samples showed slip lines around the notch but no fracture signs. Fracture toughness measured as by Di Maio and Roberts [70] gave values comparable with those presented in the only two studies on Cu-Bi bi-crystal [71]. The authors concluded that the method is valid to test grain boundaries with known misorientation, however high values of fracture toughness may be difficult to be analysed due to dependence of the specimen size on the balance between fracture and plastic flow.

Although the control over the notch geometry is not trivial using focused ion beams, Iqbal *et al.* [72] show that they obtained a low scatter on their measurements on NiAl single crystal, concluding that the size of the notch tip radius, ranging in their case from 70 nm to 120 nm, does not influence the fracture toughness.

The effect of the size of the cantilever on the stress state was also investigated in the same study as the authors were concerned about the applicability of plane-strain condition for such micro-sized specimens. Therefore, Iqbal *et al.* measured the ratio between the plane stress value of fracture toughness, named $K_{Ic}^{plane-stress}$, and the plane strain value, K_{Ic} for the two orientation <100> and <110>, respectively "hard" and "soft", of NiAl.

However, according to Anderson [25] the decreasing trend in K_{crit} with increasing thickness, attributed to a transition from plane stress to plane strain at the crack tip, is related to the crack-tip stress state but generally is characteristic of materials in which the crack propagation is ductile (e.g. microvoid coalescence).

Anyhow, Iqbal *et al.* found a $K_{Ic}^{plane-stress}/K_{Ic}$ ratio smaller than 10% and brittle fracture for both the hard and soft orientation of NiAl, claiming that "possible changes in the stress state have thus only a small effect on the fracture toughness".

The straight notched single cantilever beam is currently by far the most employed approach [70–76] owing to its relatively simple geometry and relative freedom in the positioning of the notch, convenient for the investigation of grain boundaries or interfaces. Unfortunately, this is an inherently unstable loading geometry, therefore its use is limited to the extraction of a single value of fracture toughness and does not allow the investigation of materials with R-curve behaviour [73]. Furthermore, serious concern has also been raised on the effect that the FIB-induced damage layer in the region surrounding the notch has on the value of fracture toughness measured [88].

These limitations may be overcome with configurations where stable crack growth is possible at least for small distances, in order to measure the fracture toughness after the crack has passed the damaged region. A well-known approach followed in fracture mechanics to decrease the amount of energy released at the crack front of brittle materials is the chevron notch [25,89] (see 1.2.1), in which two cuts are made at an angle such that an isosceles triangular cross section is left. Once the beam is deflected, even if under load control, the fracture begins at small loads at the apex of the triangular shaped bridge and extends deeper and wider at increasing load in a controlled manner. Crack growth becomes unstable when the increase in crack front width is no longer able to decrease the driving force. This approach has been recently implemented on microscopic single cantilever beams [76] allowing a short stable crack growth before the final failure, thereby minimising the influences of notch radius and FIB damaged layer.

As seen, for fracture toughness analysis of the single cantilever geometry, knowledge of the beam cross section dimensions is required, in particular measurement of the effective length of the beam, which is the distance between the notch and the loading point, and notch depth.

A key disadvantage of the single cantilever geometry remains the complexity of the undercutting procedure operated in FIB milling. Indeed, when fabricating specimens in bulk the angle at which FIB is able to sputter atoms away from the target is limited by the surrounding material such that it is not possible to obtain a rectangular cross-section, unless milling is operated on a polished 90° sharp edge of the specimen; as a consequence, a pentagonal or trigonal shape is usually used [70–72,74,75,90]. Therefore, the dimensions are typically measured after the test with SEM images of the fracture surface and combined with the load at fracture to generate fracture toughness values. Furthermore, in practice actuating the test in a nanoindentation system typically uses sharp indenters, rather than conical or flat punches. This has the benefit of reducing the possibility of slipping at higher deformation (as the indenter may 'dig in' to the sample), though of course this can complicate analysis as the work required to create the initial indentation needs to be taken into account when analysing displacement data.

1.5.4 Double clamped beam

The double clamped beam bending, recently employed for fracture toughness measurements by Jaya *et al.* [81], resembles a three point bending test (see 1.2.1) but with constraint at the ends of the beam, as shown in Figure 1.7-(d). The beam is loaded at the centre where a notch is milled on the bottom side. Benefits of this configuration stems from the fact that a stable crack growth is achievable after some amount of unstable fracture, i.e. once the crack length is bigger than a critical crack length/crack width ratio [81]. In this geometry, care must be taken to ensure correct mode I loading through accurate initial crack tip and loading point positioning at the middle of the beam, although incorrect positioning can be easily ascertained by observation of deviations of the crack path. This approach is excellent for coated systems, but use of this method for investigation of specific microstructural features such as interfaces is cumbersome. This geometry requires the notch to be at the exact centre of a relatively long beam to obtain mode I opening [73] and cannot be used in bulk, as the geometry requires an available polished 90° sharp edge. Moreover, no

analytical solutions exist for this configuration and this necessitates extended finite element analysis of the stresses, strains and displacements to extract fracture toughness values [81].

1.5.5 Double-cantilever beam

The DCB geometry has been employed on the macroscopic scale to measure fracture-surface energy for a long time (see 1.2.2), in that it is associated to stable fracture, simple sample preparation and simple analytical solutions [27,91–93]. At the microscopic scale the double-cantilever beam (DCB) geometry lends itself well to the investigation of interfaces and grain boundaries since in this case the geometry is small laterally around the notch. Indeed, it is possible to fabricate it in a vertical configuration so that in a top-view cross section the DCB is only as wide as the notch and is as thin as possible in the other dimension. For ease of analysis, it is preferential to mill the DCB such that the biggest dimension is the length of the interface extending into the bulk of the sample.

Only recently Liu *et al.* [77] have adapted this geometry to microscopic scale tests to measure the fracture toughness of hard coatings, see Figure 1.7-(e). Their approach was based on the use of a flat punch tip to compress the DCB in load control. DCBs were milled to produce a strut machined on each beam whose function was to move the point of force application away from the neutral axis of the beam in order to have a moment acting on them. The load-displacement curve recorded by the instrument was used to identify the fracture load, which was then used to measure the fracture toughness (see Liu *et al.* [77] for details of the analysis method). The work demonstrates that the DCB geometry can be used at the microscale to measure fracture toughness of brittle materials, however the loading configuration chosen by the authors is associated with high friction between the flat punch and DCB struts. As a consequence the friction coefficient between the tip material and the examined material needs to be known for an accurate measurement, however this can often be difficult to find in the literature. A solution was proposed by the authors to measure the friction coefficient by measuring the work from the hysteresis observed upon reloading and

following unloading of already fractured samples, by assuming that all the work was only done against friction between the punch and the sample.

As discussed by the authors, the compressive component of the force is used to create the moment to open a crack and therefore the DCBs cannot be arbitrarily set, but need to be carefully designed in light of the fracture toughness to yield stress ratio to avoid plastic deformation of the struts (or secondary cracking along the strut arms).

1.5.6 General limitations of micromechanical testing

The key limitation of existing approaches is that they typically make use of a load controlled ramp to actuate the indenter and follow crack opening indirectly, using changes in load-displacement data both to identify the crack nucleation and fracture load to be used in fracture toughness measurements. This is problematic if the loading system is compliant or stores significant energy, and load control inherently does not lend itself to stable fracture.

Unfortunately, an unstable loading geometry limits evaluation of fracture toughness to extraction of a single value. This issue is compounded by warranted concerns about the effects of notch manufacture at this small lengthscale, such as the introduction of FIB-induced damage in the region surrounding the notch [88] .

In light of these previous geometries [73], it would be ideal to have manufactured samples with geometrical features enabling:

- stable crack growth beyond any damaged region, in order to measure fracture toughness as the crack evolves and to overcome limitations imposed by FIB-induced damage;

- relative freedom in the positioning of the notch;

- minimization of the effect of frame compliance and friction between the indenter and the sample, making evaluation of the measured energy easier.

- use of a relatively simple sample geometry thus facilitating sample fabrication and fracture or surface energy analysis;

Polycrystalline diamond

Synthetic diamond and in particular polycrystalline diamond have attracted great research efforts especially in the last four decades. The international output of diamond in 2010 was measured at 4450 million carats, 98% of this is synthetically produced [94]. In the same year polycrystalline diamond (PCD) cutters accounted for 65% of the volume drilled in oil and gas exploration compared to only 2% in 1982. Advancement in the synthesis process and a better understanding of the mechanisms of failure of these products contributed greatly to the remarkable increase in their use in cutting and drilling operations. On the other hand, the tool life and performance of PCDs is still highly unpredictable, largely due to the complexities involved in their production and final microstructure.

Here an overview of production of polycrystalline diamonds and their properties is provided to expose some of the unanswered questions related to their performance.

2.1 From natural to synthetic diamond

Diamond is a material widely known for a peculiar characteristic: it is the hardest material naturally forming on earth. In addition, diamond is also endowed with the highest Young's modulus and room temperature thermal conductivity of any material (see Table 2.1). Diamond's intrinsic high hardness and stiffness are explained by the high strength of its tetrahedral, covalent bonds between each atom and its four nearest neighbours.

These features make diamond the best candidate for a number of industrial applications primarily as tooling (e.g. for indentation, cutting, drilling, grinding, shearing and wire-drawing).

A main obstacle for the use of natural diamond in industrial applications is their scarcity and affordability. For this reason, since it was discovered that diamond is an allotrope of carbon, many attempted to obtain it synthetically from cheaper forms of carbon. Diamond requires high

pressures and temperatures to form naturally, therefore such experiments tried to replicate these conditions in a laboratory.

Table 2.1 — Comparison of hardness, Young's modulus and thermal conductivity of single crystal natural diamonds with copper and tungsten carbide. Copper is often used in heat exchangers for its high thermal conductivity, yet diamond thermal conductivity can be over 5 times greater. Tungsten carbide is commonly employed for drilling tools given its high hardness; the table shows that the hardest orientation in diamond is up to 6 times harder than tungsten carbide.

Property	Diamond (single crystal, natural)	Tungsten carbide	Copper (pure)
Knoop hardness (GPa)	56-113* [95]	18 [96]	-
Young's modulus (GPa)	1013 ± 53 [95]	691 ± 23 [96]	120 [97]
Thermal conductivity (W/(m K))	600-2200** [95]	84-107 [96]	403 [98]

*depending on crystallographic direction; ** depending on the chemical impurities

Although several claims were made between the 1860s and 1890s that diamond was obtained from charcoal or mixtures of hydrocarbons and bone oil, later experiments could not reproduce these results. Furthermore, later investigations suggested that it is unlikely that the thermodynamically favourable conditions to grow diamonds were actually met in those early experiments [99]. Berman and Simon finally established the equilibrium curve between diamond and graphite in a pressure vs temperature diagram, shown in Figure 2.1, making use of experimental data in 1955 [100,101]. In addition to thermodynamic conditions, also the kinetics of transformation need to be accounted for. Although diamond is not thermodynamically stable at room temperature and pressure, the kinetics of transformation from diamond to graphite prove this to be a slow process. Similarly, the opposite also holds true, so that to transform graphite to diamond it is not sufficient to simply reach a point of the P vs T diagram above the equilibrium curve. Therefore not only higher pressure than that obtained previously needed to be reached, but also the rate of transformation needed to be increased in order to produce man-made diamond.

The first commercially successful production of synthetic diamond was finally published by General Electric Company in 1954 when significant progress was made in the design of a press that could reach pressures above 10 GPa at temperatures above 2300 K [99]. In this and other

successful experiments performed in the following months and years elsewhere, the kinetic barrier was overcome using molten nickel, cobalt or iron as carbon solvent/catalysts during the sintering process [102].
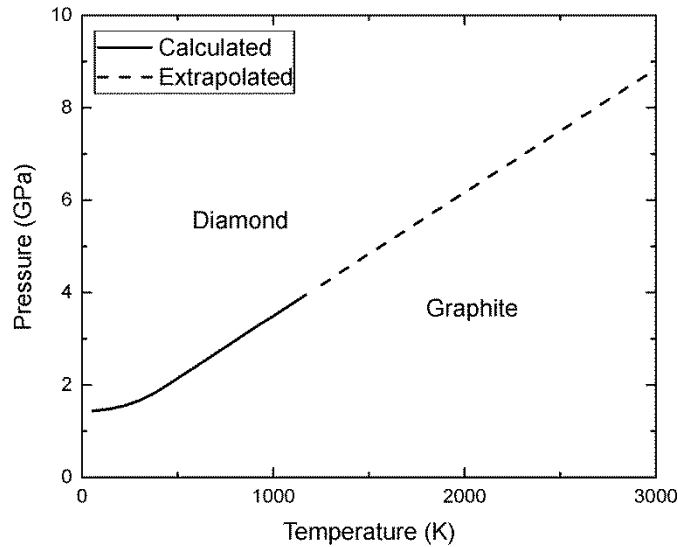
Figure 2.1 — Graphite-diamond pressure vs temperature equilibrium curve. Redrawn after data from [101].

In addition to high pressure, high temperature (HPHT) methods, since the 1960s crystalline diamond films are successfully produced also at lower pressure and temperature by chemical vapour deposition (CVD) processes [103] from energized hydrocarbon gases or plasmas mixed with an excess of hydrogen [104].

The size of single crystal diamonds produced by both HPHT and CVD methods is usually limited to a few millimetres and such products are mainly employed in the jewellery industry or for electronic and optical applications, but also as cutting tools, wire drawing dies and dressing for tools.

Other major disadvantages of using single crystal diamonds arise from their poor fracture properties that hinder their use in a broader range of engineering applications. It is well known from the jewellery industry that rough natural diamond can be relatively easily split, prior to cutting, by cleaving along a certain family of planes to obtain relatively flat surfaces. The weakest, also known as "easy", cleavage in cubic diamond (the most common lattice, although hexagonal

structures have been observed and produced [102]) is along the {111} planes and dominates its fracture properties; as a consequence, single crystal diamonds suffer from a strong anisotropy of fracture toughness. Across these planes the number of bonds per unit area is the least. In addition, the impurities, usually from atoms larger than carbon, tend to be accommodated more easily on these planes since here the misfit strain is the smallest [105].

The superior performance as cutting tool of polycrystalline diamond with respect to single crystals has been appreciated for well over a century; in 1870 natural "black diamond" was observed to last months in cutting grindstones without appreciable deterioration [106]. Unfortunately, natural polycrystalline diamonds, found mainly in two forms as carbonado and ballas, the first consisting of a porous aggregate of diamond crystallites of diameters between fraction of microns to over 20 μm often containing inclusions of a second phase while the latter forms as globular aggregates growing radially from the centre, are extremely rare and found primarily in Brazil and South Africa [107–109]. The higher fracture toughness [107] and wear resistance [106] was attributed by several authors uniquely to the higher isotropy offered by the polycrystalline agglomerate, i.e. to the fact that the crystals of which they are made are randomly oriented thus not offering an easy cleavage [1,105]. However, carbonado grains are not always randomly orientated, in fact often some degree of texture is observed that likely originates from the strong pressure or temperature gradients present during its growth [107]. It is also worth noting that the role of grain boundaries, impurities and porosity on the fracture properties of carbonado and ballas is not discussed thoroughly in literature. Studies on carbonado suggest that fracture can be both transgranular and intergranular [107,108]. A study by Trueb and de Wys found that, although fracture was mainly transgranular in their carbonado samples, when intergranular fracture occurred this was characterised by the presence of pores of ~50 nm along the boundaries [107]. Furthermore, conversely to single crystal diamond, mineral inclusion and other non-diamond phases were never observed within the diamond grains itself but always at the boundaries [107,108]. Once the non-diamond phases are leached, carbonado still shows extensive diamond-diamond bonding [107]. Besides the more

isotropic response, it is therefore likely that boundaries and pores may play an important role in the fracture properties of carbonado.

Given their superior performance carbonado diamonds were used in industrial applications for some time, yet they are difficult to shape in the form of tools owing precisely to the lack of regular cleavage planes and difficulties in cutting and polishing them [1]. Additionally, their properties vary too much as the degree of the natural sintering process is quite variable [108].

Therefore, there was interest in the possibility of producing cheap and readily available synthetic forms of carbonado by pressing together diamond particles, with the added benefit that nearly net, complex shapes could be obtained directly in a mould and their properties controlled [1].

Hall obtained synthetic carbonado by pressing natural diamond powder at pressures between 6.5 and 8.5 GPa and temperatures between 2440 and 2500 K for as little as 21 seconds [1]. Hall could obtain self-bonded polycrystalline diamonds, i.e. with nothing but the diamond itself as responsible for the bonding, but suggested that a binder in the form of hard refractory substances could be used. In addition to superior fracture performance, the samples obtained by Hall were over 0.6 cm in diameter and ~0.5 cm long, therefore much larger than the single crystal samples obtained previously.

Katzman and Libby were the first to report the production of a synthetic polycrystalline diamond composite, bonded together by 20% volume of cobalt [2]. The idea of using cobalt as a binder was borrowed from the cemented carbides production process to obtain a more homogeneous and tougher final product and to facilitate the production process. The authors dried and then mixed fine powders of diamond (0-2 μm, 1-5 μm or 10-20 μm) and cobalt (0-5 μm). The mixed powder was then sintered at 6.2 GPa at 1590 °C, above the eutectic line for Co-C system and therefore in the presence of a liquid phase. The samples showed densities above 99 % of the theoretical density with a good bonding provided by the cobalt, with the added benefit that the binder can plastically deform and potentially increase the fracture toughness [102].

Two years after the publication from Katzman and Libby, a patent from Wentorf and Rocco described a way to sinter diamond directly on top of a layer of tungsten carbide [110]. The method proposed in the patent showed that the cobalt contained in the cemented carbide powder mixture was able to both serve as metal binder for the carbide itself and as both solvent and catalyst for the diamond. The patent suggests that other metal binders (i.e. nickel and iron) and that different mixtures of carbide powders or an already cemented carbide substrate could be employed. Even in the latter case the metal binder is effective as catalysts and solvent for the diamond. The final product is a ready-made insert tool with a layer of diamond directly bonded to a sintered carbide substrate that can be brazed on a tool holder.

Although different processes and parameters have been tested and used to tweak the properties of the final product, most of polycrystalline diamonds (PCD) or polycrystalline diamond compacts (PDC) currently commercially available are fundamentally similar to those described by Wentorf and Rocco in that the diamond layer is bonded on a cemented carbide substrate (see Figure 2.2) via liquid phase sintering.
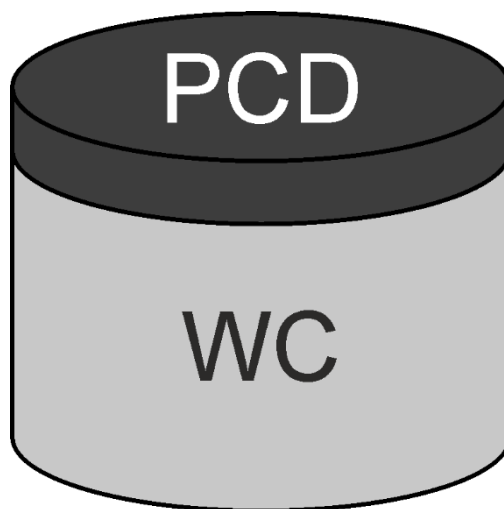
Figure 2.2 — Schematic of PCD cutters. Generally the substrate is made of WC containing cobalt or cobalt mixed to other solvent catalysts (e.g. Ni, Fe, Cr). The PCD layer is therefore a composite of diamond grains with a network of cobalt or WC-Co interfaces.

2.2 Sintering

In order to discuss the effect on the final properties of PCD of the several parameters that can be changed during production (e.g. starting powder size, temperature, pressure, chemistry of the binder), the general phenomena occurring during sintering, in particular liquid phase sintering, are introduced here.

2.2.1 Solid state sintering

Owing to the generally high melting points of the raw materials involved, the fabrication of ceramic materials commonly includes a heat treatment in which a powder compact, already formed into a required shape, is converted into a dense solid. Sintering can be seen, in a broad sense, as the extension of the contact area between powder particles through the transport of material to or around the pores under appropriate conditions of temperature, pressure and environment [111]. Sintering is commonly divided into three stages, which are not to be considered discrete, in fact usually overlap. The *initial stage* is characterised by the neck formation and growth. This means that the contact area between the particles increases, however only a very small fraction of densification occurs. The most of densification takes place during the *intermediate stage*. At this stage, a network of open, cylindrically shaped, pores is present and starts to shrink, while the grains start to grow. In the *final stage* the pores continue to shrink until they form isolated and spherical pores, "closed porosity".

The starting particulate is characterised by an excess of free energy, caused by the large surface area to volume ratio, and that represents the driving force behind sintering. As the sintering proceeds, porosity reduction translates in a reduction of the solid-vapour interfacial area, replaced by solid-solid interfaces. The grain growth, instead, causes a solid-solid interfacial area reduction. The change in free energy can be written as:

$$\delta G_{system} = \delta \int \gamma_{SV} dA_{SV} + \delta \int \gamma_{SS} dA_{SS} \tag{2.1}$$

where δG_{system} is the change in the free energy of the sintering system, γ_{SV} is the energy per unit area of the solid–vapor interface, and γ_{SS} is the energy per unit area of the solid-solid interface. As during sintering the area of the solid-vapour interface (A_{SV}) decreases the first term in the equation is negative. Sintering also causes the area of solid-solid interface to increase, however grain growth results in its decreasing. Consequently, depending on the grain growth rate the second term can be either positive or negative. Since for all crystalline solids $\gamma_{SV} > \gamma_{SS}$, it can be shown that two concurrent and competing mechanisms exist for the free energy reduction. One is the densification, where the transport of matter occurs from the contact area to the pore (decreasing A_{SV} and increasing A_{SS}) reducing the pore volume. The other is the coarsening, where the matter is transported from one region of the pore to another. The surface area of the pore changes, whereas its volume does not.

The mechanisms of matter transport, necessary to reduce the porosity and move from the initial state of higher energy of compacted powder and achieve the final state of lower energy of consolidated material, are activated thermally to overcome the potential barrier between the two states. Pore volume fraction approaches zero asymptotically, but complete densification can be prevented by trapped gases in some of the pores exerting a pressure opposed to further shrinkage.

2.2.2 Liquid phase sintering

Polycrystalline diamonds are produced by liquid phase sintering (LPS) in which the matter transport occurs by diffusion of atoms through the liquid phase formed by the partial melting of one of the components and which is present in a few volume percent. This enhances the densification rate due to the higher diffusion rate, with respect to solid state sintering (in addition to act as a catalyst for the transformation of graphite into diamond, as already cited).

Several parameters control densification such as grain size and shape, pore size and shape, liquid volume and viscosity, solubility of the solid in the liquid phase, wetting of the solid by the liquid, phase distribution and phase-boundary energies.

A necessary condition for LPS is that the liquid must wet the solid phase. A drop of liquid on the surface of the solid phase reaches the equilibrium when this exists between the three components of surface energies of the three different interfaces (SV= solid/vapour, SL= solid/liquid, LV= liquid/vapour). Such equilibrium is represented by:

$$\gamma_{SV} - \gamma_{SL} = \gamma_{LV}\cos(\theta) \tag{2.2}$$

where γ is the surface energy and the subscript specifies the interface, and θ is the angle formed by the drop of liquid onto the surface, following the convention shown in Figure 2.3.
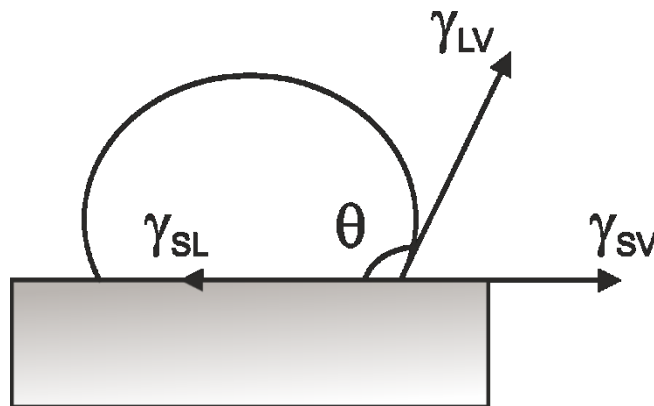
Figure 2.3 — Drop of liquid at equilibrium on a solid surface. γ is the surface energy and the subscript specifies the interface, with SV= solid/vapour, SL= solid/liquid, LV= liquid/vapour

If $\gamma_{SV} < \gamma_{SL} + \gamma_{LV}$ the liquid minimises the free energy by assuming the shape of a droplet with finite angle; this is defined as partial wetting. For $\gamma_{SV} = \gamma_{SL} + \gamma_{LV}$ the angle $\theta = 0°$, i.e. the liquid spreads on the solid surface for complete wetting. The situation in which a vapour layer is interposed between the solid and the liquid is thermodynamically equivalent to complete wetting and is known as complete drying, however this is rare in practice as van der Waals forces tend to reduce the vapour volume. When the liquid is surrounded by the solid, as it occurs in a pore, its spreading causes the generation of new liquid/solid interface without increasing the liquid/vapour

interface area. In this case the equilibrium between the surface energies of solid grain boundary, GB, and liquid is given by:

$$\gamma_{GB} = 2\gamma_{SL}\cos(\phi/2) \tag{2.3}$$

where ϕ is the dihedral angle that controls the penetration of the liquid through the grain boundaries, until a possible grain separation, as shown in Figure 2.4.
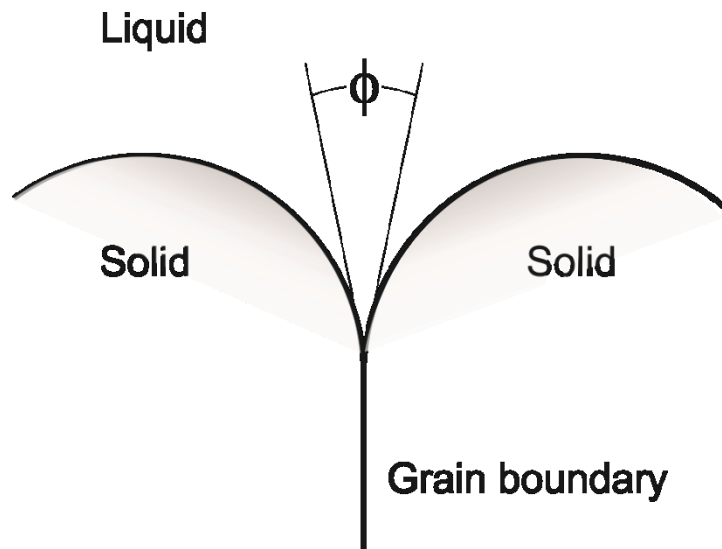
Figure 2.4 — Dihedral angle, ϕ, for a solid-liquid system. This angle controls the liquid penetration along a grain boundary through the equilibrium between the surface energies of solid grain boundary and liquid.

A driving force for densification in the case of LPS arises from the capillary pressure in the pores, whose magnitude is so high that often suppresses the need for external forces application [112]. Similarly to solid state sintering, the densification occurs also through three stages.

- In the first, the rearrangement stage, as soon as the liquid forms it is drawn towards the point of contact between the grains by the capillary forces; such viscous flow helps the particle rearrangement.

- The second stage, in which the atom transports is the main process, can be subdivided itself in three steps. First, the atoms migrate from the bulk of the grain towards the surface, here react and dissolute in the liquid phase. Second, the atoms diffuse through the liquid

away from the contact points. Finally, the atoms reprecipitate at grain boundaries, dislocations or existing seeds.

- The third stage involves the grain growth or coalescence. The rate of densification decreases as the grain growth generates closed porosity that act as an obstacle to further transport of the liquid phase and can trap gases that oppose to further shrinkage.

Application of external pressure can assist the sintering process as it acts as additional driving force for matter transport, reducing the time for densification. This in turn has also the effect of reducing the grain growth, resulting in a more homogeneous fine-grained microstructure.

The sintering of polycrystalline diamonds is indeed assisted by high pressure in addition to high temperature, not only for the reasons above listed but especially to maintain the diamond in its stable region of the P vs T diagram (see Figure 2.1).

2.3 Production of polycrystalline diamond

As anticipated in the previous paragraphs, PCD cutters are manufactured by liquid phase sintering (LPS), by subjecting diamond powders to high pressures and high temperatures on top of a carbide substrate containing a metal binder. During sintering, the metal binder plays the role of the liquid phase and acts both as solvent and catalyst for the diamond. The whole production process consists of a sequence of several stages that include pre- and post-sintering processes, described in the following paragraphs.

2.3.1 Pre-sintering

The first step of production consists of powder selection and mixing. The final grain size strongly influences the performance of PCDs, as discussed in the following paragraph (see 2.4), and it partly depends on the particle size distribution (often referred as grade) of the starting powders. Since during compaction the particles tend to crush, the final grain size is not necessarily the same as of

the starting powders, rather it depends on pressure applied, initial shape and dimension. Multimodal powders, i.e. with more than one grade, are usually favoured to monomodal in commercial products. The former, indeed, reach a higher densification percentage during the pre-sintering phase and are chosen to achieve a good compromise between the performances of fine and coarse grains (see 2.4). Higher densification before the sintering translates also into fewer voids and, as a consequence, a smaller amount of infiltrated cobalt during the sintering process.

The chemistry of the final product is influenced by the metal binder mixed in the substrate chosen or directly in the diamond powder. The most popular substrates are made of tungsten carbide with a varying amount of cobalt [113], alternatively other additives in addition to cobalt are employed, e.g. nickel and chromium, in smaller percentage.

To manufacture multimodal commercial products the first step consists of powders mixing in a planetary ball mill together with acetone to help the homogenisation, then these are dried and sieved. The powders are then pre-compacted, outgassed at high temperature and high vacuum and finally sealed in a metallic container placed in pressure and heat transfer media inside a graphite tube.

2.3.2 Sintering

A typical sintering profile is designed to be always in the region of pressure where diamond is stable as the temperature changes to pass the eutectic point in the C-metal diagram at said pressure, e.g. the W-C-Co eutectic temperature is ~1320 °C at atmospheric pressure [114], 1570 °C at 6.2 GPa [2]. This is achieved increasing first the pressure to reach the desired value, which usually sits in the range between 5 and 10 GPa (to obtain good diamond-diamond bonding), thereafter the temperature is increased.

During the stage when only pressure is applied, i.e. cold compaction, an initial rearrangement of the particles takes place under pressure, then densification increases when they start to crack and

crush causing a change in the particle size distribution and the smaller fragments start filling the voids between bigger particles.

The extent of the comminution and the change in particle size distribution modality ensuing was found by Gruzdeva *et al.* [115] to depend on the initial particle size. After cold compaction a maximum in the particle size distribution was found between 1 and 2 μm for all powders of initial size in the range 3-60 μm. Then, as initial particle size is increased, a second maximum was found to shift to larger sizes. As such a bimodal distribution formed after cold compaction with the ratio between the size of the two grades increasing for larger initial particles. Bochechka [116] found that for pressure of up to 8 GPa the diamond particles fail mainly by a mechanism of mutual indentation caused by sharp edges of one particle on flat surfaces of a second particle. Furthermore, at any given external pressure there is a critical particle size below which failure does not occur; Bochechka found this critical size to be inversely proportional to the square of the pressure. As a consequence smaller initial particle size tend to crush less or not at all, thus justifying the presence of the same maximum at small sizes for all starting powders. Furthermore, since the packing density of powders with a bimodal distribution is higher than that of a single fraction [115], finer particles tend to densify less. In particular, the highest density is obtained when the volume of fine particles matches that of the voids formed between the coarse particles. Gruzdeva found the density to start increasing when the ratio of the linear dimensions characterizing the coarse and fine fractions is higher than 3-5, and reaching a plateau for a ratio equal to 8-10 [115]. Once the desired pressure is reached, the temperature is increased by resistance heating arising from electric current flowing through the anvils to the temperature transfer disks and the graphite tube. Although the externally applied pressure is close to hydrostatic, this only transfers to surfaces in contact whilst surfaces within interstitial voids are at lower pressure. Consequently, as the temperature increases diamond in the pores becomes unstable and graphitises [117]. When the temperature reaches the eutectic point of the WC-Co phase, the driving force for the penetration of cobalt between diamond particles stems from this high difference in pressure between the solid

mass and the empty pores, both open and closed since cobalt is able to dissolve the neck between diamond particles, in the diamond layer. The cobalt, thus, can infiltrate from the substrate through the diamond particles at which point graphite dissolves into molten cobalt while the pressure in the intergranular spaces increases leading to a reprecipitation of the graphite as diamond [117]. Following the same principle as during the loading ramp, the temperature is decreased before the pressure is reduced to stay within the diamond stable region. The cooling rate and the rate at which the pressure is released affect the residual stress state in the final product, as will be discussed in paragraph 2.4.4.

2.3.3 Final microstructure

The typical microstructure of PCD is characterised by mainly equiaxial diamond grains with different degrees of diamond/diamond bondings alternating to cobalt pools, as shown in Figure 2.5.
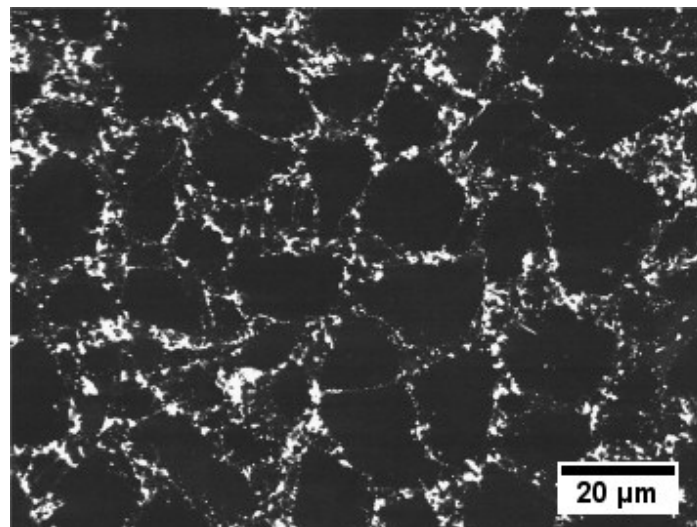
Figure 2.5 — Scanning electron micrograph of typical PCD sample. Diamond grains appear as the dark phase whereas the bright phase is cobalt. From [118].

Interestingly the average grain size of the PCD after sintering is usually found to be smaller than the starting powders [3], regardless of the initial particle size; this is due to the comminution occurring during the cold compaction stage (see 2.3.2) and the relatively quick sintering stage that

limits grain growth. However, PCDs sintered from coarser starting powders show a larger reduction of mean grain size and a wider size distribution than finer particles [3].

The cobalt content is also a function of initial particle size [3,4] as shown in Figure 2.8-(a), with the cobalt content decreasing by over a factor of two in the range between 2 and 40 μm.

In commercial products grain size typically vary from a few to ~50 μm [119] and the metal content between 5 and 20% volume. However larger grain sizes have been also investigated in the literature.

2.4 Mechanical properties

Several studies have been conducted on PCDs to assess their mechanical properties, some of them with a particular focus on the relationship between such mechanical properties and grain size and, being a two phase material, on the changes in properties related to cobalt content.

A primary difficulty in evaluating mechanical properties of PCD stems from the limitation brought by the sample dimensions for conventional methods. PCDs are indeed usually produced as discs of few tens of millimetres of diameter and in the range of 0.2-4 mm of thickness [120–122]. Besides dimensions, fabrication and preparation of samples, for instance notching the specimen for fracture testing, is particularly challenging owing to the high hardness and stiffness of diamond [119].

Since polycrystalline diamond is mostly used as cutting tools, its wear resistance, in particular abrasive wear resistance, is the characteristic of higher importance for the industrial application. However, chipping and catastrophic brittle fracture is a common problem for this material that reduces its service life. Therefore, investigation of strength and fracture of PCDs and how these can be controlled intrinsically (changing the process parameters to affect the microstructure) or

extrinsically (designing a structure independent from sintering and thermo-mechanical treatments [119]) are crucial.

Table 2.2 presents a list of the properties of PCDs as obtained by Lammer [123], however a more detailed summary of some of the findings present in the literature on strength, wear and abrasion resistance, fracture toughness and mechanisms and residual stresses in PCDs is presented in the following sections.

Table 2.2 — Properties of PCD in both supported, i.e. sintered on top of a WC-Co substrate, and unsupported, i.e. prepared directly as discs, configuration. For the supported PCD the substrate was removed before testing. Redrawn from [123]**.**

Property	Cobalt matrix PCD supported by tungsten carbide-cobalt				Unsupported cobalt matrix PCD		
Nominal grain size (μm)	2	12	30	125	30	95	150
Matrix (cobalt or silicon carbide) content (vol%)	13	11	11	12	5	6	5
Density (kg m^{-3})	4.24 ± 0.10	4.12 ± 0.09	4.10 ± 0.11	4.15 ± 0.10	3.77 ± 0.12	3.83 ± 0.06	3.79 ± 0.12
Longitudinal speed of sound (m s^{-1})	13360 ± 460	13810 ± 800	13130 ± 660	14370 ± 790	15520 ± 165	15400 ± 240	15910 ± 160
Transverse speed of sound (m s^{-1})	—	—	—	—	10520 ± 140	10450 ± 190	10820 ± 170
Transverse rupture strength (MPa)	1550	1260	1190	440	1090	520	390
Tensile strength (MPa)	—	—	—	—	1540 ± 210	300 ± 140	340 ± 75
Compressive strength (MPa)	—	—	—	—	4700 ± 1200	2500 ± 900	2000 ± 600
Fracture toughness (MPa m$^{1/2}$)	6.9 ± 0.4	8.8 ± 0.5	8.9 ± 0.4	7.5 ± 0.8	9.1 ± 0.4	7.5 ± 0.2	7.0 ± 0.6
Poisson's ratio	0.070	0.070	0.070	0.070	0.075	0.070	0.073
Young's modulus (GPa)	750	775	810	850	900	900	950
Shear modulus (GPa)	350	360	380	400	420	420	440
Bulk modulus (GPa)	290	300	310	330	350	350	370

2.4.1 Wear/abrasion resistance

Since PCD is extensively used as cutter, testing its wear mechanisms and resistance is crucial to investigate the service life and behaviour.

As abrasion can be defined as the penetration and removal of a softer material by the action of a harder material that is moved across it under an applied load, the intrinsic high hardness of diamond is crucial for the abrasive performance of PCDs. Interestingly, despite a Knoop hardness

of between 55 and 113 GPa depending on the type and orientation (see Table 2.1), single crystal diamond can be polished and the technique used for doing so, i.e. pressing the crystal on a cast iron disc charged with olive oil and diamond grit, has been unaltered for centuries [94,124,125]. However the mechanisms of wear in diamond are rather complex and only recently our understanding has deepened and allowed us to explain the anisotropy observed. When polishing in the jewellery industry the directions in which wear proceeds faster are known as 'soft', whereas those in which wear occurs slowly or not at all are named 'hard'. These are respectively the <100>-type directions in the {100} and {110} planes, while the {111} plane is fairly resistant to wear [124]. Hird and Field [124] showed that polishing in the 'soft' direction is related to a shear-induced transition of sp^3 to sp^2 material, while there is conclusive evidence that in 'hard' direction wear proceeds predominantly via microcracking. Experimental study of these mechanisms is made particularly difficult by the small amount of material loss and complexities arising by a combination of other variables difficult to control (e.g high temperature build up due to friction or catalytic effect of the iron discs, known as scaife, typically employed in the polishing of diamond) [124].

In practice the wear resistance of PCDs cutters is a combination of the intrinsic wear properties of diamond and the fracture resistance of the composite. It is therefore common practice in the rock drilling industry to test abrasive properties of PCD simulating the condition of rock cutting, i.e. pressing the cutters against spinning cylindrical rock blocks, typically granite [126]. Employing a similar configuration, Miess and Rai [4] measured the abrasion resistance as ratio of volume of granite removed to the flat area of wear generated on the rake of the tool and normalised the result with respect to that of the 30 μm grain sized PCD. The trend obtained, shown in Figure 2.6, shows a strong influence of the wear resistance from the grain size, with smaller grains exhibiting a higher abrasion resistance.
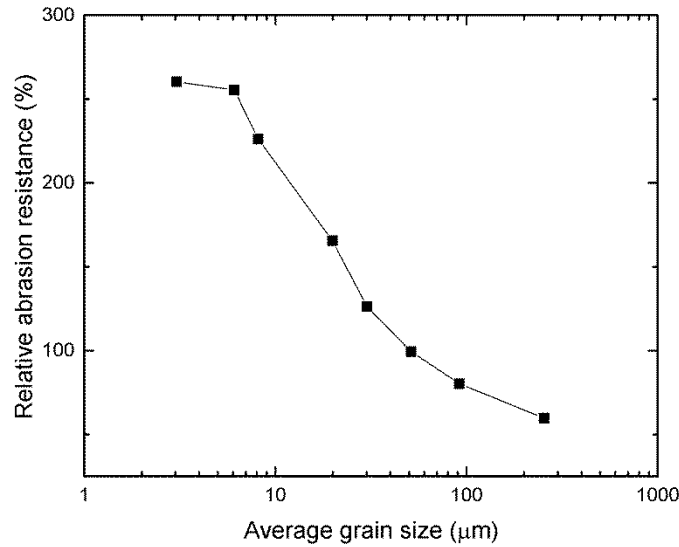
Figure 2.6 — Relative abrasion resistance of PCD plotted against average grain size. The abrasion resistance is measured in percentage normalised to the value from the 30μm PCD; the trend shows an inverse proportionality between abrasion resistance and grain size. Such results obtained by Miess and Rai [4] have not been confirmed in other studies as shown in Figure 2.7. Redrawn from [4].

By contrast, several other studies suggest that intermediate (~30 μm) starting grain size result in better cutting performance than smaller, as reported in Figure 2.7, or larger ones [127–129]. In particular, Liu *et al.* [129] reported that PCD with starting grain size of 30 μm showed significantly longer tool life in turning granite than those with a 5 μm starting grain size. The trend is confirmed by studies conducted on milling a ceramic impregnated surface of a flooring board, that showed that 25 μm grained PCD perform better than 75 μm as well as 2 and 10 μm grained PCDs.
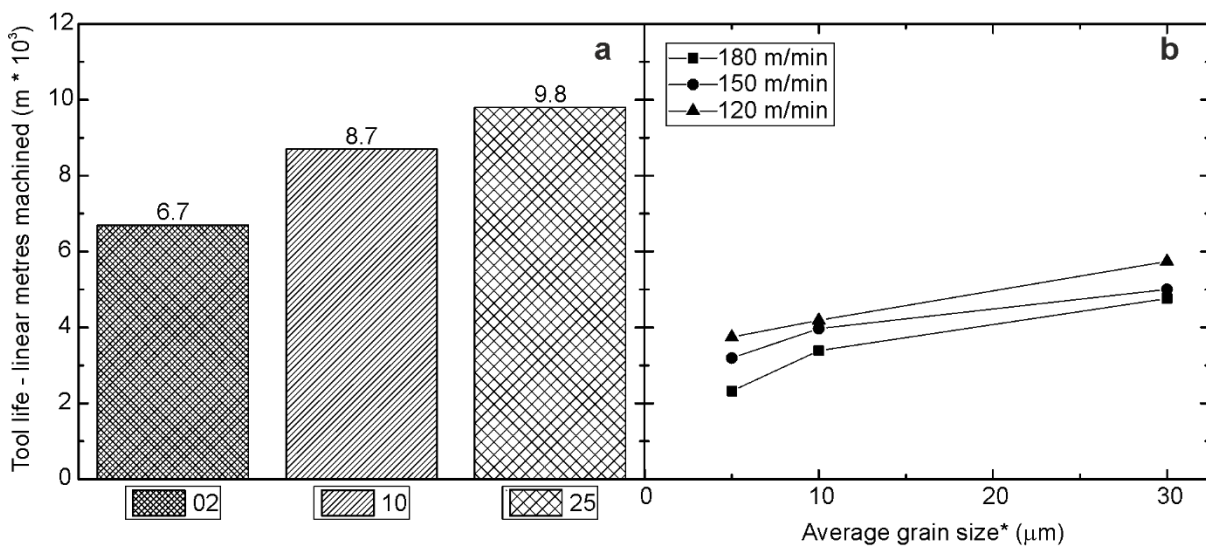
Figure 2.7 — PCD tool life as function of grain size. Tool life is expressed as linear metre of material machined before failure or excessive wear in relation to average grain size (*assumed equal to size of starting powders) **(a)** as measured by Cook and Bossom on ceramic impregnated layer (redrawn after data from [127]) and **(b)** by Liu *et al.* on granite (redrawn after data from [129])

Different wear mechanisms occurring at different grain sizes and testing conditions are likely responsible for the different trends in performance against grain size observed by the different authors. Liu *et al.* [129] observed that abrasive wear mechanism prevails at smaller grain sizes, while at 30 μm intergranular and cleavage fracture appears to be a dominant mechanism. Moseley *et al.* [130] identify at least five different mechanisms, highly dependent from the complex loading conditions, that lead to end of tool life in PCD with 25 μm sized grains, with gross fracturing, chipping and abrasion wear as the three main ones.

From the evidences of these studies and consideration on the microstructural changes with grain size, the trend at the two extremes could be explained as follows:

- Fine grained PCD tends to have a higher content of cobalt. This has a twofold effect: a) it lowers the overall hardness of the tool (see Figure 2.8); b) acting as catalyst, cobalt promotes the faster transformation of the diamond surface, already thermodynamically unstable at room temperature and ambient pressure, to graphite as the temperature increases due to friction [131].

- Coarse grained PCD hardness approaches that of single crystal diamonds, however larger grains will have a higher probability of containing defects larger than the critical size to cause crack growth. Ultimately gross fracturing is responsible for loss of larger volume of materials and catastrophic failure.
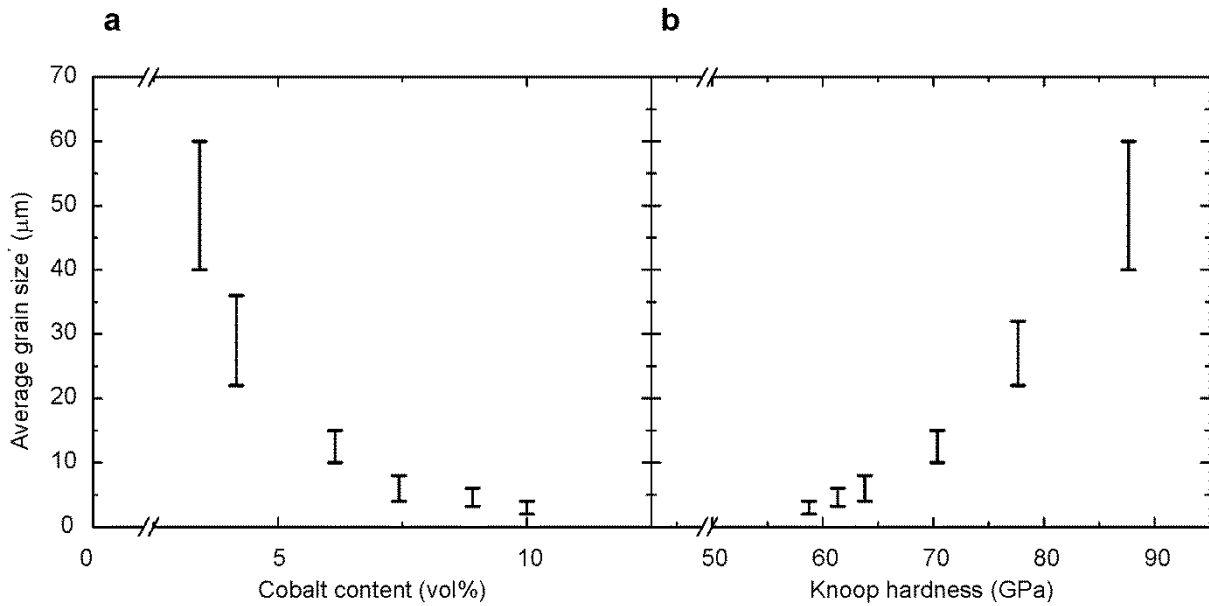
Figure 2.8 — Variation of cobalt content (a) and hardness (b) as function of the average grain size (*assumed equal to size of starting powders). Redrawn after data from [3].

Therefore intermediate grain sizes offer a compromise between hardness, strength and toughness (see 2.4.2).

However, it is noteworthy that different studies are clearly also subject to differences in the product investigated as modifications in the synthesis process was shown to produce an increase in the performance of tool life of ~60% between two products of same grade [127].

2.4.2 Transverse rupture strength

Transverse rupture strength (TRS), also known as flexural strength, is usually assessed by testing a bar in bending (see paragraph 1.2.1). However, because PCDs are produced as discs, testing is often carried out through three point bending on discs or plate [102,123]. As in other polycrystalline brittle materials, the TRS has been found to decrease with increasing grain size and displays two characteristic regions when plot against (grain size)$^{-1/2}$ [123,132]. Lammer discussed two mechanisms to explain this behaviour:

- the first based on the effect of dislocation activity leading to crack nucleation dominant in the region of small grains while for larger grain sizes it is the biggest grain to be the dominant flaw;

- the second based on the relationship between the crack length a and the grain size dimension d.

Although plastic flow is observed in diamond subject to high pressures even at room temperature, Lammer deemed the first mechanism as unlikely and showed the second interpretation predicted the grain size transition zone correctly in the case of PCDs. According to Rice [133] the size of the inherent flaw, a, in several ceramics is independent of grain size, d, therefore for coarser grains the a/d ratio is smaller and the flaw is more likely to be entirely contained in a single grain. In this case the strength is controlled by the single crystal surface energy; that is, the crack extends when the value of critical stress intensity factor of the single crystal is reached. Finer grains lead to a bigger ratio, so that in this case the strength is controlled by the polycrystalline fracture energy. The change from one regime to another occurs for $a \approx d$. Lammer calculated the critical crack lengths from the measured K_{Ic} values for the PCDs and assuming a simple flaw geometry finding that the transition should be observed between 12 and 30 μm, which is indeed what the experiment showed. Similarly, Huang *et al.* found a transition between the two regimes at 35 μm, which the authors considered to be the flaw size.

Lammer [123] also investigated the influence of cobalt content on the TRS. Although the author claims that the content of cobalt in the product is of statistical nature with no possibility of controlling it systematically during processing the work shows that a trend towards direct proportionality between strength and cobalt content exists. As discussed in 2.3.3 a direct proportionality exists between cobalt content and grain size, but due to the sintering process used it is very difficult to control cobalt content independently from grain size.

2.4.3 Fracture toughness

The relationship between fracture toughness of PCDs and grain size has also been investigated, employing either diametral compression [4,123], consisting in the loading of a disk with a notch in the centre aligned along the load axis, or single-edge precracked beam [132].

It should be noted that the value obtained with diametral compression tests should not be referred to as fracture toughness as the fracture initiates from a sharp notch and not a crack, yet to be consistent with the published research the term fracture toughness will be used here.

The three studies consistently show that fracture toughness increases with increasing grain size. However, Lammer's results [123] show that after reaching a maximum for grain size of 30 μm the fracture toughness decreases with increasing grain size, no direct explanation of such inverse proportionality is provided by the author. Such trend was not confirmed in the measurements made by Miess and Rai [4], who found that beyond 30 μm grain size the fracture toughness had a constant value, up to the maximum grain size examined of ~120 μm, and Huang *et al.* [132], who conversely observed almost negligible increase in fracture toughness in the range 5-20 μm and thereafter a 40% increase for particle size of 75 μm.

The fracture toughness values reported in the three works span a quite wide range (see Figure 2.9). Lammer [123] reports values between 6.8 to 9.1 MPa m$^{1/2}$ depending on the grain size ranging from 2 to 150 μm and cobalt content, whereas Miess and Rai [4] measured values between 2 and 6 MPa m$^{1/2}$ for particles in the range 2 to 120 μm. Discrepancies between the values measured in the two studies are attributed to differences in manufacturing process [4], however the difference in the trend for higher grain size is not addressed. The results published by Huang *et al.* show a significantly higher value of about 10 to 14 MPa m$^{1/2}$ in the range of particle size from 5 to 75 μm [132], although in this case the fracture test method is different and not directly comparable.

It is noteworthy that although PCDs with smaller particle size tend to have a higher metal binder content that would suggest higher plastic deformation, their fracture toughness is in fact lower

than that of PCDs with larger particle size. This suggests that the higher content of metal binder alone does not contribute significantly to increase the fracture toughness [132]. Interestingly, Miess and Rai found that the toughness increases of a factor of three while the cobalt content decreases of factor of two in the range of 2 to 40 µm [4]. Lammer [123] and Huang *et al.* [132] point out that changes of fracture toughness with grain size can be attributed to the difference in thermal expansion between diamond and cobalt, leading to high stresses at the interface; this is further discussed in 2.4.4.
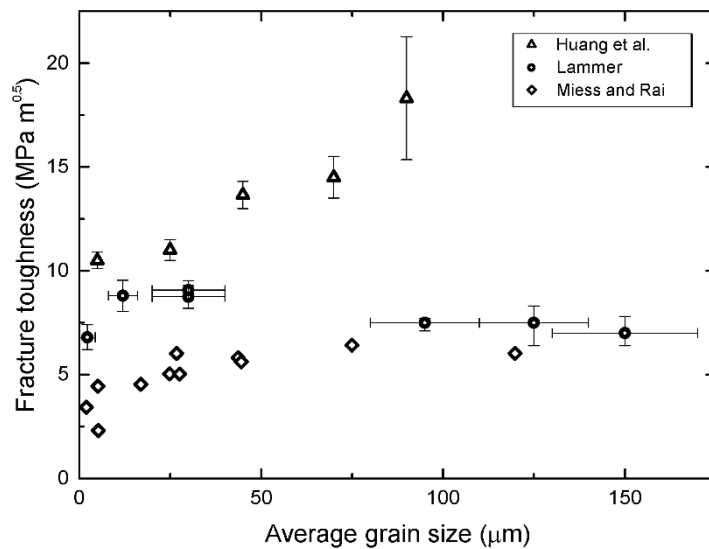
Figure 2.9 — Fracture toughness with average grain size of PCD. The values are those reported by Huang *et al.* [132] obtained via single-edge precracked beam; and by Miess and Rai [4], and Lammer [123] employing diametral compression. It should be noted that the value obtained with diametral compression tests should not be referred to as fracture toughness as the fracture initiates from a sharp notch and not a crack, yet to be consistent with the published studies the term fracture toughness is used here.

However, none of the three studies gives a conclusive justification to the variation of fracture toughness with the two parameters (i.e. cobalt content and grain size).

The loading rate at which tests are performed also has an effect on the fracture toughness of PCDs, as shown by Petrovic *et al.* [134]. The authors performed fracture tests in single edge V notched bend (SEVNB) specimen in three point bending at 5 different loading rates (ranging from 1 mm min^{-1} to 5 m s^{-1}) and 2 temperatures (25 °C and 300 °C) on G6 (6 µm grain size) and G30 (30 µm grain size) specimens. Their tests revealed that fracture toughness values remained relatively constant for lower loading rates up to 100 mm s^{-1} for G6 and up to 0.3 m s^{-1} for G30

specimens and dropped significantly thereafter at higher loading rate; on the contrary, the increase in temperature did not appear to particularly affect the fracture toughness in the range investigated.

2.4.4 Residual stresses

Diamond is characterised by a relatively low coefficient of thermal expansion (CTE), between 1.18 and 4.8×10^{-6} K^{-1} [5,11,18], with respect to both cobalt, between 12 and 14.4×10^{-6} K^{-1} [5,11], and carbides used as substrate, with 5.2×10^{-6} K^{-1} [11,18]. Given the large CTE mismatch the different phases constituting the PCD cutters contract at different rates when the product cools after the application of high temperatures, e.g. after sintering, thus generating residual stresses. These stresses superpose to in-service or further processing stresses and can be beneficial or detrimental depending on whether they hinder or favour reaching the failure stress of the component. It is therefore important to know their value and sign. As binder and carbide contract more than diamond upon cooling, the latter would be subject to compression while the former to tension after sintering, however this is a simplistic view that does not account for changes to the geometry of the cutters and the effect of microstructure.

Macroscopic residual stresses, i.e. those varying continuously across large distances and known as type I stresses, are deemed responsible for delamination of the PCD layer from the carbide substrate during drilling, brazing or even spontaneously after sintering, and for gross chipping under impact loading [11,13,15,17]. These have been evaluated using numerical analysis and measured using strain gauges while releasing the stresses, neutron diffraction and Raman spectroscopy (see section 3.4.1).

Numerical analyses based on linear elasticity [5,11,17] predict that for large substrate to PCD layer thickness ratio, i.e. for substrates that are at least 3 times thicker than the PCD layer, the latter is subject to high radial compressive stresses while the carbide to relatively lower radial tensile stresses. Experimental results have shown that these stresses can commonly reach values of up to between 1.2 and 1.4 GPa in compression in the PCD layer [11,15,16] with some authors finding

stresses of up to 1.9 GPa [4,17], which compare to a compressive strength for PCDs in the range of 1.9-4.7 GPa [123]. The experimental observations highlight a significant departure from linear elastic predictions in the study from Lin *et al.*, explained by a plastic accommodation of the stresses within the PCD [11,18], although it is not specified if this occurs in both phases or just in the binder.

Linear elastic models also fail to explain the effect of cooling rates on the magnitude of residual stresses found in the final products. Paggett *et al.* tested different samples treated with different HPHT, comprising conventional sintering, rapid cooling, a modified process thought to decrease residual stresses and stabilising post-sintering thermal treatments [18], however details of the different conditions are not disclosed. The authors employed Raman spectroscopy to find variations in the average in-plane compressive stresses from a minimum of 250 ± 50 MPa for the "stabilised" product to a maximum of 416 ± 50 MPa for the rapid cooled sample. The reasons behind this behaviour is explained in a study carried out by Kanyanta *et al.* who employed an elastic-plastic-creep model to investigate the effect on the stress transients and final residual stresses of different pressure and temperature ramps from sintering to ambient and room conditions respectively [13]. The study suggests that a slower cooling of the material results in lower stress transients while also allowing for larger creep and plastic deformations as the tool is held at higher temperatures for a longer period, therefore leading to lower final residual stresses. The transient stresses are showed to reach maximum values that are more than twice the final residual stresses, indicating that delamination and micro-cracking might occur during cooling even when final residual stresses appear much lower than the compressive strength of PCD. Analogously to temperature, the paper seems to suggest that pressure should be released slowly to reduce residual stresses, however the results seem to suggest differently and this is not discussed by the authors.

Similarly to Paggett *et al.*, Erasmus *et al.* employed Raman spectroscopy to measure the residual stresses of samples at different temperatures and after annealing cycles at 600 °C and 800 °C [16].

These temperatures were chosen by the authors to investigate two mechanisms that cause volumetric change, namely the cobalt phase transformation from hexagonal close-packed to face-centred cubic occurring at ~420 °C and the graphitisation of diamond occurring at ~750 °C. While the study finds that as the temperature is increased the compressive residual stresses are relaxed from 2 GPa at room temperature to 0.7 GPa at 620 °C, this phenomenon is reversible and the original residual stresses are reintroduced even after 5 annealing cycles to 600 °C. The authors conclude that the cobalt phase transformation does not play an important role on the surface stress state. Conversely, when brought to 800 °C the residual stresses decrease considerably at each cycle, from 0.9 GPa to 0.4 GPa after 3 cycles. Since change in the diamond grains, e.g. possible dislocation movement, would cause changes in Raman peak shape and these are not observed by the authors, the reduction in residual stresses is attributed to changes occurring within the diamond-matrix boundaries. Erasmus *et al.* also showed that the average stress present in the PCD surface layer is significantly affected by the surface preparation technique, with values varying from 1.4 GPa for roughly lapped samples to 0.1 GPa for polished samples. This is again attributed to the effect of local heating due to friction that favours local plastic flow and a rearrangement of the stress state. Miess and Rai found that increasing the temperature not only can relax the stresses, but they also found evidence that the stress state can change sign above 750 °C and become tensile in the PCD, so that spontaneous cracking starts occurring accompanied by binder extrusion from the interfaces [4]. The mechanisms through which the residual stresses change sign are not clear. The average residual stress value obtained is also affected by a number of other parameters. In particular, a decrease in the substrate to PCD layer thickness ratio in favour of the diamond can be responsible for a significant reduction of the residual stresses. Lin *et al.* calculated that a reduction from -1.4 GPa to nearly 0 is observed when the ratio is brought from 7 to below 2 [11]. A similar trend in the average in-plane stress, although with lower values varying from -0.5 to -0.15 GPa, was measured using neutron diffraction on PCD by Krawitz *et al.* when changing the ratio from 4 to 1 [12]. Interestingly, if the thickness of the substrate is reduced below 1.5 times

that of the PCD by substrate backing removal, i.e. following the HPHT process, the radial stresses on the top surface of the PCD can modify from compressive to tensile. This analytical result was confirmed by experimental observations in two different studies by collecting data with a rosette strain gauge placed on top of PCD cutters while the substrate was gradually removed [11,17]. This was explained by Lin *et al.* [11] to be the consequence of a convex bending, observed by the authors via simulation, in the carbide substrate towards the diamond layer upon cooling from sintering temperature. Due to the residual stresses, the bending is aggravated when the carbide thickness is reduced until it puts the centre region of the PCD in tension. Following further removal of carbide the residual stresses are eventually brought to zero.

Since the composite CTE of the PCD is a function of the relative volume fractions of diamond and binder, the cobalt content is responsible for changes in type I stresses. A finite element analysis study from Li *et al.* [5] found that as the cobalt content increases from 1 to 10 vol% the PCD and tungsten carbide substrate CTE reach the same value and the residual stresses are brought to zero. Thereby, further increase in the cobalt content generates a new mismatch causing the stresses to rise again. The stresses were measured by the same authors via micro-Raman on samples with 4, 9 and 15 vol% of cobalt and were observed to be 150, 100 and 640 MPa respectively, therefore showing a similar trend. A minimum in the residual stresses while increasing the binder content was also found by Jia *et al.* for PCD sintered using nickel-based additives [6]. As occurs for the other properties, also residual stresses appear to be influenced by the starting powders size, whereby smaller grain size leads to lower stresses than larger grain sizes [14]. However, in these three studies it is not clarified how the effect of grain size and binder content is decoupled, given the inverse proportionality between the two found by other authors (see Figure 2.8). Furthermore, other authors seem to observe the opposite trend with 5 µm grained PCDs exhibiting stresses up to 1.9 GPa while 30 µm grained PCDs only 0.5 GPa.

Although the PCD layer is mainly under compression given the smaller CTE, the stress state varies strongly with location on the PCD layer. Maximum principal stresses align with the radial and thickness directions in the centre of the cutter, but at the edges both simulations and experiments confirmed that radial tensile stresses can be present and generate shear [11,13,17]. These also locate the maximum compressive stresses in the centre of the PCD layer at the interface with the substrate in both radial and axial direction. Measurements of the residual stresses performed via neutron diffraction on the "conventional" PCD, i.e. sintered using a typical temperature-pressure profile, confirmed that the top surface of the PCD is subject to lower stresses than the regions at the interface [12,18]. Raman spectroscopy shows large fluctuation of the stress values over relatively short distances across the surface of the sample with tensile stresses, however the spot size of 50 and 100 μm used by Erasmus *et al.* compares to an average grain size of 10 μm, thus not large enough to average many grains for gradients in the type I stress distribution and the authors deem this to be "a random distribution of fluctuating stress values" [16].

Although the spot size of the laser beam used in other studies of residual stresses in PCD via Raman spectroscopy enables evaluation of the stress state of individual grains, none of these actually exploits the possibility to map the type II stresses and limit the investigations to average values or gradients. It is however reasonable to think that local variations of the cobalt content would affect the stress of the grains also at short range. Investigations on the residual stresses in the two phases after sintering can supply information to support the theory for which the propagation of microcracks along the diamond-metal interfaces is thought to be promoted by the high stresses due to the great difference in thermal expansion between the two phases [4]. A study in this direction was presented by Belnap [135], who examined the effect of cobalt on fracture toughness employing, as in the studies from Lammer and Miess and Rai, diametral compression tests on PCD disks of both unleached, i.e. as fabricated with cobalt present in the PCD, and leached, i.e. chemically treated to remove the cobalt. The tests showed that the removal of cobalt

by leaching is accompanied by a drop in the fracture toughness from 9.9 ± 0.4 MPa m$^{1/2}$ of the unleached samples to 7.2 ± 0.5 MPa m$^{1/2}$ of the leached samples. Raman spectroscopy was used to probe the fracture surfaces revealing that the diamond phase in unleached samples was in compression relative to the leached samples, as expected from the difference between the relatively high thermal expansion of cobalt and low of diamond, with stress in excess of 230 MPa in compression. The toughening effect of cobalt is then attributed to the residual compressive stress it generates on the diamond grains [135].

The only study known to the author of this thesis on the measurement of residual stress gradients within the grain, i.e. type III stresses, in diamond composites was conducted on a diamond–silicon carbide composite by Wieligor and Zerda employing Raman spectroscopy [10]. In this study 20-30 spectra were collected within each of 5 large diamond grains with a laser spot size of 1.5-2 μm and a 1 μm step size. The authors were therefore able to map the residual stresses within the grains. Interestingly they found a non-uniform distribution of stresses varying in the range 0-2.8 GPa in compression, with the highest stresses observed in proximity of the diamond grains boundaries. The presence of strong residual stresses were attributed to a combination of CTE and bulk moduli mismatch and oriented growth of the SiC, that was deemed by the author to be the reason for the concentration of maximum stresses near grain boundaries. The authors notice that uncertainties regarding the orientation of the grains can cause an error of up to 50% on the value measured and this is also dependent on the model used to relate peak shifts to stresses, however the distribution would be independent of the model employed.

Unfortunately, there seems to be no literature available on the direct investigation of local variations of residual stresses within grains of PCD and more importantly a correlation between this and fracture mechanisms.

2.4.5 Fracture mechanisms

The fracture path followed by ensuing cracks in PCDs varies strongly between different products and under different conditions causing in some cases transgranular [6,123,132,136] and in other intergranular [4,128] fracture or a combination of both [137].

The effect of grain size on the fracture mechanism is not clear from the literature. Lammer reported transgranular fracture for coarse grains but did not specify or showed what type of fracture occurred for finer grains [123]. Huang *et al.* observed that the "crack front interacts more" with the metal-diamond boundaries in smaller grained PCDs, i.e. < 20 μm [132].

Miess and Rai do not report the fracture mode at room temperature but noticed that at high temperatures (above 750 °C) in both hydrogen- and nitrogen-rich environments the PCDs started cracking, because of differences in thermal expansion coefficients according to the author, generating predominantly intergranular fracture that changed to mixed mode with further increase in temperature [4]. The cracking was also accompanied by extrusion of the cobalt phase, thus probably due to inversion of the residual stresses from compressive to tensile, as confirmed by Raman measurements.

Also the rate of deformation in fracture tests affects the mechanisms, as shown by Petrovic *et al.* [134]. The authors observed that the fracture surface was a combination of transgranular and intergranular crack propagation, yet at higher loading rate the intergranular mechanisms prevailed and revealed a rougher surface. The authors suggest that the observed behaviour at higher rates is caused by adiabatic conditions prevailing at the crack tip that generate high temperature gradients able to plasticise the metal binder. This in turn makes the interface weaker and promotes intergranular fracture.

Under even higher rates and more complex stress state conditions, i.e. simulating impact loading encountered in rock drilling conditions, Dunn and Lee [137] described that in the first stage of cyclic loading the local stresses are responsible for the creation of microcracks yet are not large

enough to cause the fracture of an entire grain. A single grain would then undergo a fatigue fracture process at this small scale, until the whole grain is chipped away. At this stage the fracture surface shows cleavage and intergranular fracture. However, as the process continues the crack grows until the critical condition for spontaneous crack growth are reached. At this stage, massive fracture would occur and the remaining part would fail in a rapid manner to leave a fracture surface that is mostly transgranular in type with many large cleavage planes.

2.5 Summary

Polycrystalline diamonds are produced and employed in many industries at an ever faster rate. The established and most common synthesis process involves liquid phase sintering. In such process diamond powders of a few microns or few tens of microns are sintered through the aid of a metal binder, which acts both as catalyst and solvent, on top of a sintered tungsten carbide substrate. The final microstructure of these products is composed by diamond grains either bonded to other diamond grains or partially surrounded by metal binder pools. Hardness, fracture toughness and general performance of these PCDs vary greatly with grain size, metal content and other processing parameters. As a rule of thumb, chipping and fracture resistance can be improved at the expense of hardness and wear resistance of the materials [138]. However, our knowledge of the direct correlation between the final properties and the processing recipes remains limited. In particular, our understanding of the preferred mode of fracture propagation in this material relies on empirical observations.

Materials and Methods

This chapter provides a description of production processes for the materials investigated together with the techniques used in this work.

In order to investigate the mechanical properties of diamond cutters, samples were produced using the facilities at the Element Six Global Innovation Centre. High pressure high temperature sintering was used to obtain cutters with different grain sizes and chemistry. Subsequently, samples from the cutters were prepared to observe microstructure morphology, texture and residual stresses of the final components using electron-microscopy-based techniques.

Small scale fracture testing was developed to test the fracture performance of individual interfaces. This was developed using SiC, SiC bi-crystals, Al_2O_3 + Nb and diamond.

3.1 Production and preparation of polycrystalline diamond samples

As described in chapter 2, PCD cutters commercially available are usually made in the form of a polycrystalline diamond layer sintered on top of a pre-sintered cylindrical WC substrate, as shown in Figure 2.2. Different substrates exist with different geometries of the top surface and different metal solvent catalysts binders (e.g. Ni, Cr, Fe, etc.) added to the WC to aid the sintering process of diamond. In this work the author aimed to focus on the differences between products with different grain size and chemistry of the binder, thus two different chemistries and two monomodal grain sizes were chosen.

3.1.1 Pre-sintering preparation

For each PCD cutter, ~2 g of diamond powder of select particle size, i.e. 4 µm or 30 µm, were placed at the bottom of a niobium cup. A cylindrical WC substrate was subsequently manually pressed on top as cap [see Figure 3.1-(a)]. The cups then underwent two pre-compaction stages by

positioning them inside PTFE moulds that were clamped on a vibratory sieve shaker set at 0.45 and 0.60 mm amplitudes for a total duration of 2 minutes. Following this the powders were outgassed, see Figure 3.1-(b), by inserting the cups in a Torvac vacuum furnace, at $\sim 10^{-5}$ bar and 1100 °C for 12 hours to eliminate adsorbed gases and moisture that would affect the sintering process. Given the relatively high temperature reached at low pressure, the outgassing stage is found to cause partial graphitisation of the diamond particles surface. Despite being generally undesired in the final product, this graphitisation does not cover the whole surface of each particle [139].

Afterward, a Ti cup was used as casing and welded by electron beam welding so as to seal the pre-compacts and prevent new gases adsorption, see Figure 3.1-(c,d).
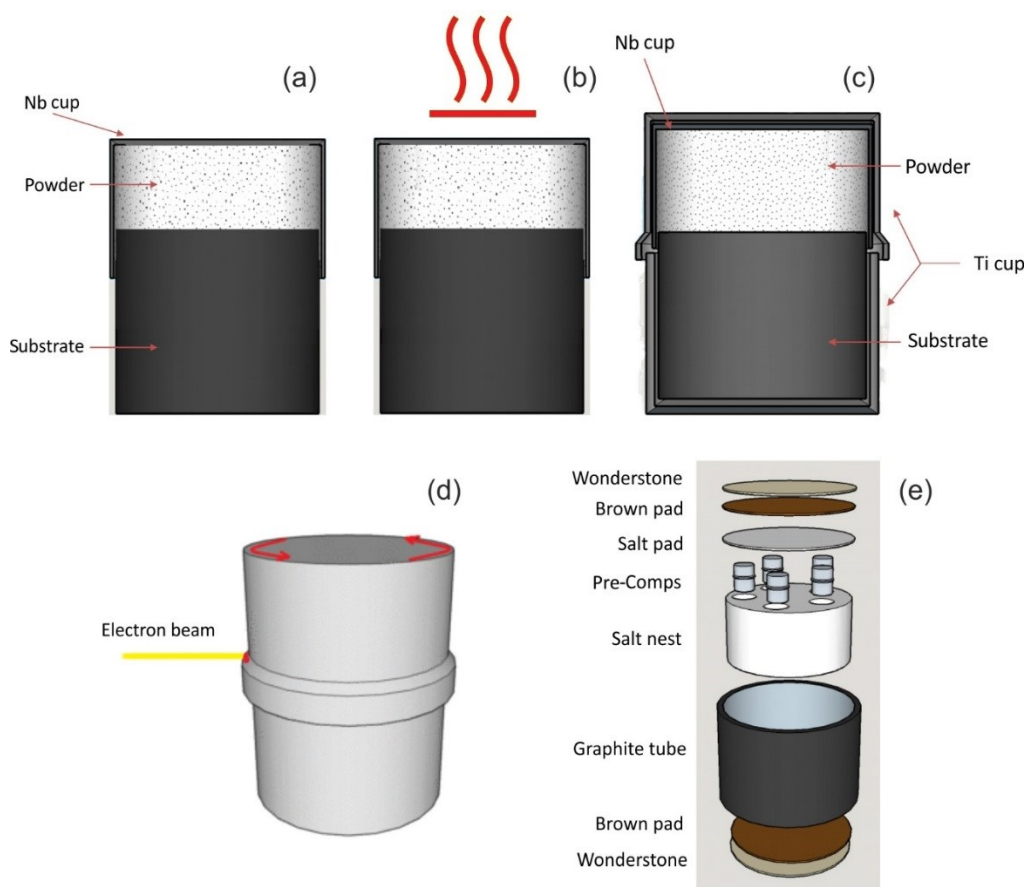
Figure 3.1 — Schematic of the capsule assembly operation preceding the sintering. (a) powder pre-compaction on carbide substrate; **(b)** outgassing; **(c)** and **(d)** capsule sealing; **(e)** assembly of several capsules in pressure and temperature transfer media for sintering.

Finally, five cups were placed inside a salt nest which was itself enclosed in a graphite tube with several layers of different ceramic pads placed on top and bottom that serve as pressure transfer media [Figure 3.1-(e)]. The graphite tube was finally closed on both sides by Ti discs so that both graphite and Ti can act as heat transfer media. The tube so assembled was placed in a high pressure, high temperature (HPHT) press known as "belt press" (see Figure 3.2). This press is designed to supply pressure through the top and bottom anvils while the "belt" serves as lateral constraint to maintain this pressure inside the chamber.
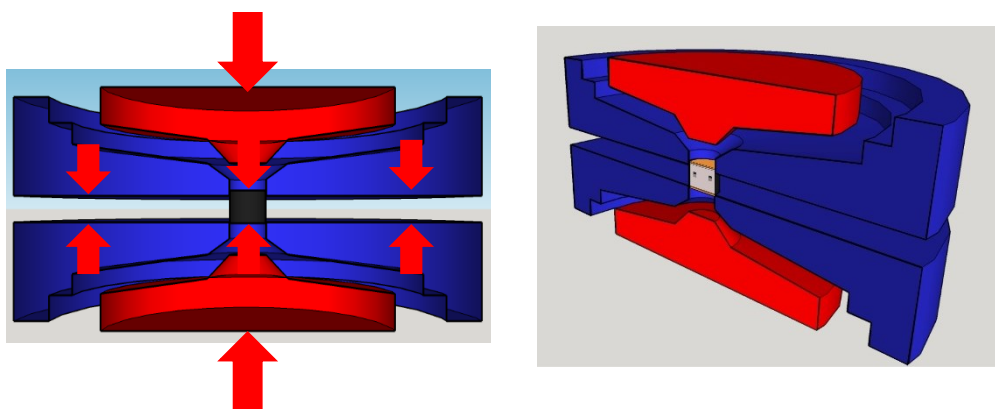
Figure 3.2 — Schematic sections of a belt press. The anvils are represented in red, the "belt" in blue and the capsule in black.

3.1.2 Sintering

As mentioned in chapter 2, the sintering of polycrystalline diamonds is aided by the presence of a liquid phase that also acts as solvent and catalyst. For the sample produced in this work cobalt or cobalt with addition of small amount of nickel and chromium played the role of the liquid phase. Co or Co-Ni-Cr are initially present in the pre-sintered WC substrate in solid state and infiltrate through the diamond particles during the sintering. Therefore, a temperature above 1400 °C is needed during sintering to reach the eutectic temperature for the W-C-Co system or W-C-Co-Ni-Cr. At the same time the pressure needs to be held within the stable region for diamond (see paragraph 2.1). During the sintering two different profiles were applied, one to reach ~6.8 GPa and a temperature between 1500 and 1550 °C and the other to reach ~5.5 GPa in a temperature

range between 1350-1400 °C. The temperature was increased in the press using the aforementioned graphite tube as resistance and passing an electric current through it to generate the heating.

3.1.3 Components produced

Following the process described above 20 cutters were prepared. Two different grades were selected, a finer grade of 4 μm (named G4) and a coarser of 30 μm (i.e. G30). Part of the cutters fabricated is supported by a standard WC-Co substrate (indicated as STD) with ~13% wt of cobalt while the rest (indicated as STD+Ni) by a WC-Co-Ni-Cr where the total amount of additives is again ~ 13% wt, where ~11% wt is cobalt and the rest is Ni and a very small amount of Cr.

In Table 3.1 are summarised the cutters made specifying grade, substrate and sintering pressure adopted.

Table 3.1 — PDC (polycrystalline diamond cutters) produced to be investigated. STD indicates a standard WC-Co substrate, whereas STD+Ni indicates a WC-Co-Ni-Cr substrate.

Qty.	Grade (μm)	Substrate	Pressure (GPa)
2	4	STD	6.8
3	4	STD+Ni	6.8
2	30	STD	6.8
3	30	STD+Ni	6.8
2	4	STD	5.5
3	4	STD+Ni	5.5
2	30	STD	5.5
3	30	STD+Ni	5.5

3.1.4 Additional diamond samples

In addition to the components produced listed above, Element Six provided two more samples. One was a stack of CVD-grown diamond and PCD on a WC substrate.

The other sample, named here PCD G4/30 TC, was produced using two diamond powders with fine and coarse particles that were mixed with binder respectively to obtain homogenous slurries, which were then tape-casted into diamond tapes. These tapes were rolled together and cut into small sections to place into a canister. A WC-Co substrate was placed on the top and de-binding, out-gassing, and sealing was carried out in similar way described for the other samples. The unit was sintered at 6.8 GPa and 1400 °C using a cubic type HPHT press to infiltrate cobalt from substrate to the diamond powder to form polycrystalline diamond (PCD). After sintering, the PCD construction was recovered and fully processed to a PCD table thickness of 2.2 mm, a diameter of 16 mm with an overall height of 13 mm.

3.1.5 Polishing

The high hardness of diamond makes it the best material choice as abrasive powder for polishing other hard materials; on the other hand this means that there are no harder candidate materials available to mechanical polish diamond, so that the best candidate remains diamond itself. Polishing of diamond is historically related to the transformation of rough gemstones into precious jewellery object and has always required substantial skills and experience. In the last, at least, 600 years the polishing of diamond gems has been performed using a cast iron disc, known as scaife, charged with olive oil and diamond grit [94].

Currently, with an international output of 4450 million carats of diamond in 2010 [94], whose 98% was synthetically produced, the polishing of this material represents a big challenge and the techniques available have rather evolved from the ones developed in the gemstone trade industry. However, the process still requires empirically-developed knowledge.

The approach employed mainly varies for final roughness target, specimen size and materials composition and includes both contact and non-contact techniques. Polycrystalline diamond polishing techniques include: a) chemo-mechanical polishing, in which crystalline potassium nitrate is used as chemically etchant on a heated (above the melting point of KNO_3, i.e. 324 °C) rotating

plate in conjunction with the mechanical abrasive action of diamond powder; b) thermo-chemical polishing, involving pressing the diamond sample on a rotating catalytic metal plate heated at between 730 and 900 °C; c) laser ablation; d) ion beam polishing; e) plasma etching; f) electric discharge machining. A complete review of these methods applied on diamond is available elsewhere [94].

All the first stages of mechanical polishing of the samples produced were operated by Element Six. A first stage of lapping follows the sintering to remove the Ti and Nb cups and finally rough surface asperities. The actual mechanical polishing is performed using resin-bonded diamond powder discs rotating at speed of up to 3500 rpm for up to 15 hours without lubricants. The cutters are pressed on the rotating disc by a spring which is deemed to act a significant pressure on the specimen, although actual values are undisclosed.

The obtained surface finishing is satisfactory for SEM observations, however investigations by EBSD reveal that it is not sufficient to obtain the pattern quality required for high angular resolution analysis (see paragraph 3.4).

Therefore, a further polishing stage was operated employing an ion beam etching system. This non-contact method enables the removal by sputtering of atoms through energy transferred from the ions impinging on the surface. In this work a Gatan PECS II system with argon ion beam was used. The rate of removal of the atoms, i.e. the sputtering yield, depends on the kinetic energy of the impinging beam, which is controlled through the acceleration voltage, the glancing angle and the target material itself.

The recipe tailoring for PCD is particularly difficult as the sputtering yield for carbon in diamond by argon ions is very low [94]. In addition the angle of highest yield depends on the crystallographic orientation, therefore the use of ion beam polishing can result in small local roughness but highly faceted samples [94,140].

Ion beam polishing was only employed on samples with the smoothest surface, since a pre-existing high roughness would further complicate the procedure. Given the limited availability of samples with a mirror-like finishing operated by Element Six, also the attempts at tailoring an ion beam polishing recipe were limited.

As this polishing was targeted at obtaining better EBSD pattern quality, the evaluation of successful polishing was based on the number of indexed patterns and visual assessment of the EBSP quality. A comparison for a good pattern quality is shown in Figure 3.3-(CVD); these are patterns obtained on a CVD-grown crystal as received by Element Six.
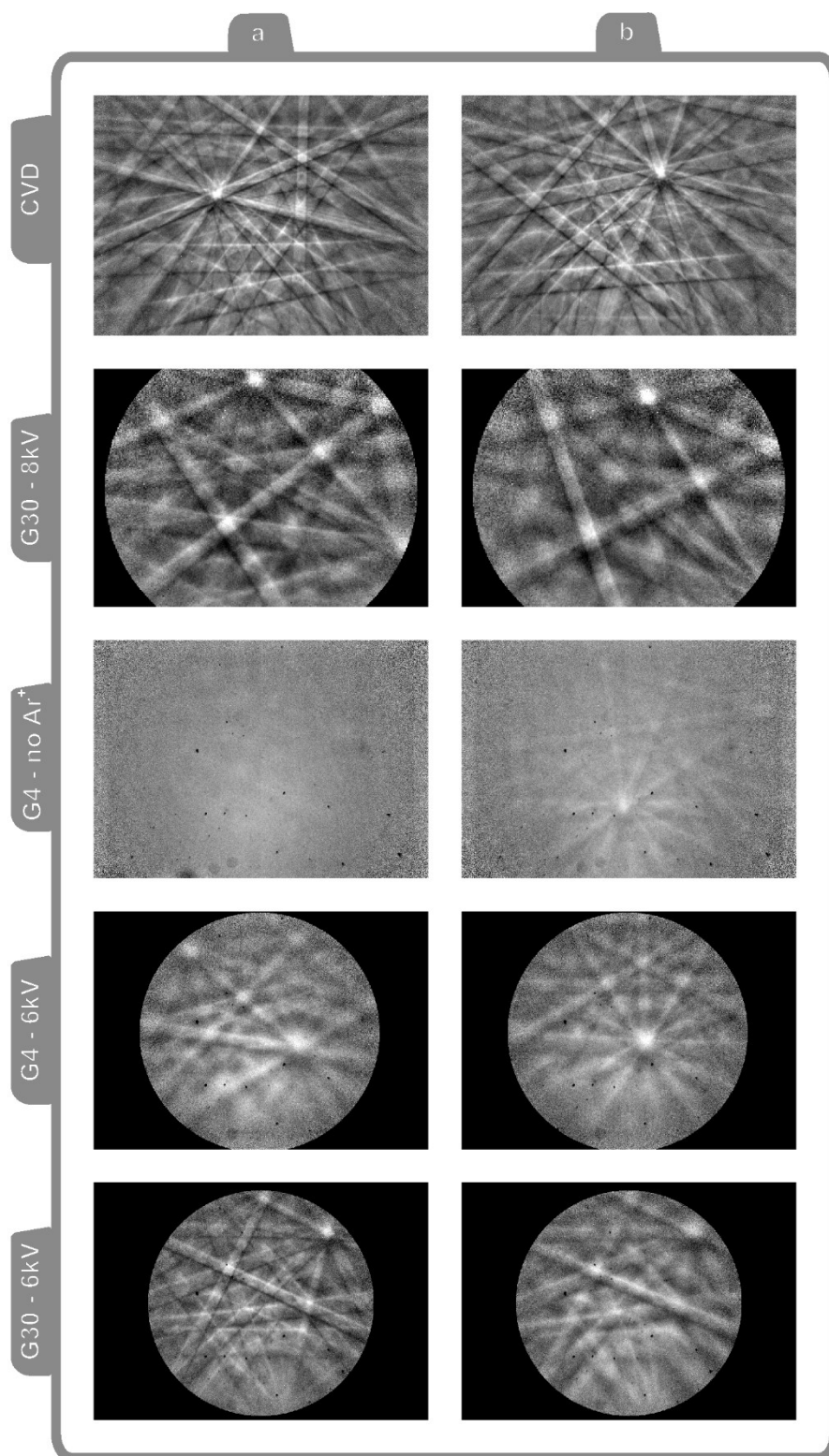
Figure 3.3 — EBSPs collected from different samples polished with different techniques

The first attempt was carried out on a PCD G30 sample, polished for 1 h at a glancing angle of 5°

with respect to the sample surface plane with an acceleration voltage of 8 kV while rotating at

6 rpm. The sample was found to have turned grey and to show high roughness even at the naked eye on all five exposed sides (the bottom was glued on a SEM stub), this is likely to be graphitisation although no further analysis was conducted and the sample discarded. The same recipe was then used on a second PCD G30 sample, but this time the sample did not change aspect to the naked eye. A quick EBSD map reveals that the indexed patterns appeared sharper [Figure 3.3-(G30-8 kV)], however the surface presented streaks, also known as "theatre curtain" or "waterfall" effect, due to ion channelling so resulting much rougher than before etching, as shown in Figure 3.4-(a). As a result only 14% of the patterns were indexed.

For the following sample, a PCD G4, the voltage was decreased to 6 kV for 1 h at 3 rpm and 3° followed by a cleaning step of 30 min at 1 kV in order to remove amorphous layers that might form during the etching. This sample, in its as-received state, was not suitable for EBSD indexing at all, as shown in Figure 3.3-(G4-no Ar$^+$). After the etching, the indexed pattern appeared significantly sharper [Figure 3.3-(G4-6 kV)]. The number of indexed pattern increased from 16.8% for the as-received sample to 54.6% after the etching. Yet signal to noise ratio appears still poor even in the best patterns and the number of indexed patterns is not sufficient even for conventional EBSD analysis.

Therefore for the next sample, a PCD G30, a longer etching was performed at 3° and 6 kV for 3 h followed by 1 h at 1 kV at 3 rpm. Here, although individual selected patterns showed a much improved signal to noise ratio with respect to the PCD G4 above [Figure 3.3-(G30-6 kV)-(a)], the surface had developed evident faceting, as can be noticed in Figure 3.4-(b), that makes the pattern quality not uniform, even within the same grain as shown in Figure 3.3-(G30-6 kV) where two patterns from the same grain are compared. In an attempt to reduce the faceting, another PCD G4 sample was then etched for only 30 min at 5 kV followed by 30 min at 1 kV at 5° and 6 rpm, yet curtaining appeared on the surface. Even at much lower voltages of 3 and 2 kV and for 30 and 20 min respectively faceting started appearing, whilst poor EBSPs were collected.

One PCD G4 was etched at 6 kV at 18° to assess whether a higher angle would suppress faceting and curtaining, however here an orange peel texture was obtained and no significant improvement of the pattern quality.
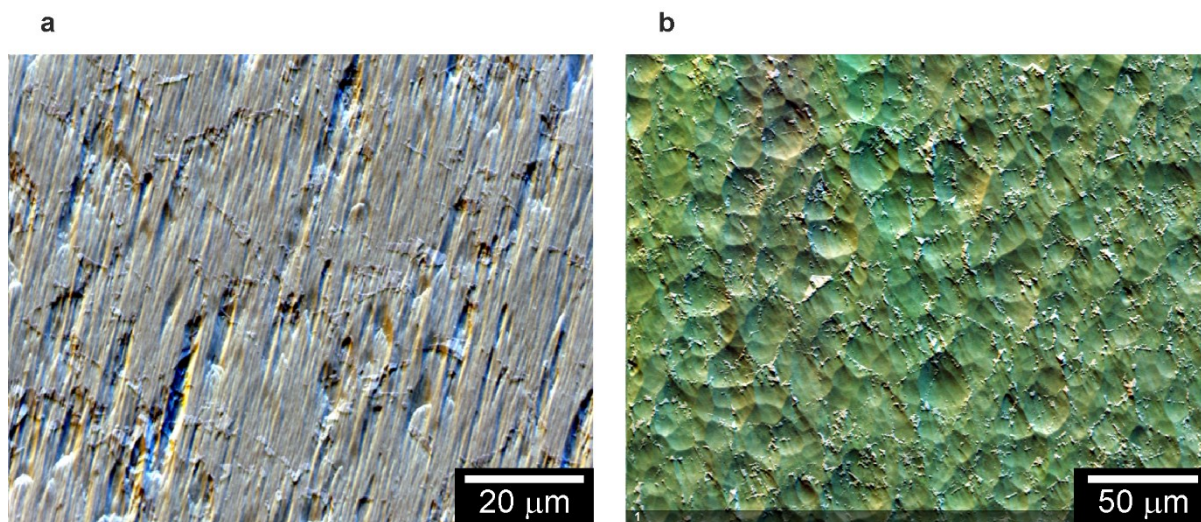
Figure 3.4 — Undesired effects of ion beam polishing captured using the forescatter detector at short working distance. **(a)** curtaining effect due to ion beam channelling. **(b)** faceting due to different wear rates of the different diamond crystallographic planes

It follows that no evident trend to follow for the development a correct recipe could be found in this configuration.

Further experiments were carried out with the samples mounted on a cross section blade with the beam impinging the sample from a 0° angle. This was first tried on one of the PCD G4 already etched and showing streaky patterns. Given the lower sputtering yield of this configuration the sample was etched at 8 kV for 4h, followed by 1 h at 3 kV and a further 2 h at 1 kV. The streaky patterns in the centre of the sample, i.e. the region most bombarded by the ion beam, became deeper and presented poor patterns. However, areas outside this central region seemed still flat and showed a better pattern quality.

This configuration was therefore repeated on PCD G4/30 TC. This sample was etched in cross-section at 8 kV for 5 h. Once inspected under the SEM the surface remained flat and the pattern showed a good quality. This time, the final cleaning step at lower voltage was replaced by a 30 min polishing step utilising an active oxide polishing suspension (OPS) on a soft polishing cloth at

200 rpm. This combination, among those tried, was found to give the best EBSP quality across the sample.

3.2 Scanning electron microscopy

Scanning electron microscopy (SEM) was used to produce high resolution images of the samples for microstructural and compositional investigation, as well as for direct observation of fracture during *in situ* testing (see chapter 4). High resolution images are created using the interaction of an electron beam with the surface of a sample. All microscopes used in this work (Zeiss Auriga, FEI Quanta, FEI Helios Nanolab SEM/FIB) generate the electron beam by cold emission using field emission tungsten sources. Once generated the beam was accelerated to a range of 2-5 keV for high resolution secondary electron images or to 20-30 keV for backscatter images.

The primary beam passes through a series of electromagnetic lenses located inside a column by an applied voltage difference. The electromagnetic lenses deviate and deform the electron beam to collimate it onto the surface to be analysed. The surface is then scanned by rastering the beam in a rectangular area, thereby higher magnification is obtained when the rastered area is reduced.

The collision of the primary electron beam with the atoms of the sample generate a series of interactions within a teardrop-shaped volume. Of particular interests for the analysis conducted in this work are: secondary electrons, backscatter electrons and X-rays. The interaction volume and characteristics of interactions depend on energy, current and angle of incident beam together with topography and chemistry of the sample. Higher applied voltage translates into a higher kinetic energy for the electrons, consequently the interaction volume extends deeper in the sample. Additionally, for a given voltage the interaction volume is larger for materials with a lower density. The electron interaction with the atoms consists of Coulomb attraction with the nuclear positive charge and of repulsive nature with the electrons from the sample. Therefore an entering electron beam is deflected by the target electrons through elastic and inelastic scattering and collected by

secondary or backscatter detectors. An image is then formed based on the energy and intensity (number density) of the electron hitting the detectors.

Secondary electrons generated from inelastic collision have lower energy than backscatter electrons, thus only those generated in the first nanometres from the free surface are able to escape from the sample and reach the detector. Moreover, relatively more electrons escape for a given time from regions with a positive curvature for they have a higher surface-to-volume ratio; the opposite holds true for negative curvature. For this reason secondary electron detectors were used to characterise the topography of a sample.

If the incident beam possesses enough energy it can promote the back-scattering of electrons from the sample. The probability of producing backscatter electrons is dependent on the average atomic number (Z) of the phase in a sample. Therefore, high resolution compositional maps can be obtained using backscatter detectors as phases with higher average Z appear brighter and phases with lower average Z darker. Backscatter detectors were therefore used to highlight phase contrast in the microstructure of the samples investigated.

Given that SEM works by shining electrons onto the sample surface, poorly conductive materials hinder the flow of electrons from the surface to the ground and promote local charging of the sample surface. Electron charging compromises the imaging as incoming electrons from the primary beam are repulsed by the accumulated negative charges on the sample causing beam shifts, abnormal contrast or image distortion. In such cases a solution is to coat the sample with a thin layer of conductive material, i.e. gold, chromium or carbon, or to efficiently tweak the beam acceleration voltage and current to minimise charging.

Although PCD and SiC investigated in this work are poorly conductive, in the present work no coating was sputtered onto the samples prior to SEM imaging. This was done as the coating would affect other investigations, such as EBSD or *in situ* mechanical testing. In order to minimise the charging, the samples were grounded to a metal SEM stub using a conductive silver-based paint.

3.3 Electron Backscatter Diffraction

Electron backscatter diffraction (EBSD) is a SEM-based diffraction technique used to obtain microstructural information from crystalline samples. In particular, it provides the crystallographic orientation of each scanned point of the sample and consequently grain orientation and grain size as well as macro- and micro-crystallographic texture.

The operating principle is based on the illumination of a well-polished crystalline samples with an electron beam of high voltage (~10-30 KeV) and suitable current (1-50 nA) at a low glancing angle (~20°) to produce electron backscatter diffraction from the surface at the point of incidence (see Figure 3.7-(1) for a schematic of the setup geometry in the SEM). The electrons of the primary beam interact with the crystal planes of the sample and diffract according to the Bragg's condition producing a sphere of low-energy-loss backscatter electrons. A phosphor screen placed in proximity of the sample intersects the cones emanating from each family of lattice planes of the sample that form bands and transforms the signal to light. Then the light of the phosphor screen illuminates a CCD camera that finally transforms the signal to an image. The image so obtained is an EBSD pattern (or EBSP) consisting of several bands orientated in different directions, known as Kikuchi bands.

The EBSP is uniquely defined by the lattice parameters of the particular crystal under the beam; by the crystal orientation in space; the wavelength of the incident electron beam (which is proportional to the acceleration voltage) and the proximity of the EBSP detector to the sample [141].

With knowledge of the phases investigated, the EBSPs are analysed to find the best fit among all the possible orientations of each phase. The EBSP is then considered indexed when its orientation and phase are known. This operation is nowadays performed at high speed by software, simultaneously to EBSP collection. EBSPs are therefore not necessarily stored, unless further offline analysis is required for specific applications.

Lines are not easily detected by automated image analysis, especially in conditions of poor signal to noise ratio. To overcome this limitation the images collected by the EBSD camera are converted through the following Hough transformation from points in the coordinate (x,y) of the EBSD image to the coordinate (ρ,θ) in Hough space where

$$\rho = x \cos \theta + y \sin \theta \qquad\qquad (3.1)$$

with ρ being the perpendicular distance from the line to the origin in the (x,y) space and θ the angle between the x-axis and ρ.
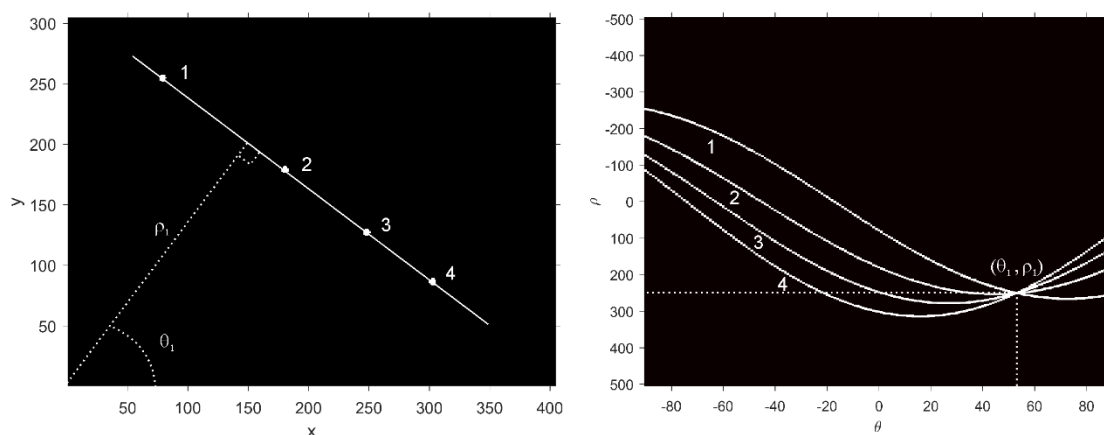
Figure 3.5 — Hough transformation of co-linear points. The four co-linear points in the image space (x,y), left, are transformed in four sinusoidal curves, right, that intersect in a common point in the Hough space (ρ,θ). Thence, the intensities of all the pixels along a straight line are accumulated at the intersection generating a peak of high intensity in the Hough space that is more easily identified by image analysis software.

Through this transformation all the possible straight lines passing through each pixel in the (x,y) image is mapped into a sinusoidal curve in the Hough space (ρ,θ), as shown in Figure 3.5. The intensity of the pixel is not changed in the transformation, therefore pixels with higher intensity will be transformed into sinusoidal curves of high intensity. Then, all the sinusoidal curves are superimposed on the same image. As a consequence, a straight line of pixels with higher intensities in the (x,y) space, that is similar to how a Kikuchi band appears, will be mapped into an equivalent number of sinusoidal curves that intersect in a single cell in which all the intensities are summed. In this way a line in the image space (x,y) is transformed in a point in the Hough space; therefore, in the latter, Kikuchi bands appear as bright peaks and are more easily identified and located.

A map of EBSPs can be generated by rastering the electron beam on a specific area, as it is commonly done for SEM images.

EBSD systems and relative analysis software are currently commercially available to be mounted on regular SEM instruments. Being the electron column generally mounted vertically, the sample is tilted at 70° using the SEM stage or alternatively a pre-tilt sample holder to achieve the 20° glancing angle with the beam. The camera is mounted horizontally on one of the SEM ports and inserted in the chamber to a distance of ~10-20 mm from the sample surface for regular analysis. The sample size is limited only by the specific SEM's chamber and stage ability to tilt the sample at the required working distance.

Pattern quality

As it is common in other diffraction techniques and in electron microscopy, the quality of the signal, and thus of the EBSPs, depends on many parameters that can affect the interactions between the primary beam and the sample. Acceleration voltage, beam current, working distance, EBSD detector distance, dwell time are all parameters that require tailoring according to the material of the sample under investigation. In addition, given the low incidence angle, the backscatter electron escaping from the surface originate from a volume penetrating just tens of nanometres below the surface [142]. Therefore, the sample is required to have a fine surface finishing and reduced plastic deformation.

A difficult challenge is posed by phases with low atomic number (Z) because of their poor backscattering efficiency. However, modern softwares can index even EBSPs with relatively low signal to noise ratio. EBSD analysis software usually provides a pattern quality (PQ) map, generated assigning an intensity value of the greyscale at each pixel (i.e. each EBSP) based on band contrast of the brightest band in the EBSP over a normalised background. In a PQ map grain boundaries usually appear dark due to their poor band contrast [143]. Moreover, band contrast is highly dependent on grain orientation, therefore different grains have different grey intensity on a PQ map [143].

Orientation

Crystal orientation with respect to detector plane or sample surface plane in the Bruker system is recorded and described using the Euler angle convention. This consists of rotating a solid about various axes until its orientation in space is coincident with that to describe. Several convention exist on how to operate the rotations, however the most common used in the EBSD systems is the Bunge notation. Following this convention the three Euler angles φ_1, Φ, φ_2 represent the following:

1. a rotation of φ_1 about the z-axis followed by

2. a rotation of Φ about the rotated x-axis followed by

3. a rotation of φ_2 about the rotated z-axis.

Each of the three Euler angles can then be associated with a colour of the RGB scale (i.e. red, green and blue) and their value combined into a single colour. This transformation performed on each EBSP, and therefore pixel, creates a coloured orientation map whereby grains with different orientations have different colours. However, this colour scheme can produce sharp change in colour between grains even when the misorientation angles are small, resulting unintuitive. For such a reason an alternative colour scheme is often preferred to represent the orientation maps, namely the inverse pole figure (IPF) colour scheme. This scheme uses the corner of an inverse pole figure to assign a colour of the RGB scale, with respect to a chosen reference sample direction (therefore a colour key is linked to each presented map).

Commercial softwares can also quickly analyse data offline to provide additional information. In polycrystalline samples grain differ from each other for their crystallographic orientation. Once a critical misorientation between two neighbouring grains is defined, the software is able to delineate grain boundaries whenever that critical angle threshold is passed by comparing pixel pairs.

Once the data are collected and saved, offline statistical analysis can be performed. In particular in this work crystallographic orientation distribution (i.e. texture), grain size distribution and grain aspect ratio were investigated.

Bruker System

In this work EBSD datasets were generated using a Bruker High Resolution e⁻Flash^{HR} detector with a 1600×1200 pixels native resolution and analysed using eSprit software.

The EBSD camera was connected to the either Auriga SEM or Quanta SEM (see section 3.2). For the diamond samples the acceleration voltage was set to 20 keV for the initial investigations, however given the low atomic number of C the voltage was later increased to 30 keV to extract more electrons. Samples were tilted at 70° with respect to the horizontal SEM stage and at a working distance between 12 and 15 mm from the SEM pole piece. For conventional EBSD analysis the EBSP were usually acquired with a 400×300 pixel resolution.

Forescatter images

The Bruker EBSD systems is also equipped with three diodes below the screen that can capture forescattered electrons. Signal detected by each of the three forescatter detectors (FSDs) is assigned to red, green or blue colour respectively. The exit angle of the forescattered electrons depends on the crystal orientation at the point illuminated by the electron beam, once fixed all other distances between sample, EBSD camera and SEM pole piece; thereby orientation contrast images can be acquired where the colour changes from grain to grain. At the same time intensity of the signal depends on the atomic number and topography of the sample. At long distances from the sample the orientation contrast between two grains is larger and easier to detect with the diodes. At short distances from the sample the electron path from the sample to the diodes positioned at the bottom of the camera is steep and closer to be parallel to the sample surface, thus enhancing the topographic contrast [144].

Therefore the FSDs provide a fast qualitative evaluation tool for the quality of the EBSPs in a certain region of the sample and quality of the polishing. Forescatter images were acquired with the phosphor screen positioned at ~40 mm to evaluate orientation contrast and at 15-20 mm to check the topography.

3.4 High angular resolution EBSD

3.4.1 Local strain mapping – available techniques

Several techniques are available to map the local state of strains in a region of material, the most popular of which are listed in Figure 3.6 on a plot of their strain sensitivity against the length scale at which they can operate. These techniques follow different approaches that can be separated in three categories:

a) material removal and direct observation of deformations following relaxation of internal stresses;

b) spectroscopic techniques to observe strain-induced shift of peaks in spectra;

c) diffraction techniques to observe deformation of crystal structures directly.

The first involves destructive (e.g. by cutting and sectioning the part, by removal of successive surface layers, or by trepanning and coring) or semi-destructive (e.g. hole-drilling) techniques. Some of these have been adapted to the microscopic scale using FIB to remove material and SEM imaging, sometimes coupled with digital image correlation, to measure the deformations; examples include a cantilever method [145], hole drilling [146–148] and ring-core milling [149].

The second type of approach, b), offers non-destructive, indirect measurement of strains and includes luminescence or Raman based approach. Micro-Raman peaks are susceptible to shifts and degeneration if the lattices of the material are strained [150]. Therefore if the material to be investigated possesses a well defined peak and the sensitivity of the frequency of this Raman peak for strain is large enough, micro-Raman can be used to detect strain and stresses at a small scale [150]. For example, for diamond the peak shifts of 2.8 cm^{-1} per GPa [10], when assuming a hydrostatic stress. Since with a very sensitive and stable instrument it is possible to detect peak shifts of about 0.05 cm^{-1} [150] the smallest detectable stress variation in diamond would be of ~18 MPa (compare studies reported in paragraph 2.4.4).

The last category, c), including X-ray, neutron and electron beam diffraction techniques, affords non-destructive, direct measurements of strains.

Methods to measure internal strains by X-ray diffraction are well established and able to determine strains in the order of 10^{-5}, however to achieve spatial resolution better than 100 µm the use of a large facility, e.g. synchrotron, is necessary [151]. Similarly, neutron diffraction can offer high strain rate sensitivity but a spatial resolution below microstructural lengthscale [151].

TEM-based diffraction techniques achieve high spatial resolution and strain sensitivity, yet the need to prepare the sample as a thin foil is often cumbersome and results in a highly relaxed state compared to its bulk form.
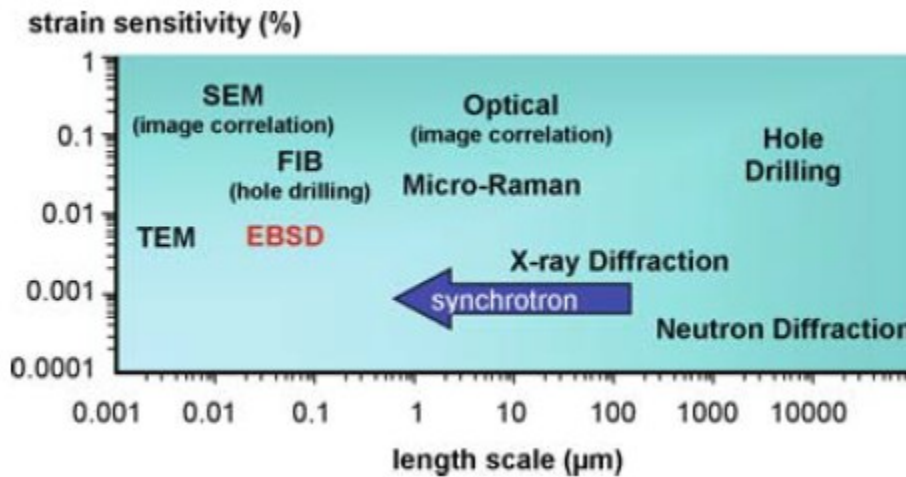
Figure 3.6 — Comparison of strain sensitivity and length scale at which the most common strain analysis techniques operate. From [151]

3.4.2 EBSD to analyse elastic strains

An alternative approach to those listed above was developed by Wilkinson *et al.* [152,153] based on a novel way to analyse EBSD patterns; using conventional EBSD systems this method is suitable for laboratory based experiments.

The method builds upon the fact that elastic strains and rotations in the target crystal generate shifts in features within the diffracted EBSPs.

Taking as example an undeformed reference crystal and a strained, rotated one, it is possible to show that a direction $\boldsymbol{r}$ along a zone axis in the former changes to $\boldsymbol{r'}$ in the latter. This is related to displacements $\boldsymbol{u}$ in the sample reference frame at the position $\boldsymbol{x}$ through the deformation gradient tensor $\boldsymbol{B}$ as in:

$$\boldsymbol{r'} = \boldsymbol{Br} \tag{3.2}$$

Where $\boldsymbol{B} = \boldsymbol{A} + \boldsymbol{I}$ and $\mathbf{A}$ is the displacement gradient tensor given by:

$$A = \begin{pmatrix} \dfrac{\partial u_1}{\partial x_1} & \dfrac{\partial u_1}{\partial x_2} & \dfrac{\partial u_1}{\partial x_3} \\[2ex] \dfrac{\partial u_2}{\partial x_1} & \dfrac{\partial u_2}{\partial x_2} & \dfrac{\partial u_2}{\partial x_3} \\[2ex] \dfrac{\partial u_3}{\partial x_1} & \dfrac{\partial u_3}{\partial x_2} & \dfrac{\partial u_3}{\partial x_3} \end{pmatrix} \tag{3.3}$$

Therefore the shift $\boldsymbol{q}$ across the EBSD screen (i.e. EBSPs) is given by:

$$\boldsymbol{q} = (\boldsymbol{A} - \lambda \boldsymbol{I})\boldsymbol{r} \tag{3.4}$$

where λ is a scalar as defined in Figure 3.7-(4)

It is clear that is not possible to obtain λ from measurements of shift along the EBSD screen, so that it needs to be eliminated by combining the equations for the individual components, giving the following two equations:

a) $r_1 r_3 \left[\dfrac{\partial u_1}{\partial x_1} - \dfrac{\partial u_3}{\partial x_3} \right] + r_2 r_3 \dfrac{\partial u_1}{\partial x_2} + r_3^2 \dfrac{\partial u_1}{\partial x_3} - r_1^2 \dfrac{\partial u_3}{\partial x_1} - r_1 r_2 \dfrac{\partial u_3}{\partial x_2} = r_3 q_1 - $

$r_1 q_3$

b) $r_2 r_3 \left[\dfrac{\partial u_2}{\partial x_2} - \dfrac{\partial u_3}{\partial x_3} \right] + r_1 r_3 \dfrac{\partial u_2}{\partial x_1} + r_3^2 \dfrac{\partial u_2}{\partial x_3} - r_2^2 \dfrac{\partial u_3}{\partial x_2} - r_1 r_2 \dfrac{\partial u_3}{\partial x_1} = r_3 q_2 - $

$r_2 q_3$

$$\tag{3.5}$$

These equations can be solved by measuring $\boldsymbol{q}$ at four different directions $\boldsymbol{r}$, that is equivalent to measure it at four different regions within the EBSP.

However, the components $\frac{\partial u_i}{\partial x_j}$ with $i = j$ cannot be determined. These are the components originating from hydrostatic stresses. Such stresses cause a change in lattice parameters, yet have no effect on the relative angles between zone axes, therefore do not appear as shifts on the EBSP. Noting that the volume depth from which EBSP form is generally within tens of nanometres from the sample surface, an assumption can be made that the stress normal to the surface is nil at equilibrium. Therefore, using this condition and Hooke's law to relate the stresses to the relative strains and elastic stiffness constants another equation is available to separate all the normal strains.

An image cross-correlation analysis performed on the EBSPs allows measurement of these shifts $\boldsymbol{q}$ comparing a reference pattern to all the other test patterns collected within each grain. To improve the efficiency of the cross-correlation analysis series of operations are performed:

a) subregions, or region of interest (ROI) are extracted at the same location of the screen for the reference and test patterns;

b) the mean intensity of each ROI is brought to zero;

c) intensity and contrast is gradually brought to zero moving from the centre to the edges (known as windowing);

d) Fourier transforms are calculated;

e) a band pass filter is applied to the Fourier transforms to reduce noise and background;

f) cross-correlation is finally performed between the test and reference ROIs in the Fourier domain.

The result of the cross-correlation is a peak for the most likely match between the test and reference ROIs. The peak height (PH) describes how well the test and reference patterns correlate and is normalized to 1 for autocorrelation.

The steps aforementioned, see Figure 3.7-(2-3), are performed on a high number of ROIs (usually 20+), far more than the minimum number of 4 required to obtain the displacement gradient tensor. This allows a "best fit" solution to be obtained that is used to calculate the expected angular shift

at each of the ROIs. In turn, this is used to assess the quality of the measurements by averaging the difference between the measured and expected value for all the ROIs, so to measure a mean angular error (MAE).

Then the displacement gradient tensor can be separated into its symmetric and anti-symmetric components, that are the elastic strains, $\boldsymbol{\varepsilon}$, and lattice rotations, $\boldsymbol{\omega}$, for which the infinitesimal solution is respectively given by:

$$\boldsymbol{\varepsilon} = \frac{1}{2}(\boldsymbol{B} + \boldsymbol{B}^T) - \boldsymbol{I}$$

$$\boldsymbol{\omega} = \frac{1}{2}(\boldsymbol{B} - \boldsymbol{B}^T)$$

(3.6)

And the finite solution to deformation by:

$$\boldsymbol{\varepsilon} = \frac{1}{2}(\boldsymbol{B}^T \cdot \boldsymbol{B} - \boldsymbol{I})$$

(3.7)

The method so described, at the core of which is the cross-correlation, can provide shift measurements that have subpixel resolution [154]. This translates to sensitivity of the order of 1×10^{-4} for the strains and 1×10^{-4} rads for the lattice rotations [153].

However, diffracted signals appear as a gnomic projection on the EBSP, therefore if large rotations are present in the target crystal these result in skew and zoom effect on the pattern, besides shift. Since the cross-correlation function described above only measures translations, skew and zoom components due to large rotations limit the accuracy and precision of the method to the measurement of rotations < 8° [154].

To overcome the limitation imposed by large rotations, Britton and Wilkinson [155] proposed the use of a robust iterative fitting routine that allows reliable measurement of strains to be obtained and rotations for applied rotations of up to 11°. In a subsequent work [154] the same authors proposed an updated algorithm that combines the robust fitting, as described in [155], performing a first pass of the cross-correlation analysis to extract the lattice rotation components with a remapping of the test EBSP using the estimated rotations. In this manner, the remapped test

EBSP, that is now in a similar configuration as the reference pattern, is analysed through a second pass of the cross-correlation function to measure the elastic strain and correct the lattice rotation.
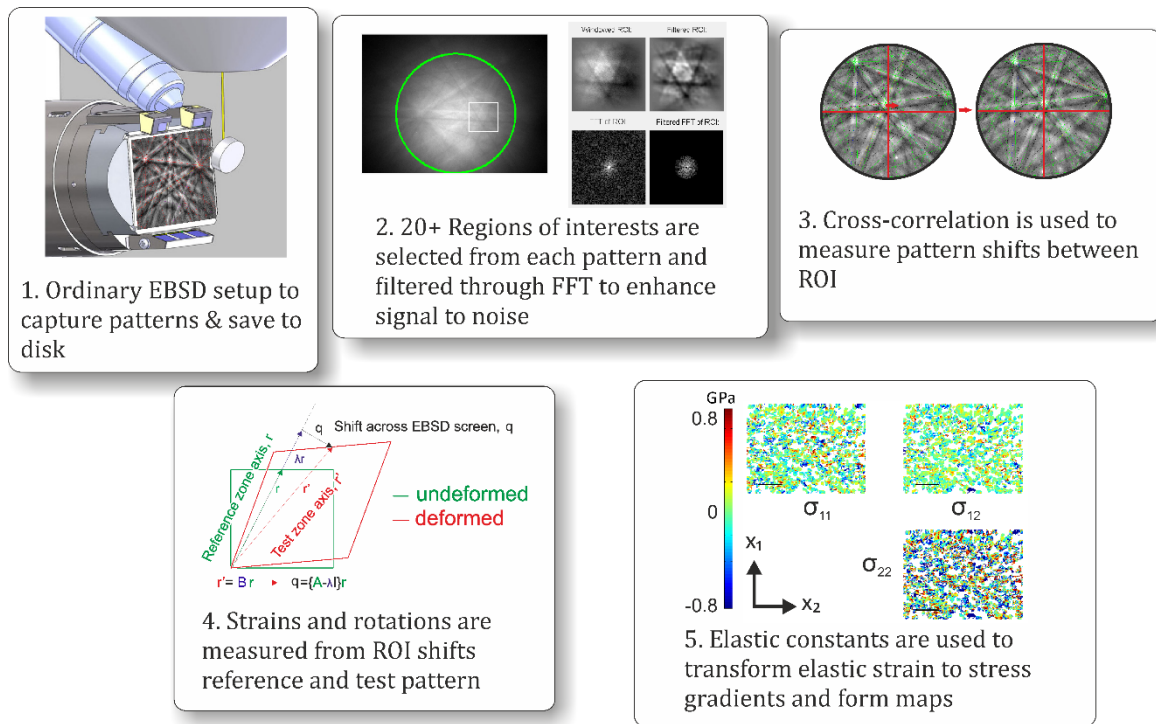
Figure 3.7. — Operating principle of HR-EBSD

PH and MAE can be used to assess the quality of the measurement. As noted above, PH is independent from the calculations of strain and rotation tensors and provides an assessment of the precision of the cross correlation procedure [155,156]. Britton and Wilkinson have shown through analysis of two simulated patterns with known applied misorientations that a PH above 0.3 provides reasonable values for misorientations of up to 10° [155]. Britton and Wilkinson, therefore, suggest that this value can be used as a threshold to filter out data for which the wrong peak was chosen due to too large shifts. The MAE, instead, provides an indication of the accuracy of the calculation of strain and tensors, with small values related to higher accuracy.

In this work, the approach proposed by Britton and Wilkinson [154] using XEBSD developed in MATLAB [157] was used.

3.5 SiC bi-crystal

Single crystal and bi-crystal of SiC were used as sample materials for the development of an *in situ* fracture testing. The single crystals of 6H-SiC were supplied by MTI Corporation as 5×5×0.5 mm coupons.

3.5.1 Diffusion bonding

The same single crystals abovementioned were used by Dr Rui Hao to produce bi-crystal samples, in which two 6H-SiC single crystals were diffusion bonded. Prior to diffusion bonding a layer of tetraethyl orthosilicate (TEOS) was spin coated to each of the component's surfaces. This was used as a precursor [158] for the silica glass forming a SiC bi-crystal with a 10 nm grain boundary. For diffusion bonding, the coupons were placed inside a vacuum furnace and kept at a pressure of $5×10^{-5}$ Pa for the entire duration of the process. The chamber was heated to 1900 °C using a heating rate of 30 °C/min. An initial load of 6 N (24 kPa) was applied normal to the area of contact between the two components. When the maximum temperature was reached the load was increased to 2000 N (80 MPa) and held for 30 minutes. The sample was then cooled at a rate of 20 °C/min to room temperature. The sample was removed from the furnace and mounted to present the interface vertically for subsequent mechanical testing.

3.6 Focused ion beam fabrication

Focused ion beam (FIB) was used to mill the double cantilever beam geometry required for the *in situ* fracture testing.

The working principle of FIB instruments is similar to that of SEMs in which, in place of the electron source, a liquid metal ion source (LMIS) is used.

Sputtering of atoms from the sample occurs as result of collision cascades originating from the interaction of the incident ion beam with the target material. An atom is sputtered from the sample

surface when the ions transfer, through elastic collisions, enough kinetic energy to the target atoms to overcome the surface binding energy of the target material [159], similarly to what discussed for the ion beam polishing. Once sputtered, the atoms are removed from the FIB chamber by the pumping system, however if they interact with other particles or surfaces they lose energy and can re-deposit. Re-deposition is frequent when narrow and deep trenches are milled and is usually an unwanted by-product of the fabrication.

In addition, the sputtering yield, i.e. the number of ejected particles per incident ion, increases with incident beam angle reaching a maximum between 75-85°, thus steep walls are milled at higher rate with respect to flat surfaces but the sputter decreases again for vertical surfaces.

Under knowledge of these phenomena, the milling steps for this work (see section 4.2) were designed to minimise re-deposition and tapering of the geometries fabricated.

In micromachining, it is useful to express the spatter yield in terms of volume of material removed per quantity of incident ions, i.e. in $\mu m^3/nC$. This provides an estimation of the time to mill a given volume of material at a select current. If we assume that the sputter yield for carbon in diamond is $0.18\ \mu m^3/nC$ at 25 keV Ga^+, it would take circa 13 minutes and 13 seconds to mill a box $20\times10\times15 = 3000\ \mu m^3$ at 21 nA (the highest ion current in the FIB system used for this work) or 46.3 hours at 100 pA.

Although the highest current clearly reduces the milling time dramatically, this is achieved at the expense of quality. As milling is operated by rastering the ion beam within a region of chosen geometry, the quality of the shape and the quality of the milled region depend on the beam size and beam overlap as this moves [160]. The beam size is in turn dependent on the beam current and instrument optics. Since the beam has a quasi-Gaussian profile, an optimal overlap is necessary to achieve a dose of ions as close as possible to uniform. In most of moderns FIB systems the desired shape is drawn by the users through a software that will consequently divide it in pixels where the beam will be stepped along. The overlapping, i.e. the pixel spacing, is a tuneable

parameter. However, the bigger the current, and thus beam size, the lower the resolution at the edges.

3.6.1 FIB-induced damage

Micromachining via FIB milling is inevitably accompanied by the creation of a FIB-induced damage volume underneath the surface, as shown in the schematic of Figure 3.8.

At each collision ions transfer momentum to the target atoms, thus losing kinetic energy. If not backscatter the ion is then implanted below the specimen surface. Maximum depth and number of implanted ions depend on both the characteristics of the incident beam (energy, angle, current) and density of target material [159]. Ga^+ implantation occurs not only for ions that impinge at normal incidence onto the sample surface but also for those at glancing angles of less than 1° [161]. The damage layer arising from FIB milling can take the form of amorphisation, defect agglomerates or even intermetallic phases, depending on the target material [161].

Bei *et al.* have investigated the effects of FIB milling on nanomechanical behaviour of Mo-alloy [162], with the intent to understand the discrepancy between measured value of yield strength and theoretical ones in micropillar small enough to be expected to contain few or no dislocations. The FIB is seen as responsible for a high dislocation density near the surface, in addition to the other defects already mentioned. The authors argue that the presence of the damage layer, whose thickness depends on material and experimental condition but generally ranges from about 10 to 100 nm, implies that a compression test on such a fabricated pillar would measure the composite properties of the investigated material and its FIB-modified surface, rather than the properties of the material under study.
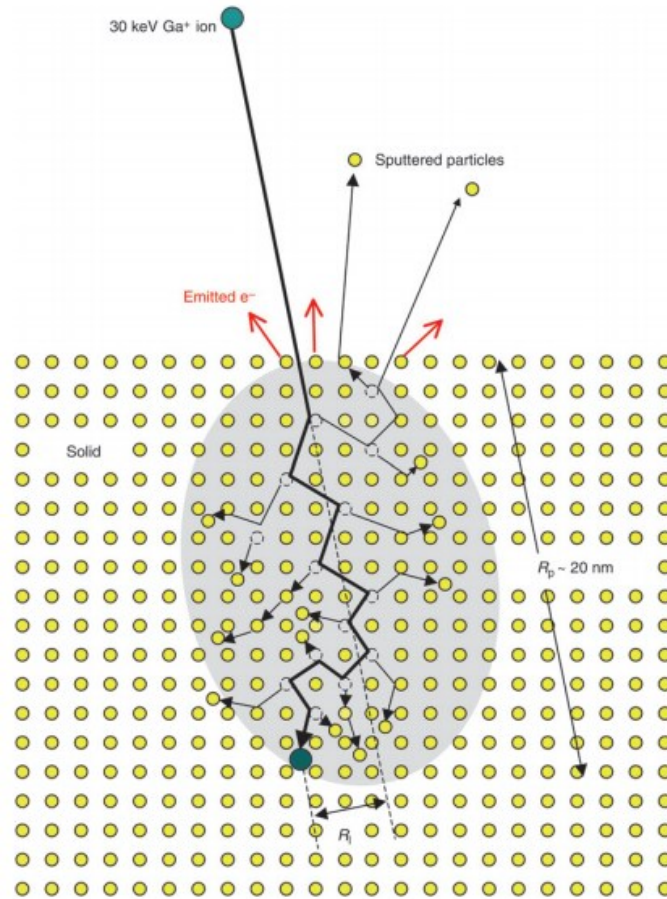
Figure 3.8 — Schematic illustration of a collision cascade generated by a 30 keV Ga+ ion incident on a crystal lattice, showing the damage created in the collision cascade volume, and the projected range R_p and lateral range R_l of the implanted ion. From [163].

Conducting nanoindentation experiments on FIB milled surfaces at different ion beam voltages and on non-FIB-ed surfaces, they found the elastic modulus not to change, whereas the hardness increased significantly with increasing acceleration voltages. Thence, the presence of a FIB damaged layer harder than the underlying material would cause a strengthening effect, making the size effect an artefact.

However, the study conducted by Greer *et al.* [164] on gold pillar fabricated both by FIB milling and electroplating exhibit a similar rise in strength as the diameter is reduced. Differences in the flow stresses measured are not attributed by the authors to the Ga^+ implantation, but rather to the fact that electroplated pillars are formed by 2-3 grains whereas FIB milled pillars are single crystals.

For this work, the depth of the damage layer compared to the dimension of the pillar (see section 4.2) is thought not to create particular artefacts on the behaviour of the material. However, the main issue may arise by the damage underneath the FIB milled notch (see section 1.5.3) whose effect would be a modification of the load at which crack starts. This issue regarding the test conducted for this work is discussed later in section 4.7.4

In this work a FEI Helios Nanolab 600 with gallium (Ga) source was employed.

3.7 *In situ* mechanical testing

Micro-mechanical testing was performed with an Alemnis nanoindenter (see Figure 3.9) actuated by a piezoelectric transducer and therefore operating in displacement control. Testing was performed using a 60° diamond wedge indenter of nominal tip length of 10 μm (Synton). The nanoindenter is equipped with three stage motors to move the sample with respect to its surface plane directions and the tip towards and away from the sample surface. The system was equipped with an additional rotational sub stage over which the sample stub was mounted, in order to control with high precision the alignment between the notch and the wedge.

All the tests were performed *in situ* in a scanning electron microscope, which provided high spatial and temporal resolution imaging of the loading and fracture processes. This proved beneficial for the alignment of the sample and loading geometry, as well as direct observation of the fracture under load. Images were obtained using 5 kV with an InLens detector in an Auriga Zeiss SEM at low working distance (~5 mm). Videos were recorded during test execution at a frame scan time of ~500 ms (using a reduced scan raster to balance dwell time, image quality and fame rate).
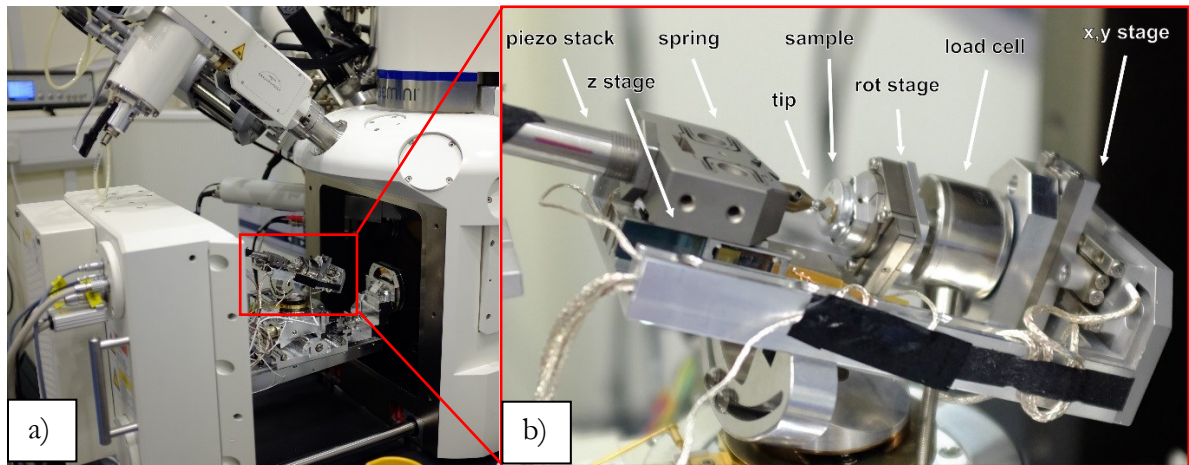
Figure 3.9 — Alemnis nanoindenter platform setup. (a) Alemnis fixed on Auriga SEM stage at 30° with respect to horizontal plane; **(b)** details of components of nanoindenter platform.

Double cantilever beam wedging at the microscale

In light of the desirable improvements to the approaches to test fracture at the micro scale previously published in the literature, including stable crack growth, easy positioning of the notch, relatively simple sample fabrication and simple result analysis, minimisation of the effect of FIB damage, frame compliance and friction between indenter and sample (see 2.5.6), here an alternative method to try and address most of those issues was developed.

In this work, a DCB geometry was tested, fabricated using FIB, and loaded with a wedge in direct displacement control *in situ* a scanning electron microscope. This geometry allows stable crack growth and direct measurement of fracture energy as the crack grows.

Surface energy measurements are demonstrated on 6H single crystal SiC samples to validate the technique and these are compared with density functional theory (DFT) calculations performed by P. Patel and Dr J.R. Kermode at the University of Warwick. The approach is subsequently used to experimentally explore the fracture of silicon carbide bi-crystals adhered together with silica and of sapphire bi-crystals adhered with niobium (both manufactured by Dr R. Hao at Imperial College London using diffusion bonding). The test was finally used to measure the fracture energy of the {110} plane in CVD-grown diamond.

4.1 Why the double cantilever geometry?

In this work, the DCB is a rectangular cross section based pillar whose height is the largest dimension and the breadth the smallest (Figure 4.1). A trough and a notch, fabricated at the centre of the top surface, create two arms that are loaded to obtain a splitting through the DCB central vertical axis. When a wedge is driven in displacement control to separate the two beams the energy spent to advance the crack increases with its growth or, in other words, for a given beam deflection

the energy released is a decreasing function of the crack length. Therefore this configuration is inherently stable [20,25,28] as the crack is afforded to grow only if at each increment more energy is available at the crack front through further displacement of the wedge (i.e. further bending of the beams). This geometry is similar to the classic design described by Lawn [20] and enables measurement of fracture energy through balancing the release of the elastic stored energy within the beams against the energy to form the crack This enables measurement of the fracture or surface energy as the crack grows through direct observation of the displacement of each cantilever beam and crack growth.

In this work this geometry was adapted to microscopic scale testing. DCBs were fabricated using FIB and loaded by a wedge in displacement control using a nanoindenter. Stable crack growth in this configuration was demonstrated in three tests on single crystal SiC through a prolonged displacement hold (between 150 and 300 s) with no observable increase in crack length.

To overcome difficulties related to the alignment of the wedge the testing was performed *in situ* a SEM with the added benefit of operating in a controlled high vacuum environment, thus reducing concerns of environmentally induced effects such as stress corrosion cracking [165].
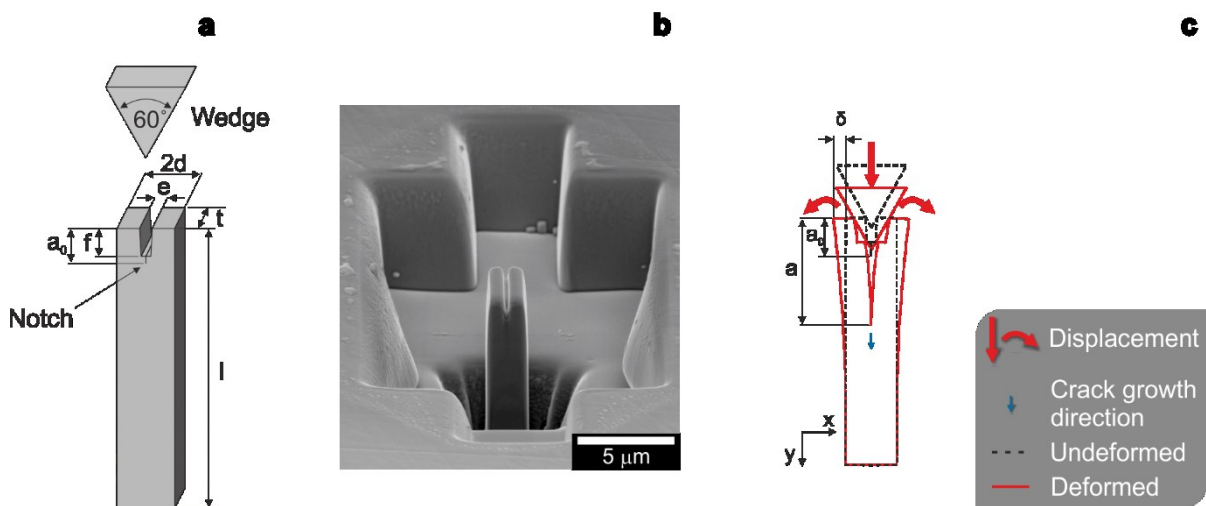
Figure 4.1 — The wedge loaded DCB geometry used in this work. Dimensions are: $10 < l < 15$ μm, $2d \sim 2$ μm, $t \sim 5$ μm, $e \sim 400$ nm, $1 < f < 2$ μm and $1.5 < a_0 < 2.5$ μm **(a)**. The beam displacement δ at the contact point between the wedge and the DCB, and the crack length a, as shown in **(c)**, allow the energy stored in the beam to be measured once beam width and stiffness are known. **(b)** SEM view of the DCB as it appears with the sample mounted on the nanoindenter platform, i.e. tilted 30° with respect to the horizontal plane of SEM stage.

4.1 Analytical solution for fracture energy

A wedge sliding through the central trough causes beam bending of both cantilevers, and the elastic energy stored within the beams is available to drive crack growth. The DCB system can be approximated as two individual clamped end-loaded cantilevers, where the clamp position is at the crack tip and the loading point is at the contact point between the wedge and the beam (cf. Figure 4.1-(c) and Figure 4.2). Therefore, by applying Euler-Bernoulli beam theory, it is possible to calculate the energy spent in beam bending in terms of the beam displacement, beam geometry and the elastic stiffness of each cantilever.
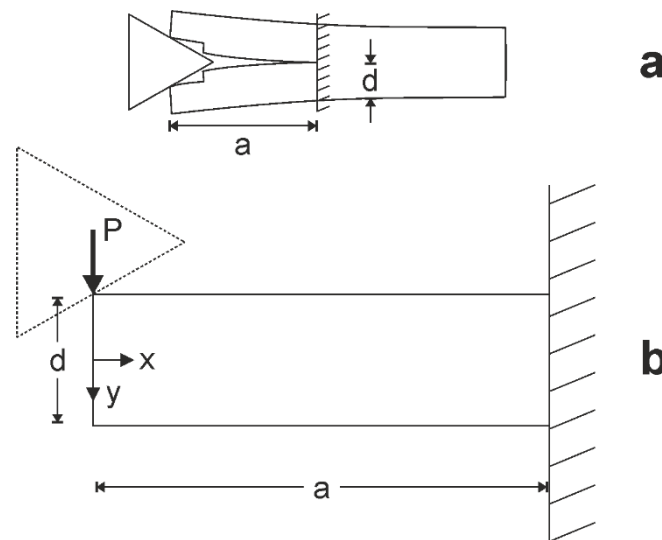
Figure 4.2 — Schematic of clamped cantilever loaded at the free end. **(a)** The double cantilever beam (DCB) system can be approximated as two individual clamped cantilevers **(b)**, each of width d end-loaded by a load P, in which the clamp position is at the crack tip (i.e. at $x = a$) and the loading point is at the contact point between the wedge and the beam (i.e. at $x = 0$).

The elastic strain energy of a volume of material can be obtained as:

$$U_E = \int \frac{\sigma^2}{2E} dV \tag{4.1}$$

where σ is the stress applied on the volume of material, E its elastic modulus and dV the elementary volume considered. From simple beam theory the stress across the beam thickness (see Figure 4.2) is given by:

121

$$\sigma = \frac{My}{I} \tag{4.2}$$

where I is the second moment of area, M is the moment and y is the distance from the neutral axis. Substituting Eq. (4.2) into Eq. (4.1) leads to:

$$U_E = \int \frac{M^2 y^2}{2EI^2} dV \tag{4.3}$$

Setting $dV = dAdx$, Eq. (4.3) can be developed as:

$$U_E = \int_0^a \int_A \frac{M^2 y^2}{2EI^2} dAdx = \int_0^a \frac{M^2}{2EI^2} \left(\int_A y^2 dA \right) dx = \int_0^a \frac{M^2}{2EI} dx \tag{4.4}$$

since $\left(\int_A y^2 dA \right) = I$.

For an end-loaded cantilever beam by a load P, at any distance from the loading point along the normal to the loading direction the moment is $M = -Px$, so that:

$$U_E = \int_0^a \frac{P^2 x^2}{2EI} dx = \frac{P^2 a^3}{6EI} \tag{4.5}$$

with a being the length of the beam and equal to the crack length in the DCB (see Figure 4.1 and Figure 4.2).

From Euler-Bernoulli beam theory the maximum deflection δ (as defined in Figure 4.1) of the beam at the neutral axis of the loaded end can also be calculated, and is equal to:

$$\delta = \frac{Pa^3}{3EI} \tag{4.6}$$

Therefore the load can be calculated knowing the displacement δ from:

$$P = \frac{3\delta EI}{a^3} \tag{4.7}$$

Being $I = d^3/12$, for a beam of unitary width and thickness d (and uniform cross section); thus substituting P in U_E we obtain, as found in [40]:

$$U_E = \frac{Ed^3 \delta^2}{8a^3} \tag{4.8}$$

The mechanical energy, U_M, stored in each beam per unit depth in the end-loaded cantilever beam system described thus far, is equal to the elastic strain energy, U_E, calculated in Eq. (4.8).

The strain energy release rate (energy per unit area), G, is given by the Griffith criterion as:

$$G = -\frac{dU_M}{da} = \frac{3Ed^3\delta^2}{8a^4} \tag{4.9}$$

4.1.1 Solution for short crack

For the initial crack growth, the beams are shorter than the approximation required for simple beam theory to hold (i.e. $d \gg a$ when the crack is short), so the model is extended using the linear elasticity solution for the short crack configuration, which includes the shear contribution. Timoshenko and Goodier [166] show that for a two-dimensional problem, when body forces are absent or are constant, the analytical solution for the elastic deformations of a body subject to external applied stresses can be found in the integration of the differential equation:

$$\frac{\partial^4 \Phi}{\partial x^4} + 2\frac{\partial^4 \Phi}{\partial x^2 y^2} + \frac{\partial^4 \Phi}{\partial y^4} = 0 \tag{4.10}$$

with the stresses given by:

$$\sigma_x = \frac{\partial^2 \Phi}{\partial y^2}; \ \sigma_y = \frac{\partial^2 \Phi}{\partial x^2}; \ \tau_{xy} = -\frac{\partial^2 \Phi}{\partial xy}; \tag{4.11}$$

Therefore, using polynomials, Φ, of different degrees, it is possible to describe the solutions to different loading conditions on rectangular bodies by adjusting their coefficients. In particular, the case of the bending of a cantilever loaded at its end can be solved by a combination of polynomials of second degree and fourth degree. Timoshenko and Goodier assume that the long upper and lower sides are free from forces, whereas the end load P is distributed parabolically as a shear force along the left face at $x = 0$.

A condition of pure shear is given by the following polynomial of second degree:

$$\Phi_2 = \frac{A_2}{2}x^2 + B_2 xy + \frac{C_2}{2}y^2 \tag{4.12}$$

when A_2 and C_2 are set equal to 0. Indeed, by using Eq.(4.12) to resolve Eqs. (4.11) with $A_2 = C_2 = 0$ we have:

$$\sigma_x = C_2 = 0; \ \sigma_y = A_2 = 0; \ \tau_{xy} = -B_2; \tag{4.13}$$

In order to have a form that may cancel the uniform shear generated on the top and bottom surfaces by Φ_2, and that generates a parabolic shear on the ends that may equal P, the following polynomial of fourth degree with all the coefficients except D_4 equal to zero can be used as solution to Eq. 4.10. This results in a normal stress σ_x that is proportional to y at a given location x along the length of the beam, as shown in the following Eqs.:

$$\Phi_4 = \frac{A_4}{4 \cdot 3}x^4 + \frac{B_4}{3 \cdot 2}x^3 y + \frac{C_4}{2}x^2 y^2 + \frac{D_4}{3 \cdot 2}xy^3 + \frac{E_4}{4 \cdot 3}y^4 \tag{4.14}$$

$$\sigma_x = D_4 xy; \ \sigma_y = 0; \ \tau_{xy} = -\frac{D_4}{2}y^2; \tag{4.15}$$

Summing the two polynomials gives, from Eq. (4.11):

$$\sigma_x = D_4 xy; \ \sigma_y = 0; \ \tau_{xy} = -B_2 - \frac{D_4}{2}y^2; \tag{4.16}$$

If we impose that the longitudinal sides at $y = \pm\frac{d}{2}$ are traction-free, we have:

$$\left(\tau_{xy}\right)_{y=\pm\frac{d}{2}} = -B_2 - \frac{D_4}{2}\left(\frac{d}{2}\right)^2 = 0 \ \rightarrow \ D_4 = -8\frac{B_2}{d^2} \tag{4.17}$$

Therefore, noting that at the loaded end the resultant of the distributed shear stress must equal P, we can integrate $-\tau_{xy}$ to obtain B_2:

$$\int_{-\frac{d}{2}}^{\frac{d}{2}} -\tau_{xy}dy = \int_{-\frac{d}{2}}^{\frac{d}{2}} \left(B_2 - 4\frac{B_2}{d^2}y^2\right)dy = P \tag{4.18}$$

$$B_2 = \frac{3}{2}\frac{P}{d} \tag{4.19}$$

Thus, the stresses are:

$$\sigma_x = -12\frac{P}{d^3}xy; \ \sigma_y = 0; \ \tau_{xy} = -\frac{3P}{2d}\left(1 - 4\frac{y^2}{d^2}\right) \tag{4.20}$$

Noting that the second moment of inertia for a rectangular cross section of unitary width is $I = d^3/12$, we can write the stresses in the form:

$$\sigma_x = -\frac{Pxy}{I}; \ \sigma_y = 0; \ \tau_{xy} = -\frac{P}{2I}\left(\frac{d^2}{4} - y^2\right); \tag{4.21}$$

From the stresses we obtain the strains as:

$$\varepsilon_x = \frac{\sigma_x}{E} = -\frac{Pxy}{EI}; \ \varepsilon_y = -\frac{v\sigma_x}{E} = \frac{vPxy}{EI}; \ \gamma_{xy} = \frac{\tau_{xy}}{\mu}$$

$$= -\frac{P}{2\mu I}\left(\frac{d^2}{4} - y^2\right); \tag{4.22}$$

where v is Poisson's ratio and μ is the shear modulus.

Hence, having both stresses and strains defined, it is possible to obtain the stored elastic strain energy, which is also equal to U_M, by integrating the strain energy density over the volume V:

$$U_M = \frac{1}{2}\int_V \left(\sigma_x\varepsilon_x + 2\tau_{xy}\gamma_{xy}\right)dV = \frac{P^2 a^3 d^3}{24EI^2}\left(\frac{1}{3} + \frac{1}{5}(1 + v)\left(\frac{d}{a}\right)^2\right) \tag{4.23}$$

Substituting Eq. (4.7) into Eq. (4.23):

$$U_M = \frac{3\delta^2 E}{8}\left(\frac{1}{3}\left(\frac{d}{a}\right)^3 + \frac{1}{5}(1 + v)\left(\frac{d}{a}\right)^5\right) \tag{4.24}$$

This results in an energy release rate, G, for each beam:

$$G = \frac{3Ed^3\delta^2}{8a^4} + \frac{3E(1 + v)d^5\delta^2}{8a^6} = \frac{3Ed^3\delta^2}{8a^4}\left[1 + (1 + v)(d/a)^2\right] \tag{4.25}$$

Note that Eq. (4.25) simplifies to Eq. (4.9) when $a \gg d$.

The total energy release rate can be calculated using Eq. (4.25), summing the G values calculated for each beam independently (which are not necessarily displaced by the same amount).

4.2 Fabrication of double-cantilever beams

The double-cantilever beams were fabricated by FIB milling (see section 3.6) in a FEI Helios Nanolab 600 DualBeam. Tuning of ion beam parameters (e.g. current, magnification, milling time), shapes and volumes milled at each stage, number of stages, etc. requires a combination of practical experience, knowledge of FIB milling mechanisms as well as response of a specific target material to the sputtering.

For these reasons, a certain number of square or rectangular pillar were first fabricated to gather useful information on the dose of ions required to mill a certain volume and design the shapes that would allow minimization of re-deposition and tapering.

Subsequently a fabrication process of the DCB was structured in several stages all executed at 30 kV and with the sample placed normal to the FIB column (i.e. at 52° tilt with respect to the SEM column in the Helios Nanolab) and with the long edge parallel to the tilt axis of the SEM stage. The first stages were executed at high currents to maximise the rate of sputtering and reduce fabrication times. However, low currents are required to minimise ion damage and obtain the milling resolution that allows the edges to be shaped with sufficient quality. Therefore, the current was reduced as the fabrication proceeded, roughing first with currents of 21, 10 and 7 nA, to create a sufficiently large trench around the DCB and to reduce the cross sectional area of the test DCB. The dimensions and shape of the trench were designed to both allow accommodation of the wedge on top of the DCB and to afford a view on the growing crack (when the sample is loaded at 30° to the electron beam). During testing the wedge indenter was placed to be flush with the edge of the DCB in order to prevent obstruction of the DCB face observed. With such a constraint the minimum distance between the trench short edge and the DCB short edge is given by the length of the tip less the length of the DCB long edge. However, since the DCB needs to be tilted with respect to the electron beam normal axis during testing to obtain a view on the wall where the crack propagates, a trench edge too close to the DCB would obstruct such view. Thereby, for

some of the DCBs a narrower trench was added to the two short sides to act as viewing window on the DCB (see Figure 4.3-(b) and Figure 4.1).

Thereafter the probe current was reduced to 1 nA to obtain the final cross section dimensions and clean all the sidewalls. Using the same current, the sample was tilted by −1° and +1° from the normal to the ion column to mill the bottom and top sidewalls (i.e. the long edges) respectively, in order to further reduce the taper. Once the rectangular sample was prepared, a trough was cut into the top at normal incidence at 1 nA. Finally, a notch was cut using a line scan at 10 pA to create a stress concentrator and initiate the crack.

Given that the fabrication of such geometry entails a significant number of steps, the drawing of rather complex shapes and accurate positioning of trough and notch in the centre of the DCB cross section, an automated routine was designed to make the process consistent and time efficient for a number of specimens. Initially, a custom script was written in AutoScript™, a language based on BASIC, and run under RunScript™ to pass instruction from the computer to the FEI FIB system. The script consists of a parent script and several child scripts. This structure was chosen to ease its reading and modification, especially when only a few parameters related to the geometry or ion currents ought to be tweaked. Furthermore, this structure allowed editing of the number of stages for the milling and their parameters without the need of creating large amounts of new code; instead, the same child script could be simply re-called multiple times, modifying or adding the new required parameters in the parent script. Additionally, the script permits the creation of a matrix of pillar of as many as desired rows and columns. To this end, in the parent script is possible to set the numbers of pillars wanted, the distance between them, the depth of milling for each stage, length and width of final pillar and surrounding trench and aperture (i.e. indirectly the current) to be used in each stage.

Later a different software, viz NanoBuilder (FEI), became available that allows graphic drawing of the desired shapes while ion beam parameters required for each set of shapes are input as separate

"layers". The procedures developed within Autoscript were translated into this new, and easier to use, scripting interface.

In both software tools an image correlation alignment procedure was implemented in between each step to correct possible beam shifts caused by the change of current. Two different alignment procedures were used, one for the rough milling and one for the fine milling at lower currents and higher magnification. For the first alignment a fiducial mark, typically a cross, was milled before starting the DCB fabrication at a known distance from the chosen location where the DCB notch was desired (Figure 4.3). The cross correlation procedure was then set to acquire images with the ion beam within a reduced window of the entire frame, so to scan a template region twice as large as the fiducial mark in the location where it was initially milled. The images acquired were then cross correlated to a reference stored image of the fiducial mark. The function then returns the location of the best match, i.e. the coordinates of the fiducial mark, if successful. Should an undesired offset be measured, the ion beam is then shifted to allow the milling to proceed at the correct location. In practice, using this alignment procedure alone for the entire fabrication the trough and notch were often found to be milled off-centre of up to ~200 nm. This is owed to the fact that in this first alignment the horizontal field width used was rather large (>50 µm) for it needed to capture the entire milled area, including the fiducial marks. As a consequence the resulting step size resolution of the FIB raster was poor and the accuracy of this alignment was deemed to be unsatisfactory for the final stages. To overcome such an issue, a second alignment was adopted to recognize the contour of the top view of the DCB at high magnification and used to position the trough and line along its central axis.
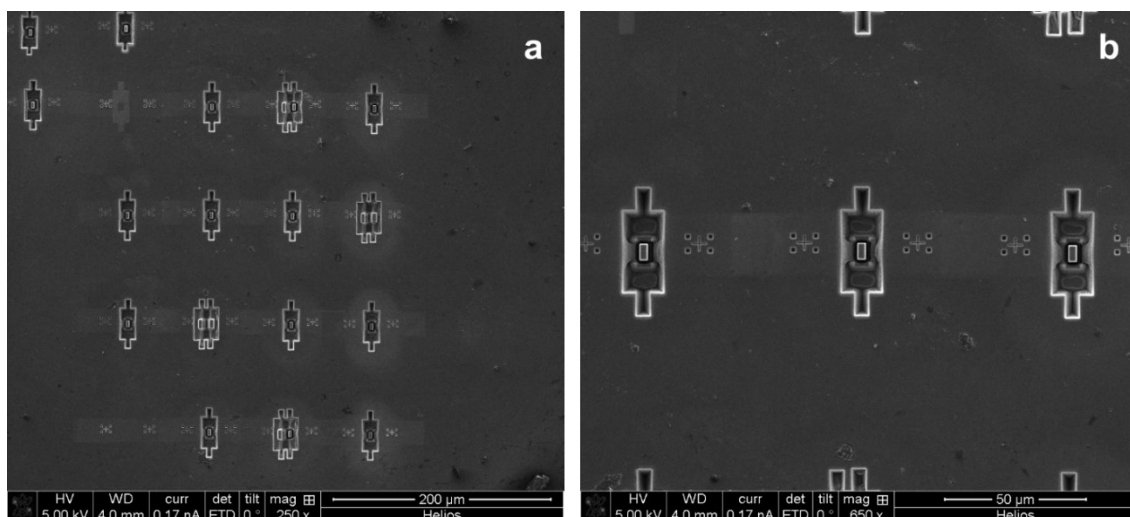
Figure 4.3 — Matrix of DCBs milled on a single crystal Si sample. A recognisable fiducial mark was milled at a given distance from the desired location from the centre of DCB top surface; in this sample the mark was a cross with four squares positioned in its quadrants. Despite a few visible failures of the beam shift adjustment between different milling steps due to errors in the cross correlation procedure **(a)**, automated milling allows the fabrication of DCBs with consistent geometry and little or absent intervention **(b)**.

The final DCB geometry had nominal dimension of between 10 and 15 µm height (*l*), 2 µm width (*2d*), 5 µm thickness (*t*), and other dimensions as outlined in Figure 4.1. Images were captured to record actual dimensions of each DCB for subsequent analysis.

In order to validate the technique, DCBs were first fabricated on one of the single crystal portion of the 6H-SiC bi-crystal specimen with the notch aligned to obtain a cleavage of the basal plane with propagation along the <a> direction. Subsequently, more DCBs were fabricated on the same sample, yet this time aligning the notch with the glassy interface bonding the bi-crystal together and vertically running parallel to the <a> direction of the 6H-SiC crystal. In this case it was difficult to image the interface because its thickness is comparable to the resolution of the SEM, i.e. a few nanometres. In addition, since the atomic mass difference between SiC and SiO_2 is small, a poor contrast is obtained in backscatter mode. However, after the sample has been imaged by FIB, due to preferential etching, the interface can be seen running through the centre of the sample as in Figure 4.4 (pointed by the arrow).

Therefore initial imaging of the sample surface was performed with a low current ion beam to locate the interface layer and the DCBs were fabricated using the same procedure as outlined above.
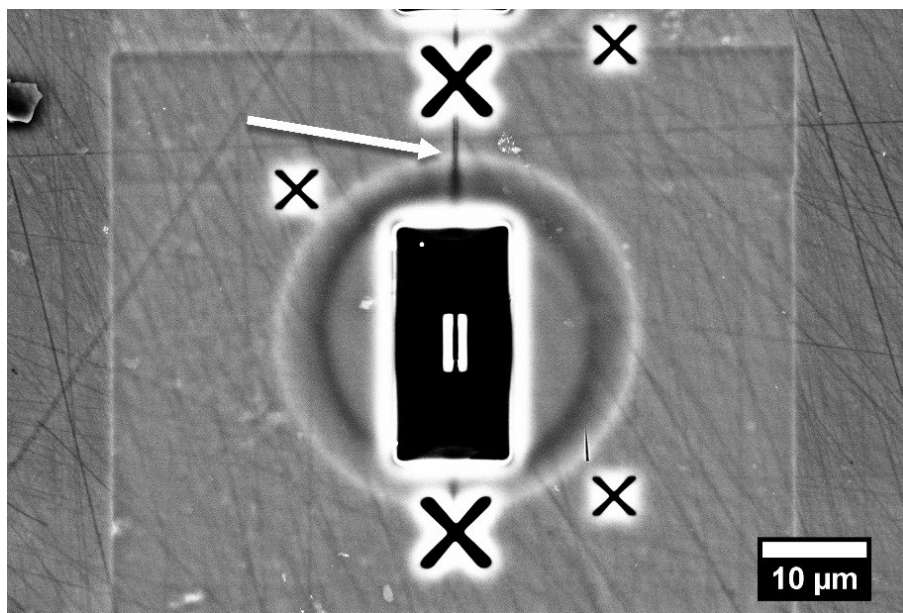

Figure 4.4 — High resolution backscatter top view image of the DCB milled along the glassy interface. The white arrow indicates the glassy interface confined between the two coupons of SiC. It is difficult to image the interface because its thickness is comparable to the resolution of the SEM. In addition, since the atomic masses between SiC and SiO2 are similar they do not show a good contrast in backscatter mode. However after the sample has been FIB'd due to preferential etching the interface can be seen running through the centre of the sample as in the image.

4.3 *In situ* mechanical testing setup

Testing was performed using the Alemnis nanoindenter used in displacement control (see paragraph 3.7). Displacement rates of between 1 nm s^{-1} and 2 nm s^{-1} [Figure 4.6-(a)] were used to achieve a low crack propagation speed and collect a high number of video frames for analysis. For the majority of tests, the displacement ramp was kept linear until the crack reached the bottom of the visible portion of the DCB and then the tip was retracted before causing complete failure of the DCB, for a test length of ~5 minutes. In three tests on single crystal SiC DCBs, after the crack had propagated a few microns into the DCB, the indenter was held in position with the DCBs still loaded for ~5 minutes to observe crack stability.

4.4 Fracture energy measurement

The measurement of fracture energy is possible once elastic modulus E and Poisson's ratio ν are known and by direct measurement of beam width d, maximum displacement δ and crack length a, as per Eq. (4.25). Measurements of each beam width were taken as the distance from the external edge to the crack wall using high resolution SEM images captured within the *in situ* experiment towards the end of the test, when the crack was longer. Three measurements along the height of each beam were averaged to obtain the final value.

Similarly, beam displacement and crack length measurement were performed on the SEM images collected during the test, adopting custom MATLAB scripts to make the process more efficient and accurate. A series of scripts were written as functions and incorporated in a parent script to make their execution and debugging easier. A first script is used to acquire all the necessary pieces of information from the recorded video such as frame rate, resolution, number of frames, duration and finally to store the video as a stack of single frames after converting them from RGB to grey scale.

A second script allows the frames to be cropped to reduce them to the region of interest for the analysis through the input of the position of two opposite corners picked by mouse clicking them on the image. This is followed by an initial registration of all frames performed in a subregion of all the frames using a MATLAB function *normxcorr2* to cross-correlate such subregion in all frames to that in the first frame, essentially obtaining that a point away from the bending DCB is fixed in the same position within the frame for all frames. This reduces the effects of image drift, caused by sample or nanoindenter compliance and sample charging under the electron beam.

Next, measurements of maximum displacement δ were performed using a similar cross-correlation procedure to track the DCB edge position at the contact point with the wedge for each frame, with respect to the position within the first frame, i.e. when the beam was still unloaded. This is done by scanning the intensities, on grey scale, along a horizontal line centred on the edge at the

first frame. The mean value of the intensity distribution along the line is subtracted to each intensity value to have a zero mean distribution. The zero mean distribution is finally normalised with respect to the standard deviation, multiplied by a periodic function and then cross correlated.

The coordinates of the crack tip position were selected 'manually', i.e. mouse clicking on their position on the image, augmenting contrast within the script to facilitate its identification (as the contrast and number of pixels made development of an automated routine difficult). Since the nanoindenter sits on the SEM stage with its indentation axis tilted 30° with respect to the horizontal plane, all the measurements along the vertical direction of the image were corrected for foreshortening.

4.5 Experimental results for fracture energy of 6H-SiC and glassy interface in SiC bi-crystal

In the single crystal SiC DCB labelled SC 4 the crack initiated at the pre-notch and grew without any bursts until the test was terminated and the tip retracted after a ~2 µm crack growth. In the other three single crystal SiC DCBs, the crack initiated ~100 nm on the left of the FIB-milled notch, indicative of a subtle asymmetry in the loading geometry or the presence of a sharp corner at the bottom of the trough where the stress concentrates. Once the DCB was loaded, the crack propagated straight and its growth was stable. This is shown in the sequence of frames extracted from the video recorded during the test of SC 2 (Figure 4.5) and the test was stopped when it reached a crack growth of ~4 µm.
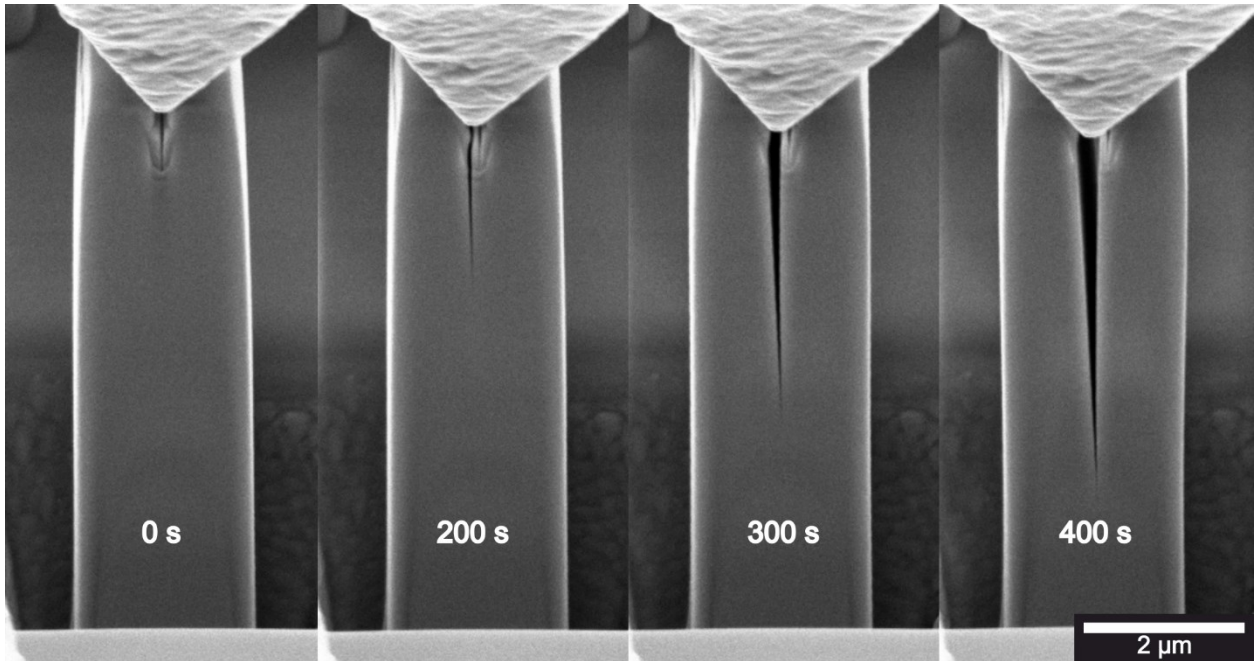
Figure 4.5 — Stable crack growth. A sequence of frames extracted from the video recorded during one of the in situ tests. The wedge tip at the top can be seen moving down as the test advances, causing the opening of the DCB; the crack slowly grows for a few microns over a total time of more than 350 s until the tip displacement is stopped and held in position.

Figure 4.6-(b) shows the deflection of the two beams of the DCB SC 3 plotted against time from the start of the test measured in pixels, then converted to microns, as obtained through image cross correlation. After an initial period of energy storing with no lateral movement of the beams, the data show a linear displacement of both cantilevers at the contact point. Although the frames were registered for overall movements independent from beam bending, as explained above, an equal and opposite movement of the two beams is evident in the first portion of the plot in Figure 4.6-(b), indicating a movement of the DCB under the initial load. The bending starts after ~200 s and continues to increase linearly until the tip displacement is stopped and held in position. The cross correlation records negligible movement of the beams during this stage; an increase in beam displacement was only recorded when the tip displacement was resumed, as can be noticed comparing Figure 4.6-(a) and (b). For the purpose of fracture energy measurements, only the time interval during which the crack growth was observed was taken into account [see crack growth interval indicated in Figure 4.6-(b)]. In order to reduce noise a linear fit of the data for the energy measurement calculation was performed.
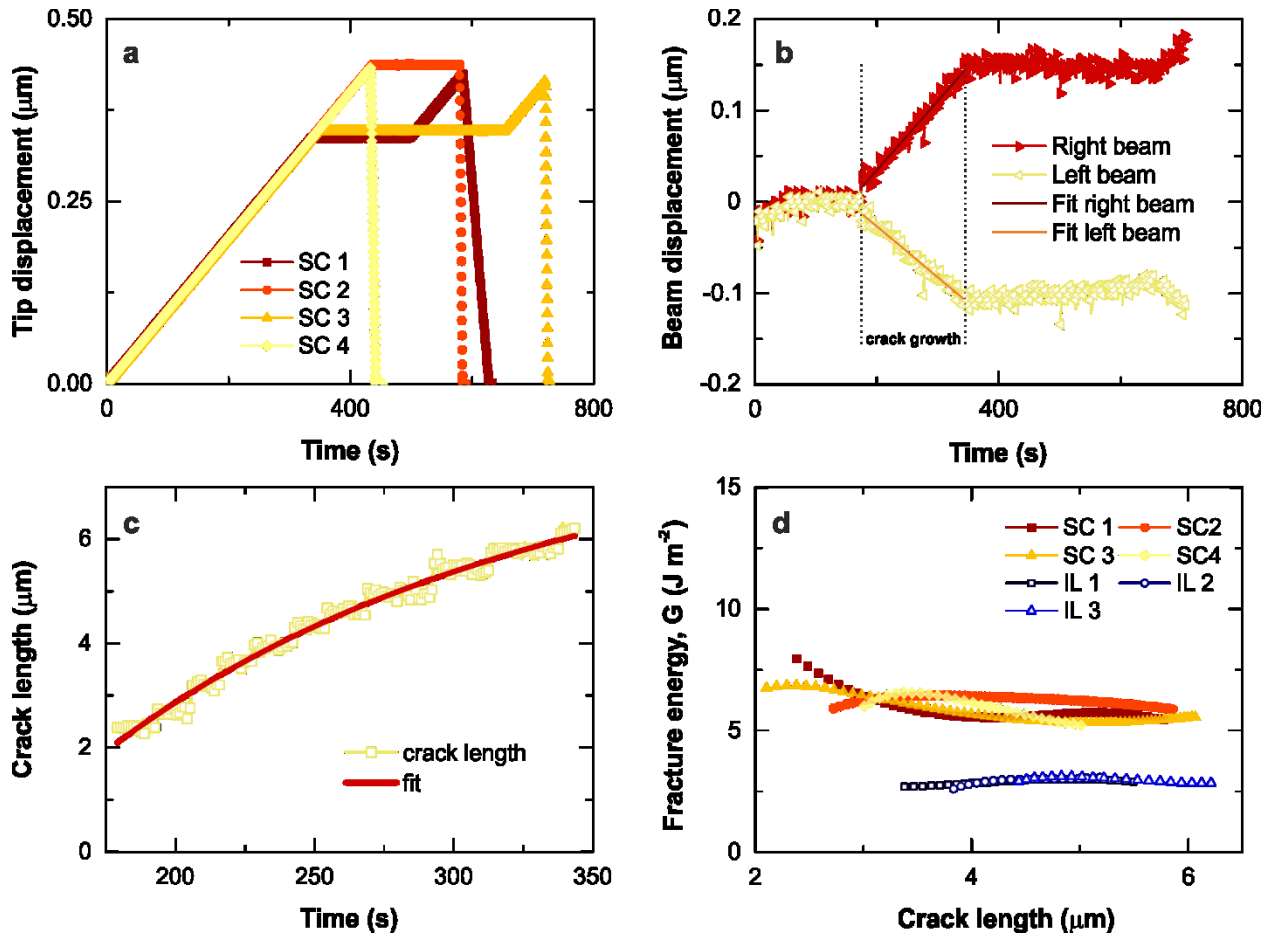
133

Figure 4.6 — Data analysis of DCB cracking. (a) Tip displacements as setup on the nanoindenter for four of the tests conducted on the single crystal (SC) SiC samples. **(b)** Displacement of left and right beams of the sample SC 3 measured by image cross correlation of the edges during the total test length. Dotted lines are used to show the interval of time in which the crack growth was measured. The curve is fitted according to a third order polynomial with R2 = 0.95 for left beam and R2 = 0.96 for right beam. **(c)** Crack length measured on sample SC 3 from the point of crack nucleation until the tip was stopped to hold position. Fitted data (R2 = 0.98) was used for the fracture energy measurement to reduce the noise in the data. **(d)** Fracture energy value measured over crack growth for the four SC SiC samples and the three SiC bi-crystals with SiO2 interlayers (IL), showing good reproducibility and a significant difference between the values of the two system.

The history of crack growth with time [one plot of which is shown in Figure 4.6-(c)], although presenting small jolts, is relatively steady and highly controlled in all the DCBs tested. This was demonstrated in three of the tests in which, after an initial crack propagation, the wedge tip was held still for 5 minutes with consequent crack arrest until the tip displacement was resumed [Figure 4.6-(a)]. Similarly to the lateral displacement data, crack length against time data were fitted to a third degree polynomial to reduce noise prior to use in the fracture energy calculation. The crack speed measured as an average from start to end is in the range between 25 and 29 nm s^{-1} for all the single crystal DCBs (this compares with a loading rate of between 1-2 nm s^{-1}).

Using the beam deflection, crack length and beam thickness as measured from the test images, along with an elastic modulus of 480 GPa and Poisson's ratio of 0.18 the fracture energy data shown in Figure 4.6-(d) and Table 4.1-(a) were obtained. Given the anisotropy of SiC, the elastic modulus used is calculated using the values of elastic constants from Landolt-Börnstein [167] and for the orientation parallel to the (0001) plane. Similarly, the appropriate Poisson's ratio was extracted for the two mutually orthogonal directions to the (0001) plane.

This same method was used to measure the fracture energy of the glassy interfaces in the three bi-crystal DCBs. For these experiments, the crack started tens of nanometres on a side of the milled notch (that acts as a stress concentrator) for all the tested specimen and proceeded constantly for ~2 μm until the tip displacement was stopped and retracted. Given the small volume of the interface compared to the silicon carbide, the same Young's modulus and Poisson's ratio used for the single crystal SiC were used to measure the fracture energy of the interfaces (as the majority of the elastic energy is stored within the SiC beams).

For completeness, the respective fracture toughness values were calculated (see Table 4.1) through $K_{Ic} = \sqrt{E_\perp G_c}$, where $E_\perp$ is the elastic modulus perpendicular to the (0001) plane (taken as 554 GPa for the current experimental work, using the values of elastic constants from Landolt-Börnstein [167]). Given the small value of Poisson's ratio in this case (of about 0.08 for ν_{12}) the difference between plane stress and plane strain assumptions is negligible.

DFT calculations of the surface energy for the 6H polymorph of SiC were performed with the CASTEP code [168]. Details of the DFT calculations method are published elsewhere [169]. The results are summarised in Table 4.1.

Table 4.1 — Comparison between experimental and simulated fracture/surface energy values of SiC and glass. (a) Simulations and experimental results for the surface and fracture energies of 6H- and 3C-SiC. **(b)** Theoretical estimate and experimental results for silica glass, and experimental results for the glassy interface of the SiC bi-crystal. The experimental values measured in the current work are the average of all the fracture energy measurement obtained with crack evolution. ± indicates the standard error as obtained by Monte Carlo based error propagation. The respective fracture toughness values from the current work were calculated as detailed in Results and Methods sections.

Description	Lattice constant a / Å	Lattice constant c / Å	Surface energy* 2γ or Fracture energy** G_c / (J m^{-2})	Fracture toughness K_{Ic} / (MPa m$^{0.5}$)	Reference
(a)					
6H-SiC (Micro-scale experiment)	–	–	5.95 ± 1.79 **	1.80 ± 0.26	Current work
6H-SiC (Macro-scale experiment)	–	–	20 ± 5 **	3.3 ± 0.2	[170–172]
6H-SiC(LDA)	3.05	15.02	8.58 ± 0.04*	2.18 ± 0.03	[169]
6H-SiC(GGA-PBE)	3.09	15.19	7.71 ± 0.04*	2.01 ± 0.03	[169]
6H-SiC DFT combined	–	–	8.15± 0.44	2.10 ± 0.08	[169]
3C-SiC(LDA)	4.34	–	8.34*		[173]
3C-SiC(Tersoff screened)	4.32	–	3.70*		[173]
3C-SiC(PBE)	–	–	8.40*		[173]
(b)					
Glassy interface of SiC bi-crystal	–	–	3.35 ± 1.16 **		Current work
Glass of different compositions	–	–	7.00-9.50**		[174]
Theoretical estimate for silica glass	–	–	1.00*		[174]

4.6 Error analysis

In order to better understand the bounds of the values obtained by experimental testing, an error propagation analysis was performed on the data for the SC and IL SiC DCBs. For such analysis, a Monte Carlo based error propagation analysis was used, whereby the input parameters, the variables in Eq. (4.25), are subjected to variation, according to a specific distribution, with known variances taken into account. Generally this is done by generating a set of random numbers to

have statistical distribution similar to the real variables and used as input, thereafter the output is observed. In this case, variables for the analysis with known errors were adjusted independently to have a Gaussian distribution with a known standard deviation. The mean of each distribution was the measurement for each test and the standard deviations based upon experimental measurement error. For each variable a set of 1000 random numbers was generated with the statistical properties mentioned, using a custom script on MATLAB. The variables and distributions are listed in Table 4.2 and Figure 4.7.

Table 4.2 — Variables for the Monte Carlo based error propagation. Variables for the analysis with known errors were adjusted independently to have a Gaussian distribution with a known standard deviation. The mean of each distribution was the measurement for each test and the standard deviations (SD) based upon experimental measurement error

| Quantity	Description	Uncertainty
Pixel to micron	pixel to micron conversion ratio used to measure distances from image analysis	1 pixel SD
Disp L	correction factor for left and right cantilever displacement to neglect initial recorded movements independent from pure bending and not	0.5 pixels SD
Disp R	corrected by frame registration	0.5 pixels SD
Viewing angle	indentation axis tilt angle with respect to SEM stage used to correct for foreshortening	3° SD
Young's modulus	elastic modulus, E, used in Eq. (4.25)	10 GPa SD
Poisson's ratio	Poisson's ratio, v, used in Eq. (4.25)	10%
Cantilever width L	left and right cantilever width, d, used in Eq. (4.25)	1%
Cantilever width R		1%
Pre-notch position	position of contact point between wedge and beam used to determine pre-notch length (and crack length by cumulative difference)	10 pixels SD
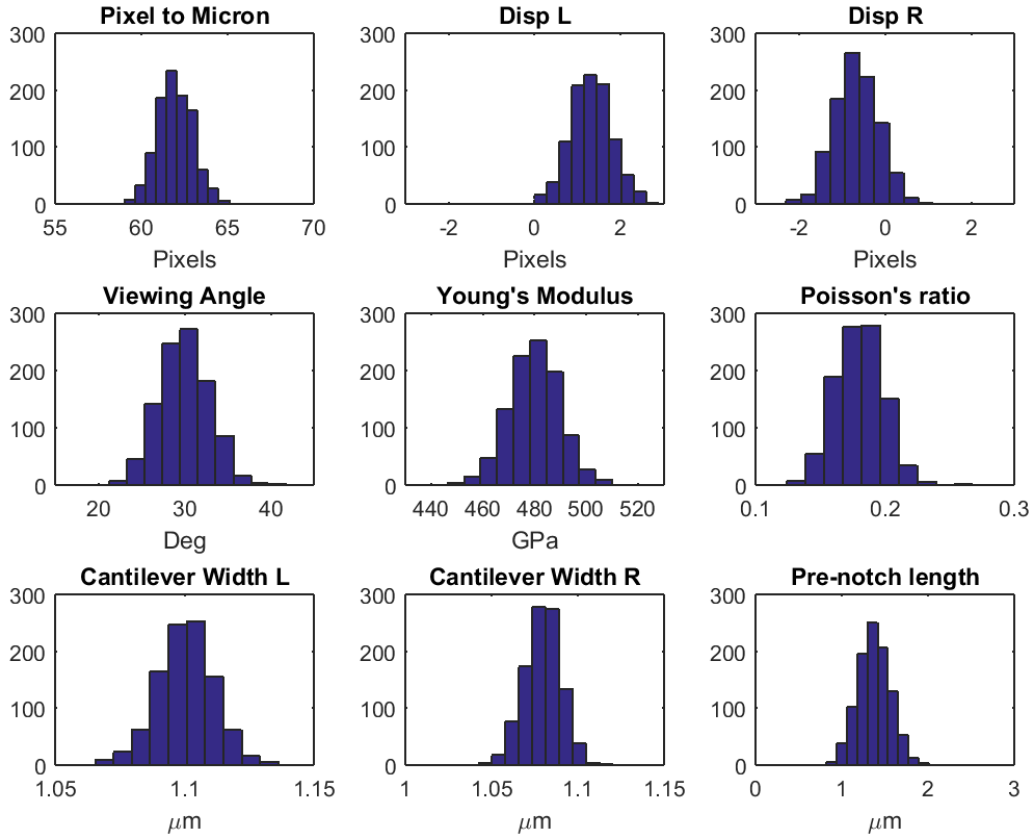
Figure 4.7 — Gaussian distribution of random inputs used for the Monte Carlo based error propagation analysis. The distributions shown were used for one of the single crystal SiC DCBs.

The total mean for each DCB was then calculated as the mean of all the mean values [Eq. (4.26)], while the standard error of the mean for each DCB was calculated as the square root of sum of squares of the standard deviations for each crack increment, divided by the square root of the number of crack increments measured during testing [see Eq. (4.27)];

$$\mu_{DCB,i} = \frac{1}{N}\sum_N \mu_{crack,n} \qquad (4.26)$$

$$s.e._{DCB,i} = \sqrt{\frac{1}{N}\sum_N (s.d._{crack,n})^2} \qquad (4.27)$$

In Eq. (4.26) $\mu_{DCB,i}$ is the total mean value of fracture energy for the ith DCB, N is the number of crack increments measured for that DCB, $\mu_{crack,n}$ is the mean value of fracture energy at the nth

crack increment as obtained by the Monte Carlo error propagation analysis. In Eq. (4.27) $s.e._{DCB,i}$ is the total standard error of the mean for the ith DCB and $s.d._{crack,n}$ is the standard deviation at the nth crack increment as obtained by the Monte Carlo error propagation analysis.

The result of the error propagation analysis for one of the SiC SC DCB is shown in Figure 4.8 where with the blue bar are plotted the standard deviations, $s.d._{crack,n}$, and with the red dot is plotted the mean value, $\mu_{DCB,i}$, of fracture energy for each crack increment.

The results are plotted together with DFT calculations and compared to values in literature in Figure 4.9.
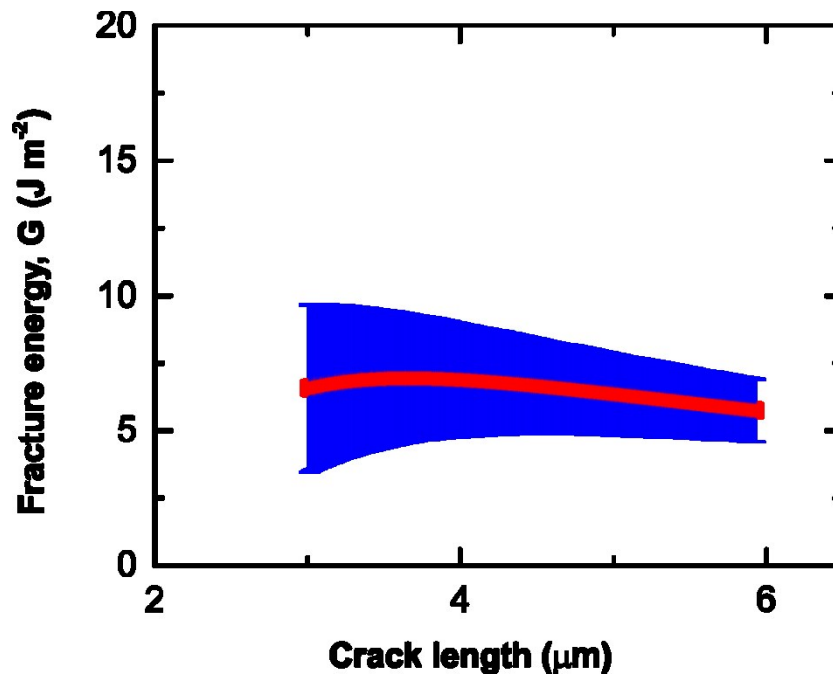

Figure 4.8 — Result of Monte Carlo based error propagation analysis on the measurement of fracture energy with crack length for one of the single crystal SiC DCB. The blue envelope represents the standard deviation, while the red line the mean value.
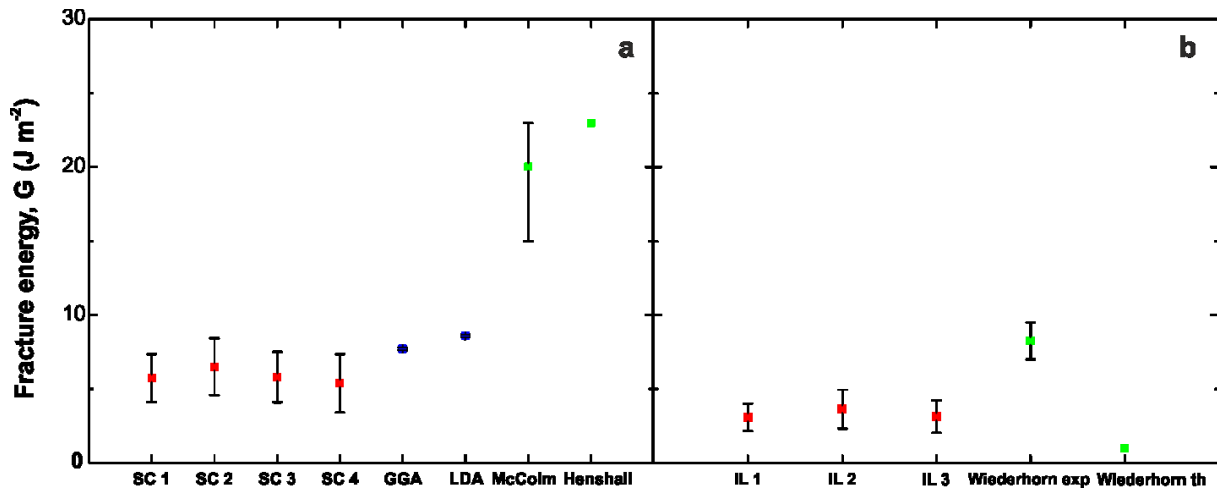
Figure 4.9 — Comparison of data obtained in current work from experiments and DFT with existing literature on macroscopic tests. Data from current experimental work are measured as the average whilst the error bar represents the standard error, both as obtained from the Monte Carlo based error propagation analysis. Data from literature (McColm [172], Henshall [170], Wiederhorn [174]) are represented as mean value, while the error bar represents the scatter. **(a)** comparison of fracture/surface energy data from micro- and macroscopic experimental testing and DFT calculations of 6H SiC (0001) plane; **(b)** comparison of fracture energies measured on glassy interlayer of SiC bi-crystals with values obtained on glass from macroscopic tests and theoretical estimate.

4.7 Discussion of technique development

4.7.1 Asymmetries and other geometrical complications

Symmetry of the DCB geometry would allow the total strain energy stored, whose rate of dissipation with crack length is equal to the fracture energy during stable crack propagation [see Eq. (4.9)], to be obtained by measurement of the strain energy stored in one of its beams and simply doubling it. However, in practice, perfectly symmetrical systems are unlikely in experimental sample preparation and testing conditions at this lengthscale. Therefore, in this work each beam was analysed independently [Figure 4.10-(b)] and the total energy term obtained by summing the two values of the left and right beams.

Asymmetry is likely caused by:

- The high lateral stiffness of the nanoindenter tip housing system, which makes any misalignment between the tip's central axis and the DCB's central axis hard to accommodate during the loading, is reflected directly in an asymmetric displacement of the beams.

- A similar effect would be caused by a misalignment between the sample surface normal and the tip's displacement axis, as the two beams would be loaded at two different apparent angles by the wedge.

- Subtle difference in beam thickness, due to difficulties in fabricating small samples (even with automated fabrication regimes as employed here).

For each of the three bi-crystal samples, cracks started tens of nanometres on the side of the milled notch. This is likely due to slight asymmetries in the overall loading geometry and the precise location of the interface.

These slight asymmetries require the energy stored in the cantilevers to be measured individually to avoid the fracture energy being significantly under- or over-estimated. While this subtlety may

not be obvious, in practice it is straightforward to implement asymmetric analysis with this *in situ* geometry. A comparison of the differences between crack growth measurements using asymmetric or symmetric analysis is presented in Figure 4.10-(a).
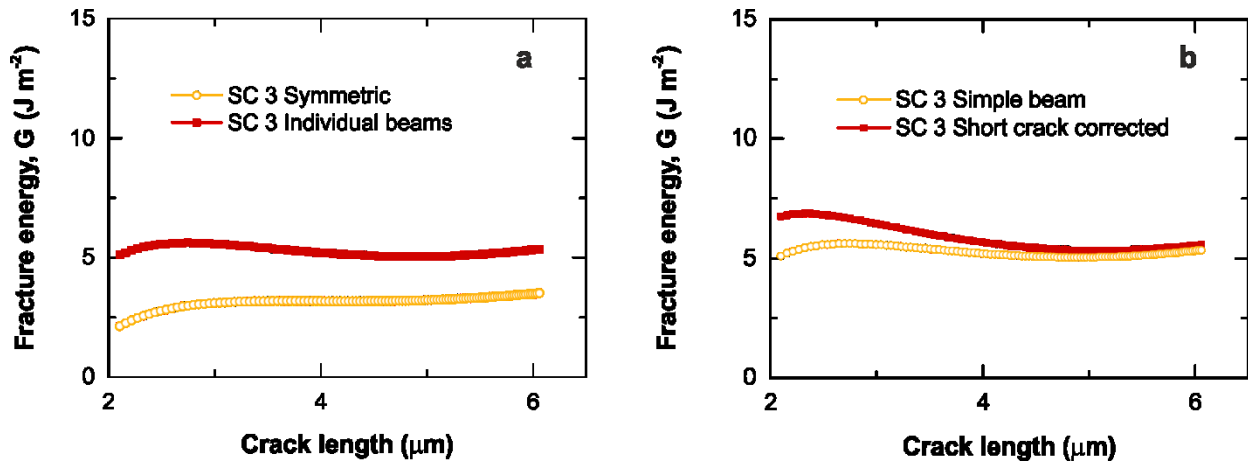

Figure 4.10 — Effect of different assumptions on DCB geometry. (a) Plot showing how the fracture energy would be erroneously measured should the DCB tested be treated as perfectly symmetrical. For "SC 3 Symmetric" the energy elastically stored in the system was measured by simply doubling the energy stored in one of the two beams. It is worth noting that the fracture energy could be under- or overestimated depending on whether the beam considered is moving more or less than the other beam respectively. "SC 3 Individual beams" was measured by measuring the energy stored in each beam. **(b)** "SC 3 Simple beam" fracture energy is measured applying the simple beam theory assumptions, whereas the values in red are corrected to take into account the effect of shear when the crack is short.

4.7.2 Short crack lengths

In this work, the fracture energy results are measured taking into account the non-negligible shear component that arises because the beam length is comparable with its thickness [Figure 4.10-(b)], i.e. when the crack is short. This low aspect ratio beam correction enables reliable measurement of the fracture energy value with variable crack length and demonstrates that the technique lends itself to the investigation of small regions of interfaces at short distances from the surface in real materials.

4.7.3 Taper

FIB milling normal to the sample surface is known to produce tapered final geometries, however the analysis presented in this work considers the cantilevers made of constant cross section along

its length. It is therefore important to design the milling steps to minimise the taper in the final geometry or alternatively the analysis would need to take this into account in the analytical solution. In the latter case, a correct elastic solution would require an accurate knowledge of the three-dimensional geometry of the DCB.

4.7.4 Fracture energy or surface energy

From the high resolution SEM images the crack propagation in the single crystal SiC appears to create two new smooth edges with no evident deviation from a linear path. The crack tip is sharp and no plastic deformation is expected around it and likewise no toughening mechanisms are available in the material examined. Furthermore, it is worth noting that the energy values were measured far from the notch and so the author does not expect it to be affected by crack initiation processes or ion penetration damage, which is found to be <100 nm from the surface [161,163]. The measured values of 5.95 ± 1.79 J m^{-2} (measured as average of all the fracture energy measurement obtained with crack evolution, where $\pm$ indicates the standard error as obtained by Monte Carlo based error propagation, see section 4.6) are thus likely to be representative of twice the surface energy (i.e. 2γ). DFT calculations performed by P. Patel and Dr. J. R. Kermode estimate the surface energy to be $2\gamma = 8.15 \pm 0.4$ J m^{-2}, taking into account uncertainties arising from the existence of three inequivalent termination planes for 6H-SiC in the [0001] direction, from the exchange-correlation functional used and numerical approximations such as finite basis set [175]. The DFT estimate of the surface energy is slightly higher than the experiment.

Similarly, the values obtained by testing the bi-crystals potentially provide the surface energy of the SiC-glass-SiC interface. Wiederhorn [174] reported values of fracture surface energy for glasses with different chemical composition in a range between 7.0 and 9.5 J m^{-2} at 300 K, comparing them with a theoretical estimate of 1.0 J m^{-2} for surface energy obtained by Charles and reported by Wiederhorn [174]. The crack surfaces obtained by Wiederhorn showed edges with angles varying as much as 30° to straight path and these deviations will result in a larger work of fracture.

Therefore the lower value obtained in the present work falls reasonably between the theoretical and experimental values found in the literature.

4.8 Fracture along the Al_2O_3/Nb interface

The systems described thus far are characterised by brittle fracture; in this case the effect of plasticity on the value of fracture energy is negligible. On the contrary, the fracture at or near interfaces between ceramic and metal can be characterised by the presence of a plastic zone ahead of the crack tip as the stress in this area reaches and passes the yield strength of the metal phase. As the metal phase is confined in smaller and smaller volume by a ceramic so is the plastic zone, therefore its effect on the energy required to propagate a crack is reduced. In chapter 1 some of the difficulties associated with the study of metal/ceramic interfaces using macroscopic tests were reviewed; a major one being the thickness of the metal layer, which tends to be larger than 10 µm. The objective of the study presented here is to establish whether a similar configuration and same analysis tools developed on the SiC samples could be employed to measure the resistance to crack growth at the interface of thin metal-ceramic interface, in particular a sapphire bi-crystal bonded by a niobium layer of thickness of few tens of nanometres. Samples of this system were manufactured by Dr Rui Hao, who subsequently manufactured them into DCBs for fracture energy testing. The thinnest metal layers obtained and tested were of 30 and 60 nm of thickness. Here the results obtained with two DCB tests of the 60 nm and one of the 30 nm interlayer are presented.

4.8.1 60 nm niobium layer

The images collected during the test show that different toughening mechanisms act during the crack propagation in the DCBs with the thicker metallic layer (60 nm). As a consequence, the

measurement here are performed using the raw data in order to follow the change in crack growth and cantilever displacement rate and consequently fracture energy.

In Figure 4.11 six frames extracted from the video recorded during the test on 60 nm - DCB 1 show that after an initial stage in which the crack extends little and is accompanied by evident crack tip blunting on the right side of the interface, occurring between frame 1 and 23, the crack extends a bit further on the right side before deflecting and then growing further on the left side. As the crack extends on the left side, a metal ligament is left behind the crack front. This creates two distinct zone in the plot of crack growth against frame number during the period examined [Figure 4.11-(b)], in the first part of which the crack grows slowly and almost stops, while after the jump, between frame 38 and 39, the crack growth proceeds at a faster rate. In contrast, the cantilever displacement appears to evolve close to linearly. It follows that the fracture energy initially increases during the period in which crack tip blunting occurs with little growth, i.e. between frames 1-23, to then start to decrease as the crack growth starts proceeding faster. The jump in the crack growth is reflected in a drop in fracture energy, however the value remains relatively high due to crack bridging. With the crack extending further, no further activations of toughening mechanisms are observed and the effect of the bridging is reduced gradually until the fracture energy drops to a nearly constant value of 21.93 ± 5.09 J m^{-2} for the last 35 data points, i.e. from frame 80.
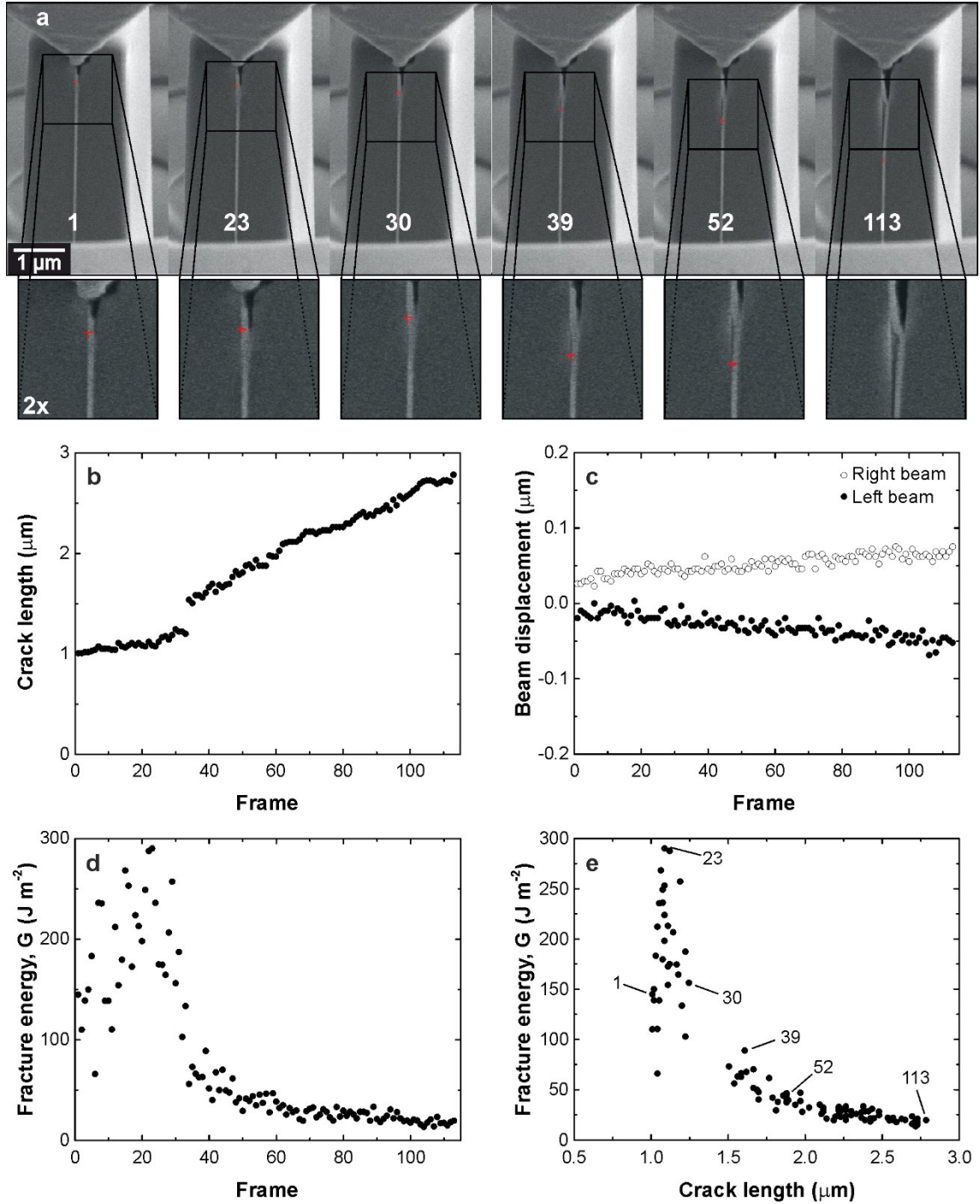
Figure 4.11 — DCB 1 on Al₂O₃ bi-crystal with a 60 nm thick Nb interlayer. (a) 6 of the 113 frames extracted from the video recorded during the test. The red crosses show the crack tip position as selected for the fracture energy measurements. Crack tip blunting can be noticed between frame 1 and 30, thereafter the crack deflect on the left side leaving a "bridge" behind and then extends without further interruptions. **(b)** Plot of crack length against frame number, i.e. time, showing the effect of the toughening mechanisms, crack tip blunting first and bridging after, on the extension rate. **(c)** Beam displacement evolution with frame number appears to be nearly linear during the crack growth. **(d)** and **(e)** Fracture energy as function of frame number and crack length shows the effect of the toughening mechanisms. Initially, the energy increases due to plastic deformation occurring at the crack front between frame 1 and 23, then a subsequent extension brings the value down again between frames 23 and 30. From here and frame 39, the crack deflection causes a drop in fracture energy, but the formation of crack bridging keeps the value high. The fracture energy then continues to reduce as the crack bridge has less and less effect on the field at the crack front as the ligament shears for the further opening of the beams and the crack extends further away from it.

The frames and the values extracted from the test on 60 nm - DCB 2, in Figure 4.12-(a), present a different case in which no crack bridging is observed, instead evident plastic deformation takes place during the majority of the crack extension. At the beginning of the crack extension, in the first ~40 frames, the rate of both the crack and cantilevers displacement is low [Figure 4.12-(b) and (c)] and the crack appears straight and sharp; in turn the fracture energy oscillates around the value of 35.23 $\pm$ 13.35 J m^{-2}. Thereafter, the crack tip radius is seen broadening ever more and the plastic zone extending further ahead of the crack, to the point that assessing what constitutes the crack tip becomes difficult, see frames 87 to 151 in Figure 4.12-(a). During this process the fracture energy reaches a value of ~150 J m^{-2} [Figure 4.12-(d) and (e)], however after frame 84 it is likely that the crack length was underestimated as it appears from frame 129. Between frames 129 and frame 151 the crack is seen to grow within the Nb interlayer. In the final 5 frames the fracture energy measured drops back to a value of 32.90 $\pm$ 5.90 J m^{-2}.
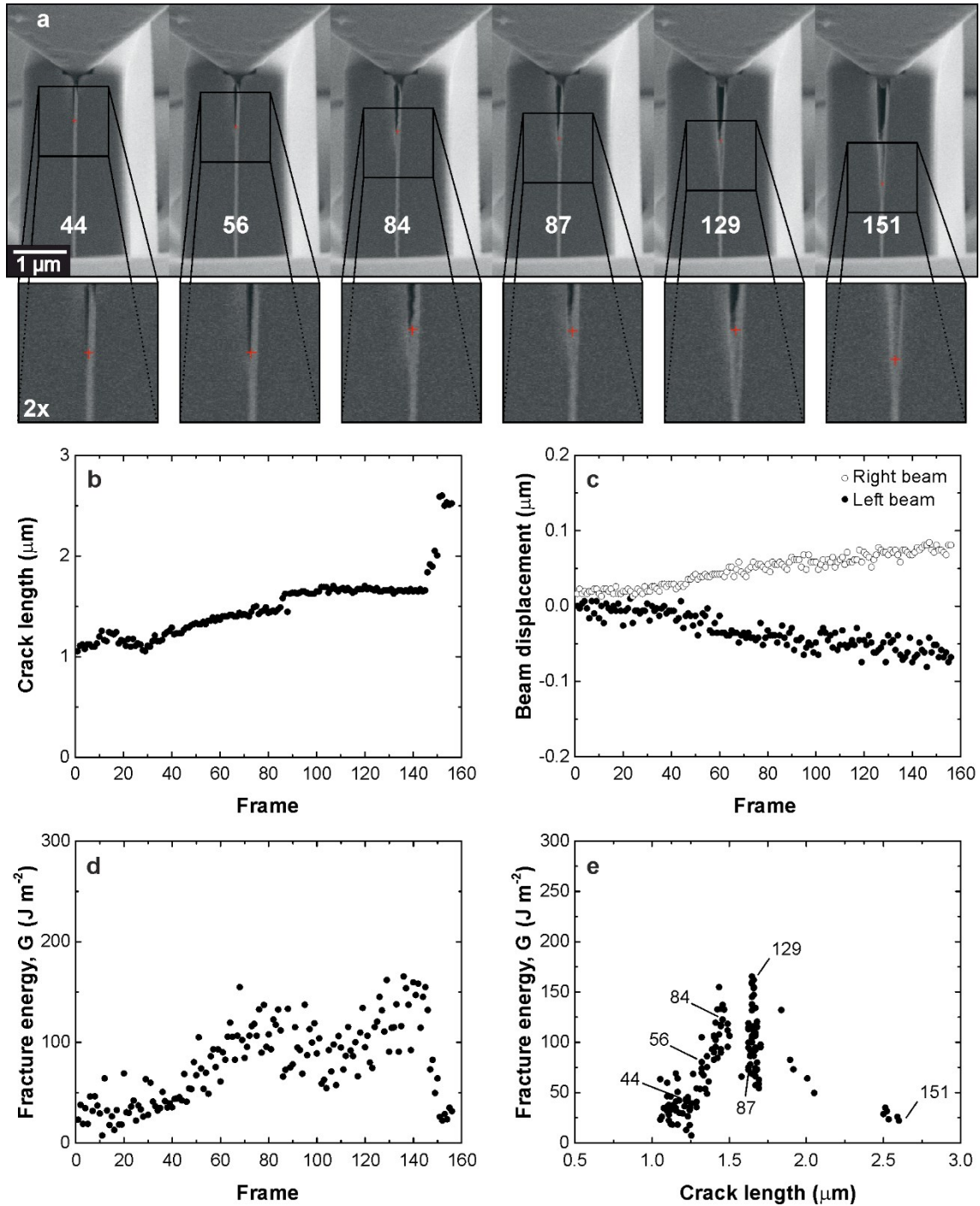
Figure 4.12 — DCB 2 on Al₂O₃ bi-crystal with a 60 nm thick Nb interlayer. (a) 6 of the 156 frames extracted from the video recorded during the test. The red crosses show the crack tip position as selected for the fracture energy measurements. The crack is seen to grow little up to frame 44, then extends between frames 44 and 56. Crack tip blunting can be noticed becoming ever more severe between frame 56 and 87, thereafter the crack tip position becomes difficult to ascertain and it likely caused underestimation of its length as shown in frame 129. Frame 151 shows how the crack grew within the metal interlayer after frame 87. **(b)** Plot of crack length against frame number, i.e. time, showing the effect of the plastic deformation ahead of the crack tip on the extension rate. **(c)** Beam displacement evolution with frame number appears to change rate too after frame 44. **(d)** and **(e)** Fracture energy as function of frame number and crack length shows that the energy value oscillates around the value of 35.23 ± 13.35 J m^{-2} in the first 44 frames to then increase rapidly due to crack blunting. The uncertainty on the crack tip position between frame 87 and 145 is likely to cause an overestimation of the fracture energy in this interval. Finally, in the final 5 frames, the fracture energy drops back to 32.90 ± 5.90 J m^{-2}, a similar value to that measured in the first 44 frames.

Despite the difficulties in assessing the location of the crack tip in some of the frames recorded during the experiments, the effect of the toughening mechanisms are captured by the measurements in both tests on the 60 nm thick interlayers.

4.8.2   30 nm niobium layer

In contrast with what observed at the interface of the 60 nm thick layer, in the DCB fabricated from the sample with the thinnest layer (30 nm) of niobium the crack propagates without showing evident plastic deformation, crack deflection or bridging [Figure 4.13-(a)]. Indeed, the fracture energy measured is 11.46 $\pm$ 1.95 J m^{-2} [Figure 4.13-(d) and (e)], i.e. a significantly lower value and a smaller standard deviation than the two DCBs with the 60 nm interlayer.

This reduction of the toughening effect of the thinner layer is expected since, as discussed in chapter 1, when the volume of metallic phase is decreased while being confined between two surfaces of a much thicker and rather stiff ceramic material the plastic zone is simultaneously confined.

It is worth commenting that the oscillation observed in the crack growth [Figure 4.13-(b)] and in the cantilevers displacement [Figure 4.13-(c)] are due to a faulty experiment setup of the Alemnis nanoindenter in which a feature was selected that attempts to hold the tip in its position at each given position of the indenter displacement ramp. As small amount of drift in the tip displacement reading is always present, this imparted a sawtooth wave movement to the tip. However, this is deemed to have had little influence on the crack growth evolution.
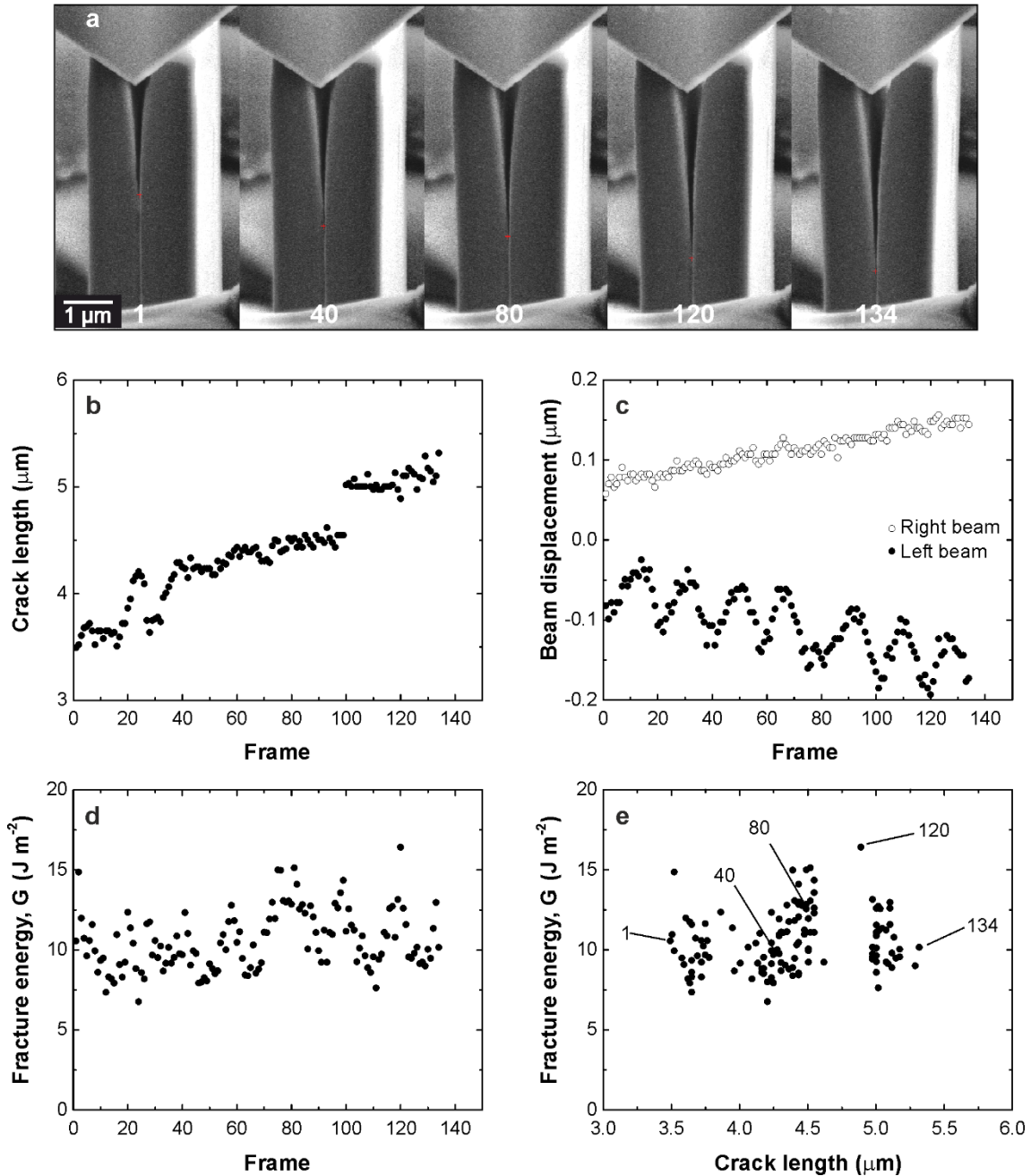
Figure 4.13 — DCB 1 on Al₂O₃ bi-crystal with a 30 nm thick Nb interlayer. (a) 6 of the 134 frames extracted from the video recorded during the test. The red crosses show the crack tip position as selected for the fracture energy measurements. Conversely to the two 60 nm interlayer, the 30 nm interlayer seems to impart no visible activation of crack bridging or blunting. **(b)** The plot of crack length against frame number, i.e. time, shows that the crack extension is irregular, moving back and forth. This is caused by the indenter tip sawtooth movement due to a wrong experimental setup. **(c)** Beam displacement evolution with frame number also reflects the sawtooth profile of the indenter tip displacement. **(d)** and **(e)** Fracture energy as function of frame number and crack length reflects once again the sawtooth profile, nonetheless the fracture energy value is measured as 11.46 ± 1.95 J m^{-2}. The small standard deviations indicates that this had little influence on the fracture energy measurement. It is interesting to notice that with the 30 nm interlayer a significantly lower fracture energy value and a smaller standard deviation was found than for the two DCBs with the 60 nm interlayer.

4.9 Fracture of diamond

4.9.1 Single crystal diamond

After the validation of the technique on all-brittle and brittle-ductile system, there was interest in testing diamond samples with the intent to then test PCDs.

It was decided to start with single crystals, i.e. fabricating the DCBs on large grain of a CVD-grown diamond sample, to see whether the test would be successful at all on diamond. Therefore, first a low scan and low pattern resolution EBSD map on a $\sim960x720~\mu m^2$ area was collected. Then the grain that could be best identified using low focused ion beam currents and related to the EBSD map was selected; this grain presented {110} perpendicular to the top surface. Therefore it was chosen to fabricate three DCBs so to have the notch aligned to cause fracture along the {110} in the [111] direction, using the same geometry and currents used for the SiC samples (see paragraph 4.2). The lower sputtering yield of diamond with respect to SiC had to be taken into account and it translated in a threefold increase in milling time, although a small part of this was due to the implementation of a frequent drift correction procedure necessary due to the diamond electrical charging during milling.

Before the test, DCB 3 had collected foreign particles on its top and was discarded. The geometry of the trough on DCB 2 presented an almost right angle at the cantilevers internal base and no sharp notch; as a result the test was concluded with a catastrophic failure of its arms as shown in Figure 4.14.
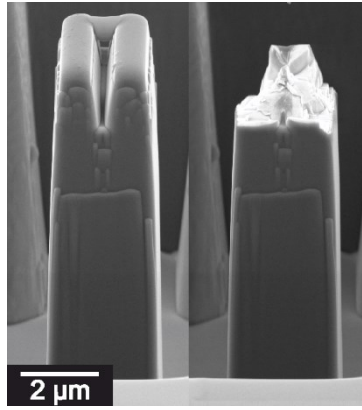
Figure 4.14 — DCB 2 on CVD-grown diamond. Catastrophic failure of the beams attributed to the right angle at the trough base, absence of a sharp notch and partially to the foreign material deposited on the top.

In the test of DCB 1 the crack initiation was accompanied by a crack growth of ~5 μm after which the crack growth stabilised for 34 s, thereafter deviated along the easy cleavage {111} plane, that is perpendicular to the {110} as visible in the last frame on the right in Figure 4.15-(a).

During this time interval in which the crack was stable, 21 frames, thus 21 data points, were collected for the fracture energy measurements. Given the lower number of frames than those collected for SiC DCBs, the raw instead of fit data were used for the measurements. The fracture energy values measured are presented together with 5 selected recorded frames in Figure 4.15. Upon further revision of the frames [Figure 4.15-(a)] it was noticed that in two of these, the 3rd and 20th frame, the crack position was significantly misjudged, and their value excluded from the average fracture energy measurement. The use of raw data inevitably generated higher noise in the results, nonetheless the average value of fracture energy for this DCB was measured as 12.80 ± 1.10 J m^{-2} [Figure 4.15-(e)] which compares well with the value of cleavage energy on {110} of 13.0 J m^{-2} reported by Field [102].

In order to further improve the test, care should be taken in introducing a sharper notch than that on the DCBs tested. Difficulty in introducing the notch arose from the lower sputter yield of diamond that hindered the milling of the notch utilizing the same low currents used for the SiC DCBs. The high stiffness and relatively high fracture energy of diamond make the notch radius particularly important to control the initial crack extension; this is further aggravated by the

relatively low stiffness of *in situ* nanoindentation platforms. The test would also benefit from the use of a sharper and smoother wedge, since friction contributes to a discontinuous release of energy.
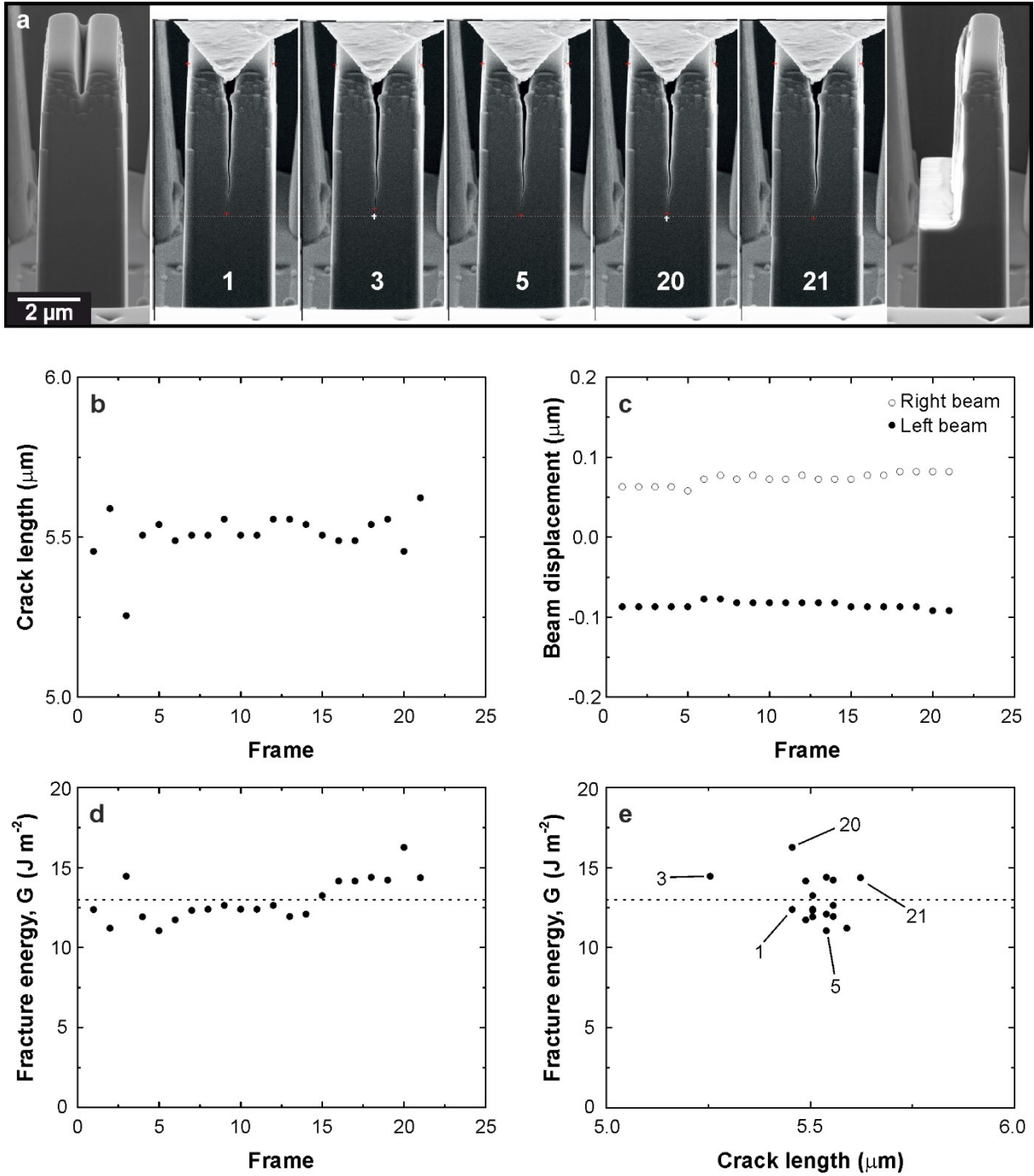
Figure 4.15 — DCB 1 on CVD-grown diamond. (a) From the left, an image showing DCB1 before the test, then 5 of the 21 frames extracted during the stable crack growth interval and finally DCB 1 after the test, showing the final failure along {111}. The red crosses indicate the location of the crack tip and beam edges as selected for the fracture energy measurements. The white crosses show the actual position of the crack tip in frame 3 and 20, discarded from the analysis. The red and white dashed line are used as visual reference to appreciate the effective crack growth between frames 1 and 3-5 to frame 21 respectively. **(b)** Crack growth as a function of frame, i.e. time; small oscillations are due to image wiggling. **(c)** Beam displacement against frame number. The simultaneous shift towards positive displacement of both beams at the 6th frames is indicative of a sudden movement of the whole DCB towards the right side of the frame. This is independent from DCB opening and generates some inaccuracy in the 6th and 7th frames measurements. **(d)** and **(e)** Fracture energy values as a function of frame and crack length respectively. The dashed line indicates the value of 13.0 J m^{-2} reported in literature [102]. The numbers in **(e)** are the frame numbers.

4.9.2 Diamond-cobalt interface

Attempts were made to fabricate DCBs that could enable the measurement of the diamond-cobalt interface energy. The boundary between CVD and PCD on the sample in Figure 4.16-(a) was chosen in order to have a straight interface running through the DCB. Unfortunately, the cobalt interface proved to be thicker than expected, so that the cobalt was always a significant portion of one of the cantilevers and not simply confined in the middle of the DCB, compare Figure 4.16-(b-d). Tests on these DCBs were conducted despite the impossibility to extract meaningful values to assess whether the crack would deviate along the interface at all.

In one case, Figure 4.16-(b), the crack started growing in the cobalt layer, yet the test concluded with a catastrophic failure of the left diamond cantilever when the right cantilever started displacing significantly due to the formation of slip bands in the cobalt volume. Similarly in the other tests the presence of the cobalt in one of the cantilevers favoured a severe deformation of this beam that caused cracking in the diamond volume of the same cantilever.
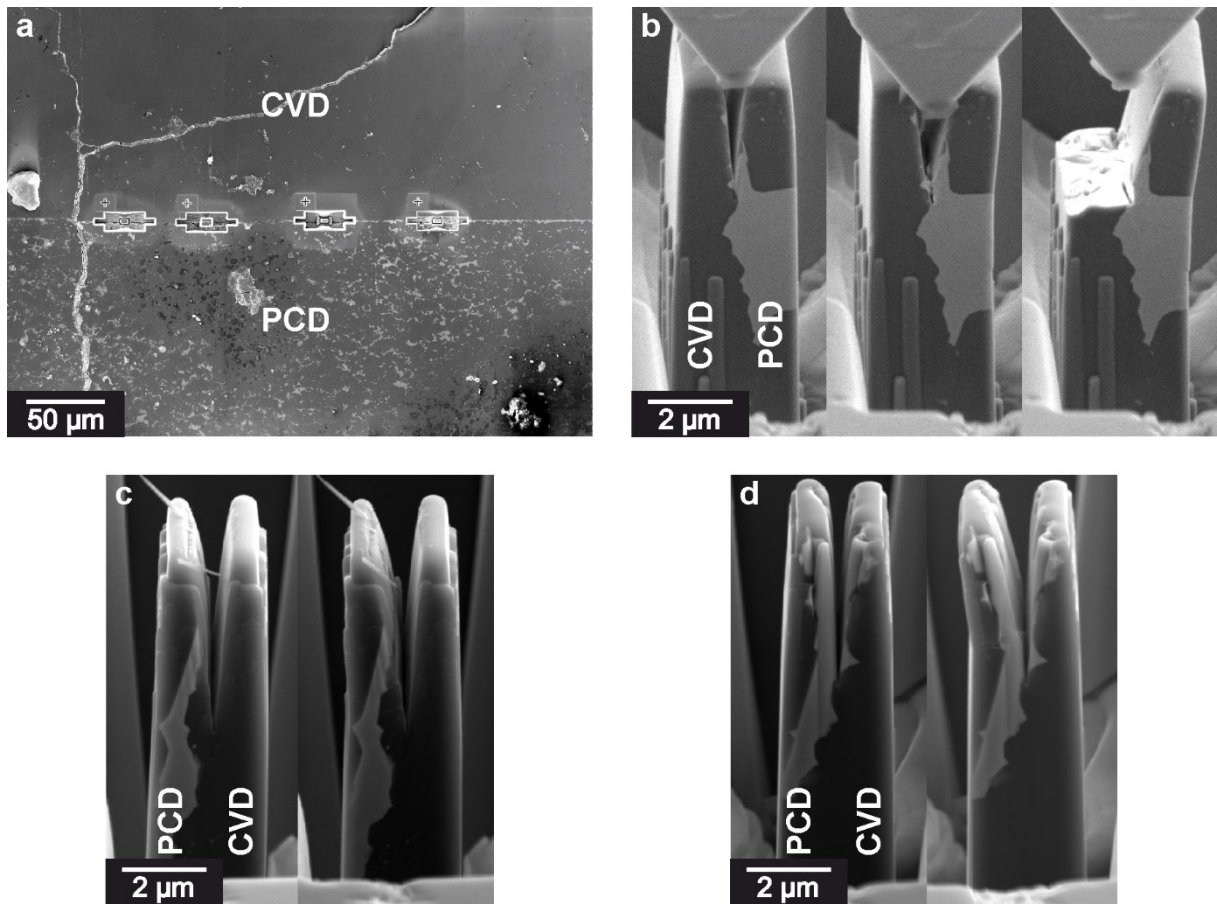
Figure 4.16 — DCB fabricated at the interface between CVD and PCD diamond. (a) top view of the two portions of the sample with CVD in the top half of the image and PCD on the bottom half. The two regions are separated by an interface were cobalt infiltrated, therefore it was chosen as a good location to have a diamond-cobalt interface running vertically in the middle of the DCB. (b-d) show the different DCB fabricated. The cobalt interface was thicker than initially thought, so to be a significant portion of the cantilevers, thus deforming plastically under bending.

4.10 Summary

In situ wedging of a double cantilever beam coupled with a displacement controlled testing machine afforded a stable and relatively long crack growth at the micrometre lengthscale to be obtained. The method was validated by fracturing single crystal 6H-SiC along the <a> direction, finding a value of the fracture energy of 5.95 ± 1.79 J m^{-2}, in good agreement with DFT calculations performed on the same cleavage plane. Tests were then conducted on a SiO$_2$ interface of ~10 nm thickness used to bond two coupons of SiC. These results show a value of 2.74 ± 0.10 J m^{-2}, which compares with the range between theoretically estimated and experimentally measured fracture surface energy of glass in the literature.

The loading geometry employed proved that measurement of the evolution of fracture energy with crack length is possible at the microscale and without the use of load data; thus reducing the effect of notch radius, ion damage and frame compliance on the value found, which are often a concern in fracture testing at this lengthscale.

The same method was then applied to study metal-ceramic interfaces, specifically two sapphire bi-crystals bonded by 30 and 60 nm thick niobium interlayers. The measurements successfully captured the fracture energy variations imparted by toughening mechanisms activated during the test.

Finally, the fracture energy of diamond on the {110}, i.e. not the weakest cleavage plane, was measured as 12.80 ± 1.10 J m^{-2}, in good agreement with the value of 13 J m^{-2} reported in the literature.

The method proposed introduces a new opportunity to study individual grain boundaries and microstructural units, thus enabling optimization of fracture properties of specific boundaries in ceramics with more complex microstructures.

EBSD analysis of polycrystalline diamonds

Here microstructure, crystallographic texture and residual stresses are investigated using a combination of SEM imaging and EBSD analysis. The information obtained is then exploited to understand their influence on the fracture mechanisms.

5.1.1 Grain size and aspect ratio distribution

Grain size measurements in PCD have been usually performed using optical microscopy or SEM images, yet given the presence of diamond-diamond boundaries and the pool-like form of the cobalt phase the detection of the individual grains is not simple. Perhaps for this reason, in the literature PCDs are often only distinguished by using the grade of the starting powder or, when measured, the grain size is expressed as average value. Differently from most sintered products the final grain size is smaller than the starting powder with a larger difference in size distribution between powder and final product observed for coarse powders and less significant for smaller grades; this is attributed to particle crushing occurring during the cold compaction stage where pressure close to that of sintering are reached without heating [115,116,176].

However, for mechanical properties in general, fracture mechanics in particular, grain size and aspect ratio distributions have a more important role than the average grain size. A study from Uehara and Yamaya [3] presents a schematic that compares the distribution of the particle size before sintering with the grain size after sintering, yet it does not provide a distribution.

In this work grain size and aspect ratio distributions of diamond crystals were evaluated from EBSD data sets adapting subroutines from the MATLAB toolbox MTEX [177]. The script was written to first import and analyse the spatially indexed EBSD data, so to individuate the grain boundaries where orientations of adjacent grains would differ of an angle of 7°. Then an arbitrary number of minimum 5 indexed patterns per grain, i.e. 5 pixels, was chosen as cut-off for all the analysis in order to remove ill-indexed grains. On the selected grains, a "smoothing" operation was

carried out using a spline filter to interpolate the missing pixels within the indexed grains. Finally, for the evaluation of quantitative data, grains at the edges of the map were considered incomplete and excluded. The grain size was then measured as the equivalent grain diameter from its area, i.e $2\sqrt{(area/\pi)}$ [178], thus considering the grain as spherical.

EBSD is a technique appreciated for the high spatial resolution at which can capture orientation data, so that usually many data per grains are measured rather than many single-grain orientations. However, for the macrotexture analysis to be statistically sound a certain number of grains is needed; this number depends mainly on crystal symmetry and texture sharpness [179]. Several studies have demonstrated, as reported in [179], that for cubic materials, such as diamond, texture could be picked analysing as little as 100 grains, but a statistically sound representation required 500-1000 grains, especially to adequately represent weaker textures.

The analysis was conducted on both fine (G4) and coarse (G30) grained PCDs sintered at 6.8 GPa at a temperature of 1500-1550 °C on a standard WC-Co substrate (compare section 3.1.3). However, the first was on the top surface of the PCD cutter, the latter was a vertical cross section of the PCD.

The map on PCD G4 was captured scanning a region of 153×115 μm^2 with a 0.38 μm pixel size. The EBSP for this map were initially set to acquire a data set suitable for HR-EBSD analysis, therefore the pattern resolution was set high at 800×600 $pixels^2$ and the exposure time at 250 ms. The map shows a uniform distribution of grain sizes across the whole region analysed Figure 5.1-(a,b). The data set collected contains 4364 grains whose size distribution indicate that after sintering 98.9% of the grains are smaller than 4 μm with the median shifted to 2 μm, as shown in Figure 5.1-(d). The minimum threshold for grain detection was imposed at 5 pixels, that is grains smaller than 0.72 μm^2 or 0.96 μm of equivalent diameter were excluded.

In the case of coarser grades (G30) three maps of 500×376 μm^2 with a 1 μm pixel size were collected and their results collated for the grain size distribution analysis, see Figure 5.2-(b). For these, the acquisition time was significantly reduced to 2 h 30 m using an EBSP resolution of

400×300 pixels^2 and an exposure time of 49 ms. The same minimum size of 5 pixels was used for the analysis, thus grains smaller than 5 µm^2 or 2.52 µm of equivalent diameter were discarded. The grain size distribution, plot from a total of 5055 grains, is not only wider than G4 but also bimodal, as indicated by the two maxima observed. Taking into account the minimum size considered, a first maximum is found between 3 and 4 µm and a second between 17 and 18 µm. This result compares well with observations from Gruzdeva [115] showing a similar distribution shape when analysing the change in diamond powder size distribution before and after cold compaction, but before sintering. Gruzdeva's study shows that the powder size distribution always has one maximum at a constant position for all powders analysed and a second maximum that would shift toward larger sizes with increasing grain size, therefore leaving a mixture of two fractions.

Assuming that the cold compaction stage imparted in PCD G30 a similar particle size distribution as observed by Grudzeva, the bimodality found in this work shows that such size distribution is preserved during the sintering.
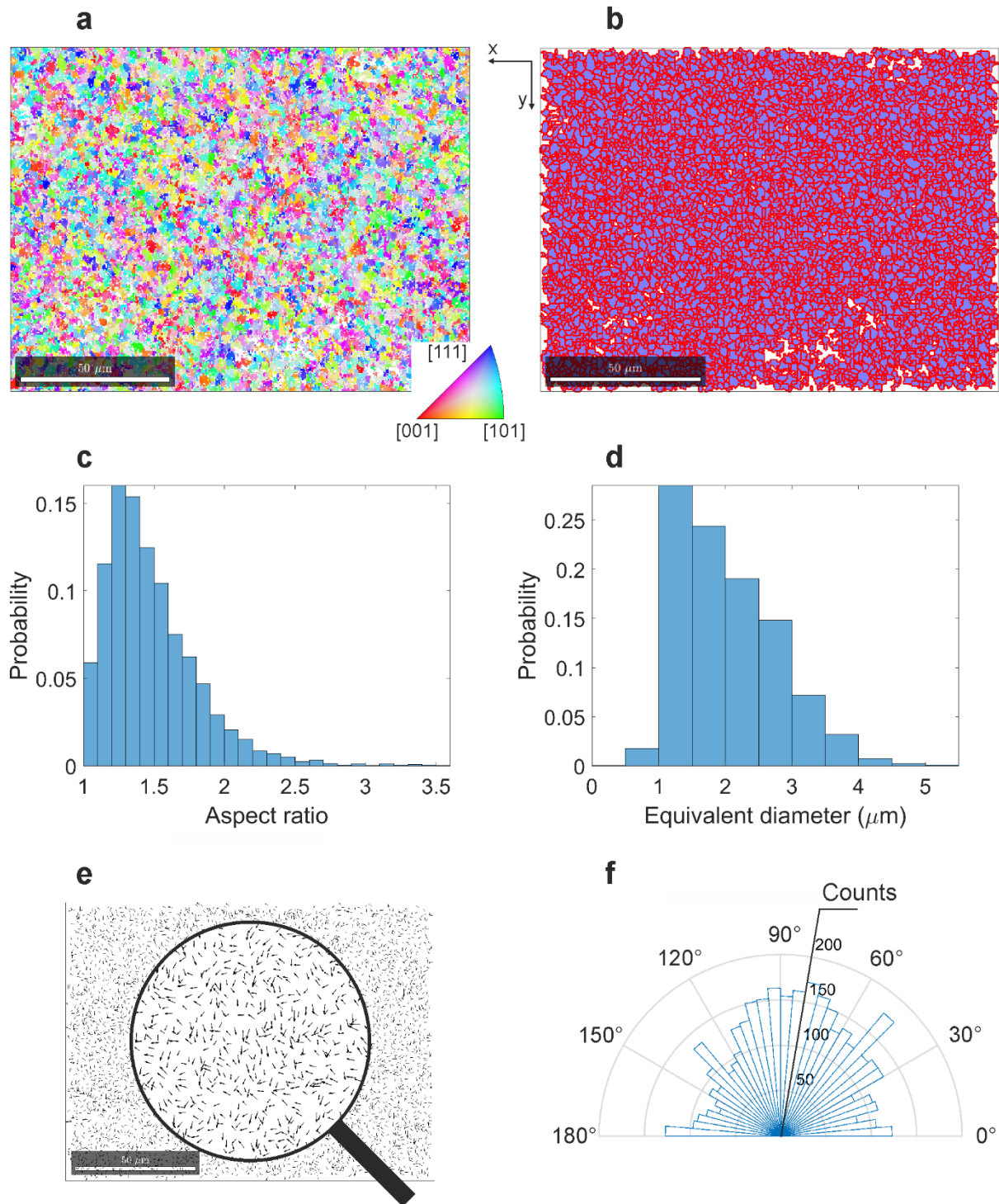
Figure 5.1 — Grain size and aspect ratio distributions for PCD G4. (a) Inverse pole figure map with respect to sample z-axis (IPFz), i.e. in this case normal to the cutter top surface. Colours in the map are related to the crystallographic orientations with respect to the sample z-axis as indicated by the legend. **(b)** Map showing the grain boundaries (in red) as calculated via MTEX after "smoothing" of the data. Only grains with more than 5 indexed patterns and not sectioned by the map frame edge are considered for the grain size and aspect ratio analysis. **(c)** Aspect ratio distribution defined as the ratio between the long and short axes of the grain. Here the mode of the aspect ratio is centred at 1.3 with only 1/3 of the grains showing a smaller aspect ratio. **(d)** Grain size distribution, measured as the equivalent grain diameter from its area. This indicates that 98.9% of the grains are smaller than 4 µm, i.e. the starting nominal particle size. **(e)** Map of long axis distribution. Here arrows are drawn at each grain centroid with their direction equal to that of grain long axis and magnitude proportional to the aspect ratio; the arrow head points arbitrarily in one of the two possible direction at 180° from one other. The area in the "lens" is magnified 2×. **(f)** Rose diagram showing the distribution of long axis direction with respect to sample x-axis. Interestingly, this sample shows a slight asymmetry with a higher frequency for angles between 30° and 90° than those in the 90°-150°.
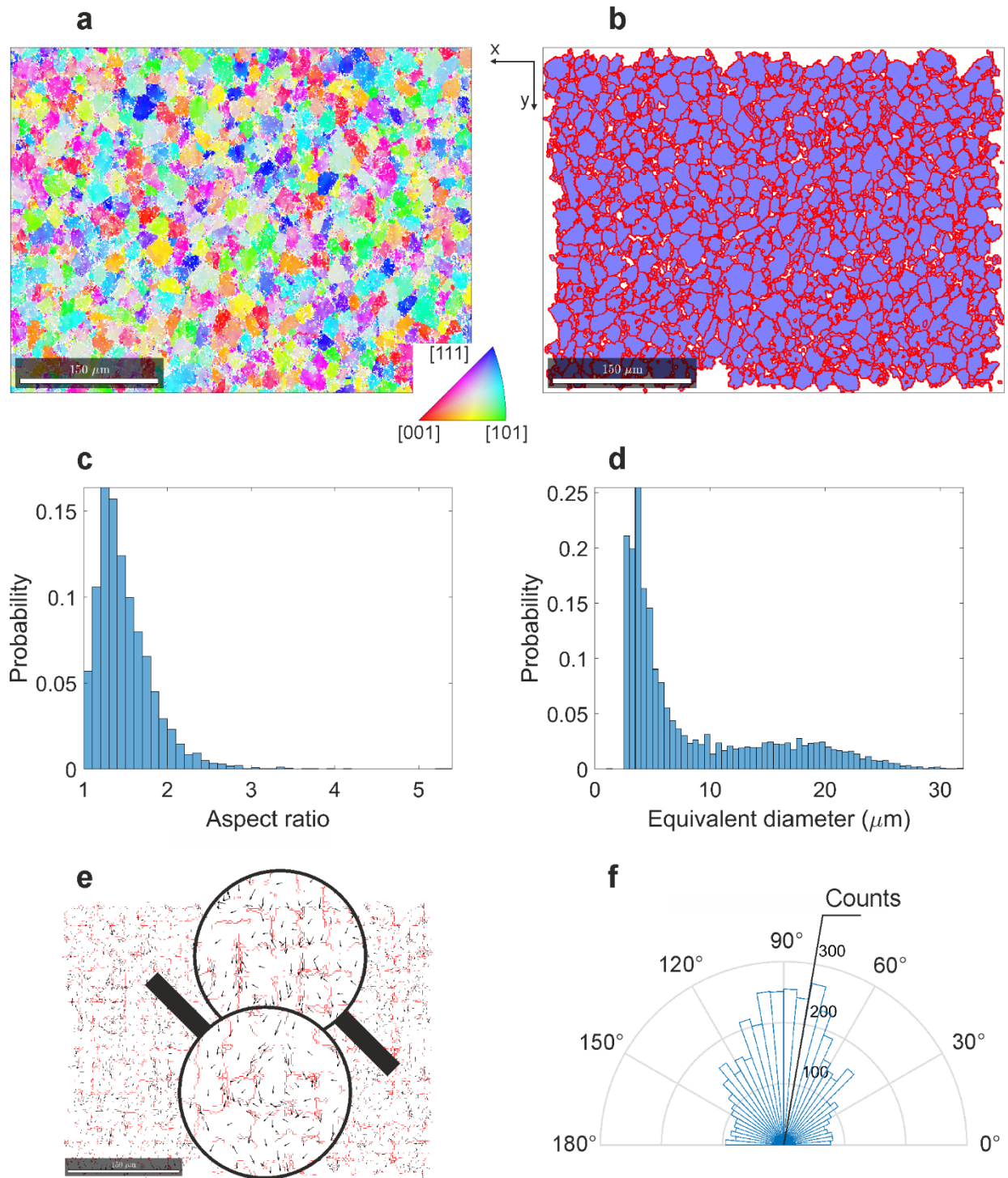
161

Figure 5.2 — Grain size and aspect ratio distributions for PCD G30. (a) One of the three IPFz maps collected on this sample; in this case normal to the cutter cross section. **(b)** Map showing the grain boundaries (in red) as calculated via MTEX after "smoothing" of the data. Only grains with more than 5 indexed pixels, with 1 μm pixel size, and not sectioned by the map frame edge are considered for the grain size and aspect ratio analysis. 5055 grains have been analysed cumulatively from the three maps on PCD G30. **(c)** Aspect ratio distribution from the aggregated data, distribution is very similar to that of PCD G4. **(d)** Grain size distribution, measured as the equivalent grain diameter from its area. Unlike PCD G4, here the distribution is very wide and shows two maxima at 3-4 μm and 17-18 μm. **(e)** Map of long axis distribution. Here arrows show that often smaller grain seem to be aligned as following a flow around bigger grains. The areas in the "lenses" are magnified 2×. **(f)** The rose diagram shows a tendency for the long-axis to align parallel to the sample y-axis, i.e. the cutter cylindrical axis.

The results obtained by using MTEX routines have been compared to the conventional intercept method for grain size measurements. In order to avoid the problem of detecting the grain boundaries from secondary electron images [Figure 5.3-(Micrographs)-(a)], the images captured by the forescatter detector [Figure 5.3-(Micrographs)-(b)] were used instead for their orientation contrast (see paragraph 3.3). These were then thresholded in ImageJ to transform the original image in a binary image with the cobalt pools in white and the diamond grain in black. Subsequently a watershed segmentation algorithm implemented in ImageJ was used to connect the cobalt pools and draw the grain boundaries [Figure 5.3-(ImageJ)-(a)]. This image processing technique essentially treats the image as a surface in which the greyscale intensities indicate the depth, with bright pixels being higher than darker ones. In this way the regions presenting minima are treated as catchment basins and separated by watersheds [180]. The image obtained was then analysed using automatic image analysis as described in the ASTM E1382 and employing the MATLAB script published by Lehto *et al.* [181]. The script measures the grain sizes as all the segments between two intercepts along evenly spaced lines arranged in four directions at 0°, 45°, 90° and 135° [Figure 5.3-(ImageJ)-(b)]. The measurements in the four directions are combined in a single array containing all the individual intercept lengths, i.e. the grain sizes. For consistency with the measurement performed via MTEX, all grains smaller than 2.5 microns were discarded from the analysis.

The values of average grain size of 8.8 μm obtained by this method is close to that of 8.4 μm obtained using the grain size analysis tool of MTEX.
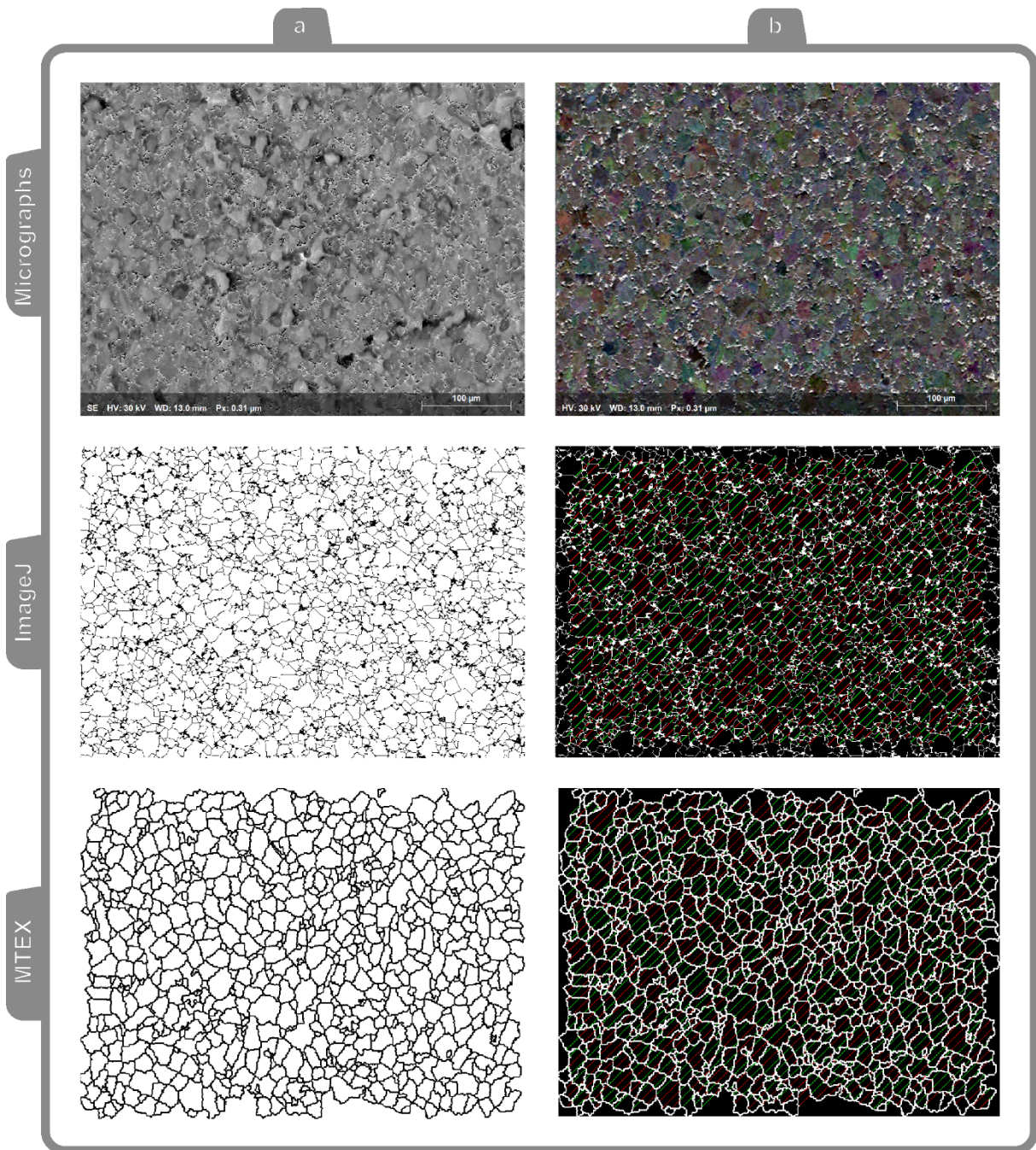
Figure 5.3 — Grain size analysis performed via intercept length method. The Micrographs tab shows the original secondary electron image (a) and forescatter image (b) for a PCD G30. The forescatter image was modified in ImageJ to segment the grains and draw their boundaries (a). Then it an automated script was used to calculate the intercept length between grain boundaries at 4 different angles, as shown in (b) for the 45° orientation. The grain size distribution so obtained was then compared to the one obtained using the same linear intercept method but this time on grain boundaries drawn using the MTEX calculations of EBSD data.

However, the results plotted in Figure 5.4 show a different distribution than that obtained using the EBSD data, lacking of clear bimodality. Comparison of the cumulative distribution function (CDF) plots highlights the differences between the two distributions. In particular, it becomes

easier to notice the regions with a smaller population of data on the distribution obtained by EBSD analysis, i.e. those with a lower slope. The CDF for the intercept can be instead fitted with a log-normal distribution.
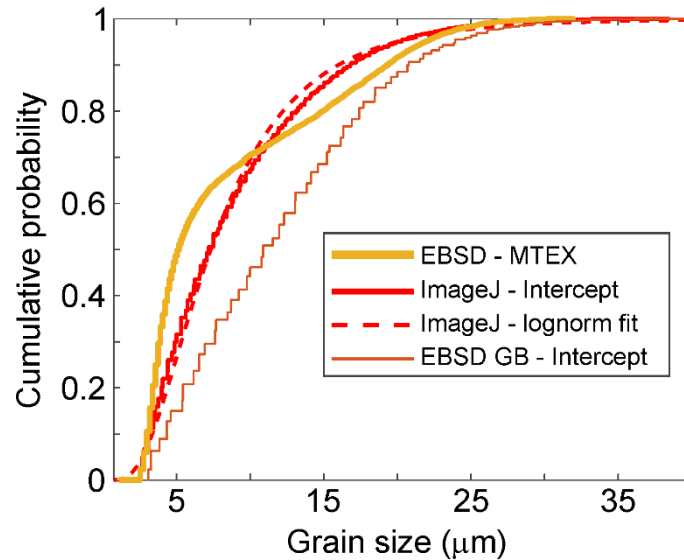

Figure 5.4 — Comparison of cumulative distribution function for the grain size distributions obtained through analysis of EBSD data via MTEX and intercept methods on the ImageJ processed image and on the grain boundaries skeleton obtained via MTEX from EBSD data.

As can be noticed in Figure 5.5, the difference is partly due to inaccuracies in drawing the grain boundaries during the image processing; boundaries that were not detected in the relative EBSD map are present in the micrograph, thus contributing to increasing the fraction of smaller particles. However, when the same method is applied to the binary image obtained by the MTEX analysis [Figure 5.3-(MTEX)-(a,b)] the distribution shape remains significantly different and closer to a log-normal distribution, see Figure 5.4. In order to obtain a meaningful representation of the grain size distribution for bimodal materials with the linear intercept method the ASTM E1181 advises to estimate the area fractions occupied by the distinct grain sizes and then determine the average sizes of the two distinct populations of grain sizes using the intercept method. For a sample like the one analysed here it is difficult to draw a clear distinction between different areas and the method described results laborious and time-consuming.
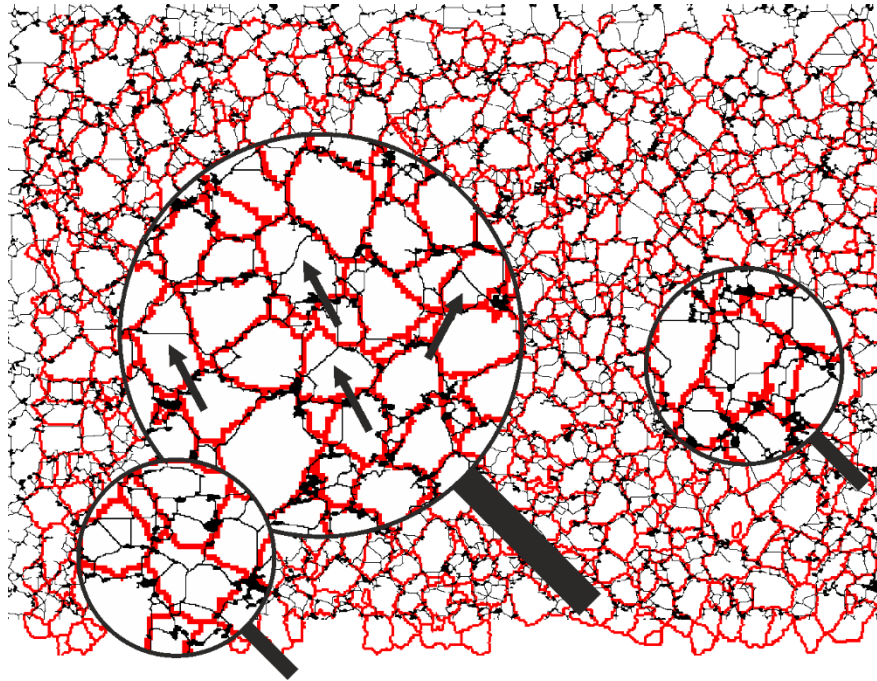
Figure 5.5 — Grain boundaries drawn using MTEX calculation on EBSD data, in red, and from modified forescattered image after binarising and applying a watershed algorithm, in black. As shown in the magnified regions, the watershed method oversegmented some of the grains. The areas in the "lenses" are magnified 2x.

It is worth mentioning that a correction factor such as that proposed by Mendelson [182], often used to relate the intercept length to grain size, is introduced to account for a more realistic grain morphology and would in this case shift all the values towards larger numbers, yet would not modify the shape of distribution.

The aspect ratio was measured as the ratio between the long and the short axis of the two principal components of a grain, therefore equiaxial and elongated grains would have aspect ratio equal to one and larger than one respectively.

The analysis found that aspect ratio distributions of both coarse and fine grades show a trend to form elongated grains. Interestingly, both samples have the mode of their aspect ratio centred at 1.3, with only 1/3 of the grains having a smaller aspect ratio, cf. Figure 5.1-(c) and Figure 5.2-(c). Figure 5.1-(e) and Figure 5.2-(e) are maps in which arrows are drawn at each grain centroid with the direction equal to that of long axis and magnitude proportional to the aspect ratio, with the arrow head pointing arbitrarily in one of the two possible direction at 180° from one other. This

map offers a visual aid to assess whether there exist areas in which elongated grains tend to form or to follow specific patterns.

It is important to remember here that the PCD G4 sample was a small section cut from the surface and unfortunately no information is available on where the sample axes point with respect to the former cutter axes. As for PCD G30, instead, the x-axis is parallel to the top surface of the cutter and the y-axis parallel to its cylindrical axis, i.e. parallel to the loading axis of the anvils in the belt press.

The arrow map for G4, which appears uniform as shown in the "magnifying lens", shows no particular identifiable patterns, i.e. both directions and magnitude seem randomly distributed.

On the other hand, G30 presents small clusters of 4-5 smaller grains surrounded by larger grains that align in the same direction. These grains, which were likely formed during the comminution phase under cold compaction, appear to often align along grain boundaries of the larger grains and at times follow their curvature. In addition, their direction tends to lie closer to the cutter cylindrical axis, or else rarely perpendicular to it.

The general distribution of the long axes angle distribution is analysed using the rose diagram in Figure 5.1-(f) and Figure 5.2-(f) that plots the angle of the long axis of each grain with respect to the x-axis of the sample, the radii of the bars represent the counts. The rose diagram for PCD G30, analogously to the grains size distribution, is plot using data from the three maps combined and confirms that the long axes tend to lie at ~90° with respect to the map x-axis. Although the standard deviation of 43° is large, it is still interesting to observe that there is a depletion of grains with the long axis parallel to the WC substrate; the distribution is fitted well with a normal distribution. One possible explanation for this is given by the infiltration of molten cobalt from the WC-Co substrate driven by the high gradient of pressure that forms between the solid WC-Co substrate and the interstitial voids between the diamond particles in the first stages of sintering. The liquid therefore flows from the bottom of the PCD layer towards the top and could be responsible for a realignment of the particles with higher aspect ratio in the direction of the flow.

The distribution for PCD G4 is wider than PCD G30, but the plot shows that although the distribution is very close to normal a weak asymmetry stemming from a higher population at the smaller angle, 0-60° is present. Further investigation would be needed to assess if this direction coincides with a particular direction on the cutter top surface, radial for instance.

5.2 Texture statistical analysis

In addition to grain size and aspect ratio, EBSD data were exploited to investigate the texture from both a macrotexture, i.e. a statistical evaluation of the population of individual orientations across the sample, and a microtexture perspective whereby individual orientations can be related to microstructure.

IPF maps in the sample z direction of both G4 and G30 PCDs do not show regions of similarly coloured grains, therefore showing no apparent texture. However, to verify this assumption a quantitative evaluation of the texture was performed by means of the probability density function of orientations in a specified orientation space (here defined through the Euler angles), better known as orientation distribution function (ODF). The ODF expresses the probability that a sampled point is oriented within a defined orientation range, i.e. an angular spread, and essentially defines the ratio of volume of grains that are oriented within this range over the total volume sampled; it follows that ODF is equal to 1 for random orientations. In this work the halfwidth, that is half of the angular spread for the ODF calculation, was set at 5°. The ODFs in Figure 5.6 and Figure 5.7 show a very weak texture with a maximum intensity of only ~1.5 and ~1.4 for PCD G4 and G30 respectively.
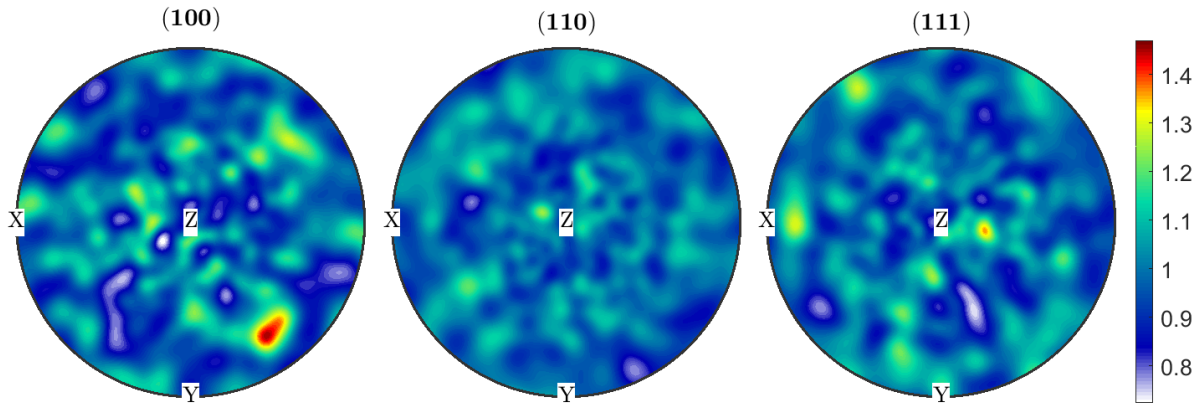
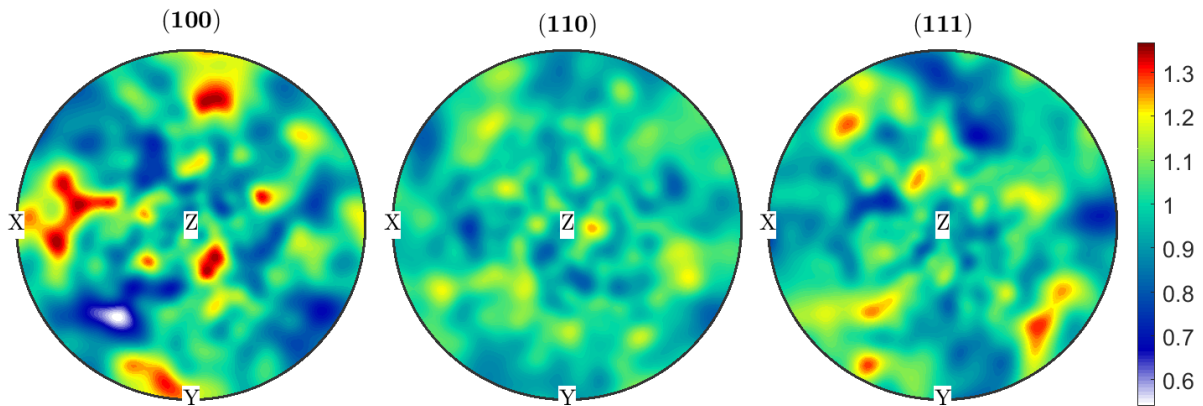**Figure 5.6 — ODF for the (100), (110) and (111) crystal orientations in PCD G4**

Figure 5.7 — ODF for the (100), (110) and (111) crystal orientations in PCD G30

5.3 Stress analysis

A preliminary study was conducted with the dual objective of evaluating whether the EBSD pattern quality of diamond was sufficient to conduct high angular resolution analysis through the XEBSD software (see paragraph 3.4.2) and evaluating the variation of stresses across large grains. The investigation on the residual stresses of type III continued by evaluating the stresses present in PCDs on CVD grown diamond and on regular WC substrates.

5.3.1 Preliminary study on CVD diamond

A preliminary study was carried out on an as-received sample consisting of the cross section of a stack of WC, CVD-grown diamond and PCD.
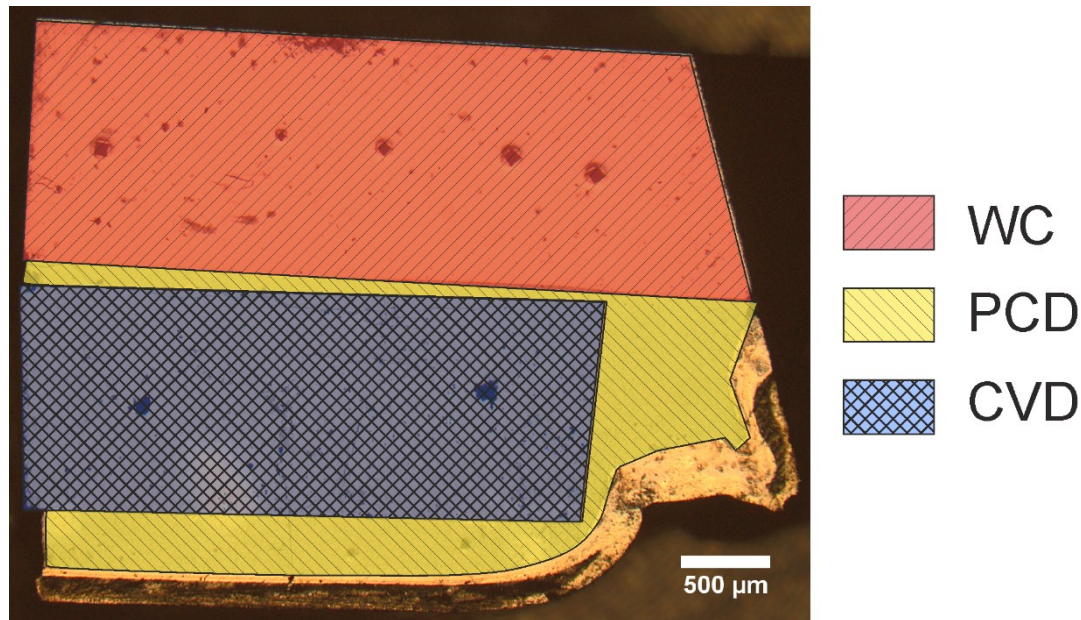

Figure 5.8 — Section of a composite sample containing both regions of sintered PCD and CVD-grown diamond on a WC substrate.

The CVD-grown diamond is composed of columnar grains up to 50 µm wide and 150 µm long. Given their large relative size, these grains were chosen as a good candidate to assess the ability of measuring the local stress gradient of a single diamond grain via HR-EBSD. The map was collected on a region of 302×226 µm^2 with a 1 µm pixels size, 800×600 pixel^2 EBSP resolution and 180 ms exposure time, thus amounting to ~3 h 30 m total scan time.
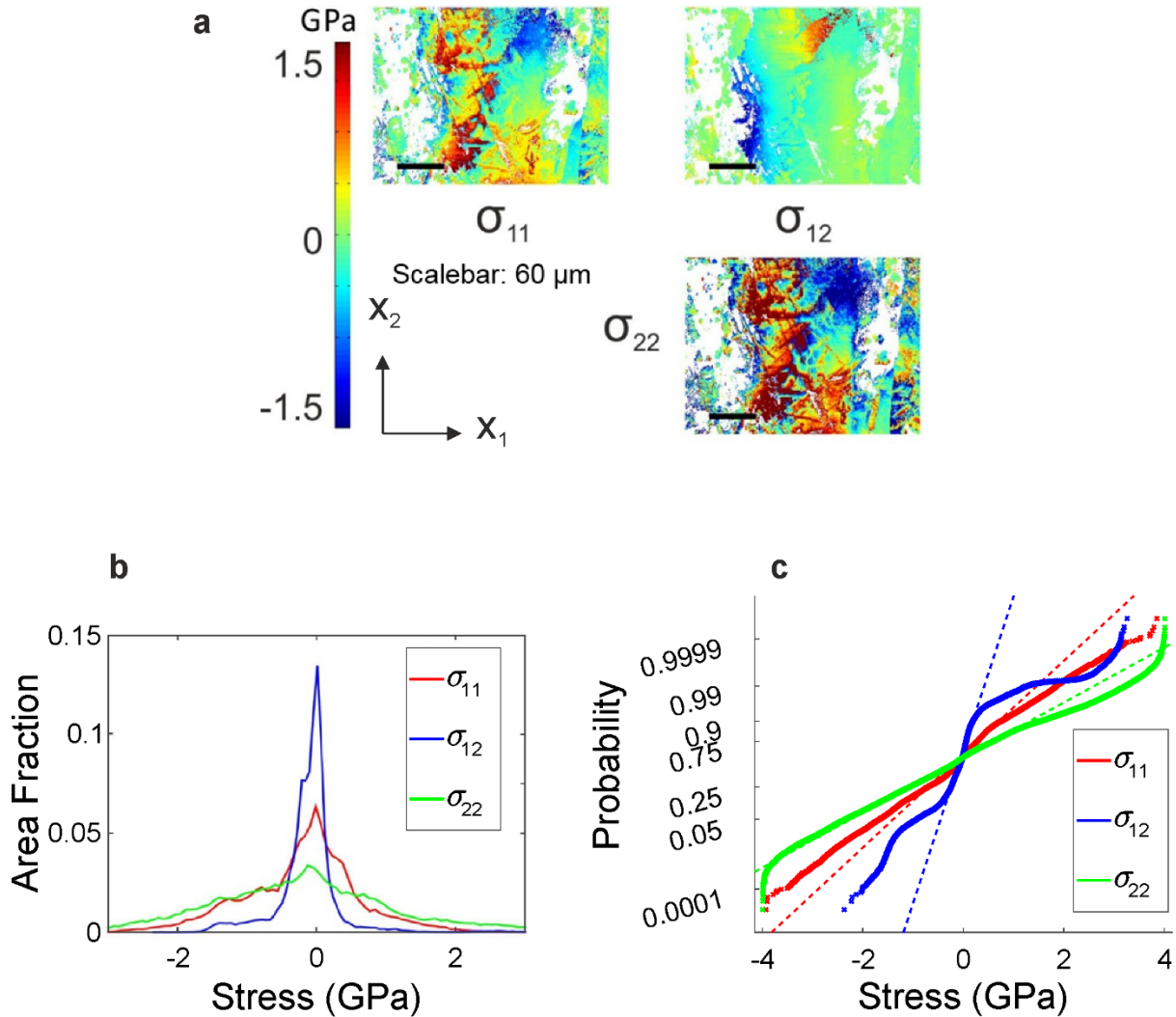
Figure 5.9 — Stress state in single grain on CVD sample (cf.Figure 5.8). (a) Map of in-plane residual stresses, two normal and one shear, measured across the grain (b) histograms of stress across the grain. (c) normal probability plots of the stress distributions. The two normal stresses follow an almost straight line up to high stresses, indicating a normal distribution. The shear stresses follow the normal distribution for a shorter range of stresses and show that some locations near the grain boundaries have exceptionally higher shear stresses with respect to the average.

The in-plane stress map on the CVD single grain shown in Figure 5.9-(a) reveals obvious stress variations across the grains of up to 2 GPa. The data were statistically evaluated by plotting the histogram of each of the three in-plane stress components, that are σ_{11}, i.e. the normal stress in direction parallel to the sample x-axis, σ_{22}, i.e. the normal stress in direction parallel to the sample y-axis, and σ_{12}, i.e. the in-plane shear stress. These histograms, in Figure 5.9-(b), provide a picture of how each of the three stresses is distributed and highlight possible differences between them. These histograms are also later used to facilitate comparisons of stress distributions among different regions of the same sample and also among different samples. In the case of this single

grain, for instance, the plane stresses in the two normal directions σ_{11} and σ_{22} have a wide and close to normal distribution. The σ_{12} component, on the other hand, has a significantly narrower variation across the grain. To further evaluate the type of distributions, the data collected were sorted on normal probability plots, where the frequency data of the stress values are arranged on the y-axis of a plot so that a normal distribution appears as a straight line. These plots allow a quick and graphic assessment of whether the data analysed follow a normal distribution and provide a clear comparison of the distribution width through their slope, with steeper lines related to narrower distributions and vice versa. From the normal probability plots [Figure 5.9-(b)] it is evident that the residual stress distributions follow the straight line of normal distribution only for small stress variations around the mean value, which is always brought to zero within each grain. The departure from normal distribution at the tails, here evident especially for the shear stresses, is indicative of the presence of localised higher stress gradients in some regions of the grain than it would occur in a normal distribution.

The standard deviation of these distributions is used to describe the range of stress state found within each grain with a single representative value. Standard deviations of up to 1.3 GPa were found in the CVD grain, indicative of the high stress gradients that this material is capable of withholding under elastic conditions. A summary of these values is presented in Table 5.1.

Table 5.1 — Standard deviations of residual stresses measured in individual grain across the entire map.

	CVD	PCD G30 on CVD — Map 1	PCD G30 on CVD — Map 2	PCD G4-Map 1	PCD G4-Map 2	PCD G4/G30-Map 1	PCD G4/G30-Map 2
σ_{11} **(GPa)**	0.8	0.7	0.3	0.6	0.3	0.3	0.2
σ_{12} **(GPa)**	0.4	0.4	0.3	0.4	0.2	0.1	0.1
σ_{22} **(GPa)**	1.3	1.1	0.6	0.8	0.5	0.3	0.4

5.3.2 Residual stresses in PCD

A similar analysis was repeated on samples with multiple grains. First, it was performed on the same sample used for the preliminary study but on the sintered polycrystalline region this time, mainly composed of coarse grains, and then on a sample sintered from G4 powders.

Two maps for each sample were analysed: for PCD on CVD two maps of 100×75 μm^2 and 144×108 μm^2 with an EBSP resolution of 1600×1200 $pixel^2$ and 850 ms and 400 ms respectively of exposure time; for PCD G4 two maps of 30×22 μm, 800×600 $pixel^2$ EBSP resolution and 280 ms of exposure time.

All regions examined presented average stress variations across the grains of not less than 200 MPa in shear and 300 MPa in normal directions, with upper bounds of 1000 and 800 MPa in σ_{22} for the PCD on CVD and PCD G4 samples respectively.

Interestingly, within the same sample one region has significantly larger standard deviations than the other region in both PCD on CVD and PCD G4.

These maps show narrower distribution than the map for the single CVD grain, with standard deviations in the range of 300 to 500 MPa. The longer tails in some of these maps indicate that much higher stress gradients than average are present in a few grains.
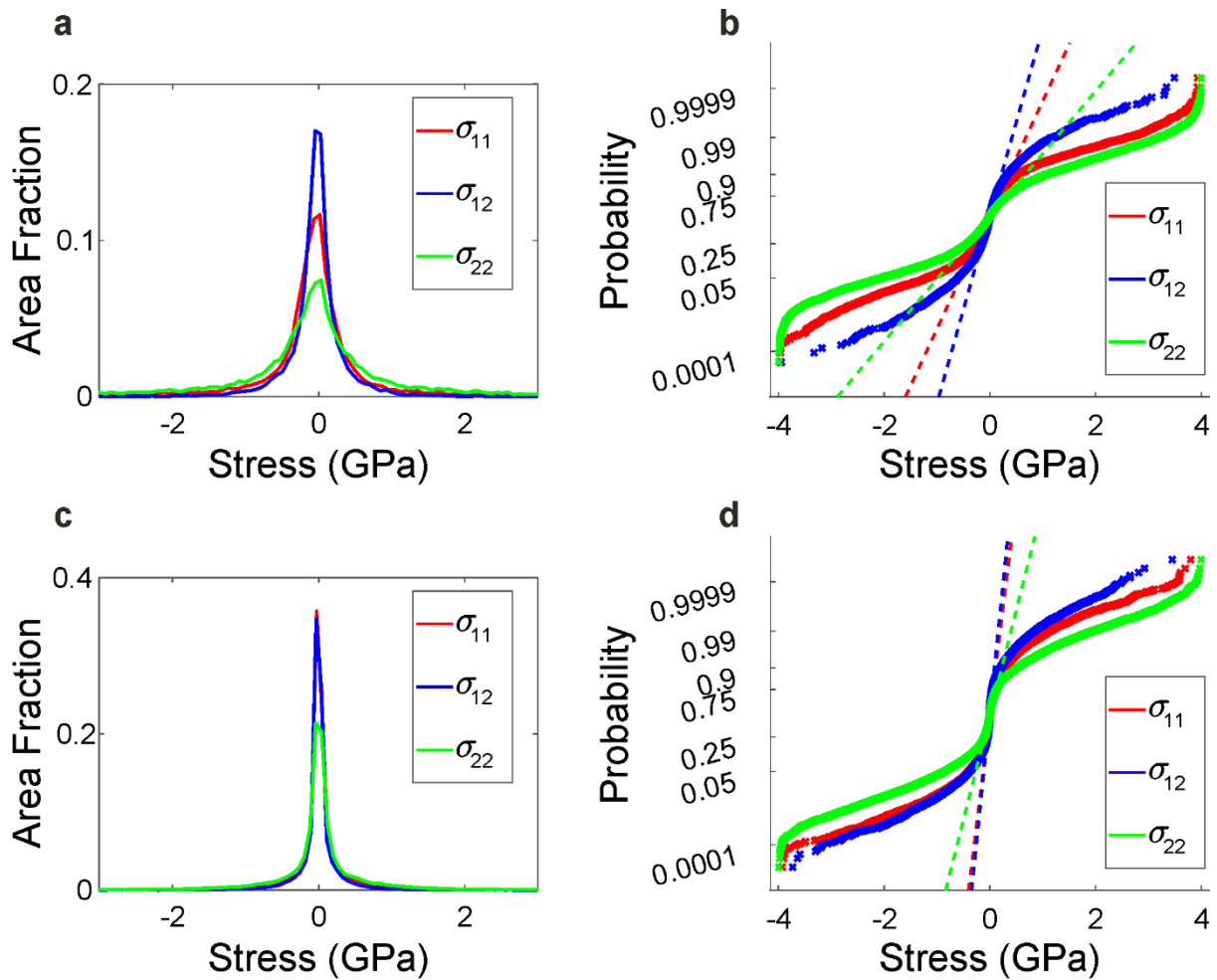
Figure 5.10 — Stress state in PCD on CVD sample (cf.Figure 5.8). (a) and (c) histograms of stress distributions measured across the map in two different regions of the sample. (b) and (d) normal probability plots of the stress distributions.

Figure 5.11 — Stress state in PCD G4. (a) and (c) histograms of stress distributions measured across the map in two different regions of the sample. (b) and (d) normal probability plots of the stress distributions
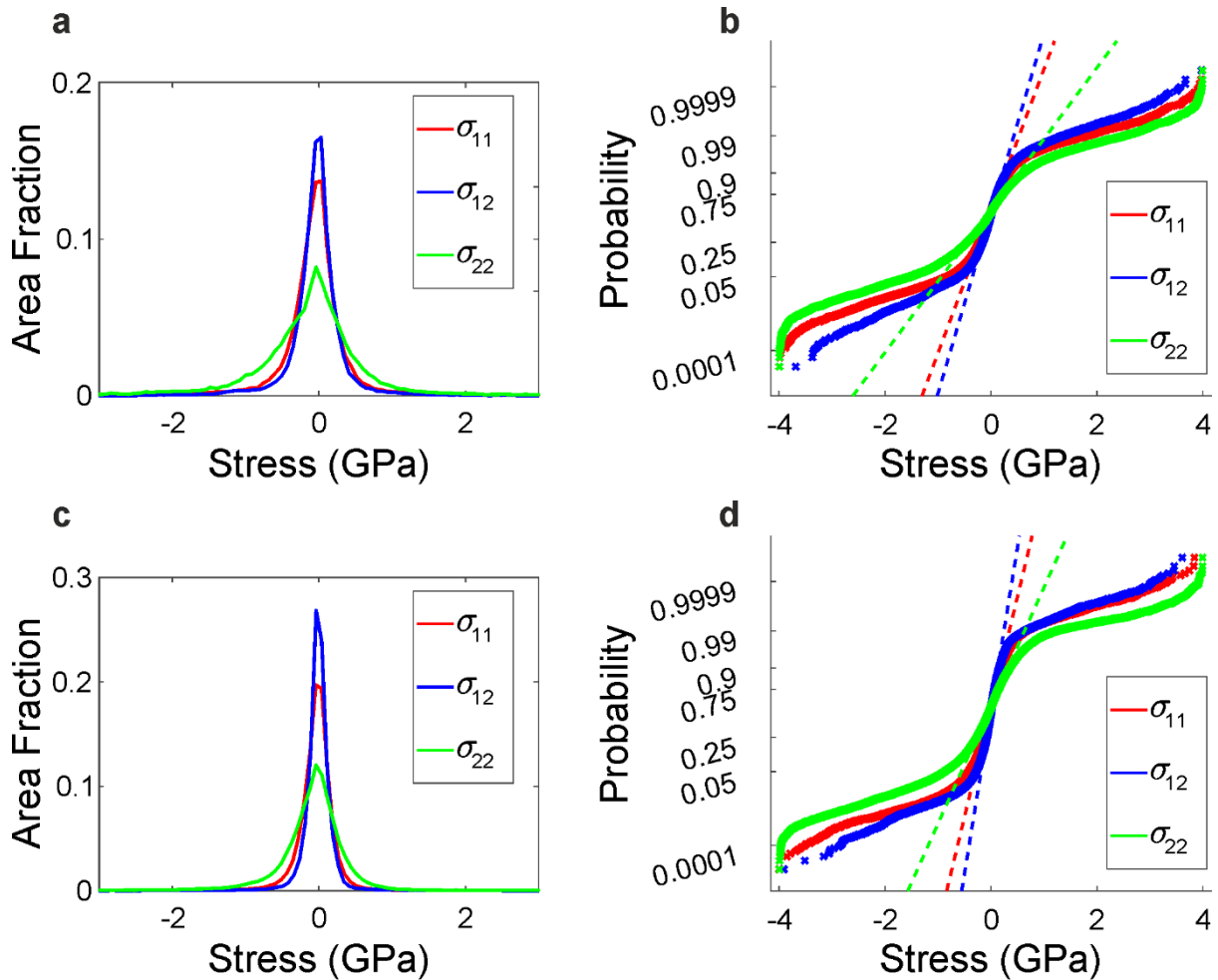
It can be noticed from both the histograms and the standard deviations it appears that the distribution of σ_{22} is constantly wider than σ_{11} in all maps. To verify whether this was related to a real difference in the sample stress state or an artefact from the analysis, the two maps on PCD G4 were collected with a relative sample rotation difference of 90°. Since the difference between the σ_{22} and σ_{11} persisted, it was concluded that this is indeed an artefact due to the quality of the EBSD patterns. To explain the difference observed in the two directions it must be noticed that, when the sample is strained, the shifts imparted to the zone axes are not of the same magnitude across the pattern; the shifts are smaller closer to the pattern centre and larger away from it. It follows that errors in evaluating the shifts in regions close to the patterns centre lead to larger errors in the strain/stress evaluation. The pattern centre is typically, and also in particular in the

case of the pattern collected for this work, located close to the half-width of the pattern frame in the x-direction and at about one-fourth from the top in the y-direction. It can be noticed from Figure 3.3 that the bottom half portion of the patterns has a higher noise level. As a consequence, it is possible to access zone axis shifts further away from the pattern centre in the pattern x-direction than in the y-direction. In other terms, the full dispersion of zone axes, i.e. the band intersections, across all angles in the EBSD pattern is not accessible. This results in a variable shift precision that brings uncertainties of different magnitudes on the different terms of the strain tensor. This can also be seen by the presence of out-of-plane shear stresses, as shown in Figure 5.12. Since it is assumed that the stress normal to the surface is absent at equilibrium and is imposed equal to zero, as discussed in paragraph 3.4.2, the out-of-plane shear stresses are expected to be equal zero too. However, noise in the displacement gradient tensor, i.e. that obtained measuring the zone axis shifts between reference and test patterns, causes an erroneous separation of symmetric and anti-symmetric components and the creation of artificial shear components in the final tensor (with standard deviations of up to 200 MPa). It is important to bear in mind that this is solely related to specific preparation of this sample and quality of the EBSD patterns.
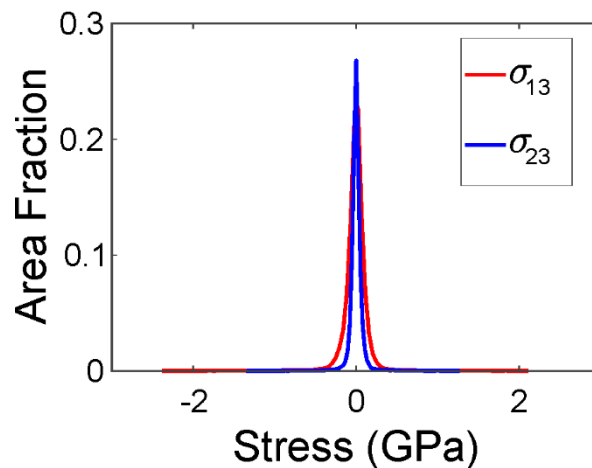

Figure 5.12 — Out-of-plane shear stresses for PCD G4 Map 2. Histograms of stress distributions for the out-of-plane shear stresses are shown. The presence of non-zero out-of-plane shear stresses is a consequence of noise in the displacement gradient tensor, in turn arising from poor pattern quality.

This study has revealed that the processing of PCD is not only responsible for generating large type I and type II stresses, as found in the literature, but also for large gradients of type III residual stresses. The presence of these stress gradients can be ultimately seen as a disruption of the individual grain homogeneity, in particular the response to fracture of this polycrystalline material does not only modify as we move across the sample in a discrete fashion from grain to grain (according to size, shape and orientation), presence of defects or interfaces, but is likely affected by such stress patterns.

5.4 Relating microstructure and residual stresses to fracture path

In chapter 1 it has been discussed how in brittle polycrystalline material the fracture path is affected, besides the far field stress, by the crystallographic orientations and local stresses ahead of the crack tip. The path followed by the crack is, therefore, of great importance to understand the conditions that triggered the failure and compare the change of fracture behaviour due to different processing. Being able to control the fracture path can yield an increase in the life of component or increase its toughness. In chapter 2 it has also been discussed how the fracture in PCDs has been observed in both transgranular and intergranular modes, yet little is known about what influences the change in behaviour.

Combining the investigation techniques presented in the previous chapter with a controlled fracture offers the possibility to gain a better understanding of the relation between microstructure, texture and type III residual stresses on fracture behaviour in PCDs. The idea was to first map the residual stress gradients present within diamond grains in a selected area and then initiate a crack within the same region to correlate crack path to pre-existing type III stress state.

A preliminary investigation was performed on PCD on CVD indenting the sample with a Vicker indenter, shown in fig Figure 5.13. The crack formed by the indent followed a straight direction, yet with a jagged path. An EBSD map taken around the crack revealed that the crack tended to

follow the {111} cleavage when growing across a grain, although it followed the boundaries for a short distance, as shown in Figure 5.13.
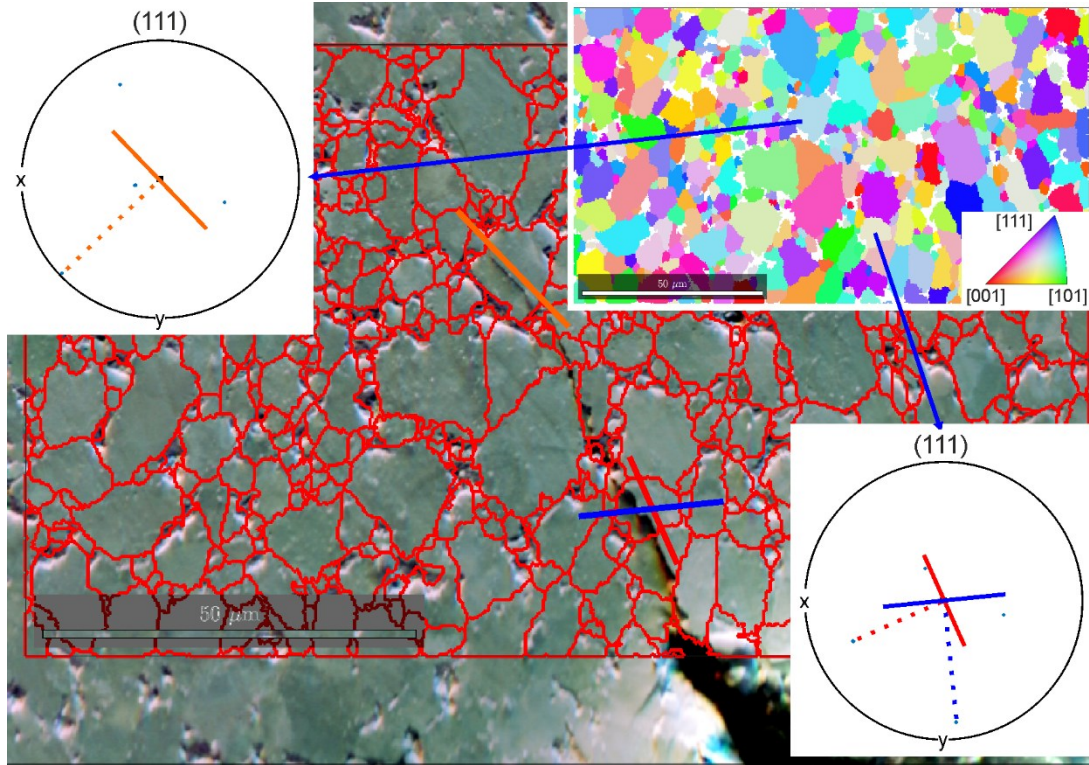

Figure 5.13 — Vickers indentation on PCD. The indentation was able to form a crack of ~ 50 µm. An EBSD map collected after the indentation reveals that the crack follows the {111} cleavage planes preferentially, however the central portion grows along the grain boundaries.

Following this experiment, microindentation was chosen as a suitable technique to initiate cracks that would grow across a few grains. These tests were performed using a Micro Materials Ltd. instrument equipped with an optical microscope in order to indent selected regions of the sample with sufficient location accuracy. Although indentation generally is relatively easy to execute, given the extreme hardness of the sample, comparable to that of any diamond indenter, this is an all but trivial task to execute successfully on PCDs; Figure 1.8 shows a typical example of indenter failure in such a test. Consequently, previously damaged cube corner and Berkovich tips were used for this type of test. Given its flat profile, the Berkovich indenter has the advantage of being less subject to gross damage but in turn the pressure it can apply before failure is significantly smaller when compared to the cube corner. On the other hand, in case of gross damage following an

indentation on diamond the cube corner might flatten, thus offsetting the original benefit of the sharper profile. Therefore, the indenter had to be selected upon empirical observation of the indents. Indentations were first performed on different fine and coarse grained PCDs to select the best indenter geometry and record the load required to form cracks that would propagate at least more than one grain. Although the indents did not present the typical well defined geometry, cracks were observed forming at the corners for both Berkovich and cube corner indentations. In the first, however, the indents were shallow, barely visible at low magnifications, and the crack formed at 20 N, i.e. the maximum load applicable by the microindenter employed, were only ~5 µm long in coarse grains. In the case of cube corner indentations, the geometry of the indent suggests that the tip was severely damaged, nonetheless cracks of ~15 µm were observed Figure 5.14. In addition to confirm the feasibility of the experiment, these indentations provided indications that the crack would not simply follow a straight line across the grains in all cases. The crack originating at the bottom left and right corners of the cube corner indent in PCD G30 is seen growing in the general radial direction while changing angle abruptly several times.
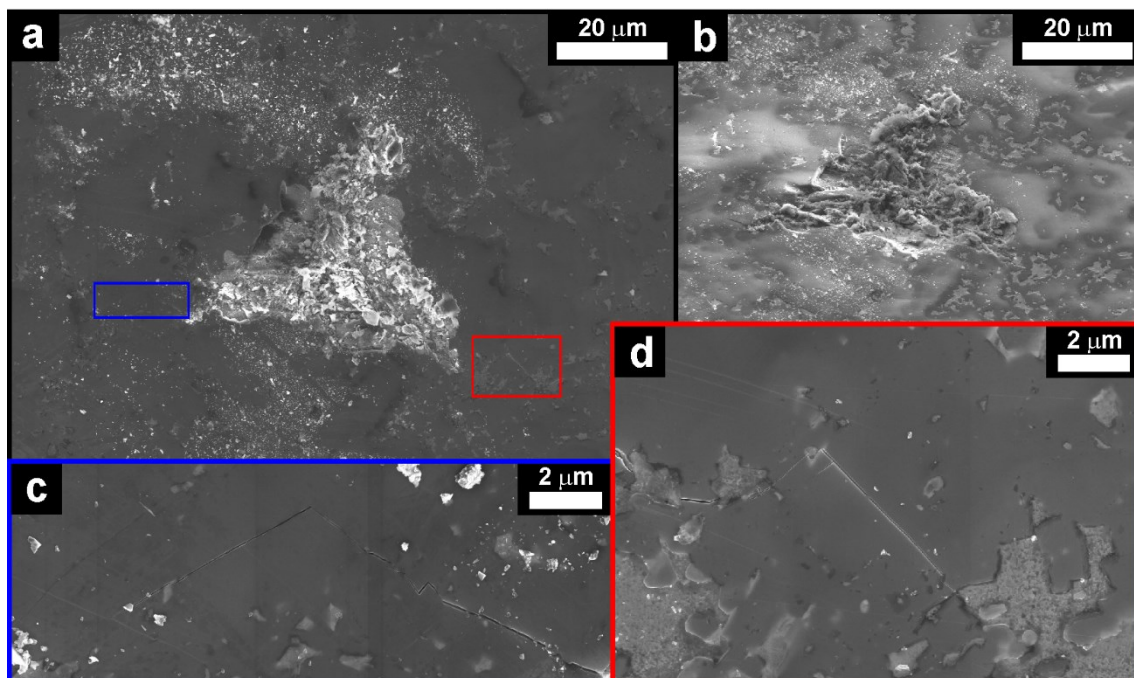
Figure 5.14 — Cube corner indent and associated cracking in PCD G30. Overview of the indent from top (a) and tilted view (b). The impression does not present the typical geometry of cube corner indentation due to failure of the indenter, however cracking ensued from the bottom left and right corner. (c) and (d) show close-ups on the crack extending from the indent, showing several deflections and interaction with the cobalt pools during its growth.

The study of the effect of residual stresses on the crack path was finally carried out on PCD G4/30 TC, a sample chosen for its good surface finishing and the banded macrostructure, i.e. with bands of fine grains (lighter bands in Figure 5.15 and Figure 5.16) alternated regularly to bands of coarse (darker bands).

A montage of SEM images taken on the top and cross section surface of the sample, together with a schematic of its location on the cutter is provided in Figure 5.15.
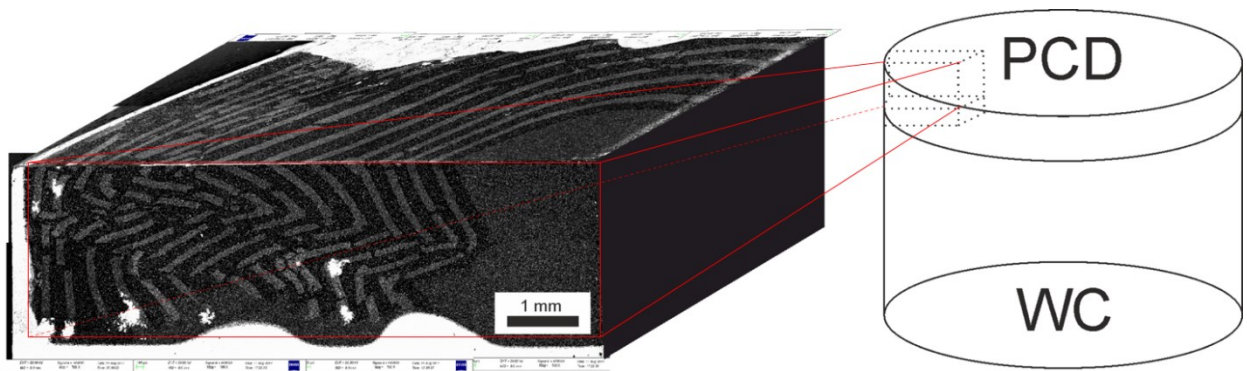
Figure 5.15 — Montage of SEM micrographs taken from the top and cross section surface of the tape casted PCD sample extracted by the cutter as shown in the schematic

Microstructure and texture of coarse grains the sample were analysed on 4 EBSD maps of 1000×750 μm^2 taken in different areas of the sample, as indicated in Figure 5.16, with a 1 μm pixel size and filtering out grains smaller than 20 pixels. Two additional EBSD maps of $\sim600\times100$ μm^2 with a 0.4 μm pixel size were collected in area 2 and area 3 to analyse the finer grains.

Figure 5.16 — Montage of SEM images showing the location of the 4 EBSD maps collected for texture and microstructural analysis

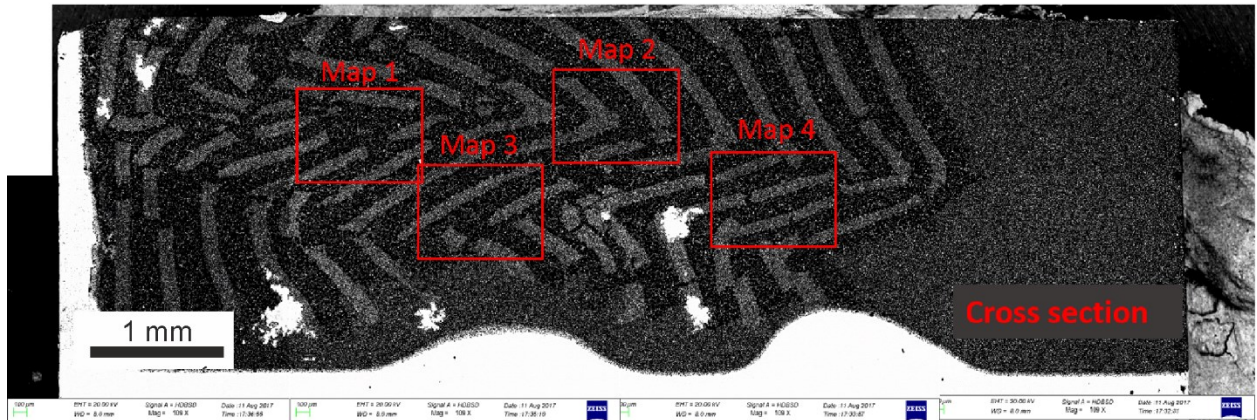The texture was analysed first by combining all data from the 4 maps in a single data set to obtain information on the macrotexture. The result shows a very weak texture and agrees well with similar analyses presented earlier in this chapter on PCD G4 and G30.

However, given the peculiar structure of the sample, microtexture analysis was also performed after isolating the grains contained in a specific band. This analysis revealed that a stronger texture, although in absolute terms still weak, forms in individual bands. In particular there seems to be a preferential alignment of the (100) with the band structure walls itself. Caution must be taken when comparing the texture analysed from a smaller number of grains to that of a larger data set as the former can bring uncertainties on statistical accuracy; it is noted however that ~500 grains is a sufficient number of single orientations for statistical accuracy as discussed at the start of this chapter.
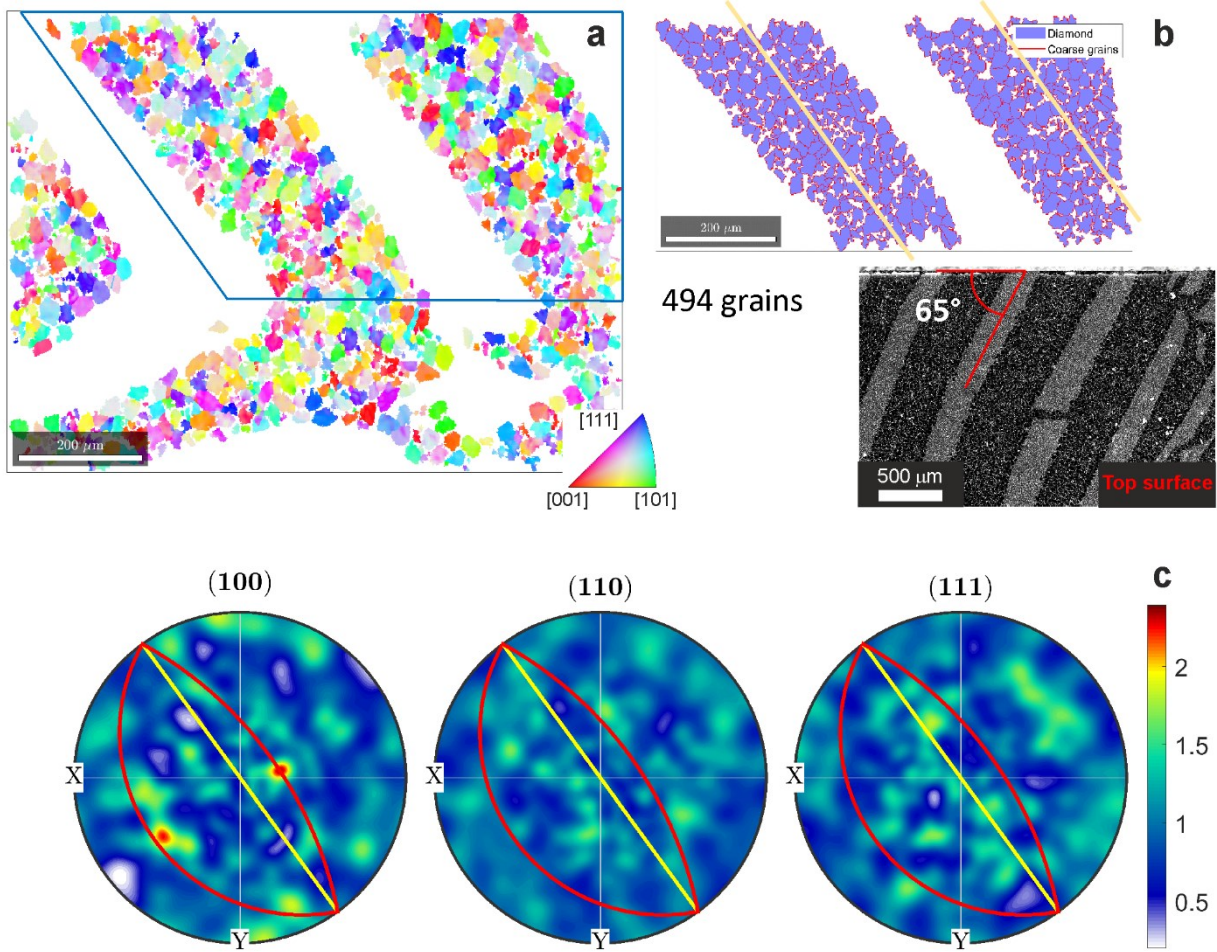
Figure 5.17 — Microtexture analysis on the coarse grained bands in the tape casted PCD. (a) IPFz map detailing the region where data were extracted to investigate the microtexture. (b) angle of the band from the cross section, i.e. as viewed from the EBSD detector, and from the top surface, that is corresponding to the angle of the band below the surface. (c) The band spatial orientation within the sample frame is compared to the crystal orientations calculated by the ODF.

Two HR-EBSD maps of 150×113 μm² with 0.25 μm pixel size, 800×600 pixel² EBSP resolution and 200 ms exposure time were taken in two different regions of the sample characterised by a different distribution of the microstructure: one comprised between a large band of fine grains at the top and of coarse grains at the bottom (named PCD G4/30 TC area 1), the other on an area presenting six coarse grains encompassed on top and bottom by two patches of finer grains (PCD G4/30 TC area 2). The two maps were analysed through XEBSD and the stress found are presented in Figure 5.18 and Figure 5.19.
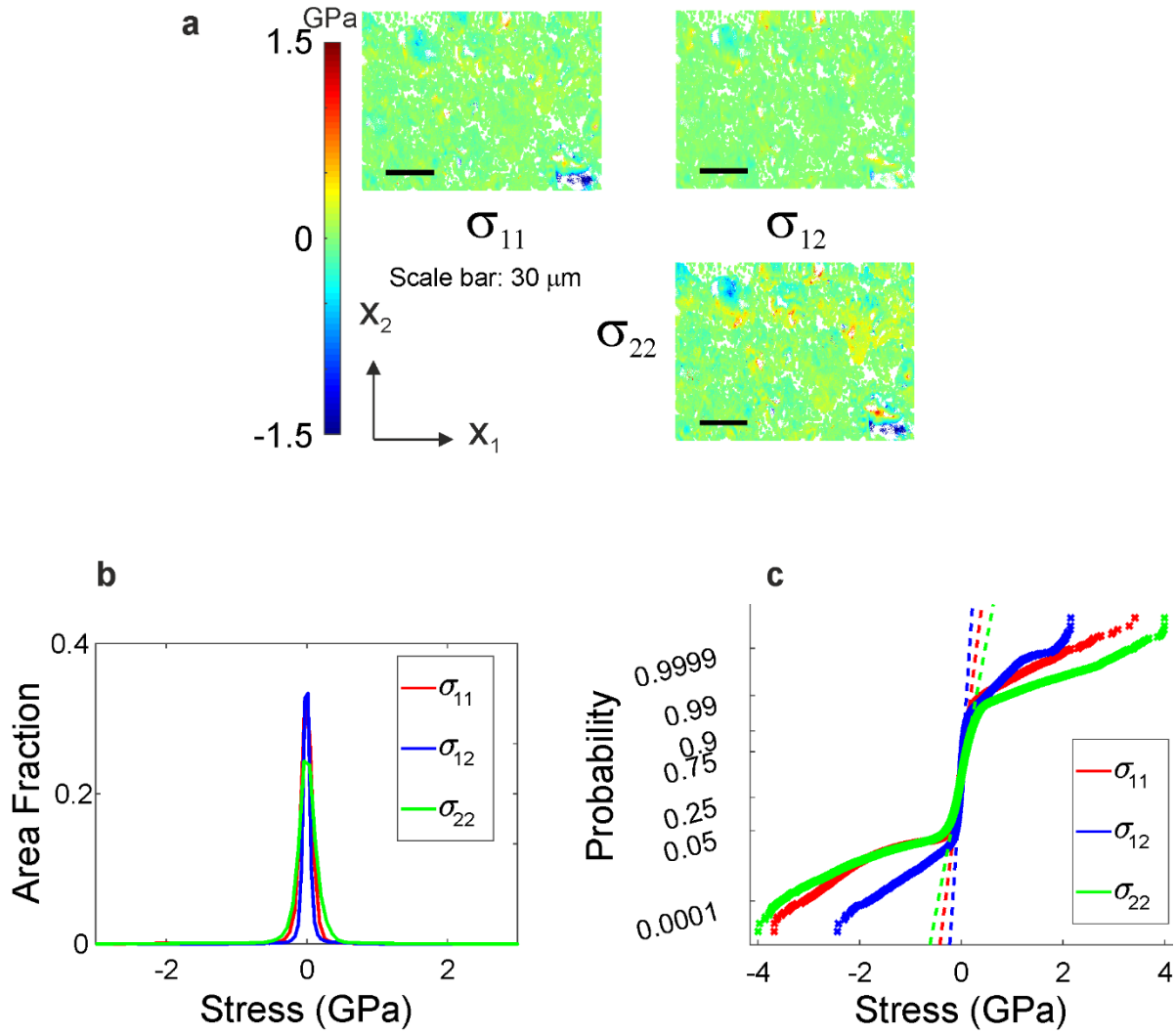
Figure 5.18 — Stress state in PCD G4/30 TC area 1. (a) Map of in-plane residual stresses, two normal and one shear, measured across the map (b) histograms of stress across the map. (c) normal probability plots of the stress distributions.
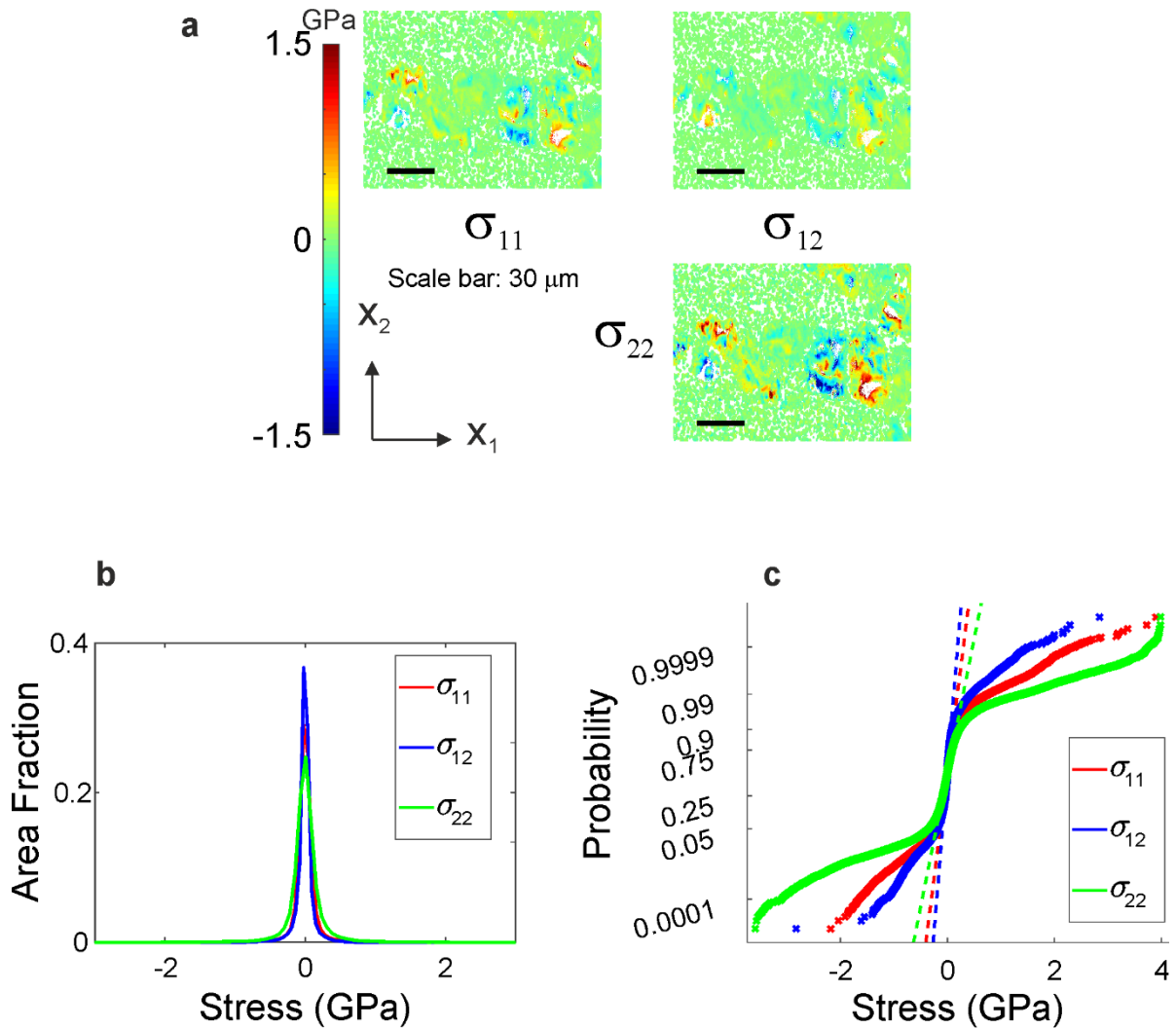
Figure 5.19 — Stress state in PCD G4/30 TC area 2. (a) Map of in-plane residual stresses, two normal and one shear, measured across the map (b) histograms of stress across the map. (c) normal probability plots of the stress distributions.

It is apparent from the stress maps [Figure 5.19-(a)] that in area 2 the finer grains have small or absent stress gradients while the coarser grain have wide stress distributions varying in sign within the grains. However, the coarse grains in area 1 are subject to weaker residual stresses, with only those towards the top portion of the map showing relatively higher gradients [Figure 5.18-(a)]. This is somewhat expected given the differences in the surrounding microstructure for both maps. Area 1 is a homogenous region of coarse grains at the top of which runs a band of finer grains, likely containing a higher volume of cobalt, while at the bottom there are more coarse grains. Area 2 was instead selected because presented a rare region within the sample in which coarse and fine grain patches alternated in a rather small volume. Given that the composite CTE for PCD is given

by the relative volume fractions of the two phases [5] and that regions with finer grains are usually surrounded by a higher volume fraction of cobalt than coarser grains [3,4], strong local variations of grain sizes increase the likelihood of strong variations of the CTE. The different volume fraction of cobalt between the different bands in this sample it is also evident by the different contrast in the SEM pictures, i.e. the bands of fine grains appear brighter than coarse grains indicating a higher average atomic number, compatible with a higher volume of cobalt.

Measurement performed in this work from backscatter images of PCD G30 and G4 indicated that cobalt content can vary from 7-10 vol% in the former to 20-22 vol% in the latter.

Subsequently, in order to assess the effect of residual stresses on the crack path indentations were performed so that one of the indenter corner would land a few microns within or just out of the frame of the maps. Three indents, two on the right and one on the left, were performed next to area 1, still none of the three indent formed significant cracks growing in the area of interest. Similarly, three indents were performed next to area 2, however in this case the third indent was accompanied by a ~35 µm long crack, see Figure 5.20-(a).

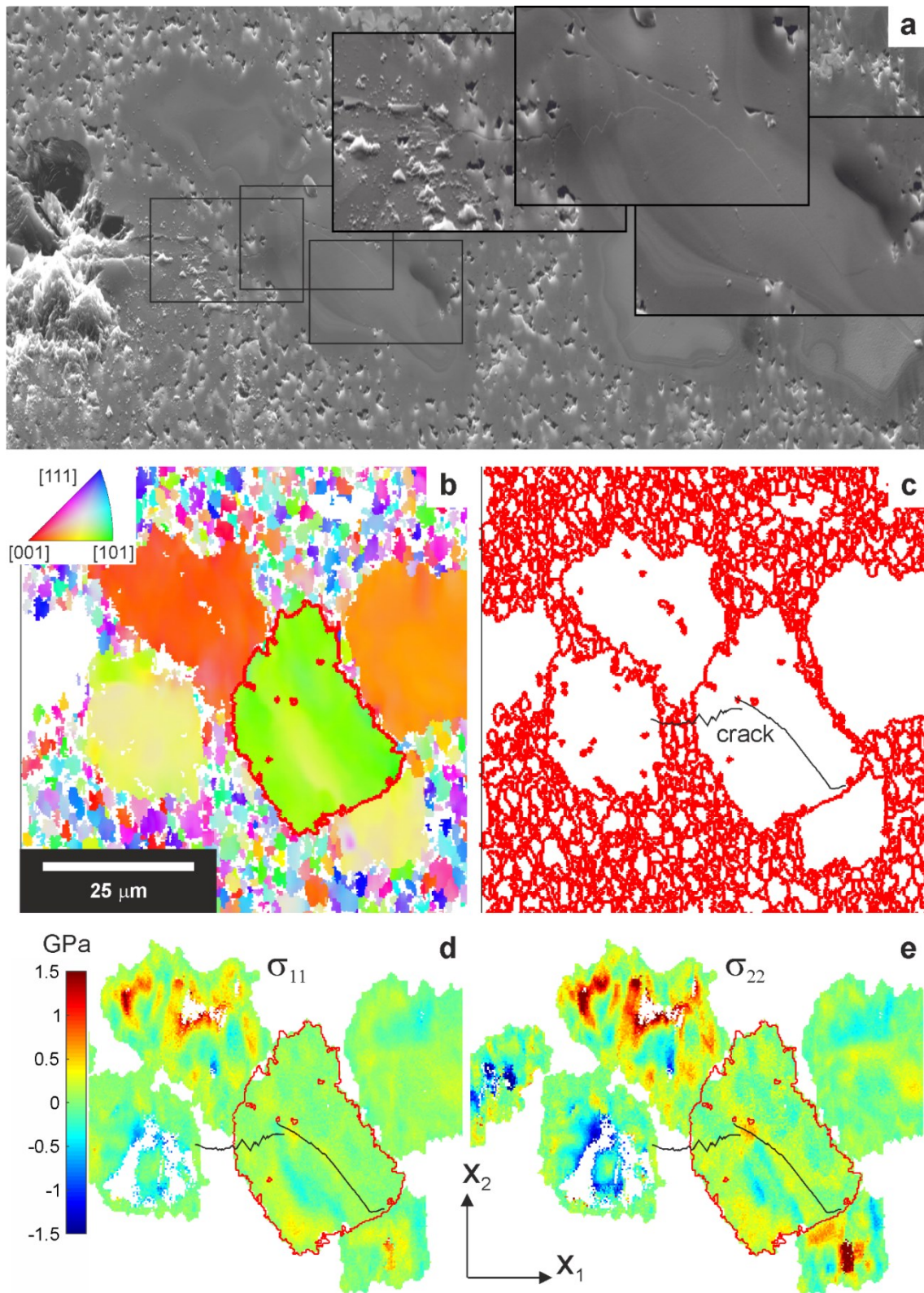**Figure 5.20 — Crack path superimposition to pre-existing residual stress state.** (a) SEM micrograph of crack ensued from indentation. (b) Detail of IPFz map from EBSD data collected before the indentation. (c) Schematic of crack path in relation to grain boundaries, in red, as calculated using EBSD data shown in (b). Detail of crack path superimposed to residual stress map for σ_{11} (d) and σ_{22} (e).

Several different behaviours can be identified along the crack path. In the first section the crack follows the radial direction of the indentation on a curved line moving along the grain boundaries of small grains until it encounters a large grain, see Figure 5.20-(a,b) and Figure 5.21-(1). As it enters this coarse grain the crack keeps advancing in the general radial direction, however here it starts deflecting several times along straight lines all lying in two different directions at the same angle between them; analysis of the grain texture reveals that the crack is following the {111} cleavage planes, see Figure 5.21-(2). Suddenly, the crack path straightens again; here the crack has entered a region where σ_{22} tensile stresses and σ_{11} compressive stresses both of 100 MPa are perpendicular and parallel, respectively, to the crack direction [compare Figure 5.20-(d) and Figure 5.21-(3)]. Given the very low or absent shear stresses in this region, the maximum principal stresses essentially correspond to the normal stresses, as shown in Figure 5.21-(3). However, a few microns ahead a spot of the σ_{11} stresses become tensile, in between the crack jumps (Figure 5.20-d and Figure 5.21-4) and then changes direction abruptly. A measurement of the average stresses on a square of 10×10 μm^2 around the location where the crack extends again with a new angle returns a value of 200 MPa in σ_{11} direction, 500 MPa in σ_{22} and -100 MPa in σ_{12}. These values result in a biaxial stress state in which the two maximum principal stresses are both tensile and nearly perpendicular and parallel to the crack direction respectively, as shown in Figure 5.21-(5). From this point the crack grows perpendicular to the maximum tensile stress and avoids the regions above and below where both the normal stresses turn compressive, as can be noticed in the close up of the stresses in Figure 5.21-(4,5).

As the crack extends in this region it also curves gradually until it finally aligns with the {111} again, Figure 5.21-(6). Towards the end, as it approaches the grain boundary, the crack deflects again at an almost right angle to finally stop shortly after Figure 5.21-(7).
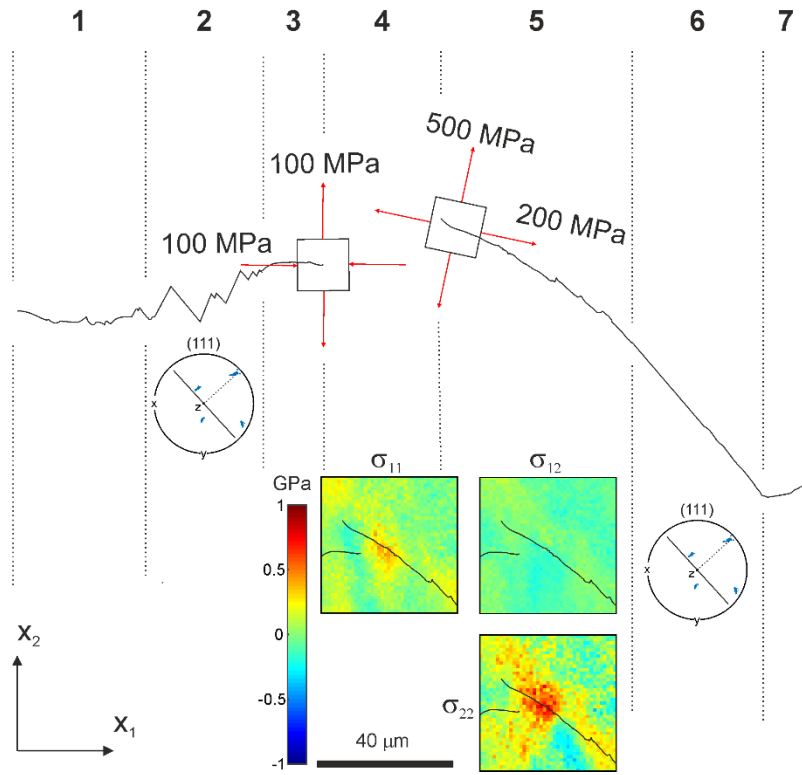
Figure 5.21 — Schematic of different stages of crack extension and their correlation with crystallographic planes and residual stress state within the grain. Note: gap in section 4 is not to scale.

5.5 Summary

- The combined use of EBSD and HR-EBSD has been exploited here to investigate microstructural features, texture and type III stresses in the sample provided.

- As observed by other authors, PCD prepared with grade 4 powders tend to have a final grain size slightly smaller than the starting particle size. PCD prepared with grade 30 powders exhibit a strong average reduction of the particle size, with a final average grain size ~8.4 μm. However, in this case the size distribution is bimodal. This is similar to what has been observed in literature after the phase of cold compaction but before sintering. The bimodality is difficult to assess using traditional methods for grain size analysis.

- Grains are weakly elongated, the long axis has wide orientation but not random especially in the direction parallel to cylindrical axis of the PCD cutters. This can be attributed to pressure gradients arising during sintering and leading to cobalt infiltration from the substrate.

- PCD G4 and PCD G30 show a weak texture. PCD G4/30 TC shows a weak macrotexture but texture in single bands is stronger.

- Type III stresses were found to vary significantly within the grains, giving rise to differences of up to 2 GPa between two different points.

- Observing the crack path in polycrystalline diamond it appears evident that the crack path has a strong tendency to follow {111} plane. However, stress and grain boundaries have the ability to deflect the crack.

Conclusions and future work

Conclusions

Through testing of single crystal SiC and diamond at the micron scale it was shown that, once the influence of microstructure is removed, the fracture energy measured is close to twice the surface energy. This result was obtained through minimisation of undesired effect caused by notching, focused-ion-beam-induced damage, influence of friction and local deformation observed in similar other works at small scales. It was also demonstrated the application of this method to more complex brittle and brittle/ductile bi-crystals. In particular, it was showed that the fracture energy of a glassy interface of ~10 nm bonding two crystals of SiC could be measured with crack extension. Furthermore, the investigation on DCBs made of sapphire bi-crystals bonded by 30 and 60 nm thick niobium interlayers showed how through this approach it was possible to capture the variations of energy expenditure needed to extend the crack when bridging or plasticity at the crack tip was activated. This study also highlighted how differences in thickness of the metal interface, even at this scale, can affect the activation or not of toughening mechanism, and proved possible to obtain a straight crack along the interface despite the large elastic mismatches between the two materials.

The method proposed introduces a new opportunity to study the fracture energy of individual grain boundaries, interfaces and crystallographic planes.

The study of grain size distribution in PCD using EBSD highlighted the importance of considering the real grain size distribution, and not an average value, when investigating the change of different mechanical properties with grain size. It was shown that the average grain size value measured for coarse grained samples in this work actually falls in a minimum of the bimodal size distribution and therefore it is within the least representative fraction to describe the grain sizes encountered across the sample. Still using conventional EBSD, while exploiting data for statistical analysis, it

was also possible to observe from the angle distribution of the longest axis of grains that elongated grains tend to align parallel to the cylindrical axis of PCD cutters. In addition, the map of these axes directions showed a tendency for smaller grains to align with other neighbouring fine grains and these together follow the curvature of larger grains. It was hypothesised that this rearrangement could occur during the stage of cobalt infiltration from the carbide substrate towards the top of the cutter. It does not seem related, instead, to preferential growth of the diamond as the local microtexture remains weak, although further data collection would be needed to confirm these assumptions.

Analysis of the local residual stress distributions also showed that stress variations can reach large gradients in diamond and along with the maps indicate that a few grains are subject to much higher stress gradients than average, within the regions investigated. This information along with data on texture, grain boundaries and residual stresses were used to explain the different stages of the crack growth observed. In particular, it was noticed that the crack path had a strong tendency to follow {111} planes. However, the presence of the stress patterns within the grain affected the crack path significantly. This essentially translates into an additional order of inhomogeneity encountered by the crack during its growth that adds to grain boundaries and defects. In particular, this highlights the importance of investigating the residual stresses present in this materials not only at the large scale, but also at the microscale.

Future work

Despite the encouraging results of the test conducted using the displacement-controlled wedge-opening of a double cantilever beam at the microscale, the method still requires detailed study of the effect of higher order terms on the fracture energy measured. In particular, it was not investigated the role of tapering of the DCB walls due to the geometry of FIB milling. Tapering is not in itself an issue for the wedge-opening DCB geometry, in fact it is exploited to achieve stability also at constant load. However, it modifies the geometry of the DCB as the cross section is not constant anymore and therefore modifies the analytical solution.

The application of the method on brittle/ductile systems also requires an in-depth study of the effect of plastic confinement at this lengthscale on the values measured.

In addition it was an objective of this work to apply this method to the investigation of diamond-diamond boundaries and diamond-cobalt interfaces. Despite a few attempts at fabricating DCBs with cobalt interfaces running through their central axis, no successful experiments were performed in this direction, yet valuable insights were gathered by these experiments:

- The sputtering yield of diamond is lower than both SiC and sapphire. As a consequence, higher currents or significantly longer time should be used for the milling of the notch in this material, since the currents used for SiC and sapphire seem to be ineffective.

- Assuring that a notch is present and that right angles at the base of the trough are avoided is of particular relevance for diamond since, given its extremely high Young's modulus, it stores a much larger amount of energy for a given displacement, thus increasing the probability of a catastrophic release of the same. For similar reasons, particular care should be taken to avoid loading misalignments.

- The thickness of cobalt layers present in PCDs is of the order of microns and might require larger DCBs to confine it in the middle. Alternatively, bi-crystal system should be produced to facilitate the execution of the experiments.

- Diamond-diamond boundaries are not easily detected through secondary electron imaging or ion beam channelling. Therefore, small regions in selected locations should be marked, e.g. using FIB, before mapping them with EBSD to facilitate the task.

The work could also be extended to the broader variety of cutters produced using different sintering conditions and would be interesting to compare the effect of different sintering apparatuses. The aspect ratio analysis has shown that an influence of the pressure gradients during sintering might cause a weak preferential alignment of the grains. A stronger microtexture was also observed in the tape casted sample and related to the spatial orientation of the layers. However, the analysis conducted here were limited to only a few samples. Analogously, the work on the residual stress gradients has provided precious insights on their role on the deflection of cracks in diamond, however further analysis should be now carried out to tie these residual stresses to processing routes. An in-depth study would also be needed to understand if these crack deflections are beneficial or detrimental in terms of fracture toughness of the material.

References

[1]   H.T. Hall, Sintered diamond: a synthetic carbonado., Science. 169 (1970) 868–9. doi:10.1126/science.169.3948.868.

[2]   H. Katzman, W.F. Libby, Sintered Diamond Compacts with a Cobalt Binder, Science (80- .). 172 (1971) 1132–1134. http://www.jstor.org/stable/1731852.

[3]   K. Uehara, S. Yamaya, High Pressure Sintering of Diamond by Cobalt Infiltration, Int. J. Refract. Met. Hard Mater. 7 (1988) 219–223.

[4]   D. Miess, G. Rai, Fracture toughness and thermal resistance of polycrystalline diamond compacts, Mater. Sci. Eng. A. 209 (1996) 270–276. doi:http://dx.doi.org/10.1016/0921-5093(95)10105-5.

[5]   Z. Li, H. Jia, H. Ma, W. Guo, X. Liu, G. Huang, et al., FEM analysis on the effect of cobalt content on thermal residual stress in polycrystalline diamond compact (PDC), Sci. China Physics, Mech. Astron. 55 (2012) 639–643. doi:10.1007/s11433-012-4654-4.

[6]   H. Jia, H. Ma, X. Jia, Research on polycrystalline diamond compact (PDC) with low residual stress prepared using nickel-based additive, Int. J. Refract. Met. Hard Mater. 29 (2011) 64–67. doi:10.1016/j.ijrmhm.2010.07.004.

[7]   F.G. Marro, A. Mestra, E. Jiménez-Piqué, S. Ozbayraktar, L. Llanes, Damage induced by monotonic and cyclic spherical indentation in polycrystalline diamond (PCD), Int. J. Refract. Met. Hard Mater. 49 (2015) 292–301. doi:https://doi.org/10.1016/j.ijrmhm.2014.09.007.

[8]   F. García-Marro, A. Mestra, V. Kanyanta, K. Maweja, S. Ozbayraktar, L. Llanes, Contact damage and residual strength in polycrystalline diamond (PCD), Diam. Relat. Mater. 65 (2016) 131–136. doi:https://doi.org/10.1016/j.diamond.2016.03.004.

[9]   T.-P. Lin, G.A. Cooper, M. Hood, Measurement of the fracture toughness of polycrystalline diamond using the double-torsion test, J. Mater. Sci. 29 (1994) 4750–4756. doi:10.1007/BF00356519.

[10]   M. Wieligor, T.W. Zerda, Surface stress distribution in diamond crystals in diamond–silicon carbide composites, Diam. Relat. Mater. 17 (2008) 84–89. doi:https://doi.org/10.1016/j.diamond.2007.10.035.

[11]   T.-P. Lin, M. Hood, G.A. Cooper, R.H. Smith, Residual Stresses in Polycrystalline Diamond Compacts, J. Am. Ceram. Soc. 77 (1994) 1562–1568. doi:10.1111/j.1151-2916.1994.tb09757.x.

[12]   A.D. Krawitz, R. Andrew Winholtz, E.F. Drake, N.D. Griffin, Residual stresses in polycrystalline diamond compacts, Int. J. Refract. Met. Hard Mater. 17 (1999) 117–122. doi:10.1016/S0263-4368(99)00007-4.

[13]   V. Kanyanta, S. Ozbayraktar, K. Maweja, Effect of manufacturing parameters on polycrystalline diamond compact cutting tool stress-state, Int. J. Refract. Met. Hard Mater. 45 (2014) 147–152. doi:10.1016/j.ijrmhm.2014.03.009.

[14]   H. Jia, X. Jia, Y. Xu, L. Wan, K. Jie, H. Ma, Effects of initial crystal size of diamond powder on surface residual stress and morphology in polycrystalline diamond (PCD) layer, Sci. China Physics, Mech. Astron. 54 (2011) 98–101. doi:10.1007/s11433-010-4202-z.

[15]   S.A. Catledge, Y.K. Vohra, R. Ladi, G. Rai, Micro-raman stress investigations and X-ray diffraction analysis of polycrystalline diamond (PCD) tools, Diam. Relat. Mater. 5 (1996) 1159–1165. doi:10.1016/0925-9635(96)00534-1.

[16]   R.M. Erasmus, J.D. Comins, V. Mofokeng, Z. Martin, Application of Raman spectroscopy to determine stress in polycrystalline diamond tools as a function of tool geometry and temperature, Diam. Relat. Mater. 20 (2011) 907–911.

doi:10.1016/j.diamond.2011.03.018.

[17] F. Chen, G. Xu, C. Ma, G. Xu, Thermal residual stress of polycrystalline diamond compacts, Trans. Nonferrous Met. Soc. China. 20 (2010) 227–232. doi:10.1016/S1003-6326(09)60126-6.

[18] J.W. Paggett, E.F. Drake, A.D. Krawitz, R.A. Winholtz, N.D. Griffin, Residual stress and stress gradients in polycrystalline diamond compacts, Int. J. Refract. Met. Hard Mater. 20 (2002) 187–194. doi:10.1016/S0263-4368(01)00077-4.

[19] A.F. Azevedo, E.J. Corat, N.F. Leite, N.G. Ferreira, V.J. Trava-Airoldi, Raman analyses of residual stress in diamond thin films grown on Ti6Al4V alloy, Mater. Res. 6 (2003) 51–56. doi:10.1590/S1516-14392003000100010.

[20] B.R. Lawn, Fracture of brittle solids, 2nd ed., Cambridge University Press, Cambridge, 1993.

[21] T.L. Anderson, Fracture mechanics : fundamentals and applications, 3rd ed., Taylor & Francis, Boca Raton, FL, 2005.

[22] A.A. Griffith, The Phenomena of Rupture and Flow in Solids, Philos. Trans. R. Soc. London A Math. Phys. Eng. Sci. 221 (1921) 163–198. http://rsta.royalsocietypublishing.org/content/221/582-593/163.abstract.

[23] C.E. Inglis, Stresses in a plate due to the presence of cracks and sharp corners, Trans. Inst. Nav. Archit. 55 (1913) 219–242. citeulike-article-id:2707156.

[24] G.R. Irwin, Analysis of stresses and strains near the end of a crack traversing a plate, J. Appl. Mech. 24 (1957) 361–364. citeulike-article-id:11674773.

[25] T.L. Anderson, Fracture mechanics : fundamentals and applications, 3rd ed., Taylor & Francis, Boca Raton, FL, 2005.

[26] ASTM C1421 - 16 Standard Test Methods for Determination of Fracture Toughness of

Advanced Ceramics at Ambient Temperature, (2016). doi:10.1520/C1421.

[27]   J.W. Obreimoff, The Splitting Strength of Mica, Proc. R. Soc. London. Ser. A, Contain. Pap. a Math. Phys. Character. 127 (1930) 290–297. doi:10.2307/95320.

[28]   S.W. Freiman, The fracture of brittle materials : testing and analysis, Wiley, Hoboken, N.J., 2012.

[29]   A. Shyam, E. Lara-Curzio, The double-torsion testing technique for determination of fracture toughness and slow crack growth behavior of materials: A review, J. Mater. Sci. 41 (2006) 4093–4104. doi:10.1007/s10853-005-5553-0.

[30]   Y. Nara, K. Kaneko, Study of subcritical crack growth in andesite using the Double Torsion test, Int. J. Rock Mech. Min. Sci. 42 (2005) 521–530. doi:10.1016/j.ijrmms.2005.02.001.

[31]   B. Pletka, E. Fuller, B. Koepke, An Evaluation of Double-Torsion Testing—Experimental, in: S. Freiman (Ed.), Fract. Mech. Appl. to Brittle Mater., ASTM International, 100 Barr Harbor Drive, PO Box C700, West Conshohocken, PA 19428-2959, 1979: pp. 19-19–19. doi:10.1520/STP36622S.

[32]   R. Marion, Use of Indentation Fracture to Determine Fracture Toughness, in: S. Freiman (Ed.), Fract. Mech. Appl. to Brittle Mater. - ASTM STP678, ASTM International, West Conshohocken, PA, 1979: pp. 103-103–9. doi:10.1520/STP36628S.

[33]   B. Lawn, R. Wilshaw, Indentation fracture: principles and applications, J. Mater. Sci. 10 (1975) 1049–1081. doi:10.1007/BF00823224.

[34]   G.R. Anstis, P. Chantikul, B.R. Lawn, D.B. Marshall, A Critical Evaluation of Indentation Techniques for Measuring Fracture Toughness: I, Direct Crack Measurements, J. Am. Ceram. Soc. 64 (1981) 533–538. doi:10.1111/j.1151-2916.1981.tb10320.x.

[35]   B.R. Lawn, A.G. Evans, D.B. Marshall, Elastic/Plastic Indentation Damage in Ceramics:

The Median/Radial Crack System, J. Am. Ceram. Soc. 63 (1980) 574–581. doi:10.1111/j.1151-2916.1980.tb10768.x.

[36] G.M. Pharr, Measurement of mechanical properties by ultra-low load indentation, Mater. Sci. Eng. A. 253 (1998) 151–159. doi:http://dx.doi.org/10.1016/S0921-5093(98)00724-2.

[37] B.R. Lawn, E.R. Fuller, Equilibrium penny-like cracks in indentation fracture, J. Mater. Sci. 10 (1975) 2016–2024. doi:10.1007/BF00557479.

[38] G.D. Quinn, R.C. Bradt, On the Vickers Indentation Fracture Toughness Test, J. Am. Ceram. Soc. 90 (2007) 673–680. doi:10.1111/j.1551-2916.2006.01482.x.

[39] A.G. Evans, The mechanical properties of reinforced ceramic, metal and intermetallic matrix composites, Mater. Sci. Eng. A. 143 (1991) 63–76. doi:http://dx.doi.org/10.1016/0921-5093(91)90726-4.

[40] W.J. Clegg, K. Kendall, N.M. Alford, T.W. Button, J.D. Birchall, A simple way to make tough ceramics, Nature. 347 (1990) 455–457. http://dx.doi.org/10.1038/347455a0.

[41] N. Al Nasiri, N. Ni, E. Saiz, J. Chevalier, F. Giuliani, L.J. Vandeperre, Effect of microstructure and grain boundary chemistry on slow crack growth in silicon carbide at ambient conditions, J. Eur. Ceram. Soc. 35 (2015) 2253–2260. doi:10.1016/j.jeurceramsoc.2015.02.020.

[42] C.J. Gilbert, J.J. Cao, W.J. Moberlychan, L.C. DeJonghe, R.O. Ritchie, Cyclic fatigue and resistance-curve behavior of an in situ toughened silicon carbide with Al B C additions, Acta Mater. 44 (1996) 3199–3214. doi:10.1016/1359-6454(95)00409-2.

[43] J.J. Cao, W.J. MoberlyChan, L.C. De Jonghe, C.J. Gilbert, R.O. Ritchie, In situ toughened silicon carbide with Al-B-C additions, J. Am. Ceram. Soc. (1996). doi:10.1111/j.1151-2916.1996.tb08145.x.

[44] N.P. Padture, B.R. Lawn, Toughness Properties of a Silicon Carbide with an in Situ Induced Heterogeneous Grain Structure, J. Am. Ceram. Soc. (1994). doi:10.1111/j.1151-2916.1994.tb04637.x.

[45] S.K. Lee, C.H. Kim, Effects of alpha-Sic versus beta-Sic Starting Powders on Microstructure and Fracture Toughness of Sic Sintered with Al2O3-Y2O3 Additives, J. Am. Ceram. Soc. 77 (1994) 1655–1658. doi:10.1111/j.1151-2916.1994.tb09771.x.

[46] Chen, X.-F. Zhang, R.O. Ritchie, Effects of Grain-Boundary Structure on the Strength, Toughness, and Cyclic-Fatigue Properties of a Monolithic Silicon Carbide, J. Am. Ceram. Soc. 83 (2000) 2079–2081. doi:10.1111/j.1151-2916.2000.tb01515.x.

[47] I.E. Reimanis, B.J. Dalgleish, M. Brahy, M. Rühle, A.G. Evans, Effects of plasticity on the crack propagation resistance of a metal/ceramic interface, Acta Metall. Mater. 38 (1990) 2645–2652. doi:10.1016/0956-7151(90)90277-N.

[48] A. Bartlett, A.G. Evans, The effect of reaction products on the fracture resistance of a metal/ceramic interface, Acta Metall. Mater. 41 (1993) 497–504. doi:10.1016/0956-7151(93)90078-7.

[49] B.J. Dalgleish, E. Saiz, A.P. Tomsia, R.M. Cannon, R.O. Ritchie, Interface formation and strength in ceramic-metal systems, Scr. Metall. Mater. 31 (1994) 1109–1114. doi:10.1016/0956-716X(94)90535-5.

[50] A.G. Evans, The mechanical properties of reinforced ceramic, metal and intermetallic matrix composites, Mater. Sci. Eng. A. 143 (1991) 63–76. doi:10.1016/0921-5093(91)90726-4.

[51] A.G. Evans, B.J. Dalgleish, The fracture resistance of metal-ceramic interfaces, Acta Metall. Mater. 40 (1992) S295–S306. doi:10.1016/0956-7151(92)90289-Q.

[52] A.G. Evans, M. Rühle, B.J. Dalgleish, P.G. Charalambides, The fracture energy of

bimaterial interfaces, Mater. Sci. Eng. A. 126 (1990) 53–64. doi:10.1016/0921-5093(90)90113-H.

[53] A. Needleman, An analysis of tensile decohesion along an interface, J. Mech. Phys. Solids. 38 (1990) 289–324. doi:10.1016/0022-5096(90)90001-K.

[54] D.R. Lesuer, C.K. Syn, O.D. Sherby, J. Wadsworth, J.J. Lewandowski, W.H. Hunt Jr., Mechanical behaviour of laminated metal composites, Int. Mater. Rev. 41 (1996).

[55] R.O. Ritchie, R.M. Cannon, B.J. Dalgleish, R.H. Dauskardt, J.M. McNaney, Mechanics and mechanisms of crack growth at or near ceramic-metal interfaces: interface engineering strategies for promoting toughness, Mater. Sci. Eng. A. 166 (1993) 221–235. doi:http://dx.doi.org/10.1016/0921-5093(93)90325-9.

[56] M. Rühle, A.G. Evans, Structure and chemistry of metal/ceramic interfaces, Mater. Sci. Eng. A. 107 (1989) 187–197. doi:10.1016/0921-5093(89)90387-0.

[57] T. Sung Oh, R.M. Cannon, R.O. Ritchie, Subcritical Crack Growth along Ceramic-Metal Interfaces, J. Am. Ceram. Soc. 70 (1987) C-352-C-355. doi:10.1111/j.1151-2916.1987.tb04917.x.

[58] M.R. Turner, A.G. Evans, An experimental study of the mechanisms of crack extension along an oxide/metal interface, Acta Mater. 44 (1996) 863–871. doi:10.1016/1359-6454(95)00256-1.

[59] A.. Volinsky, N.. Moody, W.. Gerberich, Interfacial toughness measurements for thin films on substrates, Acta Mater. 50 (2002) 441–466. doi:10.1016/S1359-6454(01)00354-8.

[60] R.M. Cannon, B.J. Dalgleish, R.H. Dauskardt, T.S. Oh, R.O. Ritchie, Cyclic fatigue-crack propagation along ceramic/metal interfaces, Acta Metall. Mater. 39 (1991) 2145–2156. doi:10.1016/0956-7151(91)90184-3.

[61]   P.G. Charalambides, J. Lund, A.G. Evans, R.M. McMeeking, A Test Specimen for Determining the Fracture Resistance of Bimaterial Interfaces, J. Appl. Mech. 56 (1989) 77–82. http://dx.doi.org/10.1115/1.3176069.

[62]   Z. Suo, J.W. Hutchinson, Sandwich test specimens for measuring interface crack toughness, Mater. Sci. Eng. A. 107 (1989) 135–143. doi:10.1016/0921-5093(89)90382-1.

[63]   J.-S. Wang, Z. Suo, Experimental determination of interfacial toughness curves using Brazil-nut-sandwiches, Acta Metall. Mater. 38 (1990) 1279–1290. doi:10.1016/0956-7151(90)90200-Z.

[64]   A.A. Volinsky, N.R. Moody, W.W. Gerberich, Interfacial toughness measurements for thin films on substrates, Acta Mater. (2002). doi:10.1016/S1359-6454(01)00354-8.

[65]   A.G. Evans, M. Rühle, B.J. Dalgleish, P.G. Charalambides, The fracture energy of bimaterial interfaces, Mater. Sci. Eng. A. 126 (1990). doi:10.1016/0921-5093(90)90113-H.

[66]   R.W. Davidge, T.J. Green, The strength of two-phase ceramic/glass materials, J. Mater. Sci. 3 (1968) 629–634. doi:10.1007/BF00757910.

[67]   K. Xia, T.G. Langdon, The toughening and strengthening of ceramic materials through discontinuous reinforcement, J. Mater. Sci. 29 (1994) 5219–5231. doi:10.1007/BF01171532.

[68]   A.G. Evans, Microfracture from thermal expansion anisotropy—I. Single phase systems, Acta Metall. 26 (1978) 1845–1853. doi:10.1016/0001-6160(78)90097-4.

[69]   C.C. Wu, S.W. Freiman, R.W. Rice, J.J. Mecholsky, Microstructural aspects of crack propagation in ceramics, J. Mater. Sci. 13 (1978) 2659–2670. doi:10.1007/BF02402753.

[70]   D. Di Maio, S.G. Roberts, Measuring fracture toughness of coatings using focused-ion-

beam-machined microbeams, J. Mater. Res. 20 (2005) 299–302. doi:doi:10.1557/JMR.2005.0048.

[71] D.E.J. Armstrong, A.J. Wilkinson, S.G. Roberts, Micro-mechanical measurements of fracture toughness of bismuth embrittled copper grain boundaries, Philos. Mag. Lett. 91 (2011) 394–400. doi:10.1080/09500839.2011.573813.

[72] F. Iqbal, J. Ast, M. Göken, K. Durst, In situ micro-cantilever tests to study fracture properties of NiAl single crystals, Acta Mater. 60 (2012) 1193–1200. doi:http://dx.doi.org/10.1016/j.actamat.2011.10.060.

[73] B.N. Jaya, C. Kirchlechner, G. Dehm, Can microscale fracture tests provide reliable fracture toughness values? A case study in silicon, J. Mater. Res. 30 (2015) 686–698. doi:doi:10.1557/jmr.2015.2.

[74] A.D. Norton, S. Falco, N. Young, J. Severs, R.I. Todd, Microcantilever investigation of fracture toughness and subcritical crack growth on the scale of the microstructure in Al2O3, J. Eur. Ceram. Soc. (n.d.). doi:http://dx.doi.org/10.1016/j.jeurceramsoc.2015.08.023.

[75] J. Tatami, M. Katayama, M. Ohnishi, T. Yahagi, T. Takahashi, T. Horiuchi, et al., Local Fracture Toughness of Si3N4 Ceramics Measured using Single-Edge Notched Microcantilever Beam Specimens, J. Am. Ceram. Soc. 98 (2015) 965–971. doi:10.1111/jace.13391.

[76] M.G. Mueller, V. Pejchal, G. Žagar, A. Singh, M. Cantoni, A. Mortensen, Fracture toughness testing of nanocrystalline alumina and fused quartz using chevron-notched microbeams, Acta Mater. 86 (2015) 385–395. doi:10.1016/j.actamat.2014.12.016.

[77] S. Liu, J.M. Wheeler, P.R. Howie, X.T. Zeng, J. Michler, W.J. Clegg, Measuring the fracture resistance of hard coatings, Appl. Phys. Lett. 102 (2013) 171907.

doi:10.1063/1.4803928.

[78]   B.N. Jaya, V. Jayaram, Crack stability in edge-notched clamped beam specimens: modeling and experiments, Int. J. Fract. 188 (2014) 213–228. doi:10.1007/s10704-014-9956-2.

[79]   V.T. Srikar, S.M. Spearing, A critical review of microscale mechanical testing methods used in the design of microelectromechanical systems, Exp. Mech. 43 (2003) 238–247. doi:10.1007/BF02410522.

[80]   M. Sebastiani, K.E. Johanns, E.G. Herbert, F. Carassiti, G.M. Pharr, A novel pillar indentation splitting test for measuring fracture toughness of thin ceramic coatings, Philos. Mag. (2014) 1–17. doi:10.1080/14786435.2014.913110.

[81]   B.N. Jaya, V. Jayaram, S.K. Biswas, A new method for fracture toughness determination of graded (Pt,Ni)Al bond coats by microbeam bend tests, Philos. Mag. (2012). http://www.tandfonline.com/doi/abs/10.1080/14786435.2012.669068#.VoAJeh-YAJw.mendeley (accessed December 27, 2015).

[82]   F. Östlund, K. Rzepiejewska-Malyska, K. Leifer, L.M. Hale, Y. Tang, R. Ballarini, et al., Brittle-to-Ductile Transition in Uniaxial Compression of Silicon Pillars at Room Temperature, Adv. Funct. Mater. 19 (2009) 2439–2444. doi:10.1002/adfm.200900418.

[83]   P.R. Howie, S. Korte, W.J. Clegg, Fracture modes in micropillar compression of brittle crystals, J. Mater. Res. 27 (2012) 141–151. doi:doi:10.1557/jmr.2011.256.

[84]   F. Östlund, P.R. Howie, R. Ghisleni, S. Korte, K. Leifer, W.J. Clegg, et al., Ductile–brittle transition in micropillar compression of GaAs at room temperature, Philos. Mag. 91 (2011) 1190–1199. doi:10.1080/14786435.2010.509286.

[85]   S. Johansson, J. Schweitz, L. Tenerz, J. Tirén, Fracture testing of silicon microelements in situ in a scanning electron microscope, J. Appl. Phys. 63 (1988) 4799–4803.

doi:http://dx.doi.org/10.1063/1.340471.

[86]   T.P. Weihs, S. Hong, J.C. Bravman, W.D. Nix, Mechanical deflection of cantilever microbeams: A new technique for testing the mechanical properties of thin films, J. Mater. Res. 3 (1988) 931–942. http://www.scopus.com/inward/record.url?eid=2-s2.0-0024069463&partnerID=40&md5=ff765606f2a6a406d752dcc6339951af.

[87]   O. Kraft, C.A. Volkert, Mechanical Testing of Thin Films and Small Structures, Adv. Eng. Mater. 3 (2001) 99–110. doi:10.1002/1527-2648(200103)3:3<99::AID-ADEM99>3.0.CO;2-2.

[88]   J.P. Best, J. Zechner, I. Shorubalko, J.V. Oboňa, J. Wehrs, M. Morstein, et al., A comparison of three different notching ions for small-scale fracture toughness measurement, Scr. Mater. 112 (2015) 71–74. doi:10.1016/j.scriptamat.2015.09.014.

[89]   ASTM E1304-97(2014) Standard Test Method for Plane-Strain (Chevron-Notch) Fracture Toughness of Metallic Materials, (2014).

[90]   G. Žagar, V. Pejchal, M.G. Mueller, L. Michelet, A. Mortensen, Fracture toughness measurement in fused quartz using triangular chevron-notched micro-cantilevers, Scr. Mater. 112 (2016) 132–135. doi:10.1016/j.scriptamat.2015.09.032.

[91]   J.J. Gilman, Direct Measurements of the Surface Energies of Crystals, J. Appl. Phys. 31 (1960) 2208. doi:10.1063/1.1735524.

[92]   S.M. Wiederhorn, Critical Analysis of the Theory of the Double Cantilever Method of Measuring Fracture-Surface Energies, J. Appl. Phys. 39 (1968) 1569. doi:10.1063/1.1656397.

[93]   D.L. Hindman, An equation for fracture energy determination by double-cantilever cleavage, J. Appl. Phys. 45 (1974) 2768. doi:10.1063/1.1663663.

[94]   T. Schuelke, T.A. Grotjohn, Diamond polishing, Diam. Relat. Mater. 32 (2013) 17–26.

doi:10.1016/j.diamond.2012.11.007.

[95]   G.E. Spriggs, Properties of diamond and cubic boron nitride, in: P. Beiss, R. Ruthardt, H. Warlimont (Eds.), Powder Metall. Data. Refract. Hard Intermet. Mater. - Landolt-Börnstein - Gr. VIII Adv. Mater. Technol., Springer-Verlag Berlin Heidelberg, 2002. doi:10.1007/10858641_7.

[96]   J.F. Shackelford, W. Alexander, CRC Materials Science and Engineering Handbook, 2001. doi:10.1016/S0969-806X(97)84047-9.

[97]   Handbook of Chemistry and Physics 98th Edition, (n.d.). http://hbcponline.com/faces/contents/InteractiveTable.xhtml?tableId=230&search=true&quick=true (accessed July 31, 2017).

[98]   G.K. White, Thermal conductivity at 273 - 300 K, in: O. Madelung, G.K. White (Eds.), Therm. Conduct. Pure Met. Alloy. - Landolt-Börnstein - Gr. III Condens. Matter, Springer-Verlag Berlin Heidelberg, 1991. doi:10.1007/10031435_3.

[99]   F.P. Bundy, H.T. Hall, H.M. Strong, R.H. Wentorf, Man-Made Diamonds, Nature. 176 (1955) 51–55. doi:10.1038/176051a0.

[100]   R. Berman, S.F. Simon, On the Graphite - Diamond Equilibrium, Zeitschrift Für Elektrochemie, Berichte Der Bunsengesellschaft Für Phys. Chemie. 59 (1955) 333–338. doi:10.1002/bbpc.19550590503.

[101]   R. Berman, J. Thewlis, The Graphite–Diamond Equilibrium, Nature. 176 (1955) 834–836. doi:10.1038/176834b0.

[102]   J.E. Field, The mechanical and strength properties of diamond, Reports Prog. Phys. 75 (2012) 126505. doi:10.1088/0034-4885/75/12/126505.

[103]   W.G. Eversole, Synthesis of diamond, (1962). https://www.google.com/patents/US3030188.

[104] P. Zorabedian, F. Adar, P.M. Bell, J.A. Xu, Measurement of local stress in laser-recrystallized lateral epitaxial silicon films over silicon dioxide using Raman scattering, Appl. Phys. Lett. 43 (1983) 177–179. doi:10.1063/1.94271.

[105] R.H. Wentorf, R.C. DeVries, F.P. Bundy, Sintered Superhard Materials, Science (80-.). 208 (1980) 873–880. doi:10.1126/science.208.4446.873.

[106] Cutting-tools of "black diamond," J. Franklin Inst. 89 (1870) 361–376. doi:10.1016/0016-0032(70)90523-5.

[107] L.F. Trueb, E.C. de Wys, Carbonado: Natural Polycrystalline Diamond, Science (80-.). 165 (1969) 799–802. http://www.jstor.org/stable/1727375.

[108] B. Lux, R. Haubner, H. Holzer, R.C. DeVries, Natural and synthetic polycrystalline diamond, with emphasis on ballas, Int. J. Refract. Met. Hard Mater. 15 (1997) 263–288. doi:10.1016/S0263-4368(97)87503-8.

[109] L.F. Trueb, C.S. Barrett, Microstructural investigation of ballas diamond, Am. Mineral. 57 (1972) 1664–1680. http://www.minsocam.org/ammin/AM57/AM57_1664.pdf.

[110] R. W, W. R, Diamond tools for machining, (1973). http://www.google.ch/patents/US3745623.

[111] R.F. Walker, Mechanism of Material Transport During Sintering, J. Am. Ceram. Soc. 38 (1955) 187–197. doi:10.1111/j.1151-2916.1955.tb14928.x.

[112] R.M. German, Liquid Phase Sintering, Springer US, Boston, MA, 1985. doi:10.1007/978-1-4899-3599-1.

[113] D. Belnap, A. Griffo, Homogeneous and structured PCD/WC-Co materials for drilling, Diam. Relat. Mater. 13 (2004) 1914–1922. doi:http://dx.doi.org/10.1016/j.diamond.2004.06.013.

[114] C.M. Fernandes, A.M.R. Senos, Cemented carbide phase diagrams: A review, Int. J.

Refract. Met. Hard Mater. 29 (2011) 405–418. doi:10.1016/j.ijrmhm.2011.02.004.

[115] E.N. Gruzdeva, V.S. Kardasevich, A. V Suranov, T.N. Nesterenko, Y.M. Rotner, Comminution behavior of ASM diamond micropowder during cold pressing, Sov. Powder Metall. Met. Ceram. 24 (1985) 603–606. doi:10.1007/BF00791946.

[116] A.A. Bochechka, Effects of thermochemical treatment on diamond polycrystal sintering, Powder Metall. Met. Ceram. 38 (1999) 220–223. doi:10.1007/BF02675764.

[117] J.C. Walmsley, A.R. Lang, Characteristics of diamond regrowth in a synthetic diamond compact, J. Mater. Sci. 23 (1988) 1829–1834. doi:10.1007/BF01115728.

[118] D. McNamara, D. Carolan, P. Alveen, N. Murphy, A. Ivanković, The influence of microstructure on the fracture statistics of polycrystalline diamond and polycrystalline cubic boron nitride, Ceram. Int. 40 (2014) 11543–11549. doi:http://dx.doi.org/10.1016/j.ceramint.2014.03.100.

[119] Z.Z. Fang, A. Griffo, B. White, G. Lockwood, D. Belnap, G. Hilmas, et al., Fracture resistant super hard materials and hardmetals composite with functionally designed microstructure, Int. J. Refract. Met. Hard Mater. 19 (2001) 453–459. doi:10.1016/S0263-4368(01)00031-2.

[120] Element six - PRECISION MACHINING AND FINISHING, (n.d.). https://www.e6.com/wps/wcm/connect/92db06fc-59c9-4958-a83e-44b9a06cc87f/E6_Metalworking_A4_English_R5_VIZ.pdf?MOD=AJPERES&CACHEID=92db06fc-59c9-4958-a83e-44b9a06cc87f (accessed May 3, 2017).

[121] Polycrystalline Diamond PCD Materials | Industrial Abrasives Ltd | Industrial Diamonds Supplier UK, (n.d.). http://indab.com/products/polycrystalline-diamond-pcd/ (accessed May 3, 2017).

[122] SANDVIK HYPERION COMPAX® PCD, (n.d.).

http://www.hyperion.sandvik.com/Documents/Product Literature/Polycrystalline Diamond/Compax Tool Blanks/SH-4011 ENG LT_Compax PCD_SCREEN.pdf (accessed May 3, 2017).

[123] A. Lammer, Mechanical properties of polycrystalline diamonds, Mater. Sci. Technol. 4 (1988) 949–955. doi:doi:10.1179/mst.1988.4.11.949.

[124] J.R. Hird, J.E. Field, Diamond polishing, Proc. R. Soc. London A Math. Phys. Eng. Sci. 460 (2004). http://rspa.royalsocietypublishing.org/content/460/2052/3547 (accessed April 20, 2017).

[125] L. Pastewka, S. Moser, P. Gumbsch, M. Moseler, Anisotropic mechanical amorphization drives wear in diamond, Nat Mater. 10 (2011) 34–38. http://dx.doi.org/10.1038/nmat2902.

[126] F. Bellin, A. Dourfaye, W. King, M. Thigpen, The current state of PDC bit technology, World Oil. 231 (2010) 53–58.

[127] M.W. Cook, P.K. Bossom, Trends and recent developments in the material manufacture and cutting tool application of polycrystalline diamond and polycrystalline cubic boron nitride, Int. J. Refract. Met. Hard Mater. 18 (2000) 147–152. doi:10.1016/S0263-4368(00)00015-9.

[128] Q.S. Bai, Y.X. Yao, P. Bex, G. Zhang, Study on wear mechanisms and grain effects of PCD tool in machining laminated flooring, Int. J. Refract. Met. Hard Mater. 22 (2004) 111–115. doi:10.1016/j.ijrmhm.2004.01.007.

[129] S.Z. Liu, Z.L. Kou, R. Zhang, C.L. Liu, Y. Li, R.Q. Li, et al., Study on Wear Behaviors and Grain Effects of PCD Cutting Tools in Turning Granite, Appl. Mech. Mater. 214 (2012) 130–135. doi:10.4028/www.scientific.net/AMM.214.130.

[130] S.G. Moseley, K.-P. Bohn, M. Goedickemeier, Core drilling in reinforced concrete using

polycrystalline diamond (PCD) cutters: Wear and fracture mechanisms, Int. J. Refract. Met. Hard Mater. 27 (2009) 394–402. doi:10.1016/j.ijrmhm.2008.11.014.

[131] J.E. Westraadt, I. Sigalas, J.H. Neethling, Characterisation of thermally degraded polycrystalline diamond, Int. J. Refract. Met. Hard Mater. 48 (2015) 286–292. doi:https://doi.org/10.1016/j.ijrmhm.2014.08.008.

[132] B.-L. Huang, C. Weis, X. Yao, D. Belnap, G. Rai, Fracture toughness of sintered polycrystalline diamond (PCD), in: F. F.H., H. J. (Eds.), Proc. 1997 5th Int. Conf. Adv. Part. Mater. Process., Metal Powder Industries Federation, Smith MegaDiamond Inc, Provo, United States, 1997: pp. 431–437. https://www.scopus.com/inward/record.uri?eid=2-s2.0-0031349390&partnerID=40&md5=838b365b9b41497439bbe66dea94f550.

[133] R.W. Rice, S.W. Freiman, P.F. Becher, Grain-Size Dependence of Fracture Energy in Ceramics: I, Experiment, J. Am. Ceram. Soc. 64 (1981) 345–350. doi:10.1111/j.1151-2916.1981.tb10300.x.

[134] M. Petrović, D. Carolan, A. Ivanković, N. Murphy, Role of Rate and Temperature on Fracture and Mechanical Properties of PCD, Key Eng. Mater. 452–453 (2010) 153–156. doi:10.4028/www.scientific.net/KEM.452-453.153.

[135] J.D. Belnap, Effect of cobalt on PCD fracture toughness, in: 2010: pp. 2424–2434. http://www.scopus.com/inward/record.url?eid=2-s2.0-799952679091&partnerID=40&md5=0bc7ca26d4a0eb5ea95c48effb71d4bd.

[136] K. Zacny, Fracture and Fatigue of Polycrystalline-Diamond Compacts, SPE Drill. Complet. 27 (2012) 145–157. doi:10.2118/150001-PA.

[137] K.J. Dunn, M. Lee, The fracture and fatigue of sintered diamond compact, J. Mater. Sci. 14 (1979) 882–890. doi:10.1007/BF00550720.

[138] Z. Fang, A. Griffo, B. White, D. Belnap, R. Hamilton, G. Portwood, et al., Chipping

Resistant Polycrystalline Diamond and Carbide Composite Materials for Roller Cone Bits, in: SPE Annu. Tech. Conf. Exhib., Society of Petroleum Engineers, 2001. doi:10.2118/71394-MS.

[139] S. Özbayraktar, R. Mulone, S. Masete, H.J. Storm, Analysis of Outgassing Stage of PCD Processing, 1997.

[140] A. Hirata, H. Tokura, M. Yoshikawa, Smoothing of chemically vapour deposited diamond films by ion beam irradiation, Thin Solid Films. 212 (1992) 43–48. doi:10.1016/0040-6090(92)90498-Z.

[141] T. Maitland, S. Sitzman, Electron Backscatter Diffraction (EBSD) Technique and Materials Characterization Examples, in: W. Zhou, Z.L. Wang (Eds.), Scanning Microsc. Nanotechnol. Tech. Appl., Springer, 2006: pp. 41–75.

[142] R.A. Schwarzer, D.P. Field, B.L. Adams, M. Kumar, A.J. Schwartz, Present state of electron backscatter diffraction and prospective developments, in: M. Kumar, A.J. Schwartz, D.P. Field, B.L. Adams (Eds.), Electron Backscatter Diffr. Mater. Sci., 2nd ed., Springer, Dordrecht, 2010: pp. 1–20.

[143] S. Sitzman, G. Nolze, M. Nowell, EBSD Pattern Quality and its Use in Evaluating Sample Surface Condition, Microsc. Microanal. 16 (2010) 698–699. doi:10.1017/S143192761005467X.

[144] S.I. Wright, M.M. Nowell, R. de Kloe, P. Camus, T. Rampton, Electron imaging with an EBSD detector, Ultramicroscopy. 148 (2015) 132–145. doi:10.1016/j.ultramic.2014.10.002.

[145] S. Massl, J. Keckes, R. Pippan, A direct method of determining complex depth profiles of residual stresses in thin films on a nanoscale, Acta Mater. 55 (2007) 4835–4844. doi:http://dx.doi.org/10.1016/j.actamat.2007.05.002.

[146] B. Winiarski, P.J. Withers, Mapping Residual Stress Profiles at the Micron Scale Using FIB Micro-Hole Drilling, Appl. Mech. Mater. 24–25 (2010) 267–272. doi:10.4028/www.scientific.net/AMM.24-25.267.

[147] N. Sabaté, D. Vogel, A. Gollhardt, J. Marcos, I. Gràcia, C. Cané, et al., Digital image correlation of nanoscale deformation fields for local stress measurement in thin films, Nanotechnology. 17 (2006) 5264–5270. doi:10.1088/0957-4484/17/20/037.

[148] K.J. Kang, N. Yao, M.Y. He, A.G. Evans, A method for in situ measurement of the residual stress in thin films by using the focused ion beam, Thin Solid Films. 443 (2003) 71–77. doi:10.1016/S0040-6090(03)00946-5.

[149] M. Sebastiani, C. Eberl, E. Bemporad, G.M. Pharr, Depth-resolved residual stress analysis of thin coatings by a new FIB–DIC method, Mater. Sci. Eng. A. 528 (2011) 7901–7908. doi:10.1016/j.msea.2011.07.001.

[150] I. De Wolf, Micro-Raman spectroscopy to study local mechanical stress in silicon integrated circuits, Semicond. Sci. Technol. 11 (1996) 139–154. doi:10.1088/0268-1242/11/2/001.

[151] Wilkinson, Angus J., Dingley David J., Graham Meaden, Strain Mapping Using Electron Backscatter Diffraction, in: Kumar, Mukul, Adam J. Schwartz, David P. Field, Brent L. Adams (Ed.), Electron Backscatter Diffr. Mater. Sci., 2nd ed., Springer, Dordrecht, 2010: pp. 231–249.

[152] A.J. Wilkinson, G. Meaden, D.J. Dingley, High resolution mapping of strains and rotations using electron backscatter diffraction, Mater. Sci. Technol. 22 (2006) 1271–1278. doi:10.1179/174328406X130966.

[153] A.J. Wilkinson, G. Meaden, D.J. Dingley, High-resolution elastic strain measurement from electron backscatter diffraction patterns: New levels of sensitivity,

Ultramicroscopy. 106 (2006) 307–313. doi:10.1016/j.ultramic.2005.10.001.

[154] T.B. Britton, A.J. Wilkinson, High resolution electron backscatter diffraction measurements of elastic strain variations in the presence of larger lattice rotations, Ultramicroscopy. 114 (2012) 82–95. doi:10.1016/j.ultramic.2012.01.004.

[155] T.B. Britton, A.J. Wilkinson, Measurement of residual elastic strain and lattice rotations with high resolution electron backscatter diffraction, Ultramicroscopy. 111 (2011) 1395–1404. doi:10.1016/j.ultramic.2011.05.007.

[156] T. Ben Britton, J.L.R. Hickey, Understanding deformation with high angular resolution electron backscatter diffraction (HR-EBSD), (2017). http://arxiv.org/abs/1710.00728 (accessed December 13, 2017).

[157] T.B. Britton, J. Jiang, R. Clough, E. Tarleton, A.I. Kirkland, A.J. Wilkinson, Assessing the precision of strain measurements using electron backscatter diffraction – Part 2: Experimental demonstration, Ultramicroscopy. 135 (2013) 136–141. doi:http://dx.doi.org/10.1016/j.ultramic.2013.08.006.

[158] O.M. Akselsen, Diffusion bonding of ceramics, J. Mater. Sci. 27 (1992) 569–579. doi:10.1007/BF00554019.

[159] A.G. Lucille, F.A. Stevie, eds., Introduction to focused ion beams : instrumentation, theory, techniques, and practice, Springer, New York, 2005.

[160] M. Utlaut, Micro-machining and mask repair, in: N. Yao (Ed.), Focus. Ion Beam Syst., Cambridge University Press, Cambridge, 2007: pp. 268–294. doi:10.1017/CBO9780511600302.011.

[161] J. Mayer, L.A. Giannuzzi, T. Kamino, J. Michael, TEM sample preparation and FIB-induced damage, Mrs Bull. 32 (2007) 400–407.

[162] H. Bei, S. Shim, M.K. Miller, G.M. Pharr, E.P. George, Effects of focused ion beam milling

on the nanomechanical behavior of a molybdenum-alloy single crystal, Appl. Phys. Lett. 91 (2007). doi:doi:http://dx.doi.org/10.1063/1.2784948.

[163] C.A. Volkert, A.M. Minor, Focused Ion Beam Microscopy and Micromachining, Mrs Bull. 32 (2007) 389–399. doi:doi:10.1557/mrs2007.62.

[164] J.R. Greer, W.C. Oliver, W.D. Nix, Size dependence of mechanical properties of gold at the micron scale in the absence of strain gradients, Acta Mater. 53 (2005) 1821–1830. doi:http://dx.doi.org/10.1016/j.actamat.2004.12.031.

[165] A. Gleizer, G. Peralta, J.R. Kermode, A. De Vita, D. Sherman, Dissociative Chemisorption of O2 Inducing Stress Corrosion Cracking in Silicon Crystals, Phys. Rev. Lett. 112 (2014) 115501. http://link.aps.org/doi/10.1103/PhysRevLett.112.115501.

[166] S. Timoshenko, J. N. Goodier, Theory of elasticity, McGraw-Hill Book Company, 1951.

[167] H. Landolt, R. Börnstein, Elektrische, Piezoelektrische, Pyroelektrische, Piezooptische, Elektrooptische Konstanten und Nichtlineare Dielektrische Suszeptibilitaten, in: Zahlenwerte Un Funktionen Aus Naturwiss. Und Tech. Vol. Grouppe III, Springer-Verlag Berlin Heidelberg, 1979. doi:10.1007/10046537_20.

[168] S.J. Clark, M.D. Segall, C.J. Pickard, P.J. Hasnip, M.I.J. Probert, K. Refson, et al., First principles methods using CASTEP, Zeitschrift Für Krist. - Cryst. Mater. 220 (2005) 567–570. doi:10.1524/zkri.220.5.567.65075.

[169] G. Sernicola, T. Giovannini, P. Patel, J.R. Kermode, D.S. Balint, T. Ben Britton, et al., In situ stable crack growth at the micron scale, Nat. Commun. 8 (2017) 108. doi:10.1038/s41467-017-00139-w.

[170] J.L. Henshall, D.J. Rowcliffe, J.W. Edington, Fracture Toughness of Single-Crystal Silicon Carbide, J. Am. Ceram. Soc. 60 (1977) 373–375. doi:10.1111/j.1151-2916.1977.tb15564.x.

[171] J.L. Henshall, C.A. Brookes, The measurement ofKIC in single crystal SiC using the indentation method, J. Mater. Sci. Lett. 4 (1985) 783–786. doi:10.1007/BF00726990.

[172] I.J. McColm, Ceramic Hardness, Springer US, Boston, MA, 1990. doi:10.1007/978-1-4757-4732-4.

[173] L. Pastewka, A. Klemenz, P. Gumbsch, M. Moseler, Screened empirical bond-order potentials for Si-C, Phys. Rev. B. 87 (2013) 205410. http://link.aps.org/doi/10.1103/PhysRevB.87.205410.

[174] S.M. Wiederhorn, Fracture Surface Energy of Glass, J. Am. Ceram. Soc. 52 (1969) 99–105. doi:10.1111/j.1151-2916.1969.tb13350.x.

[175] G. Sernicola, T. Giovannini, P. Patel, J.R. Kermode, D.S. Balint, T. Ben Britton, et al., In situ stable crack growth at the micron scale, Nat. Commun. 8 (2017) 108. doi:10.1038/s41467-017-00139-w.

[176] D. McNamara, P. Alveen, D. Carolan, N. Murphy, A. Ivanković, Fracture toughness evaluation of polycrystalline diamond as a function of microstructure, Eng. Fract. Mech. 143 (2015) 1–16. doi:10.1016/j.engfracmech.2015.06.008.

[177] F. Bachmann, R. Hielscher, H. Schaeben, Texture Analysis with MTEX – Free and Open Source Software Toolbox, Solid State Phenom. 160 (2010) 63–68. doi:10.4028/www.scientific.net/SSP.160.63.

[178] MTEX Toolbox - equivalentRadius, (n.d.). https://mtex-toolbox.github.io/files/doc/grain2d.equivalentRadius.html (accessed October 14, 2017).

[179] O. Engler, V. Randle, Introduction to Texture Analysis: Macrotexture, Microtexture, and Orientation Mapping, Second Edition, CRC Press, 2009. https://books.google.co.uk/books?id=mpLq_0Bkn6cC.

[180] I. Arganda-Carreras, D. Legland, Classic Watershed, (2014). https://imagej.net/Classic_Watershed.

[181] P. Lehto, H. Remes, T. Saukkonen, H. Hänninen, J. Romanoff, Influence of grain size distribution on the Hall–Petch relationship of welded structural steel, Mater. Sci. Eng. A. 592 (2014) 28–39. doi:https://doi.org/10.1016/j.msea.2013.10.094.

[182] M.I. Mendelson, Average Grain Size in Polycrystalline Ceramics, J. Am. Ceram. Soc. 52 (1969) 443–446. doi:10.1111/j.1151-2916.1969.tb11975.x.

Appendix 1: Content permissions

Here copies of the permission to reuse the content included in figure 1.5, 1.6, 1.7, 2.4, 3.6 and 3.8 are appended.

JOHN WILEY AND SONS LICENSE
TERMS AND CONDITIONS

Jan 11, 2018

This Agreement between Giorgio Sernicola ("You") and John Wiley and Sons ("John Wiley and Sons") consists of your license details and the terms and conditions provided by John Wiley and Sons and Copyright Clearance Center.

License Number	4265810683425
License date	Jan 11, 2018
Licensed Content Publisher	John Wiley and Sons
Licensed Content Publication	Journal of the American Ceramic Society
Licensed Content Title	A Critical Evaluation of Indentation Techniques for Measuring Fracture Toughness: I, Direct Crack Measurements
Licensed Content Author	G.R. ANSTIS,P. CHANTIKUL,B.R. LAWN,D.B. MARSHALL
Licensed Content Date	Sep 1, 1981
Licensed Content Pages	6
Type of use	Dissertation/Thesis
Requestor type	University/Academic
Format	Print and electronic
Portion	Figure/table
Number of figures/tables	1
Original Wiley figure/table number(s)	figure 1
Will you be translating?	No
Title of your thesis / dissertation	Developing small scale fracture tests for polycrystalline diamond
Expected completion date	Jan 2018
Expected size (number of pages)	200
Requestor Location	Giorgio Sernicola Dept of Materials Royal School of Mines Imperial College London London, SW7 2BP United Kingdom Attn: Giorgio Sernicola
Publisher Tax ID	EU826007151
Total	0.00 GBP
Terms and Conditions	

SPRINGER NATURE LICENSE
TERMS AND CONDITIONS

Jan 11, 2018

This Agreement between Giorgio Sernicola ("You") and Springer Nature ("Springer Nature") consists of your license details and the terms and conditions provided by Springer Nature and Copyright Clearance Center.

License Number	4265801311404
License date	Jan 11, 2018
Licensed Content Publisher	Springer Nature
Licensed Content Publication	Journal of Materials Science (full set)
Licensed Content Title	Indentation fracture: principles and applications
Licensed Content Author	Brian Lawn, Rodney Wilshaw
Licensed Content Date	Jan 1, 1975
Licensed Content Volume	10
Licensed Content Issue	6
Type of Use	Thesis/Dissertation
Requestor type	academic/university or research institute
Format	print and electronic
Portion	figures/tables/illustrations
Number of figures/tables/illustrations	1
Will you be translating?	no
Circulation/distribution	<501
Author of this Springer Nature content	no
Title	Developing small scale fracture tests for polycrystalline diamond
Instructor name	TB Britton, F Giuliani
Institution name	Imperial College London
Expected presentation date	Jan 2018
Portions	Figure 12
Requestor Location	Giorgio Sernicola Dept of Materials Royal School of Mines Imperial College London London, SW7 2BP United Kingdom Attn: Giorgio Sernicola
Billing Type	Invoice
Billing Address	Giorgio Sernicola Dept of Materials Royal School of Mines Imperial College London London, United Kingdom SW7 2BP Attn: Giorgio Sernicola
Total	0.00 GBP
Terms and Conditions	

Springer Nature Terms and Conditions for RightsLink Permissions

ELSEVIER LICENSE
TERMS AND CONDITIONS

Jan 11, 2018

This Agreement between Giorgio Sernicola ("You") and Elsevier ("Elsevier") consists of your license details and the terms and conditions provided by Elsevier and Copyright Clearance Center.

License Number	4265810429899
License date	Jan 11, 2018
Licensed Content Publisher	Elsevier
Licensed Content Publication	Materials Science and Engineering: A
Licensed Content Title	Measurement of mechanical properties by ultra-low load indentation
Licensed Content Author	G.M. Pharr
Licensed Content Date	Sep 30, 1998
Licensed Content Volume	253
Licensed Content Issue	1-2
Licensed Content Pages	9
Start Page	151
End Page	159
Type of Use	reuse in a thesis/dissertation
Intended publisher of new work	other
Portion	figures/tables/illustrations
Number of figures/tables/illustrations	2
Format	both print and electronic
Are you the author of this Elsevier article?	No
Will you be translating?	No
Original figure numbers	figures 7, 8
Title of your thesis/dissertation	Developing small scale fracture tests for polycrystalline diamond
Publisher of new work	Imperial College London
Author of new work	TB Britton, F Giuliani
Expected completion date	Jan 2018
Estimated size (number of pages)	200
Requestor Location	Giorgio Sernicola Dept of Materials Royal School of Mines Imperial College London London, SW7 2BP United Kingdom Attn: Giorgio Sernicola
Publisher Tax ID	GB 494 6272 12
Total	0.00 USD
Terms and Conditions	

RightsLink Printable License

SPRINGER NATURE LICENSE
TERMS AND CONDITIONS

Jan 11, 2018

This Agreement between Giorgio Sernicola ("You") and Springer Nature ("Springer Nature") consists of your license details and the terms and conditions provided by Springer Nature and Copyright Clearance Center.

License Number	4265810948450
License date	Jan 11, 2018
Licensed Content Publisher	Springer Nature
Licensed Content Publication	Journal of Materials Science (full set)
Licensed Content Title	The toughening and strengthening of ceramic materials through discontinuous reinforcement
Licensed Content Author	Kenong Xia, Terence G. Langdon
Licensed Content Date	Jan 1, 1994
Licensed Content Volume	29
Licensed Content Issue	20
Type of Use	Thesis/Dissertation
Requestor type	academic/university or research institute
Format	print and electronic
Portion	figures/tables/illustrations
Number of figures/tables/illustrations	4
Will you be translating?	no
Circulation/distribution	<501
Author of this Springer Nature content	no
Title	Developing small scale fracture tests for polycrystalline diamond
Instructor name	TB Britton, F Giuliani
Institution name	Imperial College London
Expected presentation date	Jan 2018
Portions	Figures 1,2,3,4
Requestor Location	Giorgio Sernicola Dept of Materials Royal School of Mines Imperial College London London, SW7 2BP United Kingdom Attn: Giorgio Sernicola
Billing Type	Invoice
Billing Address	Giorgio Sernicola Dept of Materials Royal School of Mines Imperial College London London, United Kingdom SW7 2BP Attn: Giorgio Sernicola
Total	0.00 GBP

Terms and Conditions

https://s100.copyright.com/AppDispatchServlet 1/3

ELSEVIER LICENSE
TERMS AND CONDITIONS

Jan 11, 2018

This Agreement between Giorgio Sernicola ("You") and Elsevier ("Elsevier") consists of your license details and the terms and conditions provided by Elsevier and Copyright Clearance Center.

License Number	4265820093503
License date	Jan 11, 2018
Licensed Content Publisher	Elsevier
Licensed Content Publication	Ceramics International
Licensed Content Title	The influence of microstructure on the fracture statistics of polycrystalline diamond and polycrystalline cubic boron nitride
Licensed Content Author	D. McNamara,D. Carolan,P. Alveen,N. Murphy,A. Ivanković
Licensed Content Date	Sep 1, 2014
Licensed Content Volume	40
Licensed Content Issue	8
Licensed Content Pages	7
Start Page	11543
End Page	11549
Type of Use	reuse in a thesis/dissertation
Intended publisher of new work	other
Portion	figures/tables/illustrations
Number of figures/tables/illustrations	1
Format	both print and electronic
Are you the author of this Elsevier article?	No
Will you be translating?	No
Original figure numbers	figure 4
Title of your thesis/dissertation	Developing small scale fracture tests for polycrystalline diamond
Publisher of new work	Imperial College London
Author of new work	TB Britton, F Giuliani
Expected completion date	Jan 2018
Estimated size (number of pages)	200
Requestor Location	Giorgio Sernicola Dept of Materials Royal School of Mines Imperial College London London, SW7 2BP United Kingdom Attn: Giorgio Sernicola
Publisher Tax ID	GB 494 6272 12
Total	0.00 GBP

CAMBRIDGE UNIVERSITY PRESS LICENSE
TERMS AND CONDITIONS

Jan 11, 2018

This Agreement between Giorgio Sernicola ("You") and Cambridge University Press ("Cambridge University Press") consists of your license details and the terms and conditions provided by Cambridge University Press and Copyright Clearance Center.

License Number	4265821015546
License date	Jan 11, 2018
Licensed Content Publisher	Cambridge University Press
Licensed Content Publication	MRS Bulletin
Licensed Content Title	Focused Ion Beam Microscopy and Micromachining
Licensed Content Author	C. A. Volkert, A. M. Minor
Licensed Content Date	Oct 30, 2010
Licensed Content Volume	32
Licensed Content Issue	5
Start page	389
End page	399
Type of Use	Dissertation/Thesis
Requestor type	Not-for-profit
Portion	Text extract
Number of pages requested	1
Order reference number	
Territory for reuse	World
Title of your thesis / dissertation	Developing small scale fracture tests for polycrystalline diamond
Expected completion date	Jan 2018
Estimated size(pages)	200
Requestor Location	Giorgio Sernicola Dept of Materials Royal School of Mines Imperial College London London, SW7 2BP United Kingdom Attn: Giorgio Sernicola
Publisher Tax ID	GB823847609
Billing Type	Invoice
Billing Address	Giorgio Sernicola Dept of Materials Royal School of Mines Imperial College London London, United Kingdom SW7 2BP Attn: Giorgio Sernicola
Total	0.00 GBP
Terms and Conditions	

TERMS & CONDITIONS

Cambridge University Press grants the Licensee permission on a non-exclusive non-transferable basis to reproduce, make available or otherwise use the Licensed content

RightsLink Printable License

SPRINGER NATURE LICENSE
TERMS AND CONDITIONS

Jan 11, 2018

This Agreement between Giorgio Sernicola ("You") and Springer Nature ("Springer Nature") consists of your license details and the terms and conditions provided by Springer Nature and Copyright Clearance Center.

License Number	4265820874515
License date	Jan 11, 2018
Licensed Content Publisher	Springer Nature
Licensed Content Publication	Springer eBook
Licensed Content Title	Strain Mapping Using Electron Backscatter Diffraction
Licensed Content Author	Angus J. Wilkinson, David J. Dingley, Graham Meaden
Licensed Content Date	Jan 1, 2009
Type of Use	Thesis/Dissertation
Requestor type	academic/university or research institute
Format	print and electronic
Portion	figures/tables/illustrations
Number of figures/tables/illustrations	1
Will you be translating?	no
Circulation/distribution	<501
Author of this Springer Nature content	no
Title	Developing small scale fracture tests for polycrystalline diamond
Instructor name	TB Britton, F Giuliani
Institution name	Imperial College London
Expected presentation date	Jan 2018
Portions	figure 17.1
Requestor Location	Giorgio Sernicola Dept of Materials Royal School of Mines Imperial College London London, SW7 2BP United Kingdom Attn: Giorgio Sernicola
Billing Type	Invoice
Billing Address	Giorgio Sernicola Dept of Materials Royal School of Mines Imperial College London London, United Kingdom SW7 2BP Attn: Giorgio Sernicola
Total	0.00 GBP

Terms and Conditions

Springer Nature Terms and Conditions for RightsLink Permissions
Springer Customer Service Centre GmbH (the Licensor) hereby grants you a non-exclusive, world-wide licence to reproduce the material and for the purpose and

AIP PUBLISHING LLC LICENSE
TERMS AND CONDITIONS

Jan 11, 2018

This Agreement between Giorgio Sernicola ("You") and AIP Publishing LLC ("AIP Publishing LLC") consists of your license details and the terms and conditions provided by AIP Publishing LLC and Copyright Clearance Center.

License Number	4265811352401
License date	Jan 11, 2018
Licensed Content Publisher	AIP Publishing LLC
Licensed Content Publication	Applied Physics Letters
Licensed Content Title	Measuring the fracture resistance of hard coatings
Licensed Content Author	S. Liu, J. M. Wheeler, P. R. Howie, et al
Licensed Content Date	Apr 29, 2013
Licensed Content Volume	102
Licensed Content Issue	17
Type of Use	Thesis/Dissertation
Requestor type	Student
Format	Print and electronic
Portion	Figure/Table
Number of figures/tables	1
Title of your thesis / dissertation	Developing small scale fracture tests for polycrystalline diamond
Expected completion date	Jan 2018
Estimated size (number of pages)	200
Requestor Location	Giorgio Sernicola Dept of Materials Royal School of Mines Imperial College London London, SW7 2BP United Kingdom Attn: Giorgio Sernicola
Billing Type	Invoice
Billing Address	Giorgio Sernicola Dept of Materials Royal School of Mines Imperial College London London, United Kingdom SW7 2BP Attn: Giorgio Sernicola
Total	0.00 GBP

Terms and Conditions

AIP Publishing LLC -- Terms and Conditions: Permissions Uses

AIP Publishing hereby grants to you the non-exclusive right and license to use and/or distribute the Material according to the use specified in your order, on a one-time basis, for the specified term, with a maximum distribution equal to the number that you have ordered. Any links or other content accompanying the Material are not the subject of this license.

1. You agree to include the following copyright and permission notice with the reproduction of the Material:"Reprinted from [FULL CITATION], with the permission of AIP Publishing." For